Acute and chronic effects of anti-cancer agents on cardiac mitochondrial function

Jessica Maeve O'Flaherty Elder

Myocardial Function
National Heart and Lung Institute
Imperial College London

A thesis submitted for the degree of
Doctor of Philosophy

April 2017

Abstract

Cardiotoxicity resulting from the agents used to treat neoplastic disorders is becoming increasingly clinically relevant as cancer survival rates improve. Mitochondria are a common target and potential mediator of this toxicity. Healthy mitochondrial function is integral to both the life and death of cardiomyocytes and alterations in mitochondrial function are increasingly recognised in patients presenting with cardiomyopathy. This PhD project examined the acute and chronic effects of anti-cancer agents on the heart with a specific focus on cardiac mitochondrial function.

A rat model of DOX-induced cardiomyopathy was utilised to examine the chronic effect of doxorubicin (DOX) on cardiac mitochondria. DOX-treated rats showed progressive cardiac decline with a significant reduction in ejection fraction and marked mitochondrial morphological changes. RNA sequencing of left ventricular tissue revealed that the most significantly decreased transcript levels were those related to mitochondrial function. Twenty-four hour DOX treatment of freshly isolated adult rat ventricular cardiomyocytes resulted in a significant decrease in maximal respiratory capacity and a significant increase in mitochondrial-related transcript levels. In the Langendorff-perfused rat heart DOX infusion resulted in acute progressive concentration-dependent mitochondrial membrane potential ($\Delta\Psi_m$) dissipation. Infusion of the tyrosine kinase inhibitors sunitinib or SU14813 was also found to result in a slight dissipation of the $\Delta\Psi_m$ in the isolated rat heart.

This study demonstrates that the effects of DOX on cardiac mitochondrial function are both acute and chronic and contribute significantly to the pathogenesis of DOX-induced cardiomyopathy. Overall, these findings demonstrate that mitochondrial dysfunction plays a

significant role in the development of anti-cancer agent induced-cardiomyopathy and highlights mitochondria as a novel target for cardioprotection.

Declaration of originality

All work presented in this thesis is my own, unless indicated through references or credits to others.

Copyright declaration

The copyright of this thesis rests with the author and is made available under a Creative Commons Attribution Non-Commercial No Derivatives licence. Researchers are free to copy, distribute or transmit the thesis on the condition that they attribute it, that they do not use it for commercial purposes, and that they do not alter, transform or build upon it. For any reuse or redistribution, researchers must make clear to others the licence terms of this work.

Acknowledgements

Firstly, I would like to thank my supervisors, Dr. Alexander Lyon and Prof. Sian Harding, without whom this research would not have been possible: Alex, for allowing me to undertake this research project and for encouraging my enthusiasm for cardiac mitochondrial biology; Sian, for her invaluable support and guidance, for always being available to discuss any issues that arose and for teaching me how to be a powerhouse.

I wish to express my sincerest thanks to my friends and colleagues at Imperial for their constant support and encouragement over the years and for making long days in the lab so much more enjoyable. My thanks to Benjamin Dyer for his support and assistance with the *in vivo* model and to Peter O'Gara for expertly isolating cardiomyocytes and for always providing perspective. I would like to express my gratitude to Cheuk Ting Angela Yiu for her hard work and enthusiasm, Joanne Tonkin for performing the histological sectioning and staining, Jennifer Simonotto for writing and debugging code, Matthew Tranter for helping maintain the echo and optical mapping systems and Pradeep Luther for teaching me and letting me undertake the TEM work in his laboratory.

I am grateful to the British Heart Foundation for funding the work described in this thesis. I also wish to express my thanks to all members of the CBS at Imperial who helped to facilitate my work in the unit.

Finally, I would like to thank my family and friends for their unwavering support and love while completing this work. I am especially grateful to Fränze for her support and encouragement, pertinent suggestions and kind editorial work. Kat for doing this with me every step of the way I am eternally grateful and very lucky to have you.

Abbreviations

ABCB8	ATP Binding Cassette Subfamily B Member 8
afu	Arbitrary fluorescence units
AIF	Apoptosis-inducing factor
AMP	Adenosine monophosphate
AMPK	Adenosine monophosphate-activated protein kinase
ANF	Average normalised fluorescence
ANOVA	Analysis of variance
ANP	Atrial natriuretic peptide
ANT	Adenine nucleotide translocase
ARVM	Adult rat ventricular cardiomyocytes
ASC	Apoptosis-associated speck-like protein containing a caspase-recruitment domain
ATP	Adenosine triphosphate
BAD	B-cell lymphoma-2-associated death promoter
BAK	B-cell lymphoma-2 antagonist/killer
BAX	B-cell lymphoma-2-associated X protein
BCL	B-cell lymphoma
BH3	B-cell lymphoma-2 homology 3
BIM	B-cell lymphoma-2-interacting mediator of cell death
B-mode	Brightness mode
BNP	Brain natriuretic peptide
BPM	Beats per minute
CARD	Caspase-recruitment domain
CCD	Charge-coupled device
CD	Cluster of differentiation
CDD	Continuous daily dosing
cDNA	Complementary deoxyribonucleic acid
CoA	Coenzyme A
cps	Counts per second
CsA	Cyclosporin A
CSF-1R	Colony-stimulating factor-1 receptor
DAPI	4, 6-diamidino-2-phenylindole

DAVID	Database for annotation, visualisation and integrated discovery
DIABLO	Direct inhibitor of apoptosis-binding protein with low pI
DMSO	Dimethyl sulfoxide
DNA	Deoxyribonucleic acid
DNase	Deoxyribonuclease
DOX	Doxorubicin
Δp	Electrochemical proton gradient
ΔpH	pH gradient
$\Delta\Psi_m$	Mitochondrial membrane potential
ECG	Electrocardiogram
ECM	Extracellular matrix
EDD	End diastolic diameter
ESD	End systolic diameter
ETC	Electron transport chain
FCCP	Carbonyl cyanide-4-trifluoromethoxyphenylhydrazone
FDA	Food and drug administration
FDR	False discovery rate
Flt-3	Fms-like tyrosine kinase 3
FPKM	Fragments per kilobase of transcript per million mapped reads
FS	Fractional shortening
H&E	Haematoxylin and eosin Y
HER	Human epidermal growth factor receptor
HF	Heart failure
hiPSC-CMs	Human induced pluripotent stem cell-derived cardiomyocytes
HO-1	Heme oxygenase 1
HR	Heart rate
HtrA2	High-temperature requirement A2
ICL	Imperial College London
IFN-γ	Interferon gamma
IL	Interleukin
IL-1R1	Interleukin-1 type I receptor
IL-1Ra	Interleukin-1 type I receptor antagonist
IMM	Inner mitochondrial membrane
IPA	Ingenuity pathway analysis

IRI	Ischaemia-reperfusion injury
IV	Intravenous
JC-1	5, 5′, 6, 6′-tetrachloro-1, 1′, 3, 3′-tetra-ethyl benzimidazolyl carbocyanine iodide
Kit	Stem cell factor receptor
LED	Light emitting diode
LV	Left ventricular
LVEF	Left ventricular ejection fraction
MAPK	Mitogen-activated protein kinase
MCL-1	Myeloid cell leukaemia sequence 1
MCU	Mitochondrial calcium uniporter
M-mode	Motion mode
mPTP	Mitochondrial permeability transition pore
MRC	Medical Research Council
mtDNA	Mitochondrial deoxyribonucleic acid
mV	Millivolts
NCX	Na^+/Ca^{2+} exchanger
NF-κB	Nuclear factor kappa-light-chain-enhancer of activated B cells
NHLI	National Heart and Lung Institute
NO	Nitric oxide
NRG	Neuregulin
NRVM	Neonatal rat ventricular cardiomyocytes
ns	Not significant
OCR	Oxygen consumption rate
OMM	Outer mitochondrial membrane
PBS	Phosphate buffered saline
PDGFR	Platelet-derived growth factor receptor
Pi	Inorganic phosphate
PI3K	Phosphatidylinositol 3-kinase
Ppargc1a	Peroxisome proliferator-activated receptor gamma co-activator 1 alpha
Ppargc1b	Peroxisome proliferator-activated receptor gamma co-activator 1 beta
PYD	Pyrin domain
qPCR	Quantitative real-time polymerase chain reaction
RET	Rearranged during transfection
RNA	Ribonucleic acid

RNA-seq	Ribonucleic acid sequencing
ROI	Region of interest
ROS	Reactive oxygen species
rRNA	Ribosomal ribonucleic acid
RSK	Ribosomal S6 kinase
RyR2	Ryanodine receptor 2
SD	Sprague Dawley
SEM	Standard error of the mean
SERCA2A	Sarco/endoplasmic reticulum calcium ATPase
Smac	Second mitochondria-derived activator of caspases
SODs	Superoxide dismutases
STB	Sunitinib
SU	SU14813
tBid	Truncated form of B-cell lymphoma-2 homology 3-interacting domain death agonist
TCA	Tricarboxylic acid
TEM	Transmission electron microscopy
TKI	Tyrosine kinase inhibitor
TLR	Toll-like receptor
TMRE	Tetramethylrhodamine ethyl ester
TMRM	Tetramethylrhodamine methyl ester
TNF	Tumour necrosis factor
Top1mt	Mitochondrial topoisomerase I
Top2	Topoisomerase-II
Top2b	Topoisomerase-II beta
tRNA	Transfer ribonucleic acid
VDAC	Voltage-dependent anion-selective channel
VEGF-A	Vascular endothelial growth factor A
VEGFR2	Vascular endothelial growth factor receptor 2
WGCNA	Weighted gene co-expression network analysis

Table of Contents

Abstract **2**

Declaration of originality **4**

Copyright declaration **4**

Acknowledgements **5**

Abbreviations **6**

Table of Contents **10**

List of Figures **15**

List of Tables **19**

Chapter 1 Introduction **21**

1.1 Cardiovascular disease and cancer therapy **21**

1.1.1 Cancer survivorship in the 21st century 21

1.1.2 Cardiotoxicity of anti-cancer agents 22

1.2 The effect of cancer on cardiac function **28**

1.3 Mitochondria in the heart **29**

1.3.1 Mitochondrial structure 30

1.3.2 Bioenergetics and metabolism 31

1.3.3 Mitochondria and calcium handling 34

1.3.4 Mitochondria and reactive oxygen species generation 35

1.3.5 Mitochondria and cell death 36

1.4 Proposed mechanisms of DOX-induced cardiotoxicity **40**

1.4.1 Redox cycling of DOX and ROS generation 40

1.4.2 Modulation of intracellular calcium handling with DOX treatment 45

1.4.3 Mitochondrial dysfunction in DOX-induced cardiomyopathy 45

1.4.4 Direct mitochondrial damage by DOX 46

1.4.5 Nuclear DNA topoisomerases 48

1.4.6 Inflammation and DOX-induced cardiomyopathy 49

1.5 Proposed mechanisms of sunitinib-induced cardiotoxicity **51**

1.5.1 Hypertension 51

1.5.2 AMP-activated protein kinase 53

1.6 Summary **54**

1.7 Hypothesis **55**
1.8 Aim of the study **55**
1.8.1 Aims 55
Chapter 2 Material and methods **57**
2.1 Animals **57**
2.2 Solutions and reagents **57**
2.2.1 Anti-cancer agents 58
***2.3 In vivo* studies** **59**
2.3.1 Study outline 59
2.3.2 DOX administration protocol 60
2.3.3 Echocardiography protocol 61
2.4 Isolated cardiomyocyte studies **62**
2.4.1 Isolation and culture of adult rat ventricular cardiomyocytes 62
2.4.2 Twenty-four hour anti-cancer agent treatment of ARVM 64
2.4.3 Assessing cardiac mitochondrial function *in vitro* 64
2.5 *Ex vivo* optical mapping of mitochondrial function **65**
2.5.1 Langendorff-perfused rat heart preparation 65
2.5.2 Optical apparatus 66
2.5.3 Optical mapping protocol 69
2.5.4 Optical mapping data analysis 69
2.6 Transmission electron microscopy **70**
2.7 Histology **71**
2.8 RNA extraction **72**
2.9 Quantitative real-time polymerase chain reaction **73**
2.10 RNA-sequencing **74**
2.10.1 Library preparation and sequencing 74
2.10.2 Bioinformatics analysis 74
2.11 Estimation of mtDNA copy number **75**
2.12 Statistical analysis **76**
Chapter 3 A chronic rat model of DOX-induced cardiomyopathy **78**
3.1 Introduction **78**
3.2 Hypothesis and aims **81**
3.3 Results **82**

3.3.1 Establishing a chronic rat model of DOX-induced cardiomyopathy 82
3.3.2 The effect of chronic DOX treatment on subcellular morphology 91
3.3.3 Pathological effects of DOX treatment in the heart 100
3.4 Discussion 102
3.4.1 A chronic rat model of DOX-induced cardiomyopathy 102
3.4.2 Mitochondrial dysfunction in DOX-induced cardiomyopathy 103
3.4.3 Chronic DOX treatment results in a pro-inflammatory state 105
3.4.4 Limitations and future directions 106
3.4.5 Conclusion 107

Chapter 4 Differential gene expression in a rat model of DOX-induced cardiomyopathy 109
4.1 Introduction 109
4.2 Hypothesis and aim 110
4.3 Results 111
4.3.1 RNA-seq and processing 111
4.3.2 Weighted gene co-expression network analysis 115
4.3.3 Literature-curated gene knowledge bases 119
4.3.4 qPCR validation of differential gene expression analysis by RNA-seq in DOX-induced cardiomyopathy 125
4.3.5 A reduced mtDNA copy number in DOX-induced cardiotoxicity 138
4.4 Discussion 140
4.4.1 Transcriptome profiling of DOX-induced cardiomyopathy 140
4.4.2 Mitochondrial dysfunction in DOX-induced cardiomyopathy 141
4.4.3 Chronic DOX treatment results in a pro-inflammatory state which triggers an immune response and ECM remodelling 143
4.4.4 Limitations and future directions 147
4.4.5 Conclusion 148

Chapter 5 The acute effect of DOX on cardiac mitochondria in isolated ARVM 150
5.1 Introduction 150
5.2 Hypothesis and aims 153
5.3 Results 154
5.3.1 *In vitro* assessment of cardiac mitochondrial function in isolated ARVM 154

5.3.2 The effect of 24 h DOX treatment on the mitochondrial respiratory capacity of ARVM 159
5.3.3 Differential gene expression following 24 h DOX treatment in ARVM 163
5.4 Discussion 168
5.4.1 *In vitro* assessment of cardiac mitochondrial function in isolated ARVM 168
5.4.2 The effect of 24 h DOX treatment on the mitochondrial respiratory capacity of ARVM 168
5.4.3 Differential gene expression following 24 h DOX treatment in ARVM 170
5.4.4 Limitations and future directions 172
5.4.5 Conclusion 173
Chapter 6 The acute effect of DOX on the $\Delta\Psi_m$ in the Langendorff-perfused rat heart 175
6.1 Introduction 175
6.2 Hypothesis and aims 180
6.3 Results 181
6.3.1 *Ex vivo* optical mapping of mitochondrial function in the Langendorff-perfused rat heart 181
6.3.2 Assessing the feasibility of using DOX for *ex vivo* optical mapping of mitochondrial function in the Langendorff-perfused rat heart 188
6.3.3 Acute concentration-dependent $\Delta\Psi_m$ dissipation with DOX in the Langendorff-perfused rat heart 192
6.3.4 The effect of a metabolic challenge on mitochondrial function in Langendorff-perfused rat hearts pre-perfused with DOX 203
6.4 Discussion 205
6.4.1 *Ex vivo* optical mapping of mitochondrial function in the Langendorff-perfused rat heart 205
6.4.2 DOX for *ex vivo* optical mapping of mitochondrial function in the Langendorff-perfused rat heart 205
6.4.3 Acute progressive concentration-dependent $\Delta\Psi_m$ dissipation with DOX in the Langendorff-perfused rat heart 206
6.4.4 The effect of a metabolic challenge on mitochondrial function in Langendorff-perfused rat hearts pre-perfused with DOX 208
6.4.5 Limitations and future directions 208
6.4.6 Conclusion 209

Chapter 7 The acute effect of TKIs on cardiac mitochondrial function 211
7.1 Introduction 211
7.2 Hypothesis and aims 215
7.3 Results 216
7.3.1 The effect of 24 h STB treatment on the mitochondrial respiratory capacity of ARVM 216
7.3.2 The acute effect of TKIs on the $\Delta\Psi_m$ in the Langendorff-perfused rat heart..... 218
7.4 Discussion 222
7.4.1 The effect of 24 h STB treatment on the mitochondrial respiratory capacity of ARVM 222
7.4.2 The acute effect of TKIs on the $\Delta\Psi_m$ in the Langendorff-perfused rat heart..... 223
7.4.3 Limitations and future directions..... 224
7.4.4 Conclusion..... 225
Chapter 8 Final discussion 227
8.1 Overview 227
8.2 The chronic effect of DOX treatment on the myocardium and cardiac mitochondria 228
8.3 The acute effect of anti-cancer agents on cardiac mitochondrial function 230
8.4 The acute versus chronic effect of DOX treatment on myocardial and cardiac mitochondrial function 231
8.5 Model limitations..... 232
8.6 Future directions..... 233
8.7 Conclusion 237
References 240

List of Figures

Fig. 1.1 Schematic representation of mitochondrial structure (above) and the electron transport chain in the inner mitochondrial membrane (below). Complex I (labeled I) accepts electrons from the Krebs cycle electron carrier nicotinamide adenine dinucleotide (NADH) and passes them to coenzyme Q which also receives electrons from complex II (labeled II). Coenzyme Q passes electrons to complex III (labeled III) which passes them to cytochrome *c*. Cytochrome *c* passes electrons to complex IV (labeled IV) which uses the electrons and hydrogen Ions to reduce molecular oxygen to water. The efflux of protons creates an electrochemical gradient that is used by ATP synthase to make ATP. Adapted from Agrawal and Mabalirajan (Agrawal and Mabalirajan, 2016). 33

Fig. 1.2 Schematic representation of redox cycling of DOX between the quinone and semiquinone form resulting in superoxide generation. 41

Fig. 1.3 Uptake of the mitochondrially-targeted anti-oxidant MitoQ by mitochondria within cells. This schematic shows the uptake of $MitoQ_{(C10)}$ into cells driven by the plasma membrane potential ($\Delta\Psi_p$) before being further accumulated into mitochondria driven by the mitochondrial membrane potential ($\Delta\Psi_m$). Adapted from Smith *et al*. 44

Fig. 2.1 Representative image of a freshly isolated adult rat ventricular cardiomyocyte stained for α-actinin (sarcomeric). Scale bar represents 10 μm. 64

Fig. 2.2 Schematic representation of the experimental apparatus for *ex vivo* optical mapping of mitochondrial function. 68

Fig. 2.3 Photos of the optical mapping system used for *ex vivo* imaging. 68

Fig. 3.1 Overview of chronic rat model of chemotherapy cardiomyopathy. 83

Fig. 3.2 Contractile dysfunction in DOX-treated versus control rat heart following 8 weeks of DOX dosing and 3 weeks of off-dosing. 84

Fig. 3.3 Progressive DOX-induced contractile dysfunction assessed by echocardiography…86

Fig. 3.4 Transcript levels of markers of myocardial dysfunction and ventricular remodelling in DOX-induced cardiomyopathy. 89

Fig. 3.5 Correlation analysis between LVEF and transcript levels of markers of myocardial dysfunction and ventricular remodelling in DOX-induced cardiomyopathy. 90

Fig. 3.6 Light microscopy micrographs of subcellular morphological changes induced by chronic DOX treatment. 92

Fig. 3.7 TEM micrographs of subcellular morphological changes as a result of chronic DOX treatment characterised by diffuse vacuoles and Z-line distortion. 94

Fig. 3.8 TEM micrographs of subcellular morphological changes as a result of chronic DOX treatment characterised by altered mitochondrial structure and degeneration. 95
Fig. 3.9 TEM micrographs of subcellular morphological changes as a result of chronic DOX treatment characterised by altered mitochondrial distribution and structure. 96
Fig. 3.10 TEM micrographs of subcellular morphological changes as a result of chronic DOX treatment characterised by vacuoles containing concentric sheets of inner membrane and/or granular deposits. 97
Fig. 3.11 TEM micrographs of subcellular morphological changes as a result of chronic DOX treatment characterised by vacuoles containing concentric sheets of inner membrane and/or granular deposits. 98
Fig. 3.12 TEM micrographs of subcellular morphological changes as a result of chronic DOX treatment characterised by swollen vacuoles and myofibrillar loss and disruption. 99
Fig. 3.13 Histological analysis of myocardial tissue following chronic DOX treatment. 101
Fig. 4.1 Validation and correlation of transcript level values between RNA-seq and qPCR. 112
Fig. 4.2 Differentially expressed genes between control and DOX-treated samples. 114
Fig. 4.3 WGCNA between control and DOX-treated samples. 117
Fig. 4.4 Functional annotation clustering with enrichment scores by NIH DAVID of genes present in each module significantly correlated with DOX treatment. 118
Fig. 4.5 Ingenuity Pathway Analysis of differentially expressed gene changes in DOX-induced cardiotoxicity. 124
Fig. 4.6 qPCR analysis of transcript levels of genes related to the respiratory chain complexes that were decreased in DOX-induced cardiomyopathy. 129
Fig. 4.7 qPCR analysis of transcript levels of genes related to mitochondrial function and cell death pathways in DOX-induced cardiomyopathy. 130
Fig. 4.8 qPCR analysis of transcript levels of genes related to ROS production in DOX-induced cardiomyopathy. 132
Fig. 4.9 qPCR analysis of transcript levels of genes related to inflammation and the immune response in DOX-induced cardiomyopathy. 135
Fig. 4.10 qPCR analysis of transcript levels of genes related to cardiac remodelling and dysfunction in DOX-induced cardiomyopathy. 137
Fig. 4.11 qPCR analysis of the mitochondrial to nuclear DNA ratio which was used as an estimation of mtDNA copy number in DOX-induced cardiomyopathy. 139
Fig. 5.1 The OCR of ARVM measured during the Mito Stress Test using a Seahorse XFp analyser. 156

Fig. 5.2 The OCR in control experiments examining the effect of DOX's fluorescence on the measurement of oxygen by the Seahorse XFp analyser with no cells present. 158
Fig. 5.3 Assessing cardiac mitochondrial function in isolated ARVM with 24 h DOX 3 μM treatment. 161
Fig. 5.4 Assessing cardiac mitochondrial function in isolated ARVM with 24 h DOX 10 μM treatment. 162
Fig. 5.5 qPCR analysis of transcript levels of genes related to the respiratory chain complexes following 24 h DOX treatment in ARVM. 165
Fig. 5.6 qPCR analysis of transcript levels of genes related to the mitochondrial function and ROS production following 24 h DOX treatment in ARVM. 166
Fig. 5.7 qPCR analysis of transcript levels of genes related to cardiac dysfunction following 24 h DOX treatment in ARVM. 167
Fig. 6.1 Whole heart images of setup of *ex vivo* optical mapping of cardiac mitochondrial function in the Langendorff-perfused beating rat heart. 182
Fig. 6.2 Real-time imaging of normalised whole heart and background TMRM fluorescence during TMRM loading phase in the Langendorff-perfused rat heart. 183
Fig. 6.3 Real-time imaging of epicardial TMRM fluorescence in control Langendorff-perfused rat hearts. 185
Fig. 6.4 Real-time changes in normalised epicardial TMRM fluorescence with infusion of the mitochondrial uncoupling agent FCCP and oligomycin A in Langendorff-perfused rat hearts. 187
Fig. 6.5 Fluorescence at room temperature measured using a cuvette-based spectrofluorophotometer. 190
Fig. 6.6 Fluorescence imaged every 2 min with an excitation wavelength of 530 nm and an emission wavelength of 585 ± 20 nm in Langendorff-perfused rat hearts. 191
Fig. 6.7 Real-time changes in normalised epicardial TMRM fluorescence with DOX perfusion in the Langendorff-perfused rat heart. 193
Fig. 6.8 Real-time imaging of normalised whole heart and background TMRM fluorescence during DOX 10 μM perfusion in the Langendorff-perfused rat heart. Images show normalised TMRM fluorescence across the whole heart at (A) 0 min (baseline) (B) 12 min (C) 24 min (D) 36 min (E) 48 min (F) 60 min of DOX 10 μM perfusion. Scale bar shows normalised TMRM fluorescence where 0 is the minimum and 1 is the maximum normalised fluorescence value. 195

Fig. 6.9 Real-time imaging of normalised whole heart and background TMRM fluorescence during control perfusion in the Langendorff-perfused rat heart. Images show normalised TMRM fluorescence across the whole heart at (A) 0 min (baseline) (B) 12 min (C) 24 min (D) 36 min (E) 48 min (F) 60 min of perfusion. Scale bar shows normalised TMRM fluorescence where 0 is the minimum and 1 is the maximum normalised fluorescence value. 196
Fig. 6.10 Real-time imaging of normalised whole heart epicardial TMRM fluorescence during DOX 10 μM perfusion in the Langendorff-perfused rat heart. 197
Fig. 6.11 Real-time imaging of normalised whole heart epicardial TMRM fluorescence during control perfusion in the Langendorff-perfused rat heart. 198
Fig. 6.12 Histograms of normalised TMRM fluorescence across the whole epicardial surface during DOX 10 μM perfusion in the Langendorff-perfused rat heart. 199
Fig. 6.13 Histograms of normalised TMRM fluorescence across the whole epicardial surface during vehicle control perfusion in the Langendorff-perfused rat heart. 200
Fig. 6.14 Histograms of normalised TMRM fluorescence across the whole epicardial surface during DOX 1 μM perfusion in the Langendorff-perfused rat heart. 201
Fig. 6.15 Real-time imaging of normalised whole heart epicardial TMRM fluorescence and the ANF over time in Langendorff-perfused rat hearts. 202
Fig. 6.16 The effect of a metabolic challenge on normalised TMRM fluorescence in Langendorff-perfused rat hearts. 204
Fig. 7.1 The chemical structure of the TKIs STB and SU. 214
Fig. 7.2 Assessing cardiac mitochondrial function in isolated ARVM with 24 h STB 1 μM treatment. 217
Fig. 7.3 Real-time changes in normalised epicardial TMRM fluorescence with SU perfusion in the Langendorff-perfused rat heart. 219
Fig. 7.4 Real-time changes in normalised epicardial TMRM fluorescence with STB perfusion with and without DOX in comparison to DOX alone in the Langendorff-perfused rat heart. 221
Fig. 8.1 Doxorubicin (DOX): the cellular, molecular and clinical progression of events that leads to DOX-induced chemotherapy cardiomyopathy. The present schematic exemplifies the complexity of the progression of DOX-induced cardiotoxicity from acute events to the delayed toxicity which leads to the development of congestive heart failure. Adapted from Carvalho *et al*. 235

List of Tables

Table 1 Anatomical characteristics of rats following 8 weeks of DOX treatment and 3 weeks of off-dosing 87

Table 2 Functional annotation clustering with enrichment scores by NIH DAVID of the significantly (FDR < 0.05) decreased (log_2 fold change < -1) annotations based on transcript levels, suggesting mitochondrial function, peroxisome function, fatty acid metabolism and ion transport were decreased in DOX-induced cardiotoxicity. 120

Table 3 Functional annotation clustering with enrichment scores by NIH DAVID of the significantly (FDR < 0.05) increased (log_2 fold change > 1) annotations, based on transcript levels, in DOX-induced cardiotoxicity. 121

Table 4 Differential gene expression by RNA-seq of genes related to mitochondrial function. 128

Table 5 Differential gene expression by RNA-seq of genes related to ROS production. 131

Table 6 Differential gene expression by RNA-seq of genes related to inflammation and the immune response. 134

Table 7 Differential gene expression by RNA-seq of genes related to cardiac remodelling, fibrosis and dysfunction. 136

Chapter 1

Introduction

Chapter 1 Introduction

1.1 Cardiovascular disease and cancer therapy

1.1.1 Cancer survivorship in the 21st century

Cancer survivorship has dramatically increased over the last forty years largely due to early detection and improved intervention (Howlader et al., 2010; Jemal et al., 2010; Miller et al., 2016). A growing cancer survivorship has created a population of patients in need of specialised healthcare to treat the long-term adverse effects of their therapy and improve their comorbidity and mortality (Bodai and Tuso, 2015; Ganz, 2009). Nearly two-thirds of cancer survivors report at least one chronic medical condition related to prior therapy, with 28% having a severe or life-threatening condition (Oeffinger et al., 2006).

Cardiovascular disease is the leading cause of non-malignant death among survivors of cancer (Bodai and Tuso, 2015; Miller et al., 2016). Survivors of childhood cancer are eight times more likely to die from cardiovascular disease than their age matched peers (Mertens et al., 2008). In a fully adjusted study conducted with breast cancer patients cardiovascular mortality was found to overtake cancer as the leading cause of death nine years from initiation of breast cancer treatment (Patnaik et al., 2011). Childhood survivors of cancer have been reported to be fifteen times more likely to develop cardiac failure than their contemporaries (Oeffinger et al., 2006). Adverse cardiovascular effects as a result of cancer therapy can occur immediately during administration of treatment, or they may not manifest until months, years or decades after the completion of treatment. However, it is the chronic cumulative dose-dependent effects of anti-cancer treatment that impact on the long-term

morbidity, mortality and quality of life of cancer survivors and limit the clinical success of anti-cancer therapies (Mulrooney et al., 2009; Oeffinger et al., 2006).

The incidence and severity of cardiotoxicity with anti-cancer treatment depends on many factors - the particular agent(s) used, the treatment regimen, the immediate and cumulative dose, the route of administration, the presence of any underlying cardiac condition, and the demographics of the patient. The growing use of combination anti-cancer therapies shows a greater risk of cardiac dysfunction, associated with current or previous treatment with other anti-cancer agents (Bowles et al., 2012; Cobleigh et al., 2003; Coiffier et al., 2010; Feldman et al., 2000; Slamon et al., 2001).

Both anti-cancer agents and radiation therapy are known to be cardiotoxic (Adams and Lipshultz, 2005; Henson et al., 2013; Taunk et al., 2015). Ionising radiation is postulated to cause cellular injury which results in vasodilation, increased vascular permeability and an acute inflammatory response (Taunk et al., 2015). This acute pro-inflammatory damage initiates progressive myocardial fibrosis which leads to an increase in left ventricular (LV) end-diastolic volume and a reduced left ventricular ejection fraction (LVEF) (Taunk et al., 2015).

1.1.2 Cardiotoxicity of anti-cancer agents

Anthracycline antibiotics, such as doxorubicin (DOX), are a highly effective class of anti-neoplastic agents with a high potency against a wide spectrum of human cancers including breast, leukaemia, lymphoma, uterine, ovarian, bladder and lung cancer (Weiss, 1992). In the 1950s an Italian research company began research into anti-cancer compounds isolated from soil-based microbes (Ewer et al., 2011). An antibiotic isolated from a new strain of a bacterium species (*Streptomyces peucetius*) was effective against tumours in mice (Dimarco

et al., 1963). French researchers discovered a similar compound and the two teams named the compound daunorubicin (Dimarco et al., 1963; Dubost et al., 1964; Ewer et al., 2011). Clinical trails began in the 1960s and the drug was found to be successful in treating leukaemia and lymphoma (Tan et al., 1973; Tan et al., 1967). By 1967 it was recognised that daunorubicin produced cardiotoxicity (Tan et al., 1967). A mutated strain of the bacterium used to produce daunorubicin was found to produce a compound that showed better activity than daunorubicin against mouse tumours (Di Marco et al., 1969). This compound was named DOX. DOX showed a higher therapeutic index than daunorubicin but the cardiotoxicity associated with daunorubicin was still present with DOX treatment (Bonadonna et al., 1970; Di Marco et al., 1969; Lefrak et al., 1973; Middleman et al., 1971). DOX remains in widespread clinical use owing to its high potency against many cancers.

Despite the extensive clinical use of DOX its mechanism(s) of anti-cancer action are uncertain. There are three major mechanisms proposed for the anti-cancer effects of DOX: stabilisation of the topoisomerase-II (Top2) α-DNA cleavage complex, preventing the DNA double helix from being resealed and thereby resulting in double strand breaks in DNA; direct intercalation with double-stranded DNA resulting in inhibition of DNA replication and the generation of free radicals which damage DNA, cellular proteins and mitochondria (Carvalho et al., 2009; Gewirtz, 1999). All three of these proposed mechanisms are associated with the initiation of apoptosis. DOX's anti-tumour efficacy and wide spectrum activity mean it is one of the most commonly used anti-cancer agents and is on the World Health Organisation's List of Essential Medicine (Carvalho et al., 2009). Although anthracyclines are crucial to the treatment and survival of cancer patients, they are the leading cause of cardiac morbidity in cancer survivors (Mulrooney et al., 2009).

DOX-induced cardiotoxicity is known to be dose-dependent (Jensen et al., 2002; Lefrak et al., 1973; Mulrooney et al., 2009; Swain et al., 2003; Von Hoff et al., 1979). Dose-dependent cardiotoxicity limits DOX's clinical use, particularly in patients seen to be at risk of cardiac dysfunction. DOX is typically administered to humans as an intravenous (IV) infusion of 40-75 mg/m^2 at 3 to 4 week intervals, limiting the cumulative dose to 400-450 mg/m^2. However, cardiac dysfunction is known to occur at cumulative doses well below this level (Hequet et al., 2004; Limat et al., 2003; Mulrooney et al., 2009; Swain et al., 2003). Clinically cardiac dysfunction with DOX can be classified as acute, sub-acute or chronic (Albini et al., 2010; Florescu et al., 2013). Acute or sub-acute cardiotoxicity develops any time from the initiation of therapy up to a few weeks after the completion of treatment. It can be characterised by different types of arrhythmias, acute coronary syndromes, pericardial reaction and alteration in myocardial function, or early changes in relaxation and subsequently a LVEF decline over days to weeks. Clinically chronic cardiotoxicity refers to the side effects that can occur within a year of the completion of treatment - early-onset, chronic, progressive cardiotoxicity - or more than a year after the completion of therapy - late-onset chronic or delayed cardiotoxicity. Chronic cardiotoxicity presents as progressive ventricular dysfunction, heart failure (HF) and arrhythmias. It is hypothesised that these clinical manifestations of cardiotoxicity represent a spectrum of the same disease, and their detection depends upon the rigor of cardiac assessment during chemotherapy and the follow-up period, versus awaiting the later presentation of clinical symptoms.

The incidence of late-onset anthracycline-induced cardiotoxicity has been reported to be as high as 20% in cancer survivors 15-20 years after exposure (Kremer et al., 2002; Lipshultz et al., 2005; Steinherz et al., 1991). The mechanism(s) behind the delayed DOX cardiac toxicity remain unknown. Proposed mechanisms to explain delayed DOX cardiotoxicity include progressive impairment of sarcoplasmic reticulum calcium-handling mechanisms, DOX-

induced oxidative lesions on mitochondrial DNA (mtDNA) which could contribute to a progressive decay of mitochondrial capacity which will cease to be sub-clinical after a certain threshold is crossed, free radical-derived DNA lesions and the removal of progenitor cells in young patients which will later limit the already restricted regenerative capacity of the heart (Chugun et al., 2000; De Angelis et al., 2010; Monti et al., 1995; Serrano et al., 1999). One theory suggests that DOX treatment causes sub-clinical LV dysfunction that renders the patient increasingly susceptible to progressive dysfunction related to aging and other disease processes (Jones et al., 2007). It is possible that damage caused by DOX treatment, such as mitochondrial and nuclear DNA damage, accumulates over decades to a point where cardiac function progressively worsens and the heart can no longer cope (Lebrecht et al., 2003). Despite its clinical use since the late 1960s there are few effective protective strategies in place to minimise the cardiac complications of DOX treatment.

The development of tyrosine kinase inhibitors (TKIs) is a rapidly growing area of modern cancer research (Bellinger et al., 2015; Force and Kolaja, 2011; Zsila et al., 2009). TKIs offer the potential for “targeted therapy”, a term used to describe compounds that inhibit specific pathways that drive tumorigensis rather than traditional chemotherapy agents which target all rapidly dividing cells. The structure of the ATP binding pocket of tyrosine kinases has been well studied and is highly conserved across the human kinome (Verkhivker, 2007). Some TKIs target this ATP binding pocket, preventing ATP from binding to the kinase. If ATP cannot bind the kinase cannot phosphorylate its downstream targets and signalling is inhibited. The conservation of the ATP binding pocket among kinases means TKIs may also inhibit unintended kinases not associated with angiogenesis. Inhibiting unintended kinases may lead to unforeseen “off-target” effects (Force et al., 2007). If any of these kinases are crucial to cardiac function “off-target” cardiotoxicity may result. In addition, if any of the pathways that regulate cancer cell survival also regulate critical processes necessary for myocardial function

this will lead to “on-target” cardiotoxicity (Force and Kolaja, 2011). Although inhibiting tyrosine kinase signalling is beneficial for cancer treatment, inhibiting it in the healthy heart can lead to compromised function.

Vascular endothelial growth factor A (VEGF-A) is a central pro-angiogenic protein and is expressed by up to 60% of human tumours (Folkman, 2007). It is the most common of at least six other pro-angiogenic proteins secreted by tumour cells and binds to the tyrosine kinase receptor vascular endothelial growth factor receptor 2 (VEGFR2). VEGFR2 signalling results in endothelial cell proliferation, migration and sprout formation resulting in tumour expansion. As part of a strategy to target VEGF signalling pathways the small-molecule TKIs sorafenib and sunitinib (STB; also known as Sutent and SU11248) were developed. Both sorafenib and STB are associated with cardiotoxicity (Force et al., 2007; Schmidinger et al., 2008). Sorafenib and STB are known to inhibit multiple tyrosine kinases due to their ability to bind to the ATP-binding molecular pocket and are known as “multi-targeted” agents. As part of the anti-cancer efficiency of STB it inhibits at least nine receptor protein-tyrosine kinases that play a role in tumour angiogenesis and proliferation including vascular endothelial growth factor receptors 1, 2, and 3 (VEGFR1-VEGFR3), platelet-derived growth factor receptor α and β (PDGFRα and PDGFRβ), stem cell factor receptor (Kit), fms-like tyrosine kinase 3 (Flt-3), colony-stimulating factor-1 receptor (CSF-1R) and rearranged during transfection (RET) receptor tyrosine kinase (Force et al., 2007).

The incidence of TKI-induced cardiotoxicity is difficult to quantify accurately. The clinical use of these compounds is relatively recent. Imatinib was the first to be introduced into clinical oncology and received FDA approval in 2001. Therefore, long-term studies examining the incidence of modern anti-cancer agent-induced cardiotoxicity will only be accurately known with longer follow-up and on-going clinical investigation. A TKI that is clearly associated with

clinical cardiotoxicity is STB (Chu et al., 2007; Force et al., 2007; Kerkela et al., 2009). In a retrospective review of 75 patients enrolled in a phase I/II trial investigating the efficacy of STB 8 of 75 (11%) patients treated with STB had a cardiovascular event, with congestive HF recorded in 6 of 75 (8 %) patients (Chu et al., 2007). STB treatment was found to increase mean systolic and diastolic blood pressure and 35 of 75 (47%) individuals developed hypertension (> 150/100 mm Hg). STB-induced congestive HF and LV dysfunction has been found to improve with STB treatment withdrawal and institution of HF therapy, suggesting some reversibility of STB-induced cardiac dysfunction (Chu et al., 2007; Kerkela et al., 2009).

DOX is often used as part of combination therapies. Combination therapy is particularly effective as it targets the cancer in different ways however this can also mean synergistic cardiotoxicity. The growing use of combination anti-cancer therapies, such as the use of conventional chemotherapy and targeted therapies, shows a greater risk of cardiac dysfunction and HF, associated with current or previous treatment with other anti-cancer agents (Bowles et al., 2012; Cobleigh et al., 2003; Feldman et al., 2000; Seidman et al., 2002; Slamon et al., 2001). An agent that is commonly associated with cardiotoxicity during combination therapy with DOX is trastuzumab (Bowles et al., 2012; Chen et al., 2012). Trastuzumab, also known as Herceptin, is a monoclonal antibody targeting human epidermal growth factor receptor 2 (HER2 also known as EGFR and ERBB) used in the treatment of breast cancer (Feldman et al., 2000). Up to 30% of all breast cancer cases over-express HER2 and the development of trastuzumab was a significant break-through in the treatment of this type of breast cancer (Cardinale et al., 2010b). Although the exact mechanism behind trastuzumab-induced cardiotoxicity has yet to be elucidated it is hypothesised that the neuregulin (NRG) ERBB pathway plays a key role. NRG is a ligand to the ERBB receptors and NRG-ERBB signalling is involved in cardiac development and physiology (Lemmens et al., 2007). The ERG-ERBB pathway has been found to be connected to the stress response

of the heart (Ky et al., 2009; Suter and Ewer, 2013). Patients with stable chronic HF have high levels of circulating NRG (Ky et al., 2009). Reduced ERBB signalling in the failing heart has led to work looking at the use of recombinant human NRG in patients with stable chronic HF (Jabbour et al., 2011). Although inhibition of the NRG-ERBB pathway in cardiomyocytes with trastuzumab leading to cardiac dysfunction seems plausible further work needs to be done to prove this hypothesis (Ky et al., 2013). It is possible that combination therapy leads to a greater risk of cardiac dysfunction because of a 'dual hit' that exacerbates cardiac damage and puts the myocardial under additional stress. The growing challenge faced by oncologists to treat cancer patients with the most efficient and effective cancer therapy while minimising the cardiovascular complications of therapy has lead to the development of the cardio-oncology discipline.

1.2 The effect of cancer on cardiac function

Cancer itself has been reported to have cardiotoxic effects independent of those caused by cancer treatment (Cramer et al., 2014; Pavo et al., 2015; Springer et al., 2014). In a rat model of liver cancer tumour-bearing rats showed a progressive loss of LV mass that was associated with a progressive deterioration in cardiac function before exposure to any cancer treatment (Springer et al., 2014). Clinical trials have reported that cardiovascular dysfunction as a result of cancer can precede anti-cancer therapies (Cramer et al., 2014; Pavo et al., 2015). Patients with colorectal cancer that had not received treatment had significantly reduced LVEFs compared to control (Cramer et al., 2014). In a larger clinical study with 555 patients circulating levels of cardiovascular peptides used as markers of cardiac dysfunction such as B-type natriuretic peptide (BNP) and troponin T were elevated in a population of patients with cancer prior to induction of any cardiotoxic anti-cancer therapy (Pavo et al., 2015). The elevated levels of these markers were strongly related to all-cause mortality (Pavo

et al., 2015). This suggests that the malignancy itself may exert adverse cardiac effects before chemotherapy provides an additional hit to the heart. How cancer damages cardiac function is unknown however it has been postulated that cardiac dysfunction may be as a result of muscle weakness and wasting or systemic inflammation (Pavo et al., 2015).

1.3 Mitochondria in the heart

Mitochondria allow mammals metabolic efficiency through aerobic metabolism and oxidative phosphorylation, enabling complex higher order function. The integrity of mitochondrial function, particularly in the myocardium, is crucial to cellular homeostasis. In the mammalian heart mitochondria comprise approximately 25-30% of the total intracellular cardiomyocyte volume (Barth et al., 1992; Schaper et al., 1985), one of the highest concentrations of mitochondria of any human cell. The heart, as an organ, is particularly reliant on healthy mitochondrial function as the most metabolically active organ in the body. The heart only stores enough energy to support pumping for a few heart beats, turning over the metabolic pool approximately every ten seconds at rest (Balaban, 2002). The reliance of the heart on healthy mitochondrial function is not limited to energy production; mitochondria play a crucial role in calcium handling and cell death pathways. Therefore, a perturbance in cardiac mitochondrial function can lead to contractile dysfunction, cell death and myocardial dysfunction.

DOX treatment can also cause mitochondrial dysfunction in the central nervous system, kidney and liver (Dirks-Naylor et al., 2014; Lebrecht et al., 2004; Tangpong et al., 2011). It is postulated that the heart is particularly susceptible to DOX-induced mitochondrial dysfunction because of the heart's reliance on healthy mitochondrial function, the large density/volume of mitochondria, the elevated rate of oxygen consumption and the lower amount of anti-oxidant

defences compared with other tissues such as the liver (Ascensao et al., 2005; Kaiserova et al., 2007; Quiles et al., 2002).

1.3.1 Mitochondrial structure

Mitochondria have two membrane systems Fig. 1.1, the inner and the outer mitochondrial membranes, which come together in places to form contact sites. The inner mitochondrial membrane (IMM) is largely impermeant and highly convoluted, with a series of infoldings, known as cristae. The number of cristae is three times greater in the mitochondrion of a cardiac muscle cell than in the mitochondrion of a liver cell, presumably because of the higher energy demand of cardiomyocytes (Alberts, 2002). The IMM contains a high proportion of the "double" phospholipid cardiolipin, which contains four fatty acids and is proposed to make the membrane especially impermeable to ions. The enzymes of the respiratory chain are embedded in the IMM. The outer mitochondrial membrane (OMM) contains many copies of the transport protein porin, which forms large aqueous channels through the lipid bilayer. The OMM is permeable to molecules of 5000 Da or less, including small proteins. Together these two membranes form two separate compartments: the internal matrix space bound by the IMM and the narrower intermembrane space bound by the OMM. The intermembrane space is chemically equivalent to the cytosol with respect to the small molecules it contains, however, it is its own microenvironment and houses some proteins that are required for mitochondrial function such as creatine kinase and adenylate kinase. The matrix space houses mitochondrial enzyme systems and mtDNA. Human mtDNA is a circle of 16.6 kb double stranded DNA encoding 13 proteins which are components of the respiratory chain present in the IMM (Duchen, 2004). In addition, approximately 24 other genes are present in mtDNA encoding two rRNAs and 22 tRNAs required to synthesis the 13 proteins. mtDNA only encodes a fraction of the proteins required for mitochondrial function; a total of approximately

850 proteins are required and the majority are encoded in nuclear DNA (Duchen, 2004). Cardiomyopathy is associated with specific pathogenic point mutations in mtDNA (Casali et al., 1995; Silvestri et al., 1994; Taniike et al., 1992) and has been estimated to occur in 20-40% of children with mitochondrial diseases (Holmgren et al., 2003; Scaglia et al., 2004). The proximity of mtDNA to the electron transport chain (ETC), poor repair mechanisms and a lack of protective histones means mtDNA is susceptible to mutations and oxidative damage.

1.3.2 Bioenergetics and metabolism

The fundamental enzyme systems of the mitochondria are the citric acid or tricarboxylic acid (TCA) cycle and the respiratory chain or ETC. The TCA cycle breaks down acetyl coenzyme A (acetyl CoA), which is formed from pyruvate, fatty acids (β-oxidation) and amino acids, to generate CO_2 and in the process NAD^+ is reduced to NADH and FAD to $FADH_2$. These two intermediates provide reducing equivalents to the respiratory chain, which consists of a series of enzyme systems, coupled together that are described as Complex I, II, III and IV. Complex I (NADH dehydrogenase), Complex II (succinate dehydrogenase), Complex III (ubiquinol-cytochrome c reductase) and Complex IV (cytochrome c oxidase) are all membrane spanning enzyme systems consisting of many protein subunits. Complex II proteins are entirely encoded by nuclear DNA while a mixture of nuclear DNA and mtDNA encodes the other three complexes proteins. Electrons are transferred from NADH and $FADH_2$ to Complexes I, and Complex II, respectively, and these each then transfer electrons to coenzyme Q which shuttles electrons to Complex III. Complex III accepts electrons from reduced coenzyme Q and uses them to reduce cytochrome c. Cytochrome c then shuttles electrons to Complex IV. Complex IV reduces oxygen to water. The movement of electrons along the respiratory chain results in the transfer of protons across the IMM from the matrix into the intermembrane space by Complexes I, III and IV, establishing the electrochemical proton gradient (Δp). The

influx of protons is directed through the proton channel of the ATP synthase sometimes referred to as F_1F_0-ATP synthase or Complex V Fig. 1.1. The inward movement of protons drives a motor of the enzyme to phosphorylate ADP and to release ATP. ATP is transported out of mitochondria by the adenine nucleotide translocase (ANT), which exchanges ADP for ATP.

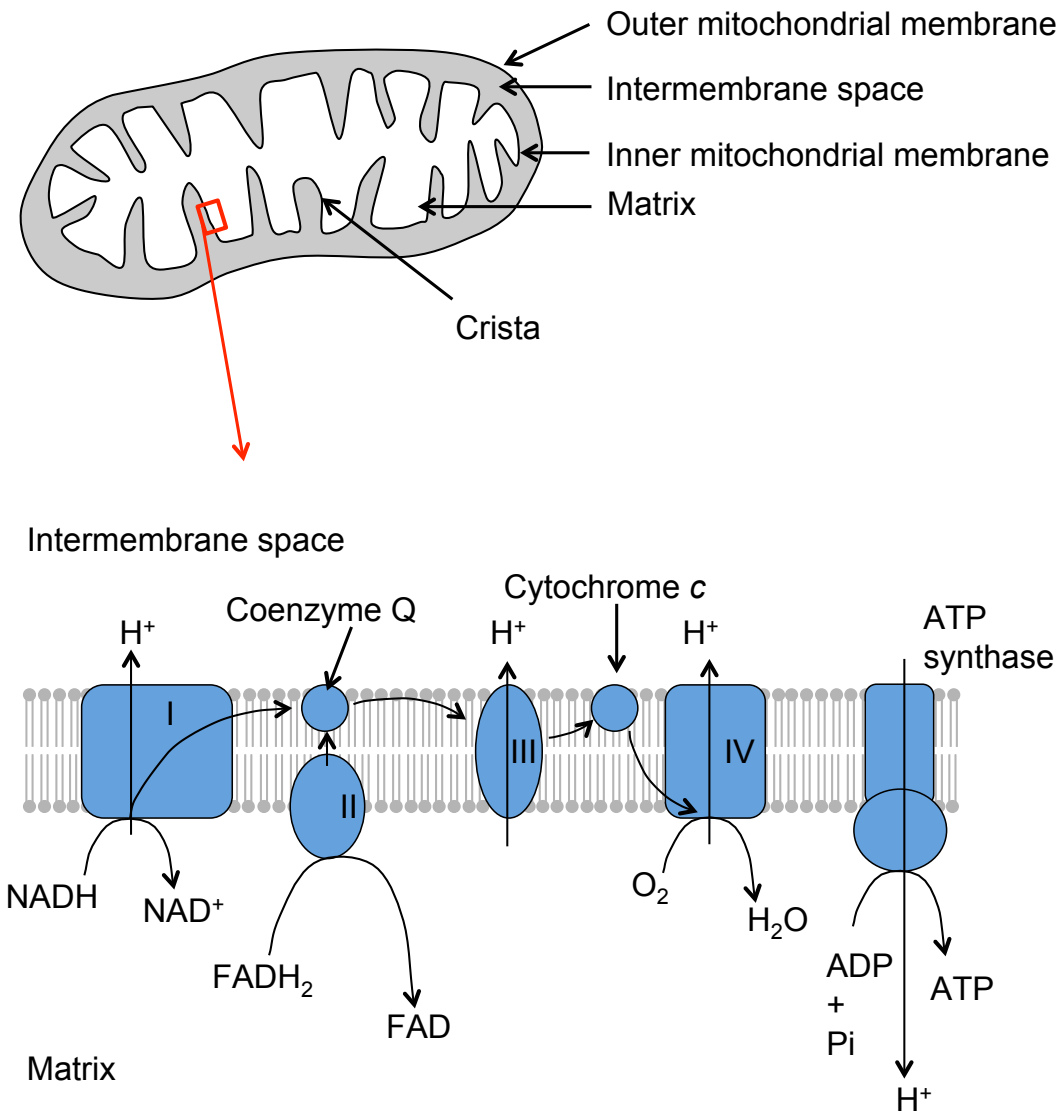


Fig. 1.1 Schematic representation of mitochondrial structure (above) and the electron transport chain in the inner mitochondrial membrane (below). Complex I (labeled I) accepts electrons from the Krebs cycle electron carrier nicotinamide adenine dinucleotide (NADH) and passes them to coenzyme Q which also receives electrons from complex II (labeled II). Coenzyme Q passes electrons to complex III (labeled III) which passes them to cytochrome *c*. Cytochrome *c* passes electrons to complex IV (labeled IV) which uses the electrons and hydrogen Ions to reduce molecular oxygen to water. The efflux of protons creates an electrochemical gradient that is used by ATP synthase to make ATP. Adapted from Agrawal and Mabalirajan (Agrawal and Mabalirajan, 2016).

1.3.3 Mitochondria and calcium handling

Calcium uptake by mitochondria is driven by the Δp and a low intramitochondrial calcium concentration under basal conditions. Calcium transits the OMM via voltage-dependent anion-selective channels (VDACs) that span the OMM. Calcium is transported from the intermembrane space to the mitochondrial matrix by the mitochondrial calcium uniporter (MCU) and by a Na^+/Ca^{2+} exchanger (NCX) for efflux (Baughman et al., 2011; De Stefani et al., 2011). Mitochondrial calcium uptake has been shown to regulate mitochondrial metabolism (Denton et al., 1980; Duchen, 1992; McCormack et al., 1990) and increase mitochondrial ATP production (Jouaville et al., 1999). In the heart an increase in contractility is mediated by an increase in the cytosolic calcium transient. An increase in cytosolic calcium is transmitted to the mitochondria via calcium uptake into the mitochondrial matrix which leads to the activation of the calcium sensitive dehydrogenases within the matrix (Denton et al., 1980) and complexes of the ETC, thereby increasing ATP production as required by an increase in contractility (Glancy et al., 2013).

A disruption to calcium levels leads to mitochondrial dysfunction. If there is a high calcium concentration in the cytoplasm it can lead to mitochondrial calcium overload. The activity of the NCX saturates as the mitochondrial matrix calcium concentration increases, whereas the MCU acts as a channel and is not saturated with an increasing matrix calcium concentration (Rizzuto et al., 2009). As a result under pathological conditions of high cytosolic calcium the calcium concentration increases in the matrix and the mitochondria can no longer regulate the matrix calcium concentration resulting in mitochondrial calcium overload. A low mitochondrial calcium concentration can also result in mitochondrial dysfunction. Mitochondrial calcium has been shown to connect to intracellular sodium levels via mitochondrial Na^+/Ca^{2+} exchange by the NCX. Elevated cytosolic sodium reduces mitochondrial calcium by accelerating calcium

efflux via the NCX (Kohlhaas et al., 2010; Liu and O'Rourke, 2008; Maack et al., 2006). Insufficient mitochondrial calcium leads to disruption of Ca^{2+}-dependent activation of the TCA cycle enzymes (Maack et al., 2006). The decrease in reducing equivalents and NADPH, necessary for anti-oxidant pathways, results in impairment of energy supply and increases mitochondrial formation of reactive oxygen species (ROS) (Kohlhaas et al., 2010; Liu and O'Rourke, 2008; Maack et al., 2006). ROS is a term used to describe reactive molecules and free radicals derived from molecular oxygen such as the superoxide anion radical ($O_2^{\bullet -}$), hydrogen peroxide (H_2O_2), peroxynitrite ($ONOO^-$) and the hydroxyl radical ($OH^{\bullet}$). Alterations in mitochondrial calcium may contribute to the development of arrhythmias (Liu et al., 2014; Shimizu et al., 2015).

1.3.4 Mitochondria and reactive oxygen species generation

Mitochondria are estimated to use approximately 90% of the cell's oxygen and as a result a by-product of mitochondrial respiration is the generation of ROS (Chance et al., 1979; Jensen, 1966; Rolfe and Brown, 1997). Side reactions of the mitochondrial ETC with molecular oxygen result in the one-electron reduction of O_2 to produce $O_2^{\bullet -}$. O_2 has two unpaired electrons in anti-bonding orbitals with parallel spin which means it accepts one electron at a time (Sawyer and Valentine, 1981). The primary sites for ROS generation are Complex I, II and III of the respiratory chain (McLennan and Degli Esposti, 2000). Excessive or diminished electron flux at these complexes can stimulate auto-oxidation of flavins or quinones that are able to act as single-electron donors resulting in superoxide generation. Superoxide dismutases (SODs) are the major anti-oxidant defence against superoxide damage (Fukai and Ushio-Fukai, 2011). SOD catalyses the conversion of $O_2^{\bullet -}$ to hydrogen peroxide and oxygen. There are three isoforms of SOD in mammals: cytoplasmic Cu/ZnSOD (SOD1), the mitochondrial MnSOD (SOD2) and the extracellular Cu/ZnSOD (SOD3), all of

which require catalytic metal (Cu or Mn) for their activation. MnSOD catalyses dismutation of superoxide free radicals to hydrogen peroxide and oxygen in the mitochondria (Weisiger and Fridovich, 1973). MnSOD-deficient mice have been shown to develop dilated cardiomyopathy (Li et al., 1995). H_2O_2 can be catalysed to H_2O by catalase, peroxiredoxin or glutathione peroxidase, however, it can also undergo further reactions to form hydroxyl radicals. At low levels ROS can act as signalling molecules which have been shown to activate downstream kinases that are involved in cytoprotection (Oldenburg et al., 2002). However, at high levels ROS result in elevated lipid peroxidation, membrane damage, oxidative modification of proteins, cell death initiation, mtDNA damage, ETC damage and nuclear DNA damage. Lower levels of anti-oxidant enzymes such as catalase, SOD and glutathione peroxidase in the mammalian heart in comparison to other tissues and the high basal metabolic activity may explain why the heart seems to have a specific sensitivity to ROS-induced toxicity (Doroshow et al., 1980).

1.3.5 Mitochondria and cell death

Mitochondria play a role in both apoptotic and necrotic cell death. Mitochondrial-mediated apoptosis is initiated by permeabilisation of the OMM. Permeabilisation of the OMM causes the release of substances that induce apoptosis such as cytochrome c, second mitochondria-derived activator of caspases/direct inhibitor of apoptosis-binding protein with low pI (Smac/DIABLO), Omi/high-temperature requirement A2 (Omi/HtrA2), apoptosis-inducing factor (AIF) and endonuclease G (Saelens et al., 2004). OMM permeabilisation is triggered by B-cell lymphoma (BCL)-2-associated X protein (BAX) and BCL-2 antagonist/killer (BAK), which are pro-apoptotic members of the BCL-2 family of proteins (Czabotar et al., 2014). BAX resides in the cytoplasm under basal conditions in an inactive conformation. Pro-apoptotic and activator BCL-2 homology 3 (BH3)-only proteins such as BCL-2-interacting mediator of

cell death (BIM), truncated form of BH3-interacting domain death agonist (tBid) and Bcl-2-associated death promoter (BAD), amongst others, trigger conformational activation of BAX and inhibit anti-apoptotic proteins (Youle and Strasser, 2008). This conformational change of BAX exposes a transmembrane domain that binds the OMM. BAK resides in the OMM and is thought to be activated in a similar manner to BAX. Anti-apoptotic proteins BCL-2, BCL-xL and myeloid cell leukaemia sequence 1 (MCL-1) inhibit BAX and BAK (Youle and Strasser, 2008). The pro-apoptotic proteins released from the intermembrane space following OMM permeabilisation are toxic in the cytosol and activate caspases. Caspases proteolyse cellular substrates, fragmenting the cell which is eliminated by phagocytosis (Czabotar et al., 2014). The plasma membrane integrity is kept intact during apoptosis. Apoptotic stimuli include inadequate survival factors, hypoxia, oxidative stress, DNA damage and toxins. These stimuli trigger the release of pro-apoptotic activator BH3-only proteins.

Mitochondrial-mediated necrotic cell death is triggered by sustained opening of the mitochondrial permeability transition pore (mPTP). Abnormal mitochondrial morphology, mitochondrial swelling and calcium overload in the heart is associated with the “mitochondrial permeability transition”. Research in the 1970s by Hunter and Haworth (Hunter and Haworth, 1979; Hunter et al., 1976) and by Crompton *et al*. in the 1980s (Crompton et al., 1987) showed that the “mitochondrial permeability transition” is caused by the reversible opening of a non-selective pore in the IMM, referred to as the mPTP which could be closed by chelation of calcium. Extensive swelling of mitochondria is as a result of the equilibration of small solutes (< 1500 Da) across the IMM, leaving behind a high concentration of proteins in the matrix which exerts a osmotic pressure that draws water into the matrix (Crompton et al., 1987). Swelling of the mitochondrial matrix compartments leads to an expansion of the matrix as the cristae unfold, resulting in expansion of the IMM and rupture of the OMM. mPTP opening results in rapid dissipation of the Δp across the IMM, as the IMM can no longer

provide a barrier. This stops ATP synthesis and results in the proton-translocating ATP synthase going in reverse, pumping H^+ out of the matrix and using ATP (Halestrap and Pasdois, 2009). ATP consumption continues during necrosis but apoptotic cells have been shown to stop ATP-requiring processes such as DNA repair, translation and proteasome function (Saelens et al., 2005; Soldani and Scovassi, 2002; Sun et al., 2004). Release of pro-inflammatory stimuli, such as ATP and ROS, trigger an inflammatory response in necrosis, whereas, apoptosis is not associated with inflammation (Rock and Kono, 2008). Opening of the mPTP can be pharmacologically inhibited by the immunosuppressant agent cyclosporin A (CsA) (Crompton et al., 1988; Duchen et al., 1993). If the mPTP closes in time to maintain ATP levels, apoptotic cell death dominates over necrotic cell death. Calcium alone has been reported to induce mPTP opening, however, other factors are able to sensitise pore opening to calcium including oxidative stress, a high Pi concentration and depletion of mitochondrial matrix ATP (Crompton and Costi, 1988; Crompton and Costi, 1990; Crompton et al., 1987).

The conditions during ischaemia and reperfusion favour mPTP opening (Crompton and Costi, 1990). The cardiomyocyte death that occurs as a consequence of reperfusion of ischaemic myocardium is mediated, at least in part, by the opening of the mPTP (Duchen et al., 1993; Griffiths and Halestrap, 1995; Halestrap et al., 2004; Halestrap et al., 1998). During cardiac ischaemia insufficient delivery of nutrients (oxygen, glucose and fatty acids) leads to inhibition of mitochondrial respiration and oxidative phosphorylation resulting in a decrease in ATP production, and an increase in ADP, AMP and Pi. The insufficient amount of ATP produced during glycolysis and the loss of blood flow to the myocardium result in a build-up of lactic acid, lowering of intracellular pH and an activation of the Na^+/H^+ exchanger. Through the extrusion of excess H^+ the cell becomes loaded with Na^+. The reduction in ATP levels and the decrease in pH inhibit the activity of the Na^+/K^+ ATPase. The increase in intracellular Na^+ leads to reversal of the Na^+/Ca^{2+} exchange, which coupled with an inhibition of the

sarco/endoplasmic reticulum calcium ATPase (SERCA2A) leads to an accumulation of intracellular Ca^{2+}. Thus, ischaemia creates an intracellular environment in which ATP is low, pH is acidic and the levels of Pi, Na^{+} and Ca^{2+} are all high. Upon reperfusion the supply of nutrients is restored, restarting the respiratory chain and leading to mitochondrial re-energisation. The restoration of oxygen causes a surge in ROS. Mitochondria take up Ca^{2+} that has accumulated during ischaemia. Thus, during the beginning of reperfusion there is a combination of a high matrix Ca^{2+} and oxidative stress, together with elevated Pi levels and a depletion of ATP. However, due to the lactic acid present there is a low pH which can inhibit mPTP opening (Halestrap et al., 2004). Therefore, as restored blood flow allows the intracellular pH to return to normal through the loss of lactic acid and the operation of pH regulatory pumps, the opening the mPTP is predicted to occur and contribute to ischaemia-reperfusion injury (IRI). The loss of cardiomyocytes and the induction of pro-inflammatory processes lead to a functional decline in the myocardium. IRI can result in subsequent myocardial infarction, cardiac arrhythmias and further contractile dysfunction (Ferdinandy et al., 2007).

The administration of CsA in patients with acute MI, at the time of reperfusion, has been reported to reduce the size of the infarction as assessed on day 5 (Piot et al., 2008). A single dose of CsA administered at the time of reperfusion following MI was found to reduce infarct size at 6 months follow up in the CsA-group (Mewton et al., 2010). However, when the stimulus is sufficiently strong CsA cannot inhibit pore opening (Halestrap et al., 1997). CsA is also non-selective, interacting with the cytosolic protein cyclophilin and blocking the transcription of cytokine genes (Matsuda and Koyasu, 2000). This combined with a narrow therapeutic concentration range means CsA is not ideal to inhibit mPTP opening. Two larger scale trials found no protective effect with CsA administration prior to reperfusion (Cung et al., 2015; Ottani et al., 2016). The exact molecular components of the mPTP remain unknown

and so targeted therapeutics aiming at stopping the mitochondrial permeability transition are limited.

1.4 Proposed mechanisms of DOX-induced cardiotoxicity

The exact mechanisms that lead to DOX-induced cardiotoxicity remain unclear but are likely to be due to a combination of multifactorial processes including redox cycling and ROS generation, a disruption of calcium handling, direct mitochondrial damage and transcriptional modulation.

1.4.1 Redox cycling of DOX and ROS generation

Redox cycling of DOX between the quinone and semiquinone forms is catalysed by NADPH cytochrome P-450 reductase, NADH dehydrogenase, endothelial nitric oxide synthase and xanthine oxidase, amongst others, and induces substantial ROS production (Keizer et al., 1990; Vasquez-Vivar et al., 1997). During redox cycling one-electron reduction of the aglycone portion of DOX results in a semiquinone radical. In the presence of molecular oxygen semiquinone radicals are re-oxidised by using molecular oxygen as an electron acceptor, resulting in superoxide formation (Fig. 1.2) (Keizer et al., 1990). DOX is known to undergo redox cycling with Complex I, using electrons and transferring them to molecular oxygen (Davies and Doroshow, 1986). Superoxide can then be converted to H_2O_2 and subsequently converted to hydroxyl radicals in the presence of heavy metals such as iron through the Fenton reaction (Wardman and Candeias, 1996). In addition, DOX can interact directly with iron to form a DOX-Fe complex which results in cycling between Fe(II) and Fe(III) with ROS production (Keizer et al., 1990; Myers et al., 1982).

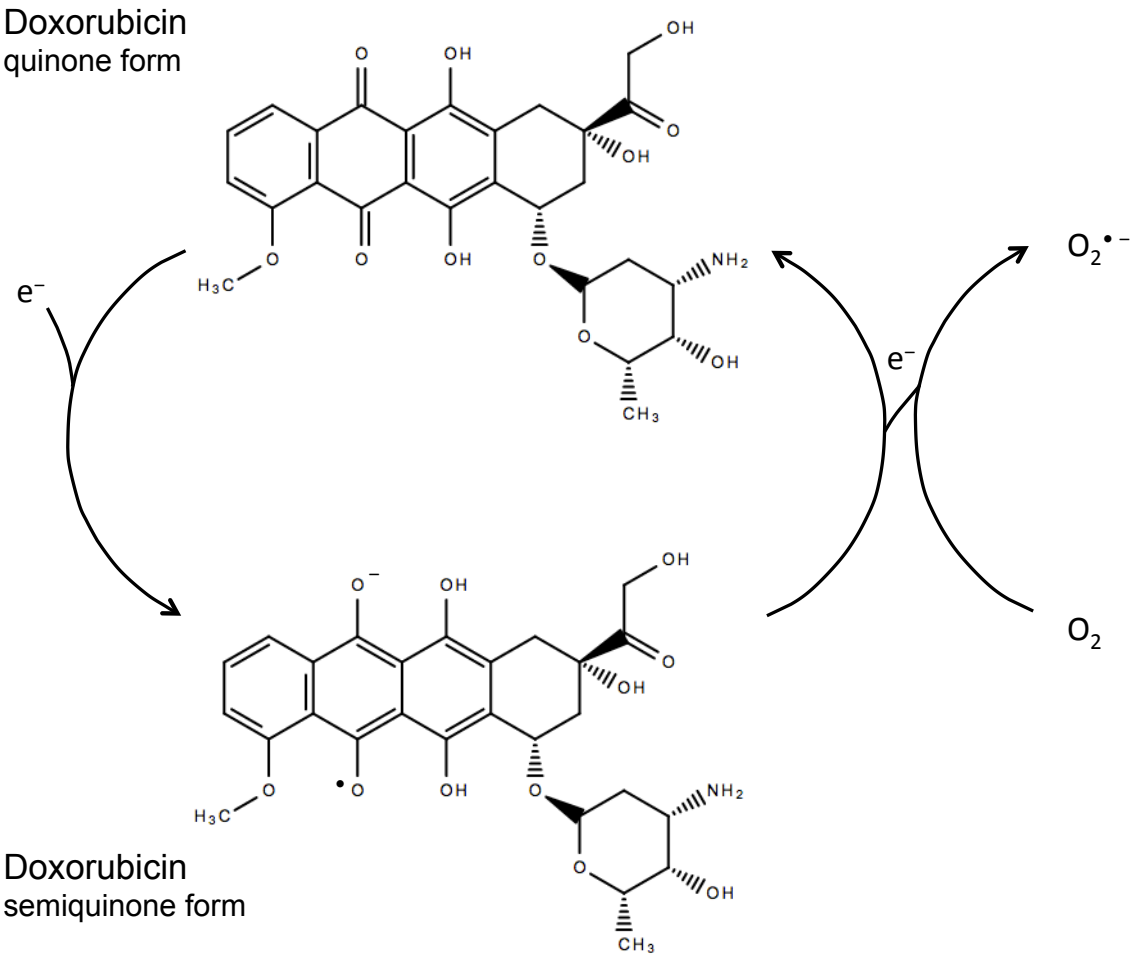


Fig. 1.2 Schematic representation of redox cycling of DOX between the quinone and semiquinone form resulting in superoxide generation.

The generation of harmful levels of ROS with DOX results in oxidative DNA damage (both nuclear and mtDNA damage), the initiation of apoptosis, lipid peroxidation and membrane damage, modulation of kinase signalling and protein damage (Deavall et al., 2012). Oxidation-sensitive proteins include mitochondrial proteins and those involved in energy metabolism, amongst others (Schmalhausen et al., 2003; Tretter and Adam-Vizi, 2000). Dexrazoxane has been shown to reduce the cardiotoxic effects of DOX in both pre-clinical and clinical studies (Agen et al., 1992; Asselin et al., 2016; Herman et al., 1979; Speyer et al., 1988; Swain et al., 1997). One of the proposed mechanisms of protection is attributed to iron chelation by the hydrolysis product of dexrazoxane, thereby reducing ROS formation (Hasinoff et al., 1998).

Some anti-oxidant therapies, however, have had little success in preventing DOX-induced cardiotoxicity (Berthiaume et al., 2005; Bjelogrlic et al., 2005; Martin et al., 2009; Myers et al., 1983). In a rat model of DOX-induced cardiotoxicity the mitochondrially-targeted anti-oxidant MitoQ was shown to protect against DOX-induced cardiac dysfunction (Chandran et al., 2009). This suggests that to overcome ROS generation it may be necessary to specifically target cardiac mitochondrial ROS.

MitoQ is an anti-oxidant ubiquinol moiety covalently attached to a triphenylphosphonium cation by an aliphatic carbon chain (Fig. 1.3) (Asin-Cayuela et al., 2004; Kelso et al., 2001). The large membrane potential across the mitochondrial inner membrane (-150 to -180 mV, negative inside) drives the accumulation of lipophilic cations such as triphenylphosphonium into the mitochondrial matrix (Smith et al., 2004). The Nernst equation indicates that these cations will accumulate about 10-fold for every 61.5 mV of membrane potential, thus accumulating several-hundred fold within mitochondria (Flewelling and Hubbell, 1986; Smith et al., 2004). Cells will also accumulate lipophilic cations into the cytoplasm about 5 to 10-fold

driven by the plasma membrane potential (-30 to -60 mV, negative inside) from where they will be further concentrated several-hundred fold inside mitochondria (Fig. 1.3) (Smith et al., 2004). Lipophilic cations pass easily through phospholipid bilayers by a non-carrier-mediated process (Murphy, 1997). This is because the phosphonium in these lipophilic cations is surrounded by three hydrophobic phenyl groups and, therefore, has a large effective ionic radius that lowers their activation energy barrier for movement through lipid bilayers (Flewelling and Hubbell, 1986). Alkyl triphenylphosphonium cations, such as MitoQ, first bind to the outer surface of the inner membrane of mitochondria then permeate the hydrophobic potential energy barrier of the phospholipid bilayer, before binding to the inner surface of the membrane from where they desorb into the mitochondrial matrix (Asin-Cayuela et al., 2004).

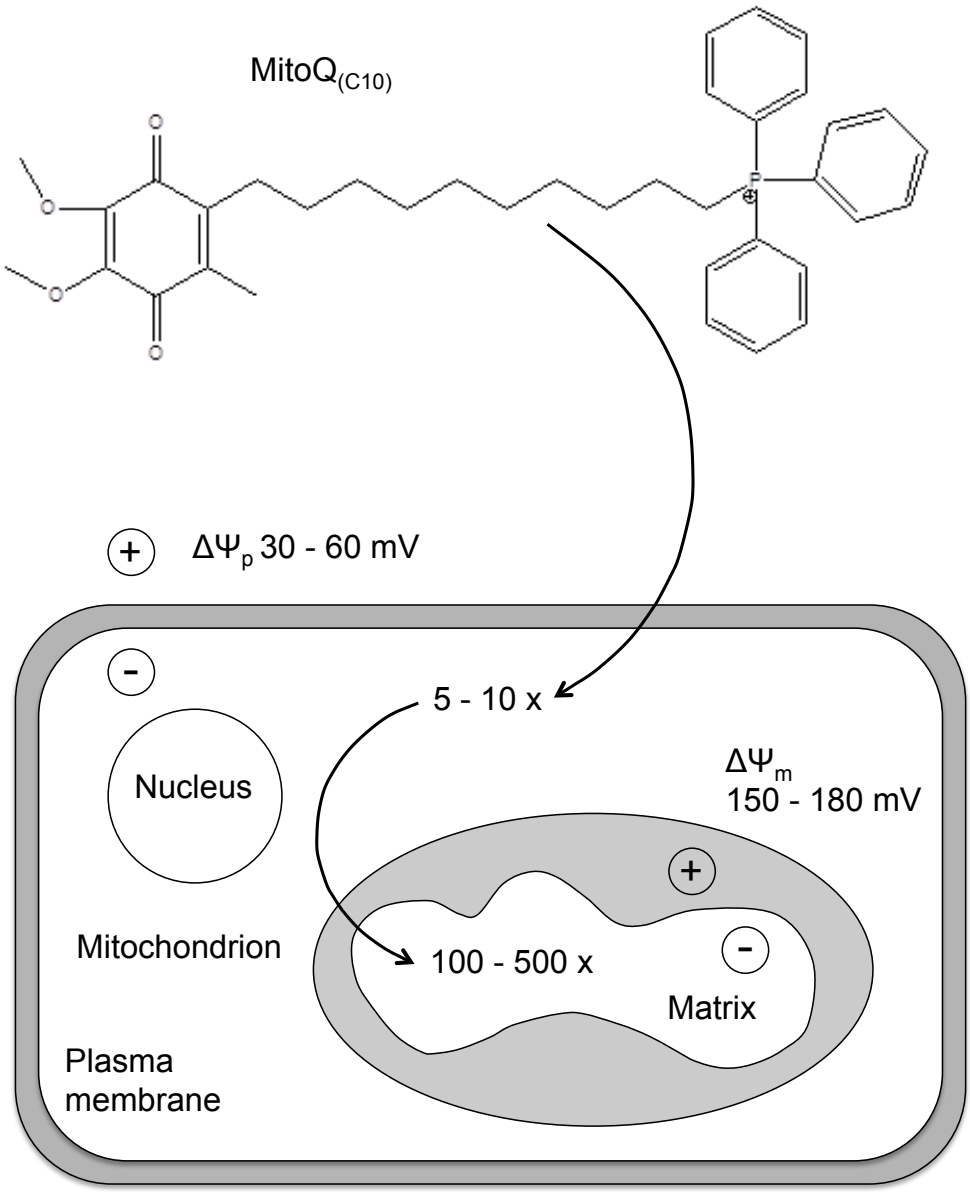


Fig. 1.3 Uptake of the mitochondrially-targeted anti-oxidant MitoQ by mitochondria within cells. This schematic shows the uptake of $MitoQ_{(C10)}$ into cells driven by the plasma membrane potential ($\Delta\Psi_p$) before being further accumulated into mitochondria driven by the mitochondrial membrane potential ($\Delta\Psi_m$). Adapted from Smith *et al*.

1.4.2 Modulation of intracellular calcium handling with DOX treatment

DOX and its metabolite, doxorubicinol have been shown to have adverse effects on the cardiac ryanodine receptor 2 (RyR2) and SERCA2A (Hanna et al., 2014; Holmberg and Williams, 1990). Addition of 0.01 μM of DOX caused a significant increase in RyR2 channel open probability (Hanna et al., 2014). A similar effect was observed with doxorubicinol. Pre-incubation with the reducing agent dithiothreitol prevented drug-induced inhibition of channel activity (Hanna et al., 2014). Both compounds were found to bind to RyR2 and reduce the abundance of thiol groups. Calcium uptake into the sarcoplasmic reticulum by the SERCA2A was inhibited by doxorubicinol, at concentrations as low as 0.01 μM, but DOX itself was not found to inhibit SERCA2A function. Dithiothreitol pre-treatment prior to doxorubicinol incubation significantly increased Ca^{2+} uptake by the SERCA2A, indicating that the effect of doxorubicinol on SERCA2A function is oxidation-dependent and involves redox modification (Hanna et al., 2014). This work suggests that DOX and its metabolite doxorubicinol disrupt Ca^{2+} handling and impair cardiac function by directly affecting RyR2 and SERCA2A function. Impaired calcium handling may lead to calcium overload and contractile dysfunction.

1.4.3 Mitochondrial dysfunction in DOX-induced cardiomyopathy

One of the earliest histomorphological changes associated with DOX-induced cardiomyopathy was mitochondrial dysfunction (Lefrak et al., 1973). In human biopsies individual mitochondria were found to be swollen and had fragmentation and disruption of the cristae (Friedman et al., 1978; Lefrak et al., 1973). There is a significant decrease in myocardial ATP, lactate, phosphocreatine and free creatine in chronic DOX-treated myocardial tissue, suggesting a decrease in both glycolytic and oxidative metabolic processes (Dekker et al., 1991; Ferrero et al., 1976; Kawasaki et al., 1996). Dekker *et al*.

reported that at rest the inorganic phosphate to phosphocreatine ratio for hearts from DOX-treated rats was initially unaltered; however there was a significant treatment-related loss of high energy phosphate when hearts were stimulated (Dekker et al., 1991); similar declines in ATP have also been reported in rats treated with DOX (Chatham et al., 1990), suggesting that DOX reduces the bioenergetic reserve of cardiomyocytes. In patients a decrease in the phosphocreatine to ATP ratio was present years after completion of treatment, suggesting the effects on mitochondrial bioenergetics persist in the absence of DOX treatment (Eidenschink et al., 2000). During exercise the heart can use 80-90% of its maximum oxidative capacity, suggesting there is little aerobic ATP production reserve (Mootha et al., 1997). Compromised bioenergetics has been hypothesised to be a common factor in the development of cardiomyopathies (Ingwall and Weiss, 2004; Olson and Schwartz, 1951; Ventura-Clapier et al., 2004).

1.4.4 Direct mitochondrial damage by DOX

Adding DOX directly to isolated mitochondria *in vitro* blocks oxidative phosphorylation, indicating a direct inhibitory effect on one or more electron transporting elements of the respiratory chain (Bianchi et al., 1987; Ferrero et al., 1976; Montali et al., 1985). DOX, being a cationic compound, readily enters mitochondria and binds to cardiolipin (Davies and Doroshow, 1986; Doroshow and Davies, 1986; Goormaghtigh et al., 1987). Since cardiolipin is necessary for ETC activity DOX directly inhibits the ETC by binding to cardiolipin, resulting in superoxide generation (Nicolay and de Kruijff, 1987).

DOX has been shown to increase mitochondrial iron accumulation, further increasing ROS production via redox cycling within the mitochondria by directly regulating ATP Binding Cassette Subfamily B Member 8 (ABCB8) gene expression (Ichikawa et al., 2014). ABCB8

facilitates mitochondrial iron export (Ichikawa et al., 2012). Ichikawa *et al*. showed that DOX significantly reduced transcript and protein levels of ABCB8 and slightly decreased or did not change levels of mitoferrin-2, a regulator of mitochondrial iron import, thereby increasing mitochondrial iron accumulation and ROS production in mitochondria (Ichikawa et al., 2014). Overexpression of ABCB8 in the heart of transgenic mice has been reported to decrease mitochondrial iron and cellular ROS and protect against DOX-induced cardiotoxicity (Ichikawa et al., 2014).

Mitochondria isolated from DOX-treated rats showed a dose-dependent decrease in calcium loading capacity before undergoing mPTP opening compared to control (Zhou et al., 2001), suggesting mitochondria in DOX-treated samples are predisposed to calcium overload. In the presence of CsA isolated mitochondria from DOX-treated animals displayed a two-fold increase in calcium loading capacity before undergoing mPTP opening, which was no different from saline control. This suggests that CsA protects against DOX-induced mPTP opening *in vitro* at non-immunosuppressive doses (Zhou et al., 2001). CsA has been shown to improve heart function and survival in a mouse model of DOX-induced cardiotoxicity (Marechal et al., 2011). Mitochondria isolated from human atrial trabeculae showed reduced transmembrane potential and calcium retention capacity when treated with DOX *ex vivo* (Montaigne et al., 2011). CsA pre-treatment at non-immunosuppressive doses prevented mitochondrial dysfunction and impaired contractile performance induced by DOX treatment at clinically relevant concentrations (Montaigne et al., 2011). This data suggests that the mPTP may play a role in DOX-induced mitochondrial dysfunction and cardiotoxicity.

1.4.5 Nuclear DNA topoisomerases

DNA topoisomerases are required for DNA replication, transcription and recombination as they relax the DNA double helix by generating breaks in DNA and relieving the helical torsion (Champoux, 2001). Top2 is a cellular target of DOX (Tewey et al., 1984). DOX binds both Top2 and DNA to form a complex that inhibits replication and triggers cell death. Top2α is expressed in tumours but is not detectable in quiescent tissues (Capranico et al., 1992; Park et al., 2010). Top2α is thus thought to be part of the molecular basis of DOX's anti-cancer activity. Adult cardiomyocytes express Top2β but no detectable Top2α (Capranico et al., 1992). The Top2β-DOX-DNA ternary cleavage complex can induce DNA double strand breaks (Lyu et al., 2007). In the presence of Top2β, DOX activates apoptosis pathways and a DNA damage response that triggers a marked alteration in the transcriptome that affects oxidative phosphorylation and mitochondrial biogenesis (Arola et al., 2000; Zhang et al., 2012). How DOX-induced nuclear DNA damage specifically targets mitochondrial-related transcripts remains unclear but it has been suggested to be linked to a decrease in transcript levels of peroxisome proliferator-activated receptor gamma co-activator 1 alpha and beta (*Ppargc1a* and *Ppargc1b*, respectively*)*, which are crucial for mitochondrial function (Zhang et al., 2012). It has been reported that Top2β in the presence of DOX binds to the promoters of *Ppargc1a* and *Ppargc1b* in isolated myocytes (Zhang et al., 2012). Cardiomyocyte-specific deletion of *Top2b* protects cardiomyocytes from DOX-induced DNA double-strand breaks and transcriptome changes that are thought to cause defective mitochondrial biogenesis and ROS formation (Zhang et al., 2012). Additionally, cardiomyocyte-specific deletion of *Top2b* has been shown to protect mice from the development of DOX-induced progressive HF, suggesting that DOX-induced cardiotoxicity is at least in part mediated through DOX's interaction with Top2β (Zhang et al., 2012). The role of Top2β in DOX-induced cardiotoxicity

means anti-cancer agents that specifically target Top2α, but not Top2β, assuming DOX interaction with Top2β does not contribute to DOX's anti-cancer efficiency have the potential to be less cardiotoxic and, therefore, more clinically useful.

Dexrazoxane can antagonise the formation of the Top2β-DOX-DNA complex through stabilisation of the ATP-bound closed-clamp conformation of Top2 (Andoh, 1998; Classen et al., 2003), thereby it is hypothesised to antagonise DOX-induced DNA damage (Lyu et al., 2007). However, a topoisomerase-inactive analogue of dexrazoxane that retains iron-chelating function has been reported to provide similar protection to its parent compound (Martin et al., 2009). In addition, knockdown of *Top2b* had no effect on DOX-induced changes in ABCB8 protein expression or mitochondrial iron content (Ichikawa et al., 2014). This data suggests that mitochondrial toxicity occurs through at least two independent mechanisms.

1.4.6 Inflammation and DOX-induced cardiomyopathy

Levels of pro-inflammatory cytokines, such as interleukin (IL)-1 and tumour necrosis factor (TNF)-α, have been found to be significantly increased following DOX treatment and blocking pro-inflammatory functions has been reported to protect against DOX-induced cardiotoxicity (Ma et al., 2012; Riad et al., 2008; Zhu et al., 2010). The IL-1 family is known to play a significant role in the pathogenesis of heart disease (Bujak and Frangogiannis, 2009). IL-1 binds the transmembrane IL-1 type I receptor (IL-1R1) and initiates downstream signalling. IL-1 receptor antagonist (IL-1Ra) competitively interacts with IL-1R1 to prevent IL-1 signalling (Eisenberg et al., 1990). Treatment with recombinant human IL-1Ra has been reported to protect mice against acute DOX-induced cardiotoxicity, suggesting DOX-induced myocardial injury triggers a pro-inflammatory state that contributes to the progression of DOX-induced

cardiomyopathy (Zhu et al., 2010). The extent and contribution of inflammation to chronic DOX-induced cardiotoxicity remains relatively poorly characterised. Targeting inflammation systemically as part of treatment strategies to limit cardiotoxicity during anti-cancer treatment is unlikely to be advantageous since an effective immune response is necessary as part of DOX's anti-tumour efficiency (Ghiringhelli et al., 2009), however minimising adverse inflammation and cardiac remodelling following DOX treatment could be beneficial. Numerous clinical studies have found that patients with chronic HF have increased circulating levels of inflammatory cytokines such as TNF-α, IL-1β, IL-6 and IL-18 (Aukrust et al., 1999; Levine et al., 1990; Mallat et al., 2004; Testa et al., 1996; Torre-Amione et al., 1996a). In HF a rise in circulating levels of pro-inflammatory cytokines is not accompanied by a rise in anti-inflammatory cytokines, such as IL-10, suggesting a chronic inflammatory state (Aukrust et al., 1999). Significantly, the failing myocardium has also been reported to have increased expression of pro-inflammatory cytokines (Eiken et al., 2001; Mallat et al., 2004; Torre-Amione et al., 1996b). Pathophysiologically relevant concentrations of pro-inflammatory cytokines in animal models have been shown to cause LV dysfunction (Bozkurt et al., 1998; Pagani et al., 1992; Tracey et al., 1986) and LV remodelling including myocyte hypertrophy (Yokoyama et al., 1997), alterations in foetal gene expression (Kubota et al., 1997), progressive myocyte loss through apoptosis (Krown et al., 1996) and extracellular matrix (ECM) remodelling (Bozkurt et al., 1998; Pagani et al., 1992). However clinical therapeutic interventions aimed at targeting inflammation in chronic HF have been largely unsuccessful. Two multicentre clinical trials of anti-TNF-α treatment in patients with chronic HF were neutral (Mann, 2002). It is possible that a better understanding of inflammation in HF could lead to more effective treatment strategies aimed at limiting pathological inflammation in the myocardium.

1.5 Proposed mechanisms of sunitinib-induced cardiotoxicity

1.5.1 Hypertension

It is hypothesised that STB-induced hypertension contributes to a deterioration in LV function with STB treatment. Hypertension is a frequent side effect associated with inhibition of the VEGF signalling pathway (Sica, 2006; Verheul and Pinedo, 2007). STB is a potent inhibitor of VEGFR2 (Mendel et al., 2003). How exactly angiogenesis inhibitors cause hypertension is unknown but may involve mechanisms including increased vascular resistance, vascular rarefaction and/or increased arterial stiffness which results in a loss of capillaries, impaired blood flow and regional ischaemia (Chintalgattu et al., 2010; Izumiya et al., 2006; Thirunavukkarasu et al., 2008; Thirunavukkarasu et al., 2007).

VEGF has been shown to induce nitric oxide (NO)-dependent relaxation in coronary arteries (Ku et al., 1993). VEGF increases endothelial NO synthase levels via activating phosphatidylinositol 3-kinase (PI3K)/Akt and mitogen-activated protein kinase (MAPK) pathways and plays an important role in maintaining baseline vascular tone via NO synthesis (Gelinas et al., 2002; Hood et al., 1998; Horowitz et al., 1997). VEGF has also been shown to induce prostacyclin production (Gliki et al., 2001; He et al., 1999). Prostacyclin inhibits platelet activation and is a vasodilator. In a clinical trial a rapid decline in mean arterial pressure (8-12 mm Hg) was observed in patients receiving an IV infusion of recombinant human $VEGF_{165}$ (Eppler et al., 2002). These findings suggest that inhibition of VEGF signalling may result in a decrease in NO and a prostacyclin production resulting in increased vascular resistance and blood pressure.

A small clinical study has demonstrated that VEGF kinase inhibitor treatment over 5 weeks resulted in capillary rarefaction and an increase in blood pressure (Steeghs et al., 2008). A reduction in capillary density has been reported in patients treated with STB (van der Veldt et al., 2010). A reduction in skin capillary density was associated with a rise in blood pressure during STB therapy (van der Veldt et al., 2010). Bevacizumab is a monoclonal anti-VEGF antibody that binds to the VEGF-A isoform (Ferrara et al., 2004). Bevacizumab treatment is associated with hypertension (Cobleigh et al., 2003; Syrigos et al., 2011). A reduction in capillary density induced by bevacizumab treatment in patients was found to be reversible (Steeghs et al., 2010).

Hypertension has been associated with an increase in arterial stiffness (Safar et al., 2003). The VEGFR2 inhibitor sorafenib has been reported to cause vascular stiffness in patients treated with sorafenib for 3 to 6 weeks (Veronese et al., 2006). PDGFRβ is inhibited by sorafenib and STB (Schmidinger et al., 2008). PDGFRβ is found in pericytes that surround capillary endothelial cells and plays a pivotal role in stabilising the vascular endothelium. PDGFRβ plays a role in mediating angiogenesis in the heart and has been shown to be key to load-induced stress in the mouse heart by promoting myocardial angiogenesis and preserving microvascular density which conserves coronary flow (Chintalgattu et al., 2010). The role of PDGFRβ signalling in the heart remains largely unknown but it may be involved in STB-induced hypertension.

STB-induced hypertension is associated with an increase in circulating levels of endothelin-1, a potent vasoconstrictor (Kappers et al., 2010). In rats an endothelin A receptor, the receptor for endothelin 1, antagonist prevented a rise in blood pressure induced by a TKI (Banfor et

al., 2009) suggesting endothelin-1 plays a role in TKI-induced hypertension. The reason why endothelin-1 levels increase during angiogenesis inhibition is not known.

1.5.2 AMP-activated protein kinase

Several patients who developed STB-induced cardiotoxicity did not have hypertension suggesting that additional mechanisms may be responsible for cardiac dysfunction (Chu et al., 2007). In addition, toxicity has been observed in isolated cardiomyocytes exposed to STB (Chu et al., 2007). Transmission electron micrographs of endomyocardial biopsies of a patient with STB-induced cardiotoxicity showed striking mitochondrial structural abnormalities suggesting energy compromise might contribute to LV dysfunction (Kerkela et al., 2009). Studies in neonatal rat ventricular cardiomyocytes (NRVM) confirmed energy compromise in STB-mediated toxicity. Paradoxically this decrease in available energy did not lead to activation of 5'-adenosine monophosphate (AMP)-activated protein kinase (AMPK). AMPK is a central regulator of cellular energy homeostasis and is activated in response to ATP depletion (Kahn et al., 2005). Energy compromise with STB treatment has been reported to be due to direct inhibition of AMPK by STB (Kerkela et al., 2009). Adenovirus-mediated gene transfer of an activated mutant of AMPK was found to partially prevent STB-induced toxicity in NRVM (Kerkela et al., 2009). This work suggests that STB-induced cardiotoxicity is mediated at least in part by inhibition of AMPK, which results in "off-target" toxicity. However, the protective role of AMPK in maintaining viability of hypoxic cancer cells suggests that this "off-target" effect may be important for STB's anti-cancer efficiency (Liu et al., 2006).

An inhibitor-binding assay predicted that inhibition of ribosomal S6 kinase (RSK) by STB could be seen at clinically relevant concentrations (Fabian et al., 2005). The RSK family signal survival through inhibitory phosphorylation of the pro-apoptotic factor BAD (Anjum and

Blenis, 2008). Inhibition of RSK could lead to BAX activation and permeabilisation of the OMM. Possible additional effects of STB on mitochondrial function have been postulated due to the abnormal mitochondrial morphology seen in patients treated with STB but the mechanisms involved remain unknown (Force et al., 2007).

1.6 Summary

As cancer survival rates improve, cardiotoxicity resulting from the agents used to treat neoplastic disorders is becoming increasingly clinically relevant. Our understanding and knowledge of the underlying mechanisms, targets involved and the combination of contributing effects that lead to myocardial damage and the cardiac complications of anti-cancer therapies is limited. A further complexity is that agents that have been reported to induce cardiotoxicity have different mechanisms of action. Furthermore, it is important to note that cancer patients undergoing treatment are often severely ill as a result of adverse effects of cancer therapy on the rest of the body and it is highly likely a number of factors contribute to the pathogenesis of cardiotoxicity. Nevertheless, it is significant that a common final organelle which is frequently affected by this toxicity is the mitochondrion. The heart as an organ is particularly reliant on healthy mitochondrial function to provide energy, participate in calcium signalling and mediate controlled cell death pathways, all of which make it particularly susceptible to pathological disorders in which mitochondria are damaged. Methods to detect early mitochondrial dysfunction, which may indicate and/or mediate pathophysiological processes, are lacking. Further animal and clinical studies aimed at understanding the mechanisms of anti-cancer agent-induced cardiotoxicity may lead to a better understanding of cardiac function as well as improved strategies to prevent cardiac damage while improving the comorbidity and survival of patients with cancer. The present study aimed to contribute to

research designed to fill the lacunae in our current knowledge of the role of cardiac mitochondria in the pathogenesis of anti-cancer agent-induced cardiotoxicity.

1.7 Hypothesis

I hypothesize that there is acute mitochondrial dysfunction with DOX treatment and that mitochondrial dysfunction contributes significantly to the pathogenesis and phenotype of DOX-induced cardiotoxicity.

1.8 Aim of the study

The main aim of this thesis was to investigate the effects of anti-cancer agents on the heart on multiple scales with a specific focus of the impact upon cardiac mitochondrial function.

1.8.1 Aims

1. To examine the chronic effect of DOX treatment on myocardial function and cardiac mitochondria using an *in vivo* model of DOX-induced cardiotoxicity
2. To further develop *in vitro* and *ex vivo* models in order to examine the acute effect of anti-cancer agents on mitochondrial function

Chapter 2

Material and Methods

Chapter 2 Material and methods

2.1 Animals

All animal procedures were carried out in accordance with the UK Home Office Animals (Scientific procedures) Act 1986 and Directive 2010/63/EU of the European Parliament on the protection of animals used for scientific purposes and approved by Imperial College London (ICL) Animal Welfare.

All animals studies described in this thesis were performed using male Sprague Dawley (SD) rats (Charles River Laboratories, UK). The SD rat is an outbred albino strain of the brown rat (*Rattus norvegicus*) bred specifically for laboratory studies. Rats were housed at a density of 2-4 per cage and maintained on a 12 h light/dark cycle at 21°C. Rats had access to standard rat chow and water *ad libitum*. The average food intake for a male SD rat is approximately 5 g/100 g body weight/day and average water intake is approximately 10-12 ml/100 g body weight/day. Rats used typically weighed 225-350 g (7-12 weeks old). Some larger rats (< 500 g) were used for optical mapping studies and cardiomyocyte isolation. All *in vivo* experiments were performed at least one week after arrival of animals to the Central Biomedical Services facility at Hammersmith campus, ICL, to allow the animals to fully acclimatise to their new environment.

2.2 Solutions and reagents

All reagents were obtained from Sigma-Aldrich (UK) unless otherwise stated.

0.9% normal saline (mM): NaCl (154).

MitoQ was obtained from Prof. Michael Murphy, Medical Research Council (MRC) Mitochondrial Biology Unit, University of Cambridge, UK.

2.2.1 Anti-cancer agents

Doxorubicin hydrochloride

All experiments undertaken using DOX used medical grade doxorubicin hydrochloride 2 mg/ml concentration solution for infusion obtained through Hammersmith hospital pharmacy from Accord Healthcare Ltd., UK.

SU14813

The compound SU14813 (SU) was obtained as part of a research collaboration with Pfizer Inc., USA. A stock concentration of SU was made in DMSO.

Sunitinib

STB 50 mg hard capsules were purchased through Hammersmith hospital pharmacy from Pfizer Inc. Contents of the STB capsules were solubilised in distilled water and insoluble material was removed by repeated centrifugation at 2500 g prior to use for the times and at the concentrations noted (Kerkela et al., 2009).

2.3 In vivo studies

2.3.1 Study outline

Male SD rats (225-250 g) were administered eight weekly doses of 1.25 mg/kg IV doxorubicin hydrochloride or vehicle alone (0.9% w/v sterile sodium chloride) via tail vein injection. Rats underwent echocardiographic assessment at baseline and at protocol week 4, 6, 8 and 11. Rats were sacrificed at week 11. Clinical observations, food and water intake and body weight were monitored daily. At sacrifice cardiac tissue was washed in ice-cold heparinised (0.2 mL/50 mL) Krebs-Henseleit solution ((mM): NaCl (121.8), KCl (4.5), $MgSO_4$ (1.2), $CaCl_2$ (1.85), NaH_2PO_4 (1.2), $NaHCO_3$ (22), glucose (11.1); pH equilibrated with 95% O_2, 5% CO_2 (BOC Healthcare, UK)), weighted and rapidly dissected into tissue samples for transmission electron microscopy (TEM), RNA sequencing (RNA-seq) and histology. Echocardiographic assessment and DOX administration was performed with Dr. Benjamin Dyer (National Heart and Lung Institute (NHLI), ICL, UK), a PhD student in the Lyon lab, who is working on the application of label-free autofluorescence lifetime metrology as a novel technique to assess heart disease (Lagarto et al., 2015).

A dose of 1.25 mg/kg DOX is equivalent to approximately 50 mg/m^2 in humans (Cove-Smith et al., 2014). DOX is typically administered in humans at a dose of 40 to 60 mg/m^2 IV every 21 to 28 days until disease progression or unacceptable toxicity. Adult male SD rats typically live 2.5 to 3.5 years. Future studies may wish to use a lower dose of DOX over a longer time period. Practically this would mean a much longer experimental protocol. The present dosing protocol was used because it has been shown to cause a significant decline in cardiac function over three months with limited adverse side effects and it is consistent with clinical sub-acute cardiotoxicity (Cardinale et al., 2015; Cove-Smith et al., 2014).

2.3.2 DOX administration protocol

Chemotherapeutic substances are an irritant at the site of injection and are known to cause damage to the tissue and veins in patients receiving chemotherapy. DOX is administered intravenously in patients. The DOX dose is often diluted in large volumes and administered as an infusion instead of a bolus to minimise damage to the vein and tissue. DOX has been reported to cause a burning sensation upon administration along the vein, severe skin irritation, and/or tissue damage in patients. DOX can also cause venous stenosis and phlebitis. A number of refinements were made to the DOX administration protocol to minimise adverse effects. DOX was administered under light general anaesthetic to permit IV cannulation and drug administration while minimising pain and/or stress to the animal. Stock DOX was diluted in saline to give a larger volume lower concentration drug bolus. A flush of saline after drug bolus was used to remove any residual DOX from the tail vein in order to try to minimise tissue damage at the site of injection.

Rats were transferred to an anaesthetic chamber and isoflurane (5% in 100% O_2 (BOC Healthcare)) was delivered until the animal was anaesthetised, as determined by a loss of the righting reflex. Following the loss of the righting reflex, the animal was moved to a bench top. Pedal and palpebral reflexes were tested at regular intervals to ensure the animal was sufficiently sedated. Anaesthesia was maintained using a Bain co-axial tube (1.5-3% isoflurane in 100% O_2, 1.5 L/min) with anaesthetic gases removed using a Fluovac scavenger (Harvard Instruments, USA). The skin was swabbed with alcohol prior to and post injection. The position and side of IV injection was alternated and moved proximally each week. Using a 26G IV cannula (Hospira, USA) a flush of saline was using to confirm that the cannula was in the vein and avoid extravasation. DOX, diluted in saline, was delivered and a flush of saline

was used to clear DOX out of the vein. Pressure was applied to the site of injection and rats were placed in a warm box to recover. The site of injection was monitored daily.

2.3.3 Echocardiography protocol

The Vevo 770 ultrasound system (VisualSonics, Canada) was utilised for echocardiographic assessment. This system was purposely designed for small animal imaging applications. Rats were brought to the echocardiography suite and anaesthetised in a chamber with an atmosphere of 5% isoflurane/95% O_2. Following the loss of the righting reflex, the animal was moved to a bench top. Pedal and palpebral reflexes were tested at regular intervals to ensure the animal was sufficiently sedated. Anaesthesia was maintained using a Bain co-axial tube (1.5-3% isoflurane in 100% O_2, 1.5 L/min) with anaesthetic gases removed using a Fluovac scavenger (Harvard Instruments). The animal was transferred and secured to a VisualSonics electrocardiogram (ECG) plate by the paws in a dorsal recumbence using surgical tape. Electrode gel was applied before fixing the paws in position. Body temperature was monitored using a rectal thermometer connected to a homeothermic temperature monitor (Harvard Apparatus, USA). The homeothermic monitor outputted to a heated blanket (Harvard Apparatus), the temperature of which was adjusted according to the animal's body temperature. Fur was rapidly removed from the pectoral region using a trimmer and hair depilatory cream (Church and Dwight, USA) was applied to the area for 3 min, after which cream was removed and the chest cleaned with damp tissue to remove any residue. Ultrasound gel (Henleys Medical Supplies, UK) was applied to the pectoral region to displace any air present between the animal's skin and the ultrasound probe head. The ultrasound probe (RMV-716, Visualsonics) was manoeuvred and held in place above the animal on a specifically designed clamp-stand. The probe was lowered into contact and imaging initiated. The view of the heart was adjusted to show the LV cavity with a clear line of sight between

the apex and the ascending aorta with the left atrial annulus visible. The brightness mode or B-mode image provided 2D images of the heart which could be acquired and saved as image loops to form videos of cardiac function. Using the motion mode or M-mode image distances between anatomical elements could be measured to calculate fractional shortening (FS) and ejection fraction from the end diastolic and end systolic diameter of the left ventricle. Following echocardiographic assessment animals were cleaned to remove any residual gel and placed in a warm box to recover. Animals were monitored to ensure full recovery post anaesthesia.

2.4 Isolated cardiomyocyte studies

2.4.1 Isolation and culture of adult rat ventricular cardiomyocytes

Rats were humanely killed by cervical dislocation after a period of anaesthesia in an atmosphere of 5% isoflurane/95% O_2. Transabdominal incisions were made across the base of the rib cage to access the diaphragm. The diaphragm was carefully cut on either side to expose the thoracic cavity. The entire contents of the cavity were promptly removed and placed in ice-cold heparinised Krebs-Henseleit solution ((mM): NaCl (119), KCl (4.7), $MgSO_4$ (0.94), $CaCl_2$ (1), KH_2PO_4 (1.2), $NaHCO_3$ (25), glucose (11.5); pH equilibrated with 95% O_2, 5% CO_2). The lungs, thyroid and superfluous pericardial fat were dissected away from the heart leaving the aorta and atria intact. The heart was cannulated via the aorta and clipped onto a Langendorff apparatus and perfusion of the heart with Krebs-Henseleit solution at 37°C was begun. Nylon thread was used to ensure that all fluid exiting the cannula was directed through the coronary circulation. The heart was surrounded by a heated jacket, to maintain the temperature at 37°C, and retrogradedly perfused with Krebs-Henseleit solution at a steady flow of 6-8 mL/min/g via a peristaltic pump to clear the vasculature of blood and to

allow steady rhythmic beating of the heart to be established. Upon full clearance of blood from the coronary circulation the Krebs-Henseleit solution was switched to a low calcium solution (12-15 μM $CaCl_2$, 120 mM NaCl, 5.4 mM KCl, 5 mM MgSO4, 5 mM pyruvate, 20m M glucose, 20 mM taurine, 10 mM HEPES, 5 mM nitrilotriacetic acid (NTA); 100% O_2) for 5 min. At this point a solution of 1 mg/ml collagenase II and 0.6 mg/ml hyaluronidase (C+H) in enzyme solution (200 μM $CaCl_2$, 120 mM NaCl, 5.4 mM KCl, 5 mM $MgSO_4$, 5 mM pyruvate, 20 mM glucose, 20 mM taurine, 10 mM HEPES; 100% O_2) was perfused into the heart for 10 min. After 10 min of enzymatic degradation the Langendorff perfusion was switched off and the heart cut down. The heart was placed in clean C+H solution and dissected. The right ventricular free wall and atria were removed. The remaining left ventricle was chopped into 2-4 mm^3 sections and placed in fresh C+H in a 50 mL falcon tube. The sample was shaken mechanically at 35°C for 5 min at which point the supernatant was filtered through 300 μm nylon gauze and undigested tissue was placed in fresh C+H in a 50 mL falcon tube. The sample was shaken for a further 30 min at which point the supernatant was strained through gauze. The resulting filtrate was centrifuged for 1 min at 700 rpm. This yielded a pellet of isolated cardiomyocytes; the supernatant was removed from the sample and the pellet re-suspended in the enzyme solution without 1 mg/ml Collagenase II and 0.6 mg/ml hyaluronidase. Mr. Peter O'Gara (NHLI, ICL, UK) performed the isolation of adult rat ventricular cardiomyocytes (ARVM).

Cells were washed twice by centrifuging for 1 min at 500 rpm and re-suspended in M199. For experiments using a Seahorse XFp Extracellular Flux Analyser (Agilent Technologies, USA) approximately 250 viable cells per well were placed onto laminin-coated Seahorse XFp cell culture miniplates. For quantitative real-time polymerase chain reaction (qPCR) analysis approximately 100,000 viable cells per well were placed onto laminin-coated 6-well plates. After a 45 min period of adhesion, dead and non-adherent cells were washed off and the

remaining myocytes were cultured in M199 media with additions (2 mg/ml bovine serum albumin, 0.02 mg/ml ascorbic acid, 0.66 mg/ml creatine, 0.63 mg/ml taurine, 0.32 mg/ml carnitine, 1% insulin-transferrin-selenium-ethanolamine, 1% penicillin-streptomycin at 37°C and 5% CO_2). Fig. 2.1 shows a freshly isolated adult rat ventricular cardiomyocyte stained for α-actinin (sarcomeric).

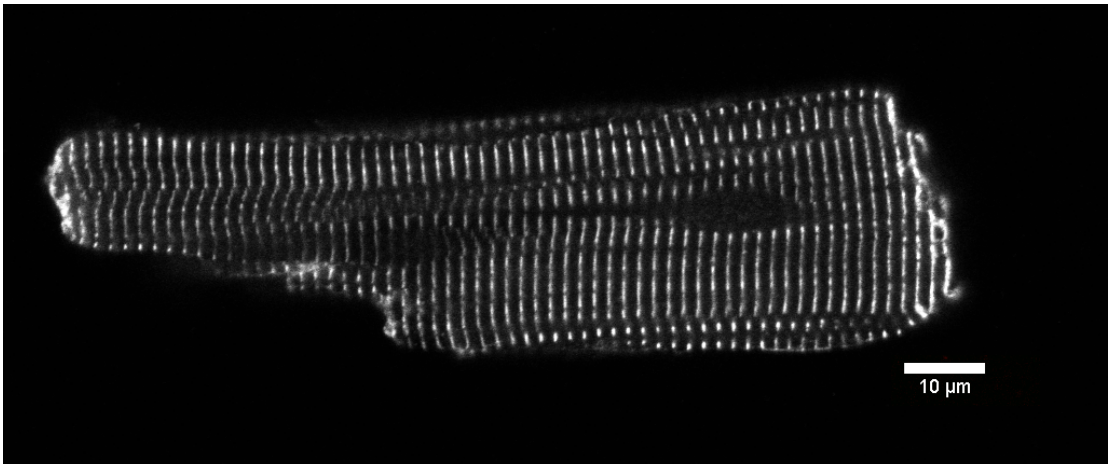


Fig. 2.1 Representative image of a freshly isolated adult rat ventricular cardiomyocyte stained for α-actinin (sarcomeric). Scale bar represents 10 µm.

2.4.2 Twenty-four hour anti-cancer agent treatment of ARVM

Cardiomyocytes were isolated and plated as described above. Following attachment, M199 was replaced with fresh M199 containing anti-cancer agents. Cells were incubated in a cell culture incubator at the dose and for the time stated for the experimental protocol.

2.4.3 Assessing cardiac mitochondrial function *in vitro*

A Seahorse XFp Extracellular Flux Analyser was used to measure the oxygen consumption rate (OCR) of freshly isolated ARVM in real-time. The Seahorse XF Cell Mito Stress Test

(Agilent Technologies) was performed with compounds that have a known effect on the cellular OCR and mitochondrial function including oligomycin A, carbonyl cyanide-4-trifluoromethoxyphenylhydrazone (FCCP), rotenone and antimycin A according to manufacturer's instructions. Prior to all assays M199 was replaced with XF Base Medium (Agilent Technologies) with additions (5.5 mM glucose, 1 mM sodium pyruvate and 1 mM L-glutamine; pH 7.4, 37°C) and the plate was placed in a non-CO_2 incubator for one h, as per manufacture's instructions. During the assay measurements were performed using a cartridge in which optical fluorescent O_2 and H^+ sensors were imbedded in individual well probes. The probes gently descended into the wells, forming a transient microchamber containing < 3 µL of medium above the cell monolayer. The sensors measure the O_2 and H^+ levels over 3 min. Four measurements were taken for each treatment period. In between measurements there are 3 min in which the well is mixed. The OCR, measured in pmol/min, was standardised with the total protein concentration in each well determined at the end of the experiment using Pierce BCA Protein Assay Kit (Thermo Fisher Scientific, USA) and normalised to baseline measurements.

2.5 *Ex vivo* optical mapping of mitochondrial function

2.5.1 Langendorff-perfused rat heart preparation

Rats were humanely killed by cervical dislocation after a period of anaesthesia in an atmosphere of 5% isoflurane/95% O_2. Rat hearts were rapidly excised and washed in ice-cold heparinised Krebs-Henseleit solution ((mM): NaCl (121.8), KCl (4.5), $MgSO_4$ (1.2), $CaCl_2$ (1.85), NaH_2PO_4 (1.2), $NaHCO_3$ (22), glucose (11.1); pH equilibrated with 95% O_2, 5% CO_2). Aortas were cannulated to allow retrograde perfusion of the coronary vessels with oxygenated Krebs-Henseleit solution on a flow-driven Langendorff apparatus (Radnoti, USA)

set at a constant flow rate of 16-18 mL/min and a temperature of 37.0 ± 1°C. Hearts were suspended in a Krebs-Henseleit solution filled perspex optical mapping chamber with a quartz window (Cairn Research, UK) (Fig. 2.3). The chamber was used to reduce movement artefact and to control the temperature (37.0 ± 1°C) surrounding the heart. Volume conducted ECG was recorded for rhythm analysis using non-contact silver electrodes (Grass Technologies, USA). ECG, heart rate (HR) and temperature signals were recorded continuously throughout the entire *ex vivo* perfusion protocol. These signals were acquired at 1000 Hz via a bioamplifier system (PowerLab 8/35; AD Instruments, UK) and displayed using LabChart 7 software version 7.3.7 (AD Instruments). Hearts were positioned such that the mapping field was centred and focused over the LV epicardium. Following 10 min of stabilisation only hearts meeting the inclusion criteria (HR 250-400 beats per minute (BPM) in sinus rhythm, coronary flow rate 16-18 mL/min and an absence of sustained (> two per minute) premature ventricular contractions) were studied. Electrical stimulation (2 ms duration and 2 times threshold voltage) was delivered with a bipolar platinum wire electrode, positioned in the left atria. A multifunction board (Micropace EPS320 cardiac stimulator software version 3.21; Micropace EP Inc., USA) generated the pulse logic to drive stimulus isolators. Hearts were paced at 400 BPM.

2.5.2 Optical apparatus

Light (530 nm) from four light emitting diodes (LEDs) (Cairn Research) was focused onto the surface of the heart. Optical images were taken through a modified microscope (Olympus, Japan) fitted with a 1x magnification camera lens (MVPLAPO; Olympus) and a 10x body zoom. Fluorescence was focused through a dichroic mirror at 45° with a cut-off of 560 nm (Chroma Technology, USA), to filter only fluorescent light down the optical path. Fluorescence was then focused onto a dichroic mirror at 45° with a cut-off of 610 nm and was

passed into one of two 128 x 80 pixel charge-coupled device (CCD) cameras (Scimeasure, USA). Fluorescence below 610 nm was reflected into a CCD camera after being passed through a 585 ± 20 nm filter and fluorescence above 610 nm passed through the mirror and was focused into another CCD camera after being passed through a 620 nm cut-off filter. Fig. 2.2 shows a schematic representation of the experimental apparatus used for optical mapping of mitochondrial function in the *ex vivo* rat heart. Fig. 2.3 shows images of the experimental apparatus. Data was acquired using CardioPlex software version 10.0.3 (Red Shirt Imaging, USA) at a rate of 1000 fps. Fluorescence intensity was measured for 3 s in 2 min intervals for the entire experimental protocol.

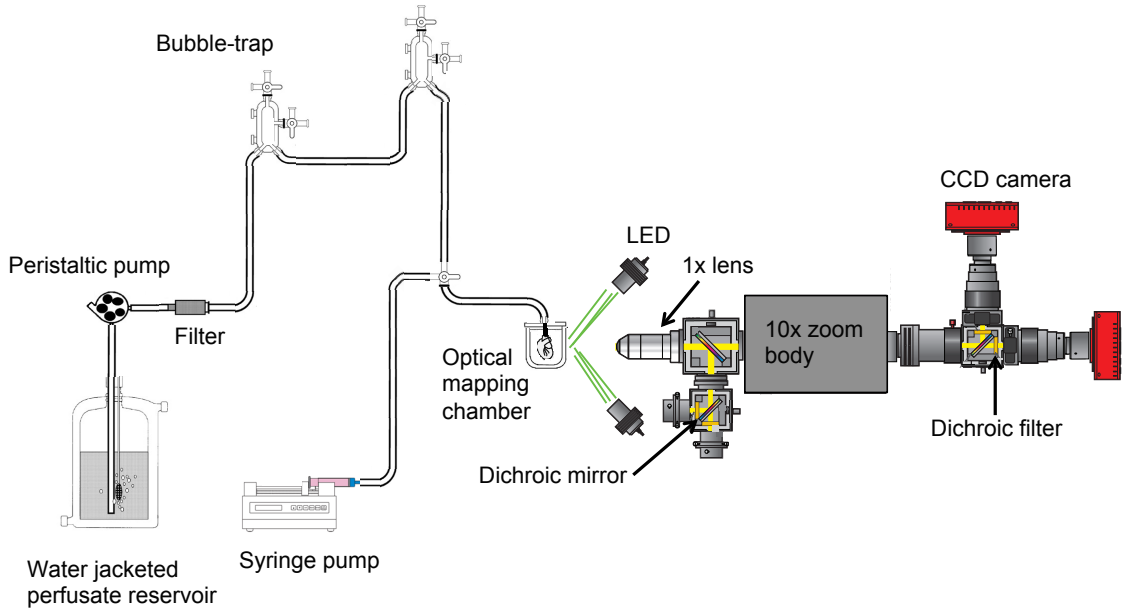


Fig. 2.2 Schematic representation of the experimental apparatus for *ex vivo* optical mapping of mitochondrial function.

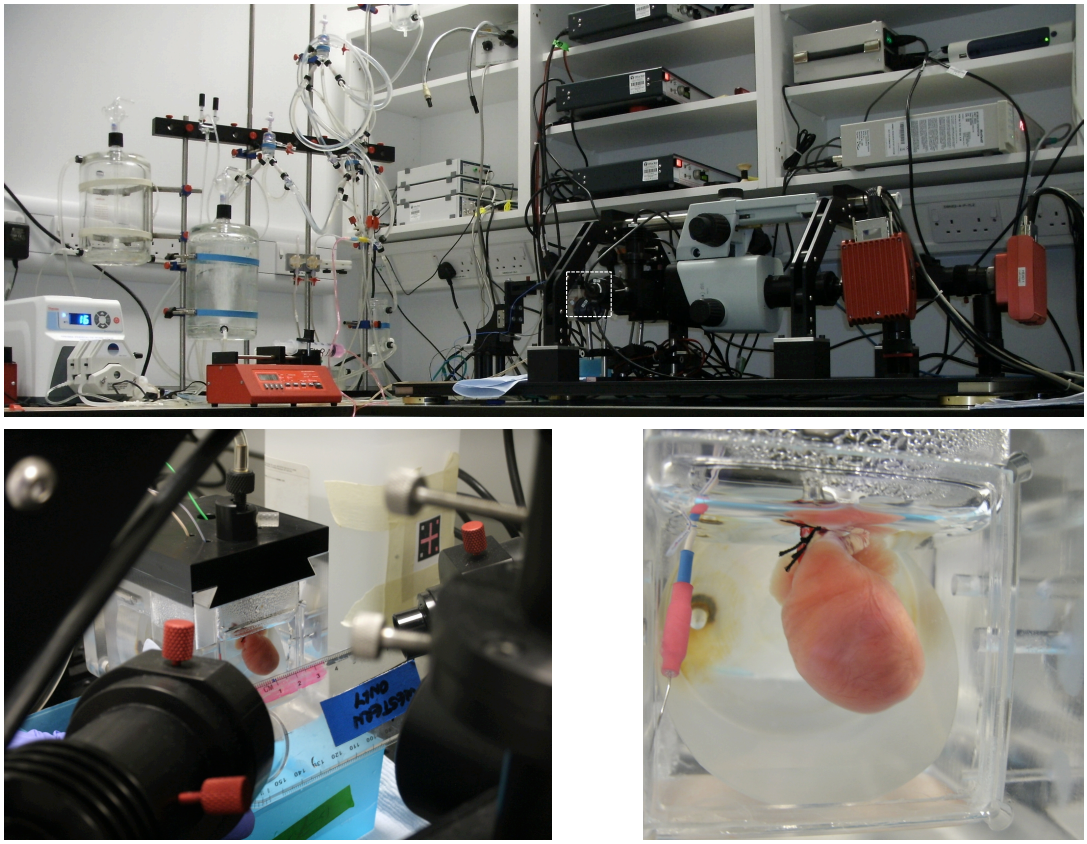


Fig. 2.3 Photos of the optical mapping system used for *ex vivo* imaging.
Images of the optical mapping system with the Langendorff apparatus (top), optical imaging setup and the perfused rat heart in the optical mapping chamber (bottom). White dashed square indicates the position of the optical mapping chamber.

2.5.3 Optical mapping protocol

Following ten min of stabilisation auto-fluorescence data was acquired for 4 min to obtain background fluorescence without fluorescent dyes. Hearts were then perfused for 20 min with Krebs-Henseleit solution containing 200 nM tetramethylrhodamine methyl ester (TMRM) (Thermo Fisher Scientific) using a syringe pump (Fig. 2.3) (Harvard Apparatus) (TMRM loading phase). This was followed by a 20 min dye washout and fluorescence signal stabilisation period during which perfusion was switched back to dye free Krebs-Henseleit solution (TMRM washout phase). Once a stable fluorescence intensity of TMRM had been achieved this was used as the steady-state TMRM fluorescence intensity and data was normalised to this point (baseline). Mitochondrial dysfunction, manifesting as depolarisation of the mitochondrial membrane potential ($\Delta\Psi_m$), was observed as a drop in steady-state TMRM fluorescence intensity.

2.5.4 Optical mapping data analysis

Data was processed with MATLAB® software version R2014b (8.4.0.150421). Custom code for bioinformatic analysis of optical mapping data was written by Dr. Jennifer Simonotto (NHLI, ICL, UK) to read in data and undertake initial processing (to remove dark frame artefact). Initial auto-fluorescence signals were subtracted for each pixel so the fluorescence analysed was from TMRM only. Following dye loading and washout phases data was normalised to one (steady-state TMRM fluorescence intensity) and this was used as a baseline to compare treatment for each pixel. For analysis a region of interest on the left ventricle was used. For whole heart epicardial fluorescence imaging custom code was designed and written with Dr. J. Simonotto to look at spatiotemporal changes in the $\Delta\Psi_m$.

2.6 Transmission electron microscopy

LV tissue was rapidly dissected under oxygenated ice-cold Krebs-Henseleit solution with 30 mM 2,3-butanedione monoxime (to ensure relaxed state of the muscle), pinned to sylgard gel in a petri dish and fixed in 3% glutaraldehyde in Krebs-Henseleit solution for 1 h. Samples were stored in 2.5% glutaraldehyde in 0.1 M sodium cacodylate buffer at 4°C until processing. Samples were rinsed 3 times for 5 min in Krebs-Henseleit solution (lacking $CaCl_2$) and fixed in 1% aqueous osmium tetroxide on a rotator for 1 h. Samples were rinsed in distilled water 2 times for 3 min. Rinsed samples were dehydrated in acetone series for 15 min on a rotator in 50, 70, 80, 90, 95 and 100% acetone. The final dehydration step in 100% acetone was repeated. Dehydrated samples were infiltrated in a 1:1 ratio of araldite resin: acetone overnight on a rotator. The following day samples were prepared for embedding in araldite epoxy resin. The resin/acetone mixture was removed and new araldite resin was replaced for 1 h at 50°C. The sample lid was removed to allow any remaining acetone to evaporate. After 1 h fresh resin was applied and samples were left on a rotator for 30 min at 50°C. Samples were carefully cut into smaller pieces and placed into droplets of araldite epoxy resin on melinex sheets for 1.5 h at 50°C, until the droplet containing the sample was partly polymerised. Embedding capsules filled with araldite epoxy resin were inverted over the partly polymerised samples and placed in the oven at 50°C for 48 h. To remove the capsules from the melinex sheet and avoid damaging the face of the block the sheets were submerged in liquid nitrogen. Blocks, containing the samples, were removed from the capsule using a capsule press. Blocks were examined using a light microscope to see the best samples with striations for sectioning. Semi-thin (0.5 µm) and ultra thin (90 nm) sections were cut with a Reichert Ultracut-E ultramicrotome (Reichert Technologies, USA). Semi-thin sections were stained with toluidine blue, embedded in araldite epoxy resin (epon-embedded) and imaged using a light microscope to check the section for the quality of preservation of tissue

morphology. Ultra thin sections were picked on thin hexagonal grids and stained with 2% uranyl acetate followed by Reynold's lead citrate. The sections were examined in a JEOL 1200 EX transmission electron microscope (JEOL, USA) and photographed using a Tietz Fastscan-114 1024 x 1024 CCD camera operated through EM-Menu4 software.

2.7 Histology

Rat hearts were rapidly excised and flushed in ice-cold Krebs-Henseleit solution. Excess connective, fat and aortic tissue was removed. Atria were removed and ventricular tissue was quickly washed in sterile phosphate buffered saline (PBS) before being placed in neutral buffered 10% v/v formalin solution and stored at room temperature. For processing ventricular tissue was placed in plastic histo-cassettes in a sealed container of neutral-buffered 10% formalin. Ventricular tissue was processed overnight using the Miles Tissue-Tek (Sakura, UK) tissue processor. Following processing, tissue was removed from the plastic histo-cassettes and embedded in paraffin to form blocks for sectioning using the Tissue-Tek embedding system.

Tissue sections were cut at 7 μM using a Leica microtome 2040 (Reichert Technologies), floated on 35°C water and taken onto adhesive glass slides (Leica Microsystems, UK). Slides were air-dried for 10 min and then baked at 60°C on a hotplate for 30 min to bond the tissue to the glass in preparation for staining. For histological staining tissue sections were deparaffinised and rehydrated through sequential xylene and graded alcohol washes, equilibrated in PBS then stained with haematoxylin and eosin Y (H&E). Following dehydration in a series of alcohol and xylene washes the sections were mounted with DPX. For immunofluorescence staining tissue sections were deparaffinised and rehydrated through sequential xylene and graded alcohol washes then left to equilibrate in PBS for 5 min. Heat

mediated antigen retrieval was performed on the rehydrated sections by immersing them in citrate buffer pH 6.0 and heating them to 95°C for 30 min in a steamer. Tissue sections were blocked with 5% goat serum in PBS for 1 h at room temperature then incubated with the primary antibody (mouse anti-rat cluster of differentiation (CD) 68 clone ED1 (MCA 341) (Bio-Rad, USA) or chicken anti-rat anti-vimentin (ab24525) (Abcam, UK)) overnight at 4°C. After 3 washes in PBS, the sections were incubated with the appropriate secondary antibody (goat anti-mouse IgG Alexa Fluor 594 or goat anti-chicken IgY Alexa Fluor 488 (Thermo Fisher Scientific) for 1 h at room temperature. The sections were then washed a further 3 times in PBS and mounted using VECTASHIELD Antifade Mounting Medium with 4, 6-diamidino-2-phenylindole (DAPI) (Vector Laboratories, UK). Microscopy was performed with a Zeiss Axio Observer Inverted Widefield Microscope (Zeiss, USA). Dr. Joanne Tonkin (NHLI, ICL, UK) performed histological tissue sectioning and staining.

For staining ARVM were incubated in PBS for 10 min at room temperature followed by a 5 min incubation in ice-cold MeOH. Blocking solution of 10% fetal calf serum in PBS was used for 30 min at room temperature. Cells were incubated overnight with the primary antibody (monoclonal anti-α-actinin (sarcomeric) mouse IgG1 isotype (A7811)) at 4°C. After 3 washes in PBS, cells were incubated with the secondary antibody (goat anti-mouse IgG Alexa Fluor 488 (Thermo Fisher Scientific)) for 1 h at room temperature. The cells were then washed a further 3 times in PBS and mounted using VECTASHIELD Antifade Mounting Medium. Microscopy was performed with a Zeiss LSM 780 inverted confocal microscope (Zeiss).

2.8 RNA extraction

LV tissue was rapidly dissected, snap-frozen in liquid nitrogen and stored at -80°C until processing. Frozen LV tissue from the *in vivo* model was homogenized in Tri Reagent

(Thermo Fisher Scientific) using sterile 5 mm stainless steel beads and a TissueLyser LT (Qiagen, Germany) at 0.2 Hz for 1 min. Cultured cardiomyocytes were lysed in 1 mL Tri Reagent per well. 0.2 mL of chloroform was added to the lysate and shaken by hand for 15 seconds, then centrifuged for 20 min at 12,000 rpm at 4°C. RNA extraction was carried out on the top aqueous layer with RNeasy Mini kit (Qiagen) according to manufacturer's instructions. The concentration of RNA was estimated with a NanoDrop 2000 (Thermo Fisher Scientific). RNA was stored at -80°C until further processing.

2.9 Quantitative real-time polymerase chain reaction

cDNA was synthesised from the extracted RNA with High Capacity cDNA Reverse Transcription Kit (Thermo Fisher Scientific) according to manufacturer's instructions. qPCR was performed using TaqMan Gene Expression Master Mix with TaqMan Gene Expression Assay probes on a 7900HT Fast Real-Time PCR System (Thermo Fisher Scientific). TaqMan Gene Expression Assay probes (Thermo Fisher Scientific) used were: *Hsp90ab1* (Rn01511686_g1), *Atp5a1* (Rn01527025_m1), *Cycs* (Rn00820639_g1), *Ndufs7* (Rn01452715_m1), *Cybb* (Rn00576710_m1), *Sdhb* (Rn01515728_m1), *Cyc1* (Rn00470541_g1), *Acadm* (Rn00566390_m1), *Xdh* (Rn00567654_m1), *Hmox1* (Rn00561387_m1), *Postn* (Rn01494627_m1), *Cst3* (Rn01415507_g1), *Il1b* (Rn00580432_m1), *Tgfb2* (Rn00676060_m1), *Nlrp3* (Rn04244620_m1), *Ccl2* (Rn00580555_m1), *Il18* (Rn01422083_m1), *Bcl2a1* (Rn00591516_m1), *Bnip3* (Rn00821446_g1), *Ppargc1a* (Rn00580241_m1), *Nppa* (Rn00664637_g1), *Nppb* (Rn00580641_m1), *Myh6* (Rn00691721_g1), *Myh7* (Rn01488777_g1), *Atp2a2* (Rn00568762_m1), *Abcb8* (Rn01442319_m1). Cycle thresholds obtained were normalised to

Hsp90ab1 and expressed using the standard ΔΔCt method expressed as fold change relative to control. Results were analysed with RQ Manager 1.2.1 (Thermo Fisher Scientific).

2.10 RNA-sequencing

2.10.1 Library preparation and sequencing

RNA from the *in vivo* model was treated with TURBO deoxyribonuclease (DNase) (Thermo Fisher Scientific) to remove genomic DNA as per manufacturer's instructions. RNA integrity was determined using the BioAnalyzer RNA 6000 Pico Kit (Agilent Technologies). All samples had a RNA integrity number higher than 8. 500 ng RNA per sample was used to prepare cDNA libraries using the TruSeq Stranded Total RNA Kit with Ribo-Zero (Illumina, USA) according to manufacturer's instructions. Concentration and quantity of the cDNA libraries were checked with the Agilent BioAnalyser High Sensitivity DNA assay (Agilent Technologies). Sequencing was performed by the Genomics facility of the MRC Clinical Sciences Centre (ICL, UK) using Illumina HiSeq 2500 sequencer with 100-bp paired end reads.

2.10.2 Bioinformatics analysis

The Cufflinks suite (Trapnell et al., 2012; Trapnell et al., 2010) was used to analyse gene expression. The quality of raw fastq files was checked using fastqc. Poor quality bases were trimmed with fastx_trimmer (fastx-toolkit v0.0.13). TopHat (v 2.1.0) mapped the reads against rn6 reference genome, Cufflinks (v 2.2.1) assembled the transcripts then Cuffcompare (v 2.2.1) merged the assembled transcripts from all samples into a transcriptome assembly.

For unbiased analysis of the gene expressions, weighted gene co-expression network analysis (WGCNA) was carried out on log transformed ($log_2(x+1)$) fragments per kilobase of transcript per million mapped reads (FPKM) values obtained from Cufflinks (Langfelder and Horvath, 2008). The highest expressing transcript was used for each gene with more than one transcript. Low expressing genes with total FPKM less than 10 were filtered out to reduce noise.

Cuffdiff (v 2.2.1) was used to compare the expression levels of transcripts to identify differentially expressed genes. Genes with increased (log_2 fold change > 1, false discovery rate (FDR) < 0.05) and decreased (log_2 fold change < 1, FDR < 0.05) transcript levels were put through the database for annotation, visualisation and integrated discovery (DAVID) (Huang da et al., 2009) for functional annotation clustering analysis. Ingenuity pathway analysis software (IPA; v 27216297, Qiagen) was used for pathway analysis with an FDR cut-off of 0.05. IPA was used as part of the computing resources of the UK MEDical BIOinformatics partnership which is supported by the MRC (grant no. MR/L01632X/1). Library preparation and bioinformatic analysis was done in collaboration with Cheuk Ting Angela Yiu (Department of Surgery and Cancer, ICL, UK) as part of her Master's project in the Lyon lab.

2.11 Estimation of mtDNA copy number

The mitochondrial to nuclear DNA ratio was used as an estimation of mtDNA copy number (Rooney et al., 2015). DNA was extracted from LV tissue using the DNeasy Blood & Tissue Kit (Qiagen) according to manufacturer's protocol. qPCR was performed for *Mt-co1* (Rn03296721_s1), *Mt-co3* (Rn03296820_s1), *Mt-nd3* (Rn03296825_s1) and *Hsp90ab1* (Rn01511686_g1). The mitochondrial DNA content relative to nuclear DNA for each sample was calculated as $2x2^{\Delta CT}$, where ΔCT = (nuclear DNA CT – mitochondrial DNA CT).

2.12 Statistical analysis

Statistical analysis was performed using GraphPad Prism 5.0 software (GraphPad Software, USA). Normality distribution was tested with the D'Agostino-Pearson omnibus test. When comparing two groups Mann-Whitney *U* test was used for non-parametric datasets. When comparing more than two groups Kruskal-Wallis test followed by Dunn's multiple comparisons test was used for non-parametric datasets. Two-way repeated measures ANOVA followed by Bonferroni's multiple comparisons test was used to compare time-course data. Pearson product moment-correlation and Spearman rank-order correlation were used to assess correlation for parametric and non-parametric datasets, respectively. The number of animals used (biological replicate) is indicated by "n". Statistical testing is indicated on diagrams between tested groups and asterisks are used to denote the *p*-value obtained from statistical testing in the conventional manner, * = $p < 0.05$, ** = $p < 0.01$ and *** = $p < 0.001$. A *p*-value of < 0.05 was considered statistically significant. Where the abbreviation "ns" (not significant) is stated statistical tests produced *p* values greater than or equal to 0.05. Data is presented as mean with error bars that represent the standard error of the mean (SEM).

Chapter 3

A chronic rat model of DOX-induced cardiomyopathy

Chapter 3 A chronic rat model of DOX-induced cardiomyopathy

3.1 Introduction

Clinically relevant animal models are necessary to mimic and study the pathophysiological processes involved in DOX-induced cardiomyopathy. Of the chronic animal models described as exhibiting DOX-induced cardiotoxicity the rabbit was initially most widely used possibly due to the reproducibility of incidence (Mettler et al., 1977). However, it was found that rats develop cardiotoxicity at lower cumulative doses compared to rabbits and are a more cost effective animal model (Bachmann et al., 1975; Jaenke, 1974; Mettler et al., 1977; Young et al., 1975). Mettler *et al*. found 1 to 2 mg/kg/week DOX administered intravenously for 10 to 14 weeks produced reproducible cardiotoxicity phenotype in male Fischer rats, determined using histopathological evaluation (Mettler et al., 1977). Schwarz *et al*. used a chronic rat model of DOX-induced cardiotoxicity to assess cardiac dysfunction with echocardiographic assessment performed at baseline and following chronic DOX treatment (Schwarz et al., 1998). A dose of 2.5 mg/kg DOX was administered to female SD rats intravenously once a week for 10 weeks resulting in a reproducible decline in cardiac function (Schwarz et al., 1998). During a pilot study in male Hannover Wistar rats Cove-Smith *et al*. found that 2.5 mg/kg/week DOX administered intravenously had to be dose-reduced to 1.75 mg/kg/week during week 4 due to intolerance and the majority of these animals were terminated for welfare reasons between weeks 5 and 8 (Cove-Smith et al., 2014). A difference in severity between these two studies at the same dose may be due to the use of female rats by Schwarz *et al*. as oestrogen is known to have protective effects on the cardiovascular system (Mendelsohn and Karas, 1999) and sex differences have been found in a rat model of DOX-induced cardiotoxicity (Moulin et al., 2015). A dose of 1.25 mg/kg DOX (equivalent to approximately 50 mg/m^2 in humans) administered once a week for 8 weeks followed by a

further 4 week off-dosing period was generally well tolerated and resulted in a progressive decline in functional indices assessed by cardiac magnetic resonance imaging (Cove-Smith et al., 2014). The DOX dosing regimen used by Cove-Smith *et al*. resulted in a chronic progressive cardiomyopathy, consistent with clinical presentation (Cove-Smith et al., 2014; Jensen et al., 2002; Lipshultz et al., 2005; Swain et al., 2003). Although DOX can cause acute cardiac dysfunction (Bristow et al., 1978; Dazzi et al., 2001; Hayek et al., 2005; Rudzinski et al., 2007) it is the progressive dose-dependent decline in cardiac function that limits the clinical success of drug therapy. In this study, a rat model of DOX-induced cardiotoxicity using the same dosing regimen as Cove-Smith *et al*. was established to characterise the phenotype and processes involved in DOX-induced myocardial dysfunction *in vivo*.

Present rodent models of DOX-induced cardiotoxicity have inconsistencies with the clinical presentation of the disease. Rat models of DOX-induced cardiotoxicity show a progressive decline in LVEF and fractional shortening during DOX administration which is more consistent with clinical sub-acute toxicity rather than chronic late-onset cardiotoxicity (Cardinale et al., 2015; Cove-Smith et al., 2014; Migrino et al., 2008). In a prospective study involving a large, unselected population treated with anthracyclines (mean cumulative dose: 252 ± 86 mg/m^2; range 30-900) cardiac monitoring (every 3 months) of LVEF by standard echocardiography during the first 12 months after the completion of chemotherapy allowed early detection of almost all cases (98%) of cardiotoxicity; suggesting that sub-acute cardiotoxicity may be more commonly diagnosed with close cardiac monitoring (Cardinale et al., 2015). Differences in cardiac dysfunction presentation with DOX administration between rodents and humans may be due to the dose used, the level of cardiac monitoring and/or differences between the two species such as a difference in mass-specific metabolic rate or cardiac function reserve (Demetrius, 2005). If may be that if rats received a much lower dose of DOX over a longer

time course they would also develop LV dysfunction at a later time point. The typical life span for a SD rat is 2.5-3.5 years. Rats could be administered a low dose of DOX once a month for a year with cardiac function assessed before, during and following treatment. Practically this would mean a much longer experimental protocol. Another reason why rodents show a decline in cardiac function during DOX administration may be due to a difference in mass-specific metabolic rate between the two species. Rodents have a much higher mass-specific metabolic rate than humans and a faster rate of free-radical leak which accelerates senescence (Demetrius, 2005; Furness and Speakman, 2008). A higher mass-specific metabolic rate and a faster rate of free-radical leak may mean that rodents are more susceptible to a faster rate of deterioration in myocardial function in response to DOX treatment than humans. The cardiac response of small rodents and humans to exercise is also very different (Milani-Nejad and Janssen, 2014). The average human heart rate can increase from approximately 65-79 BPM during rest to 173-188 BPM during exercise an increase of approximately 140-170% (Flamm et al., 1990; Stratton et al., 1994). Rats can increase their heart rates from approximately 350-370 BPM to 500-550 BPM, a 40-50% increase (Bolter and Atkinson, 1988; Lujan et al., 2012). Contractile force (assessed *ex vivo* by isometric contraction of cardiac trabeculae) of human myocardium increases 81-168% from 0.5 Hz to 2.5 Hz (Chaudhary et al., 2004; Pieske et al., 1996; Rossman et al., 2004). There is an increase of approximately 30-40% from 4 Hz to 8 Hz in rat myocardium (Monasky et al., 2008). Cardiac output is the product of HR and stroke volume, therefore, humans have a much greater ability than rodents to increase their cardiac output during exercise by both heart rate and stroke volume mediated mechanisms (Milani-Nejad and Janssen, 2014). Therefore, the cardiac reserve of humans is much greater than rodents and rodents exposed to chronic myocardial damage may be more susceptible to a faster decline in LV function.

3.2 Hypothesis and aims

I hypothesis that weekly IV administration of DOX to male SD rats followed by an off-dosing period will result in a progressive decline in cardiac function that is associated with DOX-induced cardiomyopathy with subcellular changes, tissue remodelling and an inflammatory response.

The aims of this chapter are as follows:

1. Establish a clinically relevant rat model of chronic DOX-induced cardiomyopathy
2. Examine the subcellular changes in response to chronic DOX treatment
3. Assess the tissue remodelling and inflammatory responses to chronic DOX treatment

3.3 Results

3.3.1 Establishing a chronic rat model of DOX-induced cardiomyopathy

Experimental protocol

In order to investigate the chronic effect of DOX treatment on myocardial function adult male SD rats were administered 1.25 mg/kg DOX once a week for 8 weeks via IV tail vein injection followed by an off-dosing period (Cove-Smith et al., 2014). This dosing regimen mimics patient dosing and permits tracking of progressive cardiac decline (Cove-Smith et al., 2014; Mettler et al., 1977). Cardiac function was assessed at baseline and during protocol week 4, 6, 8 and 11 (Fig. 3.1A). DOX-treated rats showed a significant reduction in body weight gain from protocol week 3 compared to control (Fig. 3.1B) and reduced food consumption, consistent with loss of appetite with chronic DOX treatment in rats (Mettler et al., 1977). There were two unexpected deaths in the treatment group, during protocol week 6 and 10, respectively. The death during protocol week 6 occurred during the DOX administration protocol. During week 10 a rat was found dead in its cage having shown no signs of adverse symptoms the day before. Determination of cause of death by post-mortem examination was inconclusive. Death was most likely due to sudden cardiac death from ventricular arrhythmia, as it is known that DOX treatment pre-disposes the heart to ventricular arrhythmia (Rudzinski et al., 2007). Consequently animals were closely monitored, twice daily, and in protocol week 11, following eight doses of DOX and three weeks of off-dosing, one rat in the treatment group showed signs of adverse effects including piloerection, diarrhoea and porphyrin staining and severe cardiac decompensation with a dilated left ventricle during echocardiographic assessment (Fig. 3.2B & D). The study was then terminated to ensure that data could be collected and that severity limits were not exceeded.

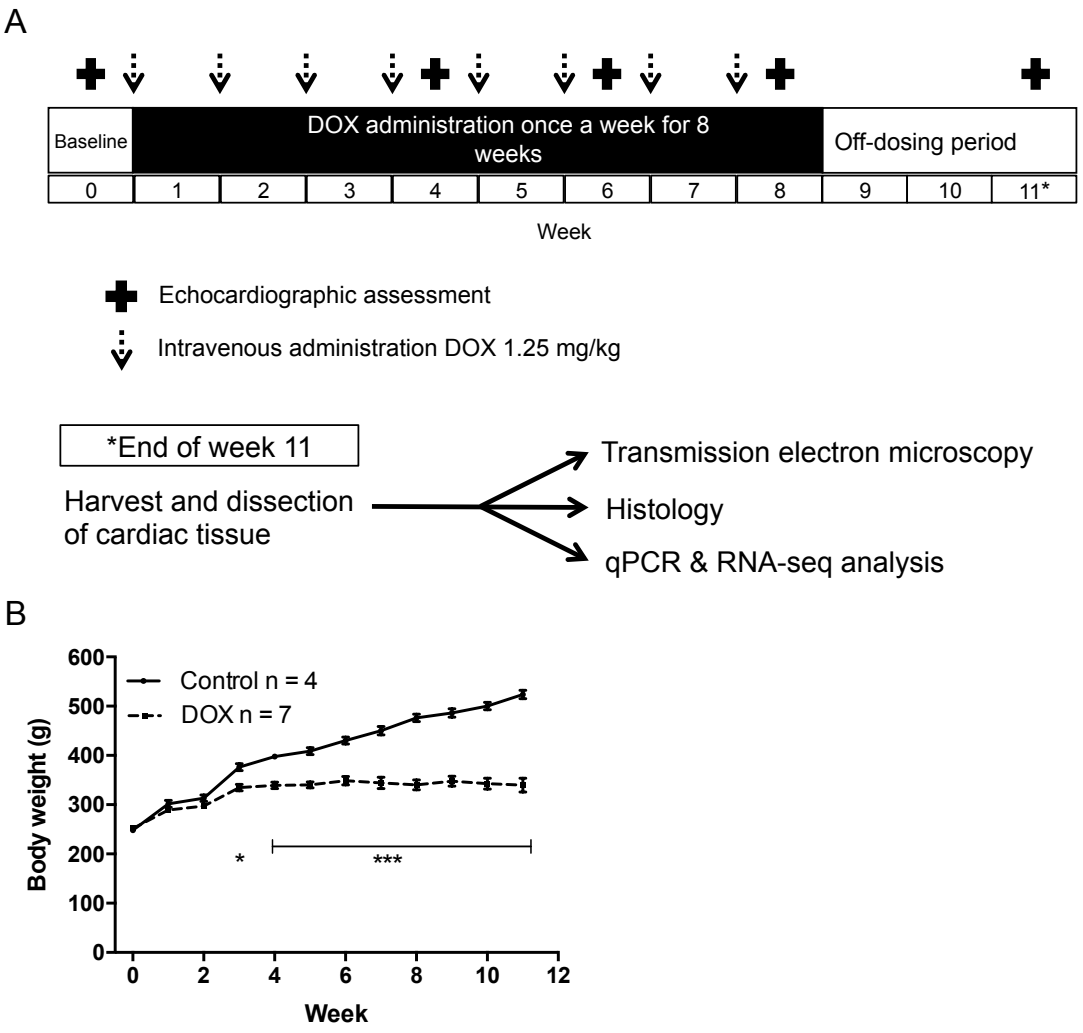


Fig. 3.1 Overview of chronic rat model of chemotherapy cardiomyopathy.
(A) Schematic representation of 11-week experimental protocol. Following an acclimatisation period male SD rats were administered 1.25 mg/kg DOX (dashed arrow) once a week for 8 weeks followed by an off-dosing period. Echocardiographic assessment was made at baseline and during protocol week 4, 6, 8 and 11 (addition symbol). At sacrifice cardiac tissue was dissected and stored for transmission electron microscopy, histology, qPCR and RNA-seq analysis (B) Body weight (g) of DOX-treated rats (dashed line n = 7) versus control (n = 4). Data is represented as mean ± *SEM.* Two-way repeated measures ANOVA with Bonferroni's multiple comparisons test *$p < 0.05$ ***$p < 0.001$ compared to control.

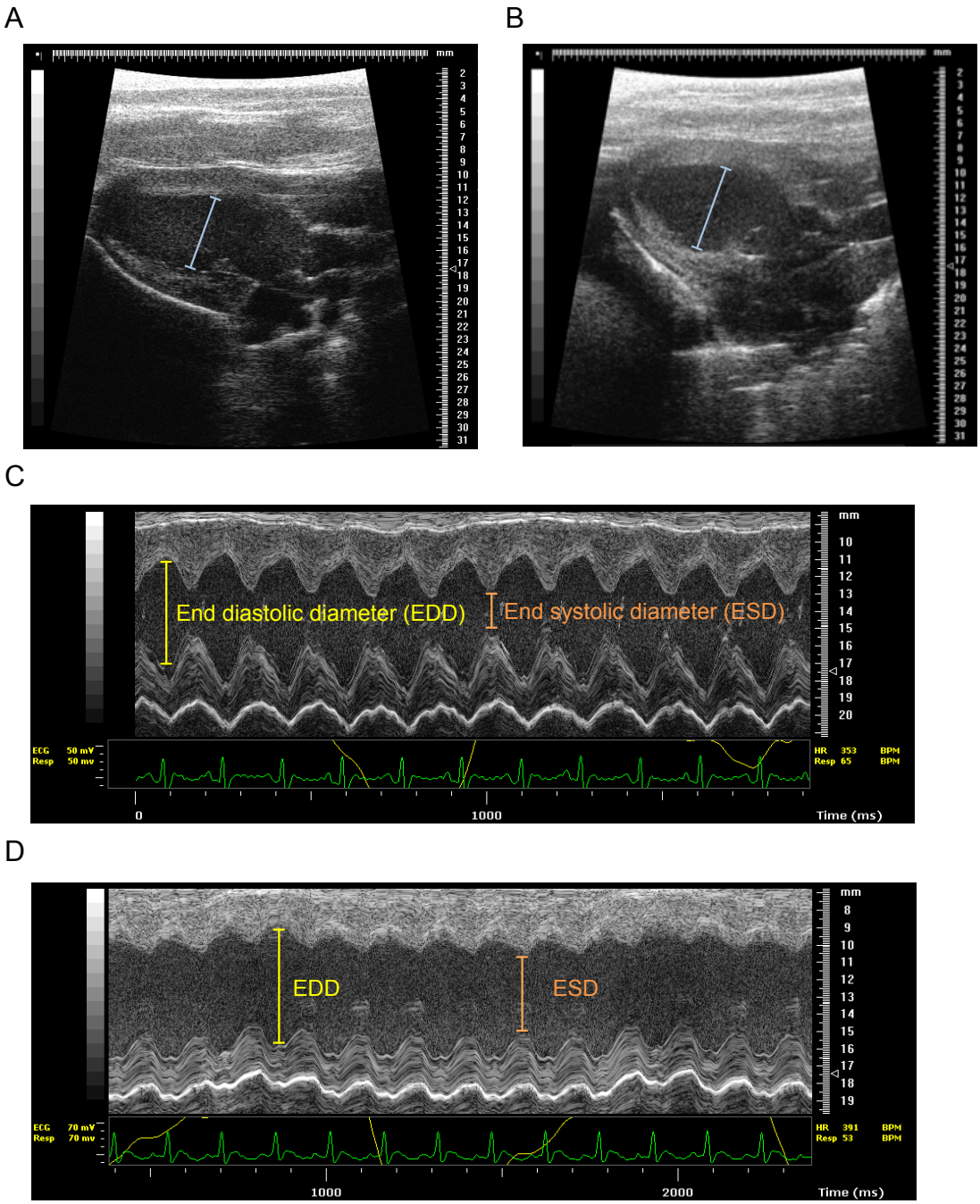


Fig. 3.2 Contractile dysfunction in DOX-treated versus control rat heart following 8 weeks of DOX dosing and 3 weeks of off-dosing.
(A) B-mode parasternal long axis image of control rat heart (B) B-mode parasternal long axis image of DOX-treated rat heart. Line indicates that the ventricle is dilated compared to control (C) M-mode image of control rat heart (D) M-mode image of DOX-treated rat heart showing contractile dysfunction and cardiac decompensation. The end systolic diameter is wider in DOX-treated compared to control.

The chronic effect of DOX on cardiac function

DOX treatment at 1.25 mg/kg over 8 weeks produced a reproducible and profound cardiotoxicity. Echocardiographic assessment showed a progressive decline in parameters of LV contractile function (Fig. 3.3). DOX-treated rats showed a significant reduction in LVEF and FS compared to control during protocol week 4 (Fig. 3.3A & B). Cardiac function decreased incrementally over time with DOX treatment and continued to decline during the off-dosing period to a mean LVEF of 50% by protocol week 11. The LV end systolic diameter (ESD) increased in DOX-treated rats, whereas the LV end diastolic diameter (EDD) remained unchanged (Fig. 3.3C & D) indicating systolic dysfunction. There were no significant changes in HR for DOX-treated rats compared to control (Fig. 3.3E). Table 1 shows animal data such as body weight, heart weight, heart weight/body weight, tibia length and heart weight/tibia length for DOX treated and control following 8 weeks of DOX treatment and 3 weeks off-dosing.

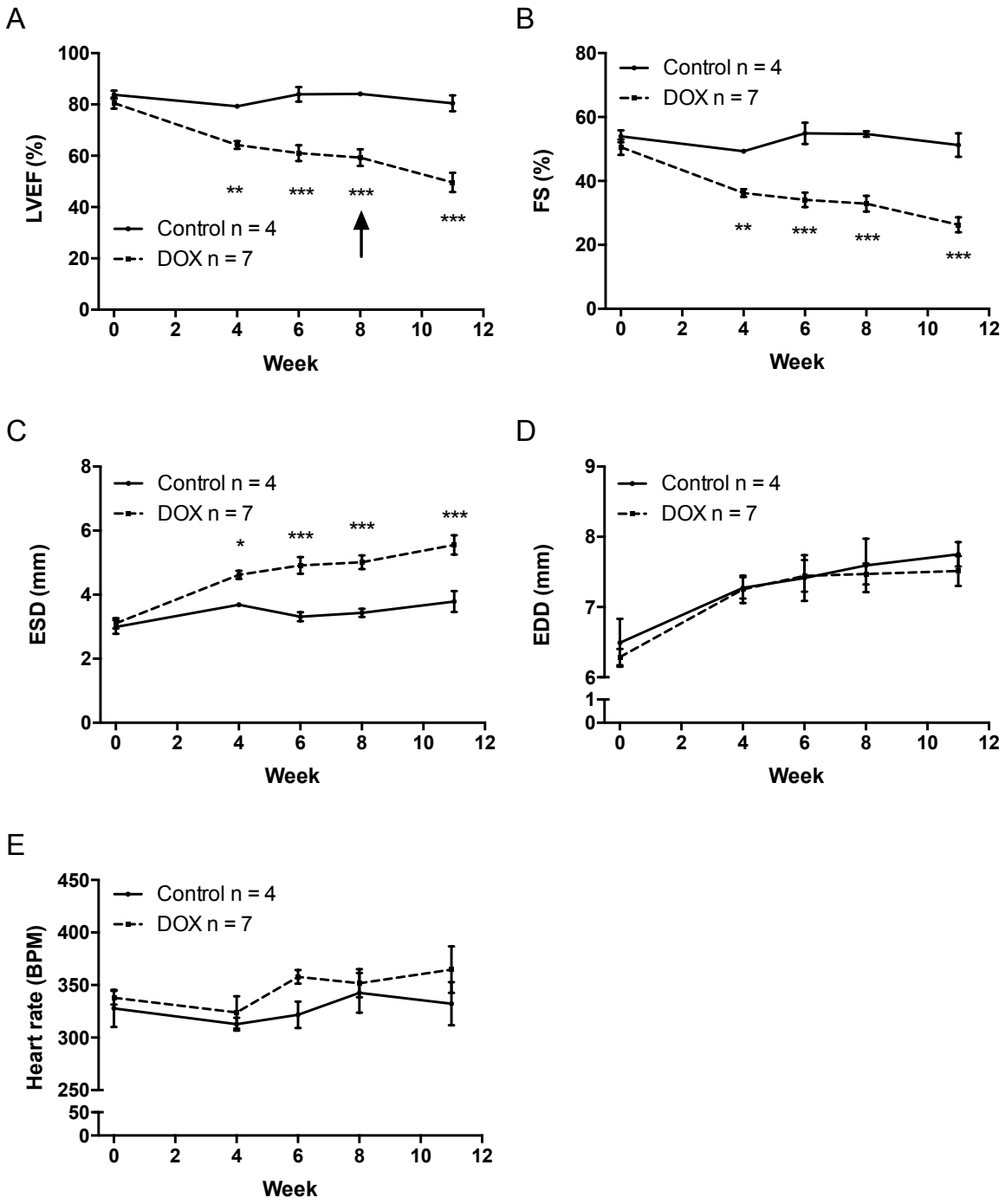


Fig. 3.3 Progressive DOX-induced contractile dysfunction assessed by echocardiography.
(A) LVEF (%), arrow shows last DOX administration, (B) FS (%) (C) ESD (mm) (D) EDD (mm) (E) heart rate (BPM) of DOX-treated SD rats n = 7 (dashed line) versus saline-treated control n = 4 as determined by echocardiography at baseline (not significant) and protocol weeks 4, 6, 8 and 11. Data is represented as mean ± *SEM.* Two-way repeated measures ANOVA with Bonferroni's multiple comparisons test *$p < 0.05$ **$p < 0.01$ ***$p < 0.001$ compared to control.

Parameters	**Control (n = 4)**	**DOX (n = 7)**	***P* value**
Body wt (g)	527 ± 9	341 ± 14	**0.006**
Heart wt (g)	1.44 ± 0.02	1.31 ± 0.07	0.155
Heart/body wt (mg/g)	2.73 ± 0.01	3.88 ± 0.23	**0.006**
Tibia length (cm)	4.85 ± 0.06	4.77 ± 0.13	0.164
Heart/tibia (mg/cm)	296 ± 3.12	276 ± 14.4	0.927

Mean ± SEM is presented. Mann-Whitney *U* test. n = total number of animals per group.

Table 1 Anatomical characteristics of rats following 8 weeks of DOX treatment and 3 weeks of off-dosing

Transcriptome analysis using qPCR on LV tissue, taken at sacrifice, showed significant changes in transcript levels of markers of myocardial dysfunction and ventricular remodelling in DOX-treated rats compared to control (Fig. 3.4). Relative transcript levels of *Nppa* and *Nppb*, encoding atrial natriuretic peptide (ANP) and BNP respectively, were significantly increased (33 and 2 fold, respectively) in DOX-treated rats compared to control (Fig. 3.4A & B). DOX-treated rats showed decreased transcript levels of *Myh6* (3 fold) and increased transcript levels of *Myh7* (2 fold) (Fig. 3.4C & D). Transcript levels of *Atp2a2*, which encode the SERCA2A, were significantly decreased (2 fold) (Fig. 3.4E) in DOX-treated rats relative to control. There was a significant negative correlation between LVEF and *Nppa*, *Nppb* and *Myh7* transcript levels (Fig. 3.5A, B & D). Additionally, there was a positive correlation between LVEF and *Myh6* and *Atp2a2* transcript levels (Fig. 3.5C & E). Together, these results confirm the establishment of a clinically relevant chronic rat model of DOX-induced cardiotoxicity.

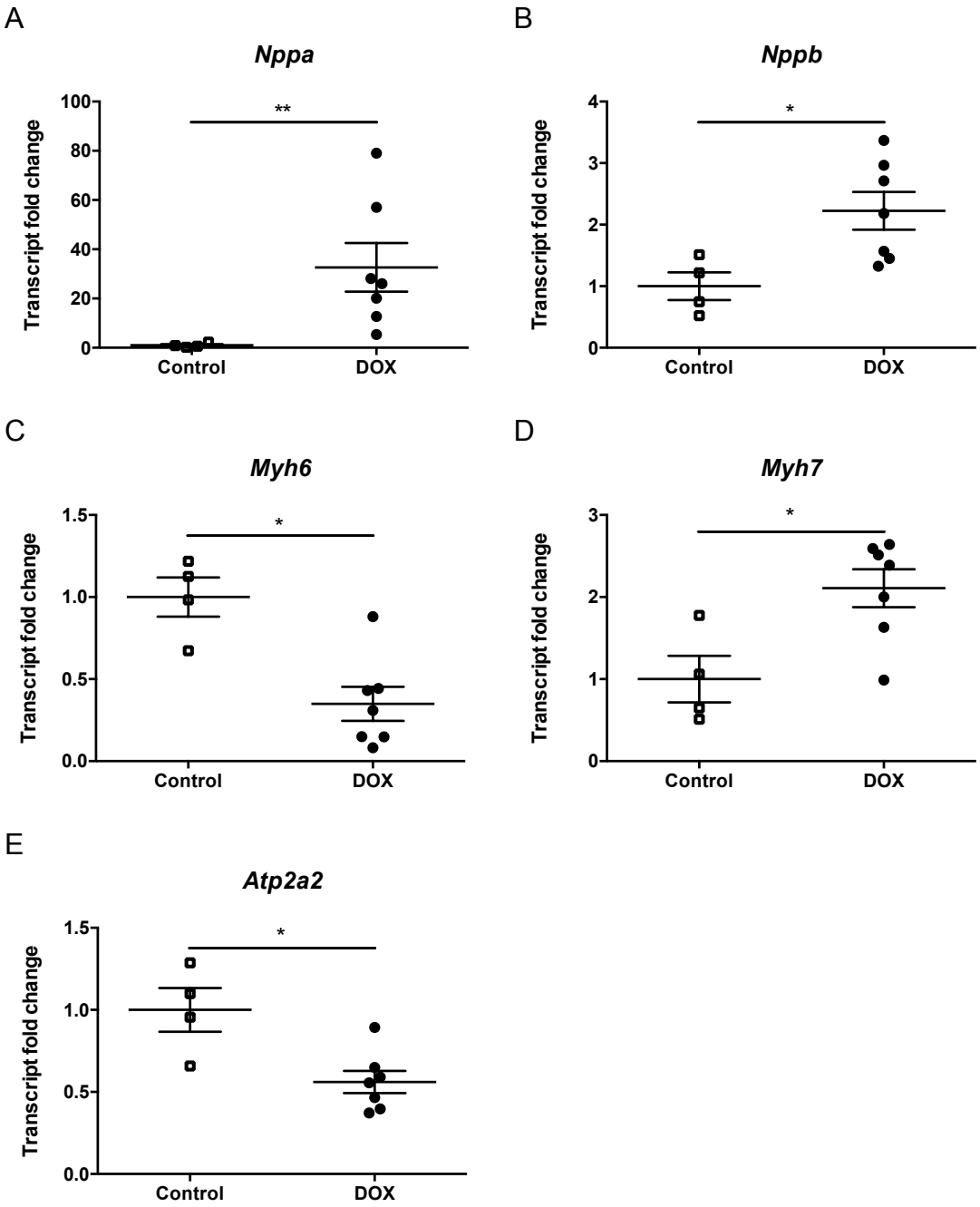


Fig. 3.4 Transcript levels of markers of myocardial dysfunction and ventricular remodelling in DOX-induced cardiomyopathy.
qPCR analysis of (A) *Nppa* (B) *Nppb* (C) *Myh6* (D) *Myh7* (E) *Atp2a2* transcript levels. Scatter plot shows transcript levels obtained for individual rats control n = 4 (clear square) DOX n = 7 (black circle), which were normalised to *Hsp90ab1* and expressed as fold change relative to average of control samples. Data is represented as mean ± *SEM*. Mann-Whitney *U* test **p* < 0.05 ***p* < 0.01 compared to control.

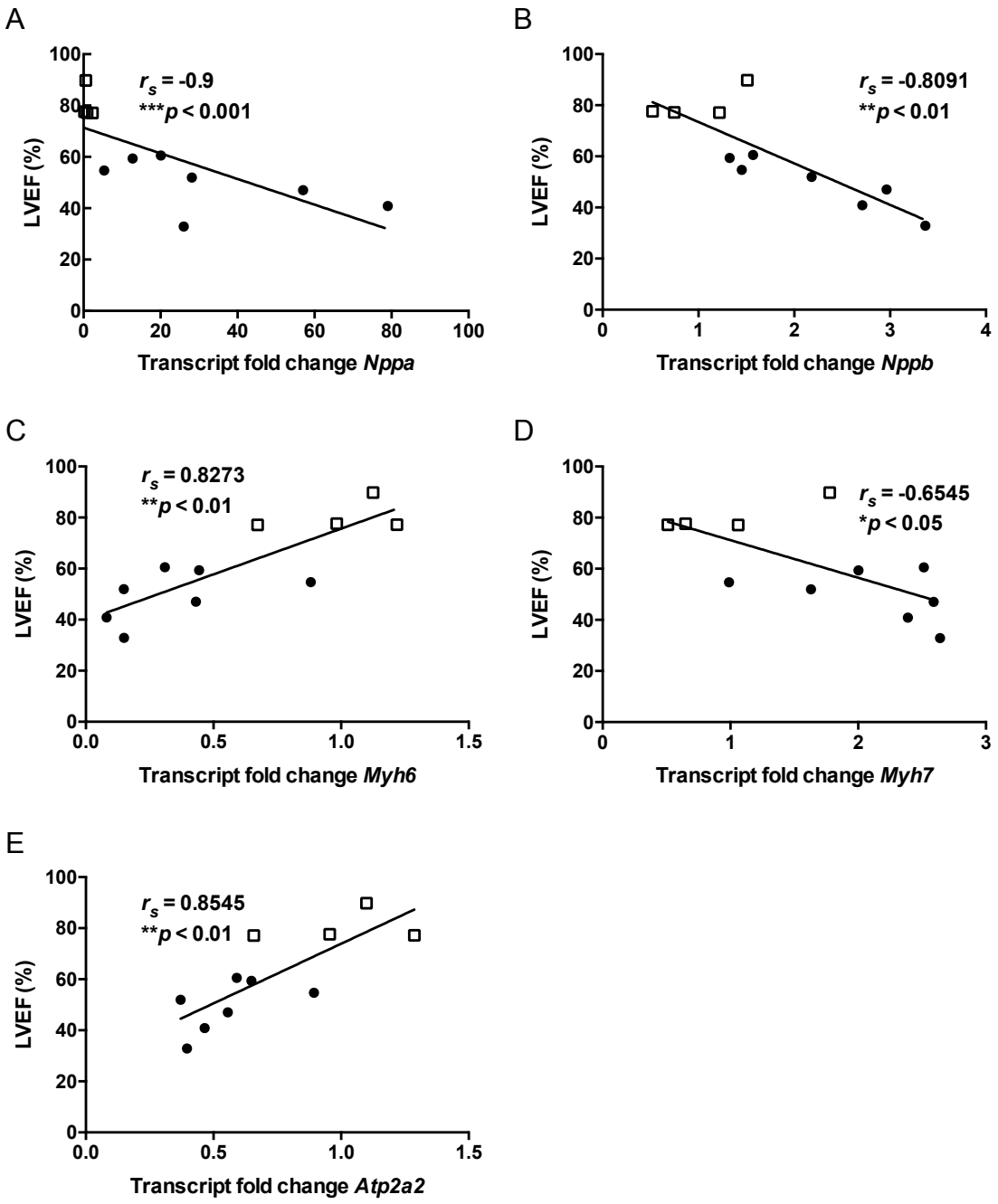


Fig. 3.5 Correlation analysis between LVEF and transcript levels of markers of myocardial dysfunction and ventricular remodelling in DOX-induced cardiomyopathy.
Correlation analysis between LVEF (%) and (A) *Nppa* (B) *Nppb* (C) *Myh6* (D) *Myh7* (E) *Atp2a2* transcript levels. Control n = 4 (clear square) DOX n = 7 (black circle). Transcript levels obtained for individual rats were normalised to *Hsp90ab1* and expressed as fold change relative to average of control samples. A significant negative correlation was present between LVEF and *Nppa, Nppb and Myh7*. Additionally, there was a significant positive correlation between LVEF and *Myh6* and *Atp2a2*. Spearman rank-order correlation coefficient r_s. Spearman rank-order correlation *p < 0.05 **p < 0.01 ***p < 0.001 compared to control.

3.3.2 The effect of chronic DOX treatment on subcellular morphology

Subcellular morphological changes induced by chronic DOX treatment were assessed by light microscopy and TEM performed on LV tissue for three control and three DOX-treated rats. Semi-thin (0.5 μm) epon-embedded toluidine blue stained sections were imaged using a light microscope. Ultra-thin (90 nm) sections were imaged using a transmission electron microscope.

Semi-thin sections from control rats showed uniform myofibrillar architecture (turquoise arrowheads) and mitochondrial distribution (green arrowheads) with clear intercalated discs (blue arrowheads) (Fig. 3.6A). Sections from DOX-treated rats showed vacuolated myocardial cells (yellow arrowheads) and diffuse degeneration of myofibrillar and mitochondrial structure and distribution (brown arrowheads) compared to control (Fig. 3.6B, D & E). These findings are consistent with previous reports in a chronic rat model of DOX-induced cardiotoxicity that used toluidine blue staining and showed the presence of extensive vacuoles within myocytes and severe myocyte degeneration (Zhou et al., 2001). To examine subcellular morphological changes in greater depth TEM was performed.

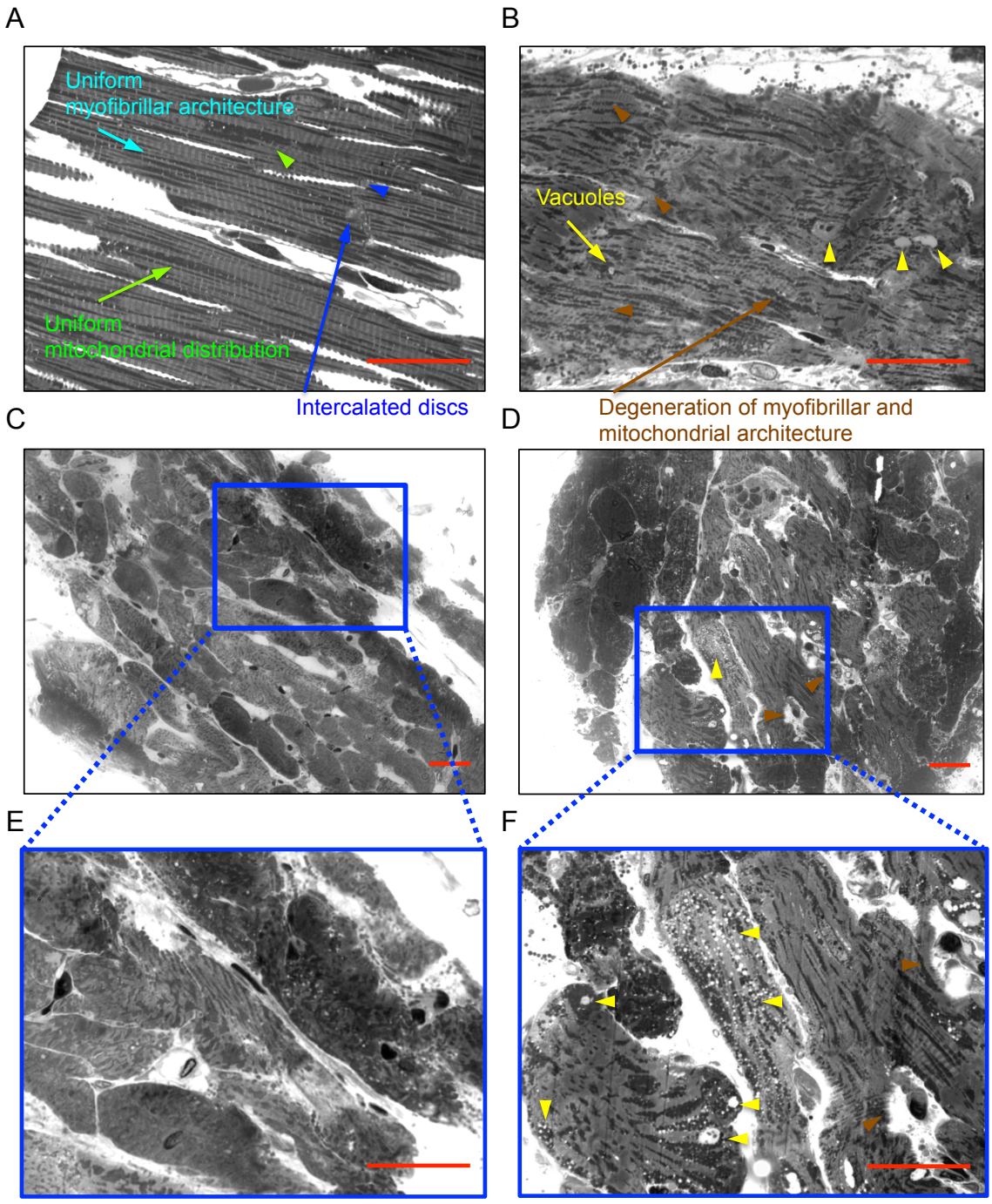


Fig. 3.6 Light microscopy micrographs of subcellular morphological changes induced by chronic DOX treatment.
Semi-thin (0.5 µm) toluidine blue stained sections were imaged using a light microscope. Micrographs were prepared of representative sections (A) Control longitudinal section (B) DOX longitudinal section (C) Control transverse section (D) DOX transverse section (E) Magnified area of control transverse section (F) Magnified area of DOX transverse section. Scale bar on each panel represents 20 µm. Control rat sections showed uniform myofibrillar architecture (turquoise arrowheads A) and mitochondrial distribution (green arrowheads A) with clear intercalated discs (blue arrowheads A). Sections from DOX-treated rats showed vacuolated myocardial cells (yellow arrowheads B, D and F) and diffuse degeneration of myofibrillar and mitochondrial structure and distribution compared to control (brown arrowheads B, D and F).

TEM micrographs of control rat tissue showed uniform myofibrillar architecture and Z-line orientation (turquoise arrowheads) and mitochondrial distribution and morphology (green arrowheads) (Fig. 3.7A & B). Dramatic changes in subcellular morphology were present in DOX-treated LV tissue including numerous diffuse vacuoles (Fig. 3.7C & D yellow arrowheads) characteristic of DOX-induced cardiotoxicity, Z-line distortion (Fig. 3.7E & F orange arrowheads) and altered mitochondrial structure (Fig. 3.8 pink arrowheads) and distribution (Fig. 3.9 pink arrowheads). Mitochondrial morphological changes were characterised by dense-body deposition within intact mitochondria, swelling and membrane distortion. In areas where mitochondria would typically be found vacuoles containing concentric sheets of inner membrane and/or granular deposits (red arrowheads) were present (Fig. 3.10 & Fig. 3.11). The position of vacuoles in relation to intact mitochondria and the concentric sheets of inner membrane and/or granular deposits present within vacuoles suggest that these structures may be mitochondria with drastically altered ultrastructure. Z-line distortion and the presence of swollen vacuoles resulted in diffuse myofibrillar disruption and loss (brown arrowheads) (Fig. 3.12). Overall, this data suggests that chronic DOX treatment results in subcellular myofibrillar and mitochondrial degeneration that most likely contributes to contractile dysfunction.

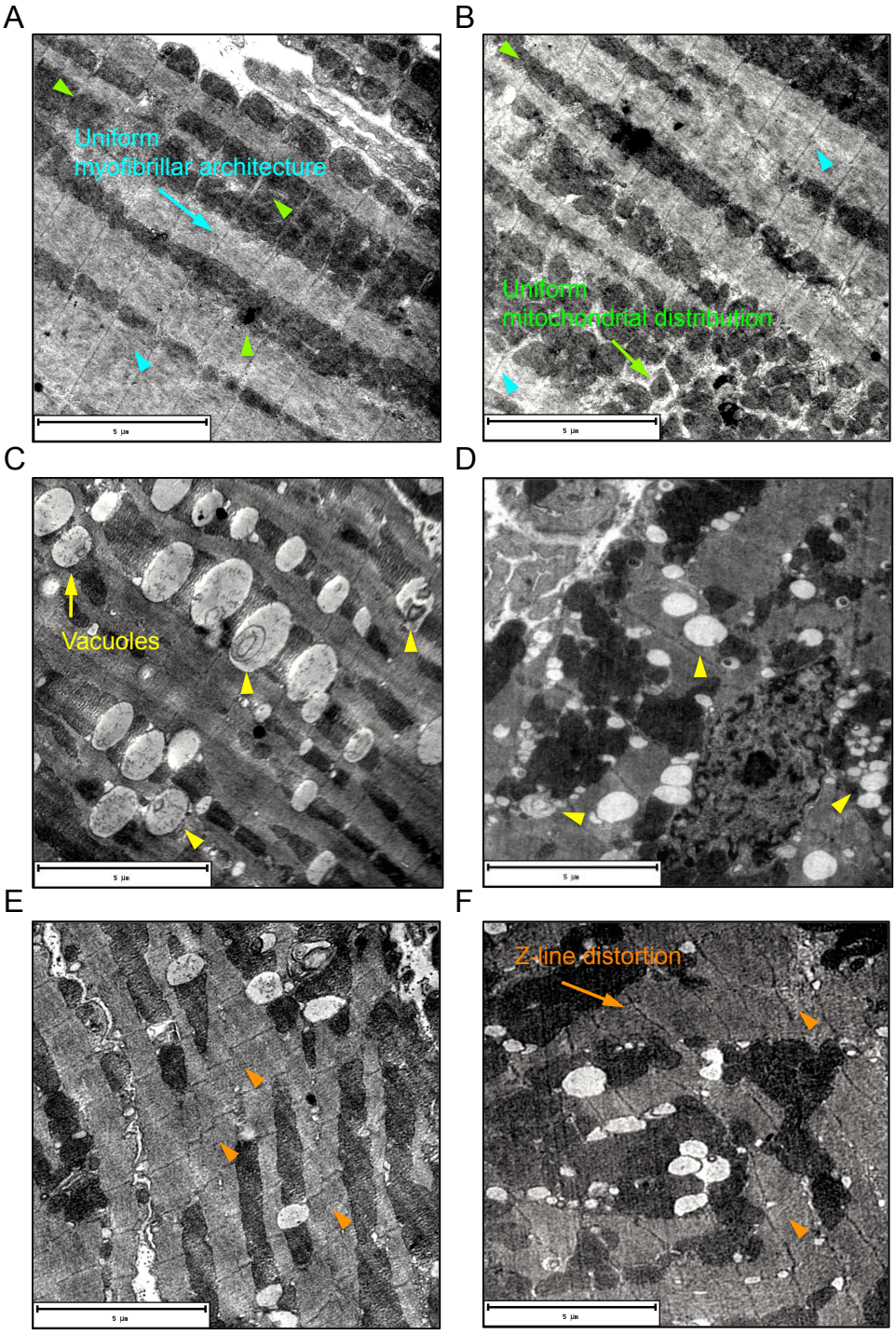


Fig. 3.7 TEM micrographs of subcellular morphological changes as a result of chronic DOX treatment characterised by diffuse vacuoles and Z-line distortion.
Ultra-thin (90 nm) sections were imaged using a transmission electron microscope. Micrographs are of representative sections. (A) Control section (B) Control section (C) DOX section (D) DOX section (E) DOX section (F) DOX section. Scale bar on each panel represents 5 µm. Micrographs of control showed uniform myofibrillar architecture and Z-line orientation (turquoise arrowheads A & B) and mitochondrial distribution and morphology (green arrowheads A & B). Dramatic changes in subcellular morphology were present in DOX sections including numerous diffuse vacuoles (yellow arrowheads C & D) and Z-line distortion (orange arrowheads E & F) compared to control.

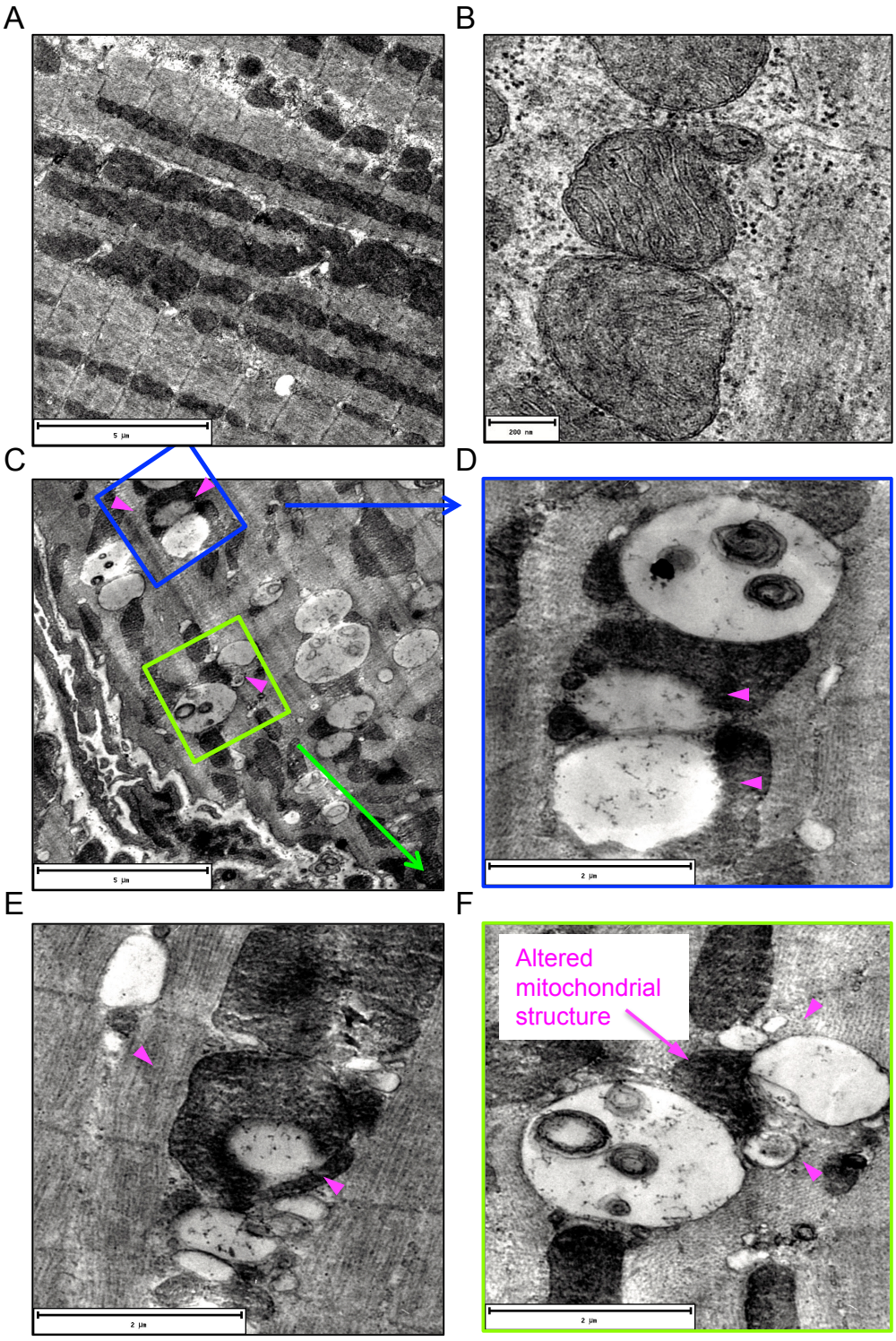


Fig. 3.8 TEM micrographs of subcellular morphological changes as a result of chronic DOX treatment characterised by altered mitochondrial structure and degeneration.
Ultra-thin (90 nm) sections were imaged using a transmission electron microscope. Micrographs are of representative sections. (A) Control section (B) Control section (C) DOX section (D) Magnified DOX section (E) DOX section (F) Magnified DOX section. Scale bar on each panel. Control sections show typical mitochondrial structure. DOX sections show altered mitochondrial structure and degeneration (pink arrowheads) compared to control.

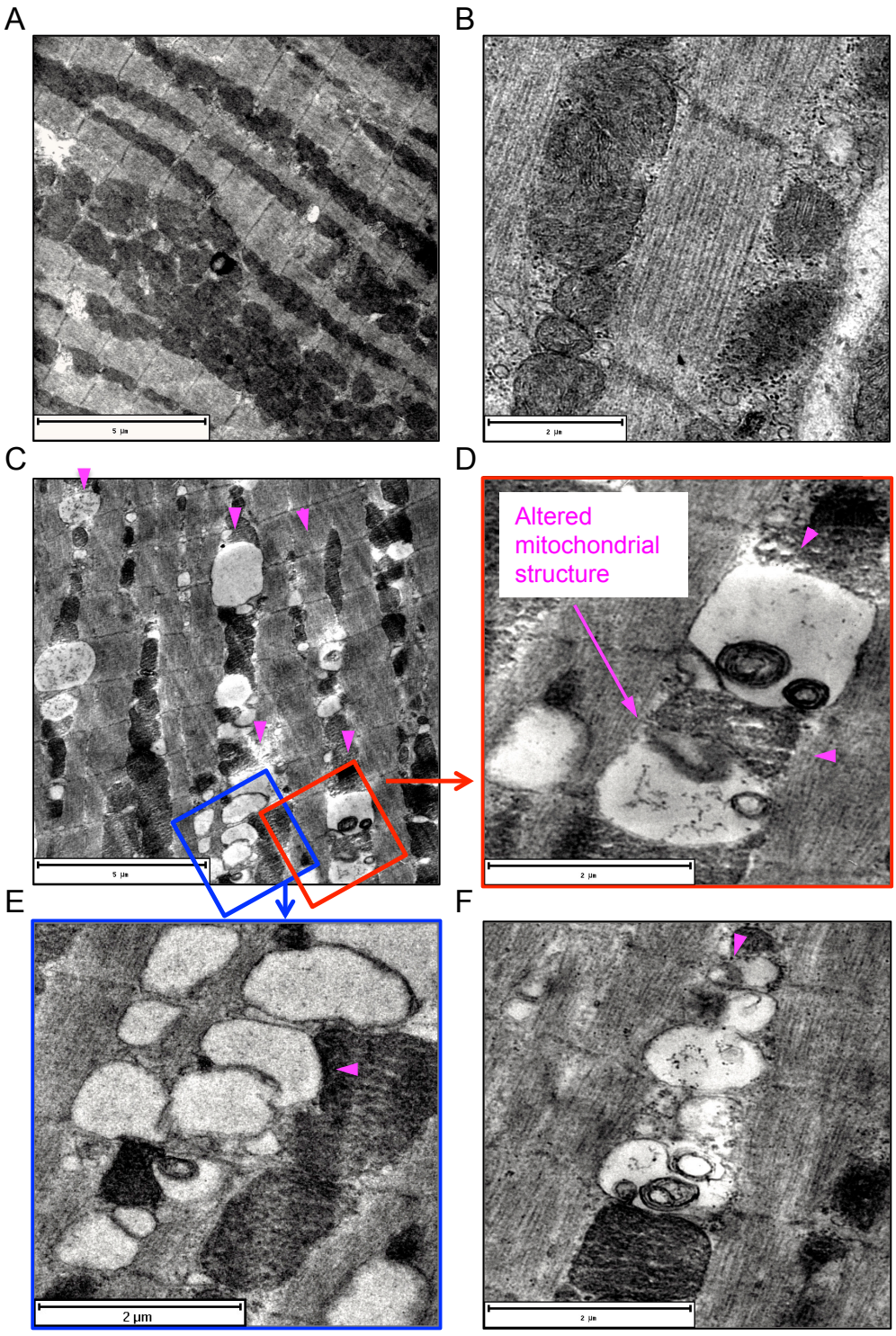


Fig. 3.9 TEM micrographs of subcellular morphological changes as a result of chronic DOX treatment characterised by altered mitochondrial distribution and structure.
Ultra-thin (90 nm) sections were imaged using a transmission electron microscope. Micrographs are of representative sections. Scale bar on each panel. (A) Control section (B) Control section (C) DOX section (D) Magnified DOX section (E) Magnified DOX section (F) DOX section. Control sections showed typical mitochondrial distribution and structure. DOX sections show altered mitochondrial distribution and structure (pink arrowheads) compared to control.

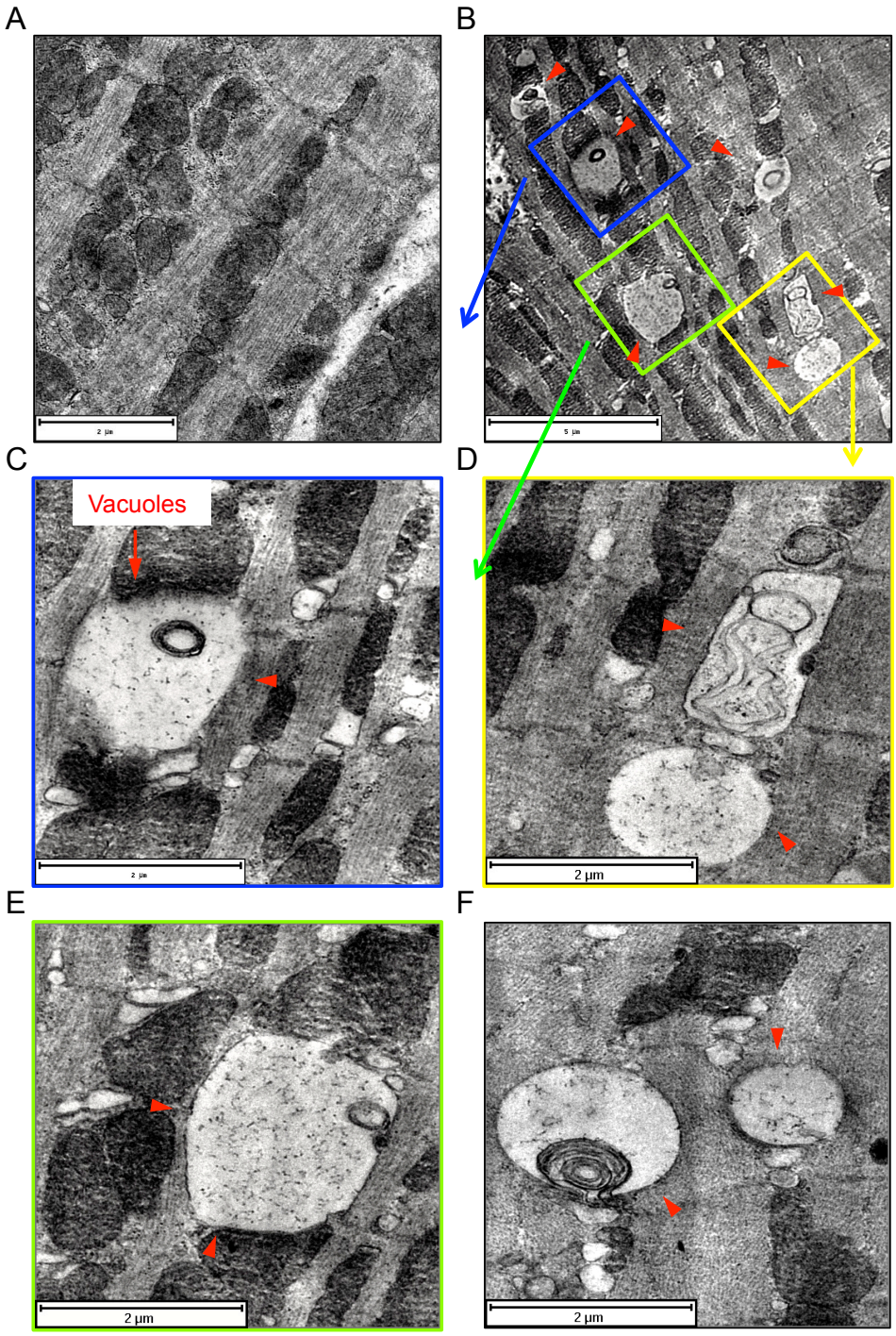


Fig. 3.10 TEM micrographs of subcellular morphological changes as a result of chronic DOX treatment characterised by vacuoles containing concentric sheets of inner membrane and/or granular deposits.
Ultra-thin (90 nm) sections were imaged using a transmission electron microscope. Micrographs are of representative sections. (A) Control section (B) DOX section (C) Magnified DOX section (D) Magnified DOX section (E) Magnified DOX section (F) DOX section. Scale bar on each panel. Control section showed uniform myofibrillar architecture and mitochondrial distribution and structure. In DOX sections in areas where mitochondria would usually be found vacuoles containing concentric sheets of inner membrane and/or granular deposits (red arrowheads) were present. The position of vacuoles in relation to intact mitochondria and the concentric sheets of inner membrane and/or granular deposits present within vacuoles suggest that these structures may be mitochondria with drastically altered ultrastructure.

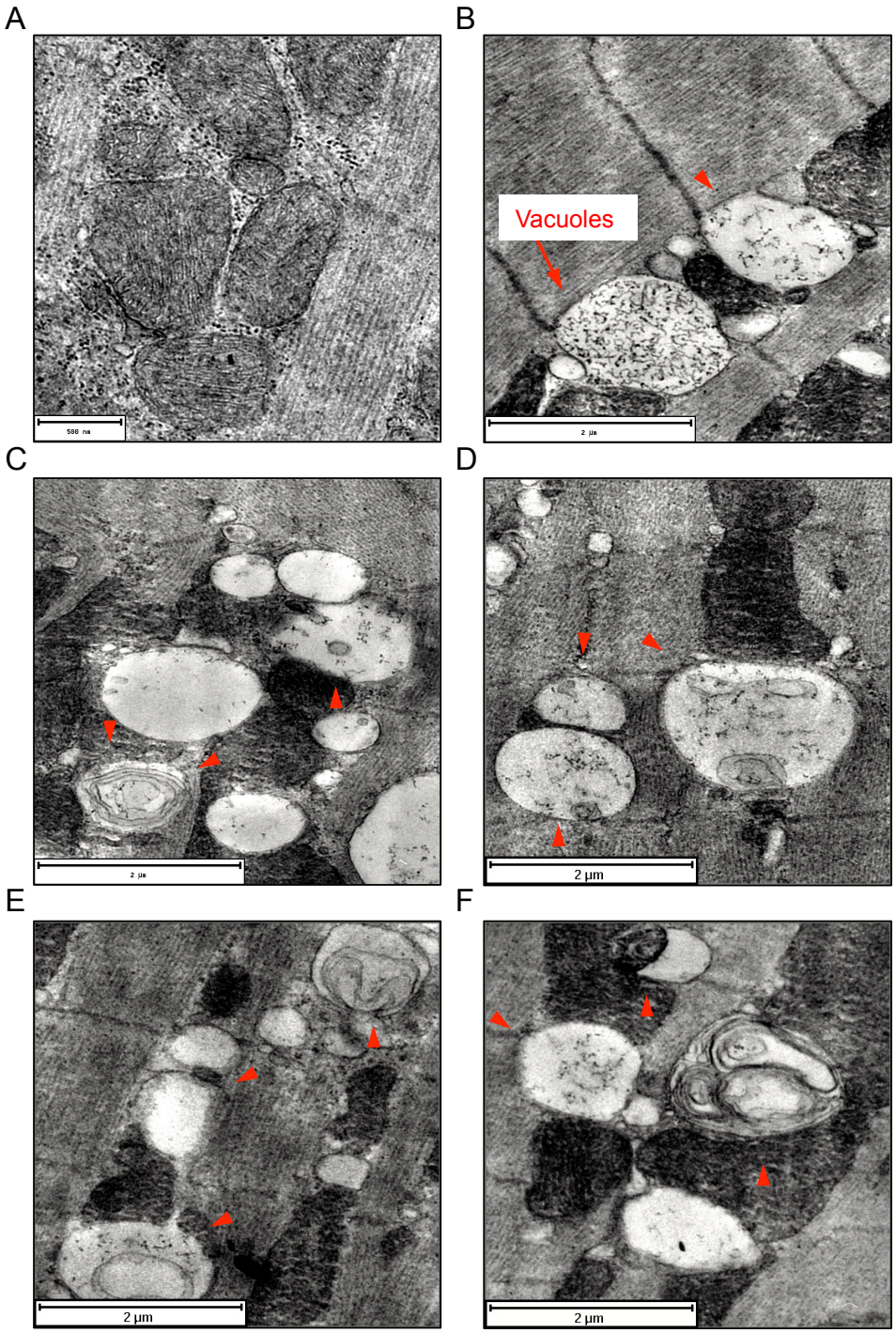


Fig. 3.11 TEM micrographs of subcellular morphological changes as a result of chronic DOX treatment characterised by vacuoles containing concentric sheets of inner membrane and/or granular deposits.
Ultra-thin (90 nm) sections were imaged using a transmission electron microscope. Micrographs are of representative sections. (A) Control section (B) DOX section (C) DOX section (D) DOX section (E) DOX section (F) DOX section. Scale bar on each panel. Control micrograph showed uniform myofibrillar architecture and mitochondrial distribution and structure. In DOX sections in areas where mitochondria would usually be found vacuoles containing concentric sheets of inner membrane and/or granular deposits (red arrowheads) were present. The position of vacuoles in relation to intact mitochondria and the concentric sheets of inner membrane and/or granular deposits present within vacuoles suggest that these structures may be mitochondria with drastically altered ultrastructure.

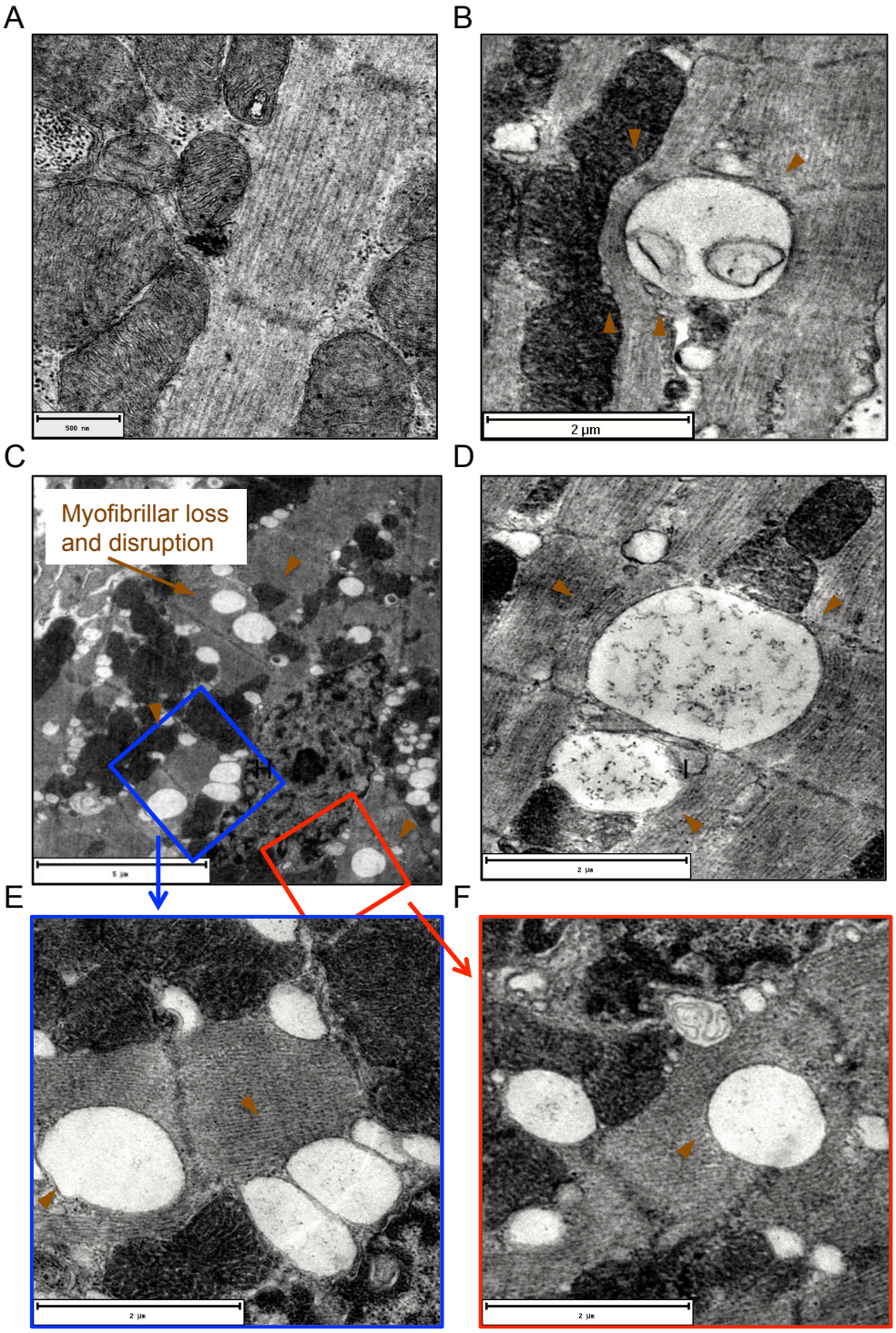


Fig. 3.12 TEM micrographs of subcellular morphological changes as a result of chronic DOX treatment characterised by swollen vacuoles and myofibrillar loss and disruption.
Ultra-thin (90 nm) sections were imaged using a transmission electron microscope. Micrographs are of representative sections. (A) Control section (B) DOX section (C) DOX section (D) DOX section (E) Magnified DOX section (F) Magnified DOX section. Scale bar on each panel. Control micrograph showed uniform myofibrillar architecture and mitochondrial distribution and structure. In DOX micrographs Z-line distortion and the presence of swollen vacuoles resulted in diffuse myofibrillar disruption and loss (brown arrowheads).

3.3.3 Pathological effects of DOX treatment in the heart

LV sections from control and DOX-treated rats were stained with H&E to visualise muscle pathology. Control rat myocardium exhibited typical myocardial morphology and architecture, with no discernible lesions (Fig. 3.13A). Severe histological damage was present in DOX-treated tissue compared to control including vacuolation of cardiomyocytes, cardiomyocyte cytomegaly, eosinophilic cytoplasm, intercellular vacuolation, loss of cardiomyocyte alignment and rigidity and infiltration of mononuclear cells (Fig. 3.13B). CD68 immunostaining confirmed that the cellular infiltrates in DOX-treated myocardium were composed primarily of macrophages (Fig. 3.13C & D). To examine the presence of mesenchymal cells, such as fibroblasts or activated fibroblasts termed myofibroblasts, an antibody to vimentin was used. LV sections showed a strong and ubiquitous increase in vimentin signal in DOX-treated compared to control (Fig. 3.13E & F). Vimentin has been shown to be upregulated in proliferating fibroblasts and myofibroblasts (Baum and Duffy, 2011; Berndt et al., 2014; Skalli et al., 1989) suggesting that the increase in vimentin signal in DOX-treated rats is due to fibroblast proliferation and activation and the presence of myofibroblasts. This data suggests that chronic DOX treatment results in vacuolation of cardiomyocytes, cardiomyocyte cytomegaly, eosinophilic cytoplasm, diffuse disruption of the myocardial architecture, inflammatory cell infiltration and the presence of myofibroblasts. The presence of myofibroblasts indicates that there may be excess ECM deposition and fibrosis.

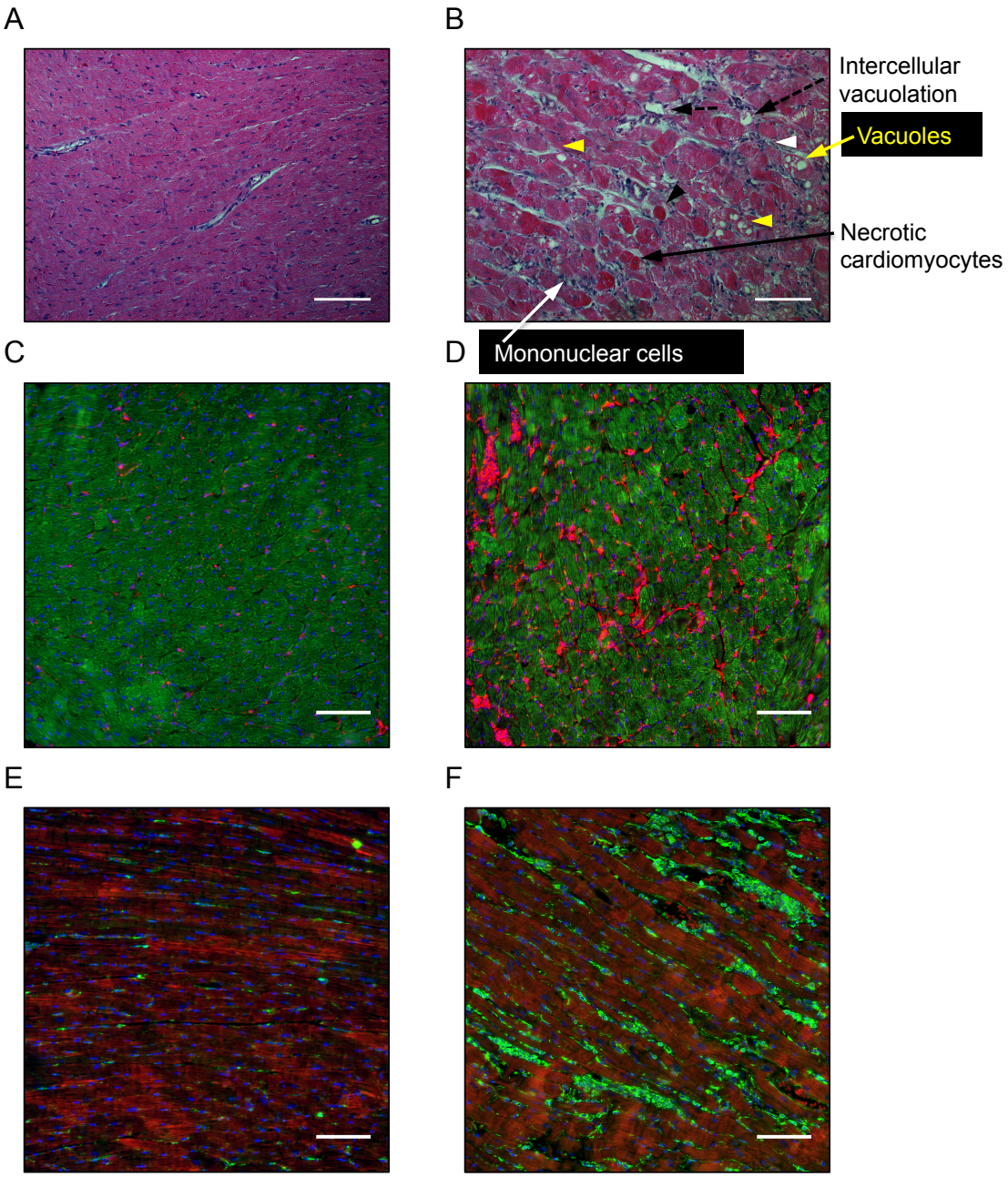


Fig. 3.13 Histological analysis of myocardial tissue following chronic DOX treatment.
LV sections were stained with H&E to visualise muscle pathology (A & B), CD68 immunostaining to visualise pan-macrophage infiltration (C & D) and vimentin immunostaining to visualise the presence of mesenchymal cells (E & F). (A) Control rat section with typical myocardial architecture. (B) DOX-treated section with severe histological damage including diffuse vacuolation of cardiomyocytes (yellow arrowheads), intercellular vacuolation (oedema) (dashed arrows), eosinophilic necrotic cardiomyocytes (black arrowheads), infiltration of mononuclear cells (white arrowhead) and diffuse cardiomyocyte hypertrophy/cytomegaly. (C) CD68 immunostaining of control section, CD68 (red), DAPI (blue) and autofluorescence (green) (D) CD68 immunostaining of DOX section showed cellular infiltrates are composed primarily of macrophages, CD68 (red), DAPI (blue) autofluorescence (green) (E) Vimentin staining of control section, vimentin (green), DAPI (blue) and autofluorescence (red) (F) Vimentin staining of DOX section showed the presence of mesenchymal cells, vimentin (green), DAPI (blue) and autofluorescence (red). Dr. J. Tonkin performed histological sectioning and staining. Scale bar on each panel represents 100 µm.

3.4 Discussion

3.4.1 A chronic rat model of DOX-induced cardiomyopathy

Chronic DOX treatment produced a progressive cardiotoxicity at a clinically relevant concentration. There was a significant decrease in cardiac function assessing during protocol week four, following four weekly doses of DOX. Cardiac function continued to decline incrementally with DOX treatment. There was a further decrease in cardiac function during the off-dosing period, indicating that the treatment protocol had caused a progressive pathological state and a non-reversible decline in myocardial function. Despite a reproducible functional decline in cardiac function the mean LVEF remained above 50% until the final echocardiographic assessment when it reached 50% (mean 49.6%), consistent with findings by Cove-Smith *et al*. who reported a final LVEF of 49.2% (Cove-Smith et al., 2014). A LVEF ≥ 50% is considered to be the clinically normal human range, whereas between 40-49% is defined as HF with mid-range LVEF (Ponikowski et al., 2016). qPCR analysis of LV tissue showed increased transcript levels of *Nppa* and *Nppb* in DOX-treated compared to control, consistent with their use as diagnostic markers of HF with LV systolic dysfunction (Falcao et al., 2004; Ponikowski et al., 2016) and as indicators of DOX-induced myocardial injury in clinical practice (Hayakawa et al., 2001; Suzuki et al., 1998). An increase in transcript levels of *Nppa* and *Nppb* was significantly negatively correlated with a decline in cardiac function. DOX-treated rats showed decreased transcript levels of *Myh6* and increased transcript levels of *Myh7* compared to control, consistent with myosin heavy chain isoform switching in human cardiac dysfunction and HF (Bugaisky et al., 1990; Nakao et al., 1997) and previous findings in chronic rat models of DOX-induced cardiotoxicity (Cappelli et al., 1989; de Beer et al., 2000), suggesting adverse ventricular remodelling. An increase in transcript levels of *Atp2a2* is consistent with findings in human HF (Mercadier et al., 1990) and decreased transcript

levels of *Atp2a2* in a rabbit model of chronic DOX-induced cardiotoxicity (Arai et al., 1998). A disruption to calcium uptake and release leads to calcium overload, which results in sarcomeric disarray and myofibril deterioration. Significant myofibrillar degeneration was observed using TEM in DOX-treated myocardial tissue. A 30% decrease in ejection fraction in young adult rats with a significantly correlated relationship with transcript levels of biomarkers of cardiac dysfunction, including *Nppa*, *Nppb*, *Myh6*, *Myh7* and *Atp2a2*, is consistent with progressive cardiac dysfunction and cardiac failure onset (Ponikowski et al., 2016). There was a premature death in our study during protocol week 10. In a previously published rat study dosing for 10 weeks with a higher dose of DOX (2.5 mg/kg instead of 1.25 mg/kg) mortality significantly increased in the off-dosing period (weeks 12-14) (Schwarz et al., 1998). A further decline in cardiac function during the off-dosing period is consistent with clinical findings where a significant decrease in mean patient LVEF during DOX dosing progressively worsened over the following 12 months despite no further DOX treatment (Cardinale et al., 2006; Dodos et al., 2008). Together, these findings confirm the establishment of a clinically relevant rat model of chronic DOX-induced cardiomyopathy.

3.4.2 Mitochondrial dysfunction in DOX-induced cardiomyopathy

Chronic DOX treatment drastically altered subcellular morphology. A key feature of subcellular changes was the presence of diffuse vacuoles and drastically altered mitochondrial morphology and distribution compared to control. These subcellular changes are consistent with previous reports in rats (Cove-Smith et al., 2014; Mettler et al., 1977; Schwarz et al., 1998; Zhou et al., 2001) and in humans (Lefrak et al., 1973) of multifocal vacuoles and abnormal mitochondrial ultrastructure. The position and composition of vacuoles in relation to intact mitochondria suggested that these vacuoles may be damaged mitochondria. Damaged mitochondria have been seen in human biopsies as early as 24 h

post DOX administration (Unverferth et al., 1983). Cove-Smith *et al*. saw subcellular mitochondrial changes following a single dose of DOX. It was found that subcellular myofibrillar and mitochondrial degeneration coincided with early DOX-induced functional impairment and preceded any overt myocardial degeneration (Cove-Smith et al., 2014).

The functional mechanisms behind these ultrastructural pathological changes to mitochondrial structure remain unclear but are likely due to a combination of multifactorial processes including redox cycling and ROS damage, direct mitochondrial damage and transcriptional modulation that alters mitochondrial structure and function. It is likely that functional mitochondrial disruption leads to ultrastructural pathological changes.

Damaged mitochondria are degraded by autophagy in cardiomyocytes (Gray et al., 1999). Autophagy is an intracellular degradation system which involves the sequestration of cytoplasmic contents in a double-membraned vacuole, the autophagosome and the fusion of the autophagosome with the lysosome (Mizushima et al., 2008). It has previously been shown that mitochondrial DNA that escapes from autophagy leads to Toll-like receptor (TLR) 9-mediated inflammatory responses in cardiomyocytes and is capable of inducing HF (Oka et al., 2012). DNase II is an acid DNase found in the lysosome and is essential to the degradation of the DNA of apoptotic cells (Evans and Aguilera, 2003; Kawane et al., 2006). Cardiac-specific deletion of lyosomal DNase II showed no cardiac phenotypes under baseline conditions but increased mortality and caused severe myocarditis and dilated cardiomyopathy 10 days after treatment with pressure overload (Oka et al., 2012). DNase II-deficient hearts exhibited infiltration of inflammatory cells and increased mRNA expression of inflammatory cytokines with accumulation of mitochondrial DNA deposits in autolysosomes in the myocardium (Oka et al., 2012). Administration of the inhibitory oligodeoxynucleotides against TLR9, which is known to be activated by bacterial DNA (Hemmi et al., 2000), or ablation of

Tlr9 attenuated the development of cardiomyopathy in DNase II-deficient mice (Oka et al., 2012). This data suggests that mitochondrial damage and mitochondrial DNA release plays a significant role in the genesis of chronic inflammation in failing hearts. Therefore, it is possible that mitochondrial DNA that has escaped from autophagy in the present model has initiated an inflammatory response via TLR9 that contributes to the HF seen with chronic DOX treatment.

3.4.3 Chronic DOX treatment results in a pro-inflammatory state

Histological staining of chronic DOX-treated myocardial tissue showed intracellular and intercellular vacuolation, eosinophilic cytoplasm which is indicative of myocyte necrosis (Majno and Joris, 1995), cardiomyocyte cytomegaly, loss of cardiomyocyte alignment and rigidity and infiltration of mononuclear cells. These findings are consistent with other reports in chronic rat (Cove-Smith et al., 2014; Mettler et al., 1977; Viswanatha Swamy et al., 2011) and human biopsies of DOX-induced cardiotoxicity (Lefrak et al., 1973) summarised as degeneration of cellular architecture, cardiomyocyte loss, cytoplasmic vacuolation, inflammatory cell infiltration and fibrosis. Myocyte necrosis is associated with mitochondrial dysfunction and swelling of the cell, which leads to leakage of cellular components resulting in a prolonged inflammatory state (Chiong et al., 2011; Lemasters et al., 1999). H&E stained sections showed infiltration of mononuclear cells. CD68 immunostaining of DOX sections indicated that the majority of cellular infiltrates are composed primarily of macrophages. These findings are consistent with reports by Cove-Smith *et al*. of multi-focal displacement of cardiomyocyte alignment with possible replacement macrophage and fibroblast infiltration on H&E stained cardiac sections (Cove-Smith et al., 2014).

Histological staining showed an increase in vimentin signal in DOX-treated myocardial tissue compared to control, suggesting fibroblast activation and myofibroblast infiltration (Baum and Duffy, 2011; Berndt et al., 2014). In the whole rat heart non-myocytes such as fibroblasts, endothelial cells and smooth muscle cells make up approximately 70% of the cellular population of the heart with myocytes making up the remaining 30% (Nag, 1980; Zak, 1974). In the healthy heart fibroblasts are arranged in networks of sheets and strands and are aligned alongside cardiomyocytes. Fibroblasts respond to mechanical and chemical stimuli, interact with other cells types using paracrine factors and are involved in the maintenance of myocardial tissue structure by producing factors such as cytokines, growth factors and matrix metalloproteinases (MMPs) that control and balance the synthesis and degradation of connective tissue components (Baum and Duffy, 2011). Pro-inflammatory cytokines, released in response to cellular damage or injury, activate fibroblasts. Activated fibroblasts, termed myofibroblasts, release components of the ECM required for tissue repair (Wynn, 2008). If the initial inflammatory response does not resolve inflammation and repair processes occur simultaneously causing excessive ECM deposition with a loss of collagen degradation by MMPs which leads to fibrosis and myocardial stiffening (Chen and Frangogiannis, 2013; Wynn, 2008). Inflammatory cell infiltration and fibroblast activation suggests chronic inflammation and adverse remodelling occur as a result of DOX treatment. Chronic inflammation and adverse remodelling are likely to contribute to the final stages of DOX-induced contractile dysfunction and HF with DOX treatment.

3.4.4 Limitations and future directions

The continued decline in cardiac function during the off-dosing period suggests DOX-induced cardiotoxicity was already irreversible and DOX treatment over 8 weeks had caused a pathological state with a progressive decline in myocardial function. In the future, it would be

informative to explore if the progressive cardiotoxicity could be halted or reversed with fewer doses of DOX. Histological findings suggest that irreversibility of cardiac dysfunction could result in part from adverse remodelling. Strategies involved in limiting adverse ventricular remodelling during chronic DOX treatment may improve cardiac function with DOX treatment.

3.4.5 Conclusion

In this chapter a clinically relevant rat model of irreversible DOX-induced cardiomyopathy was established which allowed the further characterisation of the myocardial damage that contributes to chemotherapeutic cardiotoxicity. Histomorphological documentation of subcellular and intercellular pathological changes showed myofibrillar and mitochondrial degeneration with inflammatory cell infiltration and adverse ventricular remodelling.

Chapter 4

Differential gene expression in a rat model of DOX-induced cardiomyopathy

Chapter 4 Differential gene expression in a rat model of DOX-induced cardiomyopathy

4.1 Introduction

Improved understanding of the factors that contribute to the phenotype of DOX-induced cardiotoxicity would enable the development of cardioprotective strategies, thereby allowing DOX to be used more effectively to treat cancer while minimising the cardiac complications of DOX therapy. Therefore, the aim of this area of PhD research was to identify and characterise the significant processes involved in a clinically relevant rat model of DOX-induced cardiotoxicity using transcriptome profiling. Microarrays are designed with hybridisation probes, which must be based on prior sequence knowledge that is restricted to the reference material available at the time of array production. RNA-seq results can be updated as new sequence information is obtained as every transcript in the sample is sequenced with relatively low background noise and a high dynamic range (Wang et al., 2009). To my knowledge this is the first time RNA-seq has been performed on a clinically relevant rat model of DOX-induced cardiomyopathy.

4.2 Hypothesis and aim

I hypothesis that there is a differential gene expression and that mitochondrial related transcripts are drastically altered in DOX-induced cardiomyopathy.

The aim of this chapter is as follows:

1. Identify and characterise pathways involved in the pathogenesis and phenotype of DOX-induced cardiomyopathy by performing transcriptome profiling using RNA-seq of LV tissue from a rat model of DOX-induced cardiotoxicity

4.3 Results

4.3.1 RNA-seq and processing

RNA-seq, conducted by the Genomics facility of the MRC Clinical Sciences Centre using the Illumina HiSeq 2500, was performed on cDNA generated from RNA isolated from LV tissue taken at sacrifice from three control and three DOX-treated rats. Following sequencing the Cufflinks suite (Trapnell et al., 2012; Trapnell et al., 2010) was used to analyse gene expression. FPKM for each gene sequenced were obtained for further analyses. FPKM represents normalised gene expression values for each transcript. The highest expressing transcript was used for each gene with more than one transcript. To examine if the transcript levels obtained from RNA-seq were consistent with those obtained by qPCR performed on the same tissue a correlation analysis was conducted for each sample analysed. *Nppa*, *Nppb*, *Myh6*, *Myh7* and *Atp2a2* were chosen as genes of interest to carry out this correlation analysis as a significant change in their transcript levels was detected separately by qPCR on a larger number of samples (Fig. 3.4 control n = 4 DOX n = 7). As shown in Fig. 4.1, there was a significant direct correlation between RNA-seq and qPCR *Nppa*, *Nppb*, *Myh6*, *Myh7* and *Atp2a2* transcript levels. Direct correlation of transcript levels between qPCR and RNA-seq suggests that RNA-seq was a valid and robust method to explore gene expression changes in DOX-induced cardiotoxicity.

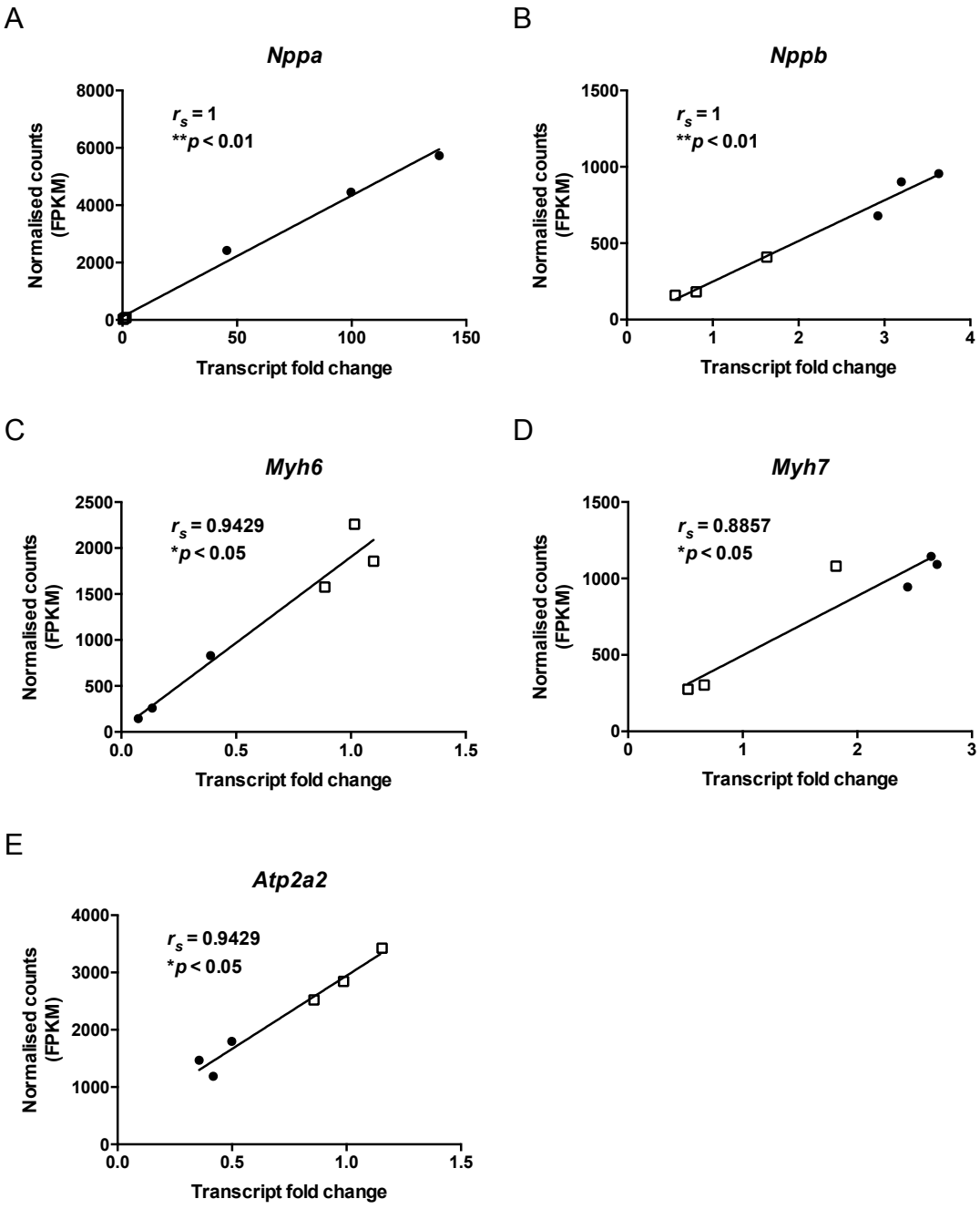


Fig. 4.1 Validation and correlation of transcript level values between RNA-seq and qPCR.
Correlation analysis between RNA-seq and qPCR transcript levels of (A) *Nppa* (B) *Nppb* (C) *Myh6* (D) *Myh7* (E) *Atp2a2*. Control n = 3 (clear square) DOX n = 3 (circle). The correlation coefficient r_s was calculated using Spearman rank-order correlation *$p < 0.05$ **$p < 0.01$. A significant correlation was present between RNA-seq and qPCR transcript levels. Transcript levels obtained from normalised counts (FPKM) from RNA-seq with relative values normalised to *Hsp90ab1* and expressed as fold change relative to average of control samples from qPCR analysis. Each symbol represents data obtained for one rat.

Cuffdiff was used to compare the expression levels of transcripts to identify differentially expressed genes between DOX-treated and control. In the Cuffdiff data set a total of 2071 transcripts had significant differences in expression between DOX-treated and control with a FDR < 0.05 (Fig. 4.2A). Genes with the highest and lowest fold changes in transcript levels were labelled (labelling threshold FDR < 0.01 and $\log_2$ fold change > 4 or < -2.6). Unsupervised hierarchical clustering of the most differentially expressed transcripts (FDR < 0.002, $\log_2$ fold change > 2.5 or < -2.5, 231) clustered the samples into two distinct groups, which when labelled post analysis showed splitting into DOX-treated and control (Fig. 4.2B). There appeared to be a correlation between the severity of contractile dysfunction, as assessed by the LVEF, and the Z-score of differentially expressed transcripts. This was particularly evident in the sample DOX1 compared to control, which showed a higher Z-score compared to control than the other two DOX samples, consistent with a lower LVEF and severity of contractile dysfunction (Fig. 4.2B).

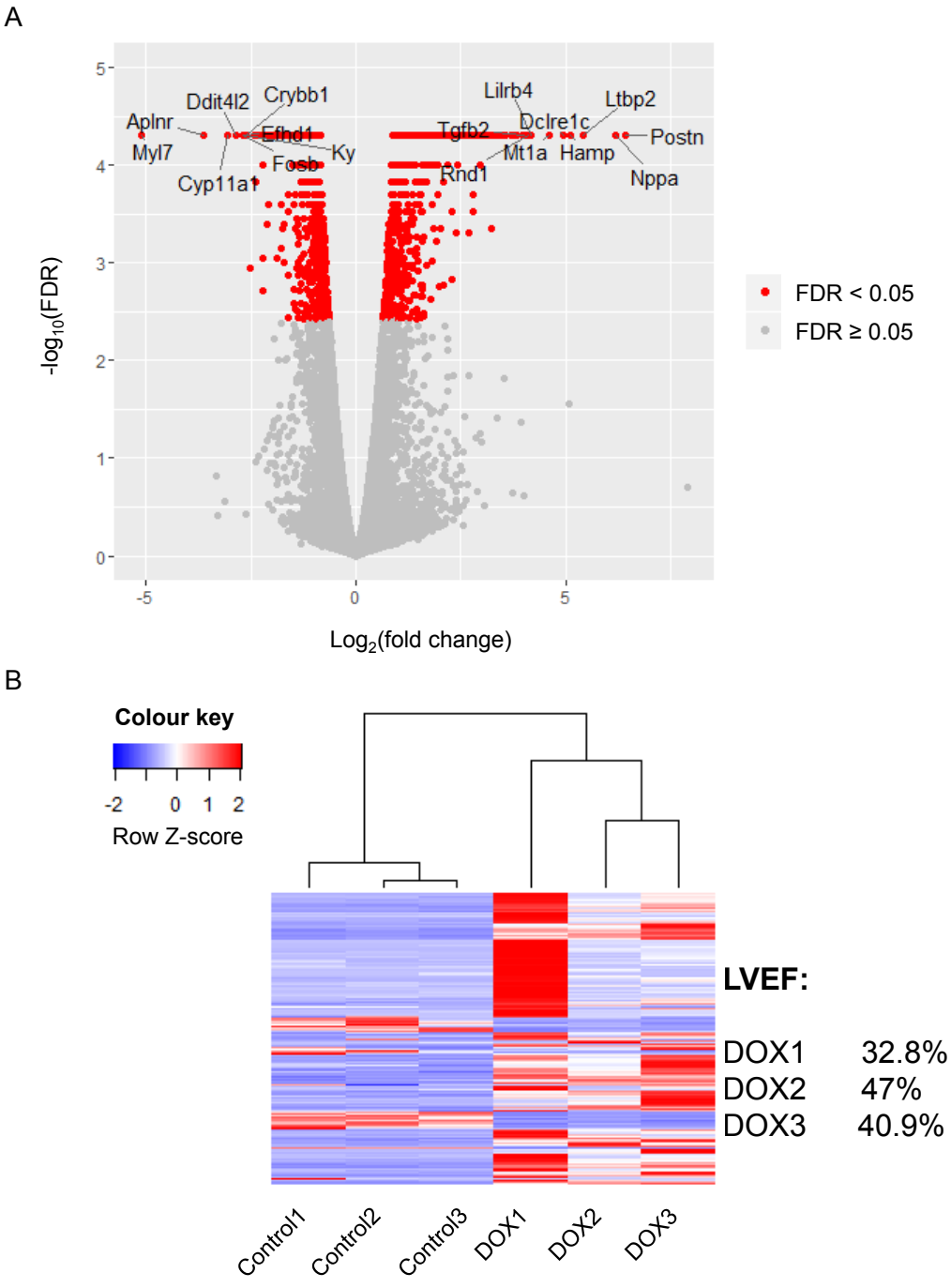


Fig. 4.2 Differentially expressed genes between control and DOX-treated samples.
(A) Volcano plot of all detected transcripts with log_2(fold change) against -log_{10}(FDR). Transcripts with significant changes (FDR < 0.05, 2071) in DOX-treated samples relative to control are indicated in red. Transcripts with the highest and lowest fold changes are labelled (labelling threshold FDR < 0.01 and log_2 fold change > 4 or < -2.6) (B) Unsupervised hierarchical clustering of the most differentially expressed transcripts (FDR < 0.002, log_2 fold change > 2.5 or <-2.5, 231) clustered the samples into two distinct groups, which when labelled post analysis showed splitting into control and DOX-treated rats. There appeared to be some correlation between the severity of cardiac dysfunction, as assessed by LVEF, and the Z-score of the most differentially expressed transcripts for each DOX-treated rat compared to control. Volcano and unsupervised hierarchical clustering plots were generated by Cheuk Ting Angela Yiu (ICL, UK).

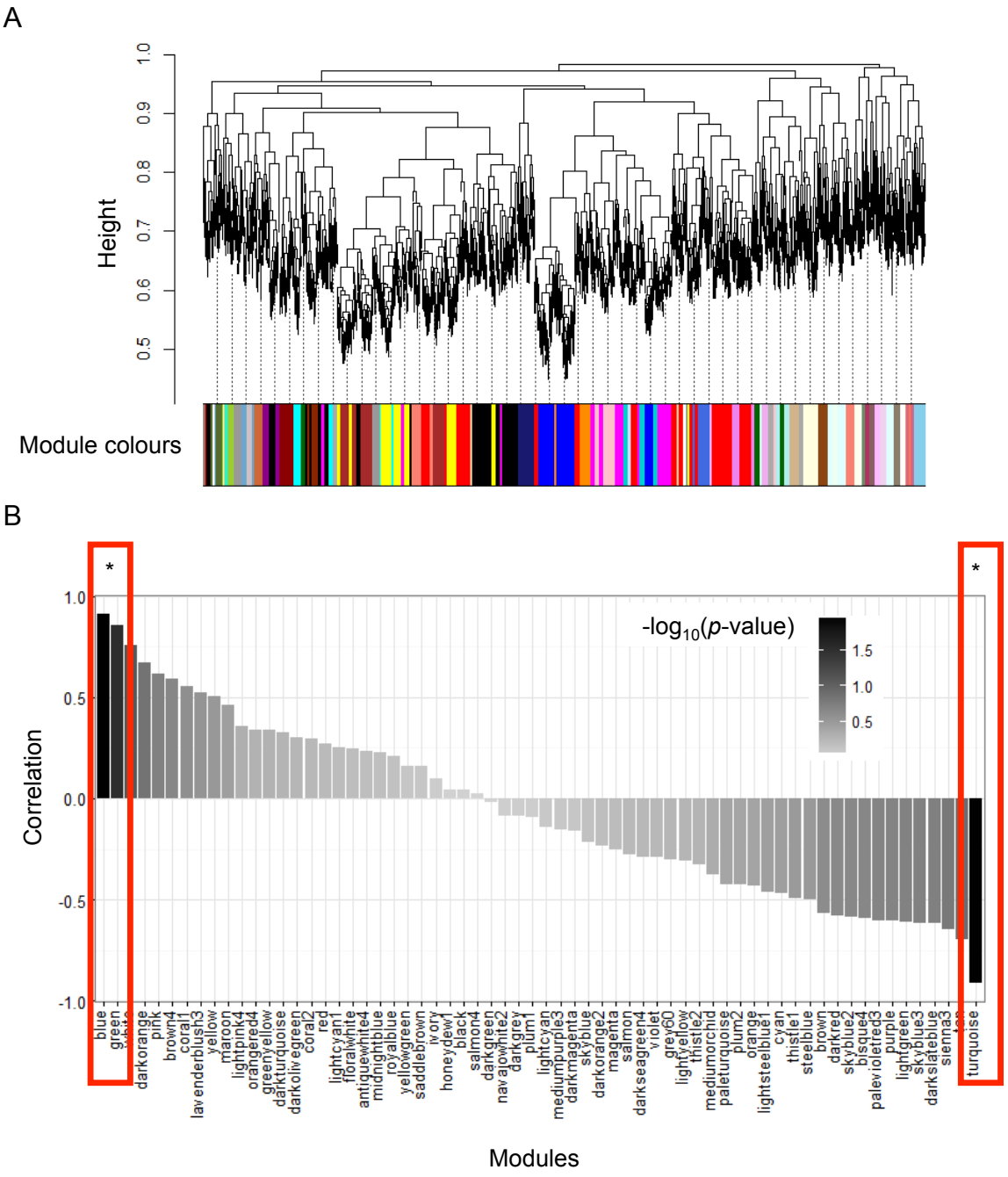
4.3.2 Weighted gene co-expression network analysis

WGCNA was performed in order to analyse gene expression changes without predetermined bias (Langfelder and Horvath, 2008). WGCNA was performed on log transformed ($log_2(x+1)$) FPKM for 9825 transcripts, regardless of whether values were differentially expressed across the samples or not. The highest expressing transcript was used for each gene with more than one transcript. Low expressing transcripts with total FPKM of less than or equal to ten were excluded as their expression values were negligible and in order to reduce noise. WGCNA performs pairwise comparison between each transcript to see if their expression changes across the samples in the same way. If the relative change over all samples was consistent between different transcripts the transcripts were grouped together into modules. Modules were assigned a colour and displayed as a dendrogram (Fig. 4.3A). Only at this point were modules correlated with treatment. Three modules were significantly ($p < 0.05$) correlated with DOX treatment: turquoise ($r = -0.91$, $p = 0.01$; 2237 genes), blue ($r = 0.9$, $p = 0.01$; 1134 genes) and green ($r = 0.86$, $p = 0.03$; 630 genes) (Fig. 4.3B).

Functional annotation clustering by NIH DAVID 6.7 was used to determine groups of gene annotations that are significantly overrepresented amongst the genes correlated with treatment (Huang da et al., 2009). Gene ontology annotations are based on the reported biology of gene products, including cellular component, molecular function and biological process. Related gene annotations are then grouped together into annotation clusters. Annotation clusters have an enrichment score to statistically highlight the most overrepresented biological annotations in the data set. The enrichment score for each annotation cluster is defined as the minus log transformation of the geometric mean of each annotation's average modified Fisher's exact *p*-value. An enrichment score of 1.3 is equivalent to non-log scale 0.05. The enrichment analysis is based on the hypergeometric

distribution described as the probability of c successes in g draws, with no replacement, from a finite population that contains z successes. Therefore, a higher enrichment score indicates more significant (enriched) biological processes in a data set (Huang da et al., 2009).

Mitochondrial related annotations were highly enriched in the turquoise module including genes involved in mitochondrion structure, the respiratory chain, the TCA cycle and oxidative phosphorylation (Fig. 4.4A). Inflammation and immune response related genes were highly enriched in the blue module including genes involved in inflammation, the positive regulation of the immune response, the adaptive immune response and leukocyte activation (Fig. 4.4B). A range of annotations of gene function were present in the green module including genes involved in functions within the nuclear lumen, proteolysis, nucleotide binding and positive regulation of the nuclear factor kappa-light-chain-enhancer of activated B cells (NF-κB) signalling cascade (Fig. 4.4B). This indicates that genes involved in mitochondrial function and inflammation and the immune response are the most statistically correlated cellular functions and pathways affected in chronic DOX-induced cardiomyopathy using WGCNA.



Three of the modules were significantly (*$p < 0.05$) correlated with DOX treatment

Fig. 4.3 WGCNA between control and DOX-treated samples.
(A) WGCNA dendrogram of differentially expressed genes in LV tissue from DOX-induced cardiomyopathy model. Modules contain groups of transcripts that are similar in their relative co-expression across the samples (B) Correlation of modules to DOX treatment. -log$_{10}$(*p*-value) denotes the colour of each module. Three of the modules were significantly (*$p < 0.05$) correlated with DOX treatment. -log$_{10}$(0.05) = 1.3 & -log$_{10}$(0.1) = 1. Hence, darker bars indicate lower *p*-values and higher statistical significance. WGCNA dendrogram and correlation plot were generated by Cheuk Ting Angela Yiu (ICL, UK).

A

Turquoise Module - Mitochondrial Function

Negatively correlated with DOX treatment (decreased transcript levels)
r = -0.91, p = 0.01; 2237 genes

NIH DAVID Annotation	Enrichment Score
Mitochondrion	77.94
Oxidative phosphorylation	27.88
Respiratory chain	8.17
TCA cycle	6.73

B

Blue Module - Inflammation and the Immune Response

Positively correlated with DOX treatment (increased transcript levels)
r = 0.9, p = 0.01; 1134 genes

NIH DAVID Annotation	Enrichment Score
Inflammation and response to injury	11.81
Positive regulation of immune system	8.41
Adaptive immune response	5.89
Leukocyte activation	3.81

Green Module - Nuclear lumen & NF-κB signalling cascade

Positively correlated with DOX treatment (increased transcript levels)
r = 0.86, p = 0.03; 630 genes

NIH DAVID Annotation	Enrichment Score
Nuclear lumen	3.01
Proteolysis	2.67
Nucleotide binding	1.82
Positive regulation of NF-κB signalling cascade	1.67

Fig. 4.4 Functional annotation clustering with enrichment scores by NIH DAVID of genes present in each module significantly correlated with DOX treatment.
(A) Functional annotation clustering with enrichment scores by NIH DAVID of genes present in the turquoise module (r = -0.91, p = 0.01) which were negatively correlated with DOX treatment. Genes identified in the turquoise module were related to the mitochondrion, respiratory chain, TCA cycle and oxidative phosphorylation suggesting mitochondrial function was decreased in DOX-induced cardiotoxicity (B) Functional annotation clustering with enrichment scores by NIH DAVID of genes present in the blue (r = 0.9, p = 0.01) and green (r = 0.86, p = 0.03) modules which were positively correlated with DOX treatment. Genes identified in the blue module were related to inflammation and the immune response suggesting these pathways were increased in DOX-induced cardiotoxicity. Genes identified in the green module were related to the nuclear lumen, proteolysis, nucleotide binding and positive regulation of NF-κB signalling cascade.

4.3.3 Literature-curated gene knowledge bases

NIH DAVID functional annotation clustering

Having conducted WGCNA in order to obtain an understanding of the functional pathways correlated with DOX treatment without predetermined bias differential gene expression analysis based on literature-curated gene knowledge bases was performed using the Cuffdiff data set. Functional annotation clustering with NIH DAVID was performed on the significantly (FDR < 0.05) increased (log_2 fold change > 1) and decreased (log_2 fold change < -1) transcript levels of genes identified by Cuffdiff. Table 2 shows the significantly decreased gene annotations in DOX-treated samples compared to control. Enriched decreased annotations included mitochondrion (structure and function), peroxisome, fatty acid metabolism, ion transport and T-tubules. Peroxisomes are involved in the β-oxidation of fatty acids and peroxisome dysfunction has been associated with cardiac dysfunction (Koh et al., 2001). Table 3 shows the significantly increased gene annotations in DOX-treated samples compared to control. Amongst those highly enriched annotates were inflammation, extracellular region parts, cell migration and the immune response. Other increased annotations included cell adhesion, cell death, macrophage activation, TLR signalling, NF-κB signalling cascade, T cell activation, and positive regulation of TNF and IL-6 production.



Decreased Transcript Levels

FDR < 0.05

log_2 fold change < -1 (fold change < 0.5)

NIH DAVID Annotation	Enrichment Score
Mitochondrion	11.03
Peroxisome	4.31
Fatty acid metabolism	3.98
Ion transport & T-tubule	3.19

Table 2 Functional annotation clustering with enrichment scores by NIH DAVID of the significantly (FDR < 0.05) decreased (log_2 fold change < -1) annotations based on transcript levels, suggesting mitochondrial function, peroxisome function, fatty acid metabolism and ion transport were decreased in DOX-induced cardiotoxicity.



Increased Transcript Levels

FDR < 0.05
$\log_2$ fold change > 1 (fold change > 2)

NIH DAVID Annotation	Enrichment Score
Inflammation, response to injury	28.99
Extracellular region part	12.45
Chemotaxis and cell migration	10.58
Immune response	10.39
Adaptive immune response	9.67
Response to organic substance	8.9
Positive regulation of cell migration	7.05
Positive regulation of cytokine production	6.27
Cell adhesion	5.1
Cell death	4.75
Macrophage activation, NF-κB signalling cascade,TLR signalling	3.89
T cell activation	3.88
Positive regulation of TNF & IL-6 production	3.13

Table 3 Functional annotation clustering with enrichment scores by NIH DAVID of the significantly (FDR < 0.05) increased ($\log_2$ fold change > 1) annotations, based on transcript levels, in DOX-induced cardiotoxicity.

Ingenuity Pathway Analysis

IPA (v 27216297, Qiagen) was used for pathway analysis of RNA-seq results with a FDR cut-off of < 0.05 using the Cuffdiff data set. IPA uses a data set's list of differential gene expression changes to map genes and gene products to possible functional pathways affected using a literature-curated gene knowledge base. It ranks possible functional pathways based on a significance value. The significance value (*p*-value) calculated by IPA indicates the probability of association of genes from the input data set with the pathway by random chance and is calculated by a modified Fisher's exact test right-tailed. IPA identified the top three pathways affected by DOX treatment as mitochondrial dysfunction, oxidative phosphorylation and the TCA cycle (Fig. 4.5). 118 genes, 102 with decreased transcript levels and 16 with increased transcript levels, out of a possible 156 for the IPA pathway mitochondrial dysfunction were significantly affected by DOX treatment. For the IPA pathway oxidative phosphorylation 73 genes, 70 with decreased transcript levels and 3 with increased transcript levels, out of a possible 97 were significantly affected by DOX treatment. 18 out of a possible 22 genes present in the IPA pathway for the TCA cycle had significantly decreased transcript levels. Ranked fourth and fifth of the significant pathways affected by DOX treatment were acute phase response signalling and the complement system (Fig. 4.5). 80 genes, 28 with decreased transcript levels and 52 with increased transcript levels, in the Cuffdiff data set overlapped out of a possible 158 in the IPA pathway for acute phase response signalling. Acute phase response signalling is triggered by tissue damage or infection, amongst others, and results in an increase in pro-inflammatory factors and a change in concentration of acute-phase plasma proteins resulting in an innate immune response. 16 genes, 1 with decreased transcript levels and 15 with increased transcript levels, out of a possible 34 genes in the IPA pathway for the complement system overlapped with the present data set. The complement system consists of a cascade of enzyme

activations that bridge the innate and adaptive immune responses (Dunkelberger and Song, 2010). Gene expression analysis based on literature-curated gene knowledge bases indicated that mitochondrial function and inflammation and the immune response were the most significantly affected pathways in this chronic DOX-induced cardiomyopathy model.

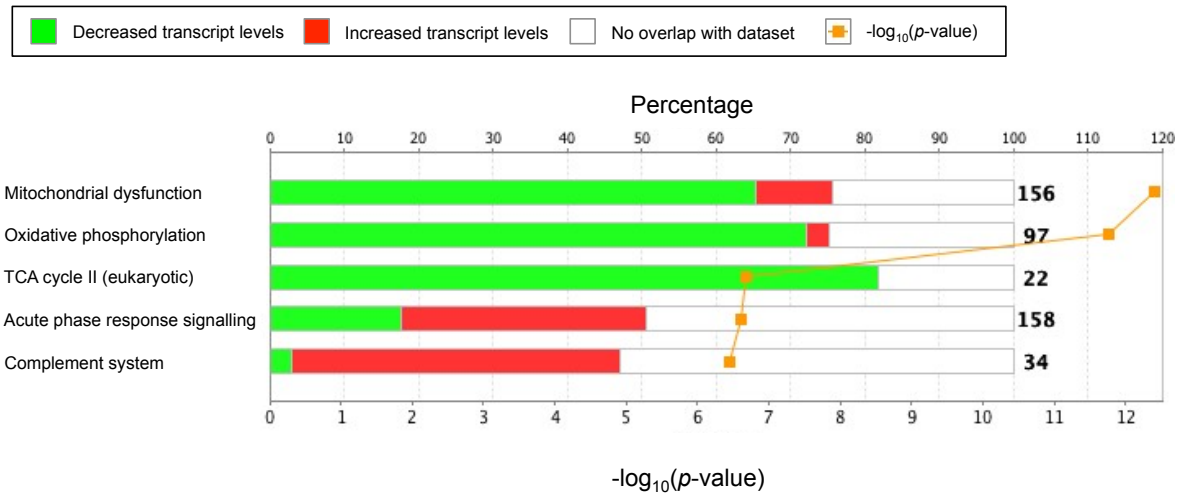


Fig. 4.5 Ingenuity Pathway Analysis of differentially expressed gene changes in DOX-induced cardiotoxicity.
The top five pathways affected by DOX treatment as identified by IPA. The *p*-value associated with each canonical pathway is a measure of the likelihood that the association between a set of focus genes from this data set and a given process or pathway is due to random chance.

4.3.4 qPCR validation of differential gene expression analysis by RNA-seq in DOX-induced cardiomyopathy

To further characterise and validate differential gene expression in DOX-induced cardiomyopathy genes identified using *in silico* analysis were categorised into biological function. qPCR was performed in order to validate *in silico* findings on selected genes of interest on a larger number of samples (qPCR control n = 4 DOX n = 7 versus RNA-seq n = 3). Tables of significant genes related to mitochondrial function (Table 4), ROS related gene changes (Table 5), inflammation and the immune response (Table 6) and cardiac remodelling, fibrosis and dysfunction (Table 7) were compiled. Genes highlighted in yellow in tables were validating by qPCR. qPCR analysis of transcript levels of the majority of genes of interest related to mitochondrial function (Fig. 4.6, Fig. 4.7), ROS (Fig. 4.8), inflammation and the immune response (Fig. 4.9) and cardiac remodelling, fibrosis and dysfunction (Fig. 4.10 - for the genes *Nppa*, *Nppb*, *Myh6*, *Myh7* and *Atp2a2* this is the same data as shown in Fig. 3.4) showed significant differences between DOX-treated and control, consistent with RNA-seq data. The exceptions were *Ppargc1a* (Fig. 4.7B), *Xdh* (Fig. 4.8B) and *Cst3* (Fig. 4.10F), where the increase in n numbers in qPCR analysis revealed variability in the RNA-seq data and, therefore, transcript levels changes were not statistically significant by qPCR analysis. *Cst3* encodes the protein cystatin C which has previously been reported to be elevated in the plasma of mice with chronic DOX-induced cardiomyopathy (Xie et al., 2010). Changes in *Myh7* and *Atp2a2* transcript levels by RNA-seq were not significant but qPCR analysis with a larger sample size showed the changes in *Myh7* and *Atp2a2* levels were significant between DOX-treated and control (Fig. 4.10D & E). In conclusion, qPCR validation of RNA-seq data revealed variability in the data, likely due to the low sample size of n = 3 in each group, highlighting the importance of independent experimental validation of gene expression analysis by microarray or RNA-seq.

Mitochondrial dysfunction and ROS

In silico analysis and ontological evaluation of RNA-seq data consistently identified gene products involved in mitochondrial structure and function to be significantly decreased in DOX-induced cardiomyopathy. Amongst those transcript levels significantly decreased were those that encode the respiratory chain complexes necessary for oxidative phosphorylation including *Cox412*, *Ndufs7*, *Atp5a1*, *Uqcrc2*, *Cyc1*, *Sdhb* and *Cycs* (Table 4). Enzymes involved in the TCA cycle were found to have significantly decreased transcript levels including *Ogdh*, *Idh3b*, *Dlst*, *Sucla2*, *Mdh2* and *Fh*, amongst others (Table 4). Other genes involved in a range of mitochondrial-related structures and functions such as IMM and OMM components, mitochondrial biogenesis and fatty acid metabolism had decreased transcript levels including *Ucp3*, *Pink1*, *Pdk1*, *Acadm*, *Endog*, *Ppara*, *Ppargc1a*, *Ppif*, *Vdac3* and *Abcb8* (Table 4). Transcript levels of *Slc25a28*, which encodes mitoferrin-2 a mitochondrial iron transporter that mediates iron uptake, were unaltered in DOX-treated samples compared to control (Table 4). Significantly, those genes related to mitochondrial function that had increased transcript levels have biological functions related to both pro- and anti-apoptotic cell death and inducible cell stress responses. Amongst those genes with increased transcript levels were *Bcl2a1*, *Bid*, *Tnfrsf21*, *Bcl2l1c* and *Bnip3* (Table 4). Similarly, ROS related gene changes showed a mixture of both pro- and anti-ROS transcript level changes, including *Cybb*, *Xdh*, *Cyba*, *Hmox1*, *Txnrd2*, *Nqo1* and *Prdx3* (Table 5). Of note, *Txnrd2* and *Prdx3* transcript levels were both decreased (Table 5). Thioredoxin reductase 2, encoded by *Txnrd2*, is a ROS scavenger in the mitochondrial matrix and is present in the highest levels in metabolically active tissues such as the heart (Spyrou et al., 1997). Peroxiredoxin 3, encoded by *Prdx3*, is a mitochondrial anti-oxidant protein present in the mitochondrial matrix. Peroxiredoxin 3 uses thioredoxin 2, with thioredoxin reductase 2, as the electron donor to detoxify H_2O_2 as part of the mitochondrial ROS scavenging system, which maintains redox

balance within mitochondria (Stanley et al., 2011). These findings suggest that a prominent feature of DOX-induced cardiotoxicity is a significant reduction in the abundance of transcripts related to mitochondrial structure and function.

Mitochondrial Function				
Gene	**↑↓**	**Log2(fold change)**	**FDR**	**Description of encoded protein function**
Respiratory Chain Complexes				
Cox412	↓	-1.76	0.001	Cytochrome c oxidase subunit 412, **Complex IV**
Ndufs7	↓	-1.33	0.001	Subunit of NADH dehydrogenase, **Complex I**
Atp5a1	↓	-0.97	0.001	Subunit of mitochondrial ATP synthase, **Complex V**
Uqcrc2	↓	-0.89	0.037	Ubiquinol-cytochrome c reductase complex, **Complex III**
Cyc1	↓	-0.86	0.014	Subunit of Cytochrome bc1 complex, **Complex III**
Sdhb	↓	-0.84	0.010	Subunit of succinate dehydrogenase, **Complex II**
Cycs	↓	-0.75	0.014	Cytochrome C, small heme protein that functions in the ETC. Involved in initiation of apoptosis
TCA Cycle				
Ogdh	↓	-1.58	0.001	Subunit of oxoglutarate dehydrogenase, **TCA cycle**
Idh3b	↓	-1.08	0.001	Subunit of NAD(+)-dependent isocitrate dehydrogenase, **TCA cycle**
Dlst	↓	-1.06	0.003	Subunit of dihydrolipoamide S-succinyltransferase, **TCA cycle**
Sucla2	↓	-0.96	0.001	Succinate-CoA ligase ADP-forming beta subunit, **TCA cycle**
Mdh2	↓	-0.87	0.022	Malate dehydrogenase 2, **TCA cycle**
Fh	↓	-0.75	0.019	Fumarate hydratase, **TCA cycle**
Mitochondrial Regulatory Functions				
Ucp3	↓	-1.74	0.001	Uncoupler proteins are mitochondrial transporter proteins that create proton leaks across the IMM. Participates in thermogenesis and energy balance.
Pink1	↓	-1.09	0.025	Kinase that localises to mitochondria. Role in mitochondrial quality control via mitophagy
Pdk1	↓	-0.96	0.001	Kinase that plays a key role in regulation of glucose and fatty acid metabolism
Acadm	↓	-0.95	0.016	Fatty acid metabolism in mitochondria
Endog	↓	-0.91	0.030	Endonuclease localised to mitochondria involved in the replication of mtDNA
Ppara	↓	-0.89	0.034	Peroxisome proliferator-activated receptor alpha, key regulator of lipid metabolism
Ppargc1a	↓	-0.80	0.017	Transcriptional co-activator that regulates the genes involved in energy metabolism
Ppif	↓	-0.80	0.012	Cyclophilin D, part of the IMM linked to the mitochondrial permeability transition pore
Vdac3	↓	-0.77	0.036	Membrane protein that traverses the OMM. Conducts ATP and other small metabolites.
Abcb8	↓	-0.71	0.034	Multi-pass membrane protein that is targeted to the IMM, faciliates iron export from mitochondria
Cell Death Pathways				
Bcl2a1	↑	1.94	0.005	NF-κB target, anti-apoptotic member of the Bcl-2 protein family
Bid	↑	1.39	0.014	Encodes a pro-apoptotic member of the Bcl-2 protein family
Tnfrsf21	↑	1.22	0.027	Encoded protein activates NF-κB and mitogen-activated protein kinase 8 and induces cell apoptosis
Bcl2l1c	↑	1.06	0.003	Encodes anti-apoptotic OMM protein which regulates VDAC opening
Bnip3	↑	0.92	0.005	Encodes apoptosis-inducing factor, involved in mitochondria quality control
Slc25a28	↑	0.15	0.988	Multi-pass membrane protein targeted to the IMM, mitoferrin 2, mitochondrial iron transporter that mediates iron uptake

Table 4 Differential gene expression by RNA-seq of genes related to mitochondrial function. Rows highlighted in yellow show genes that were validated using qPCR.

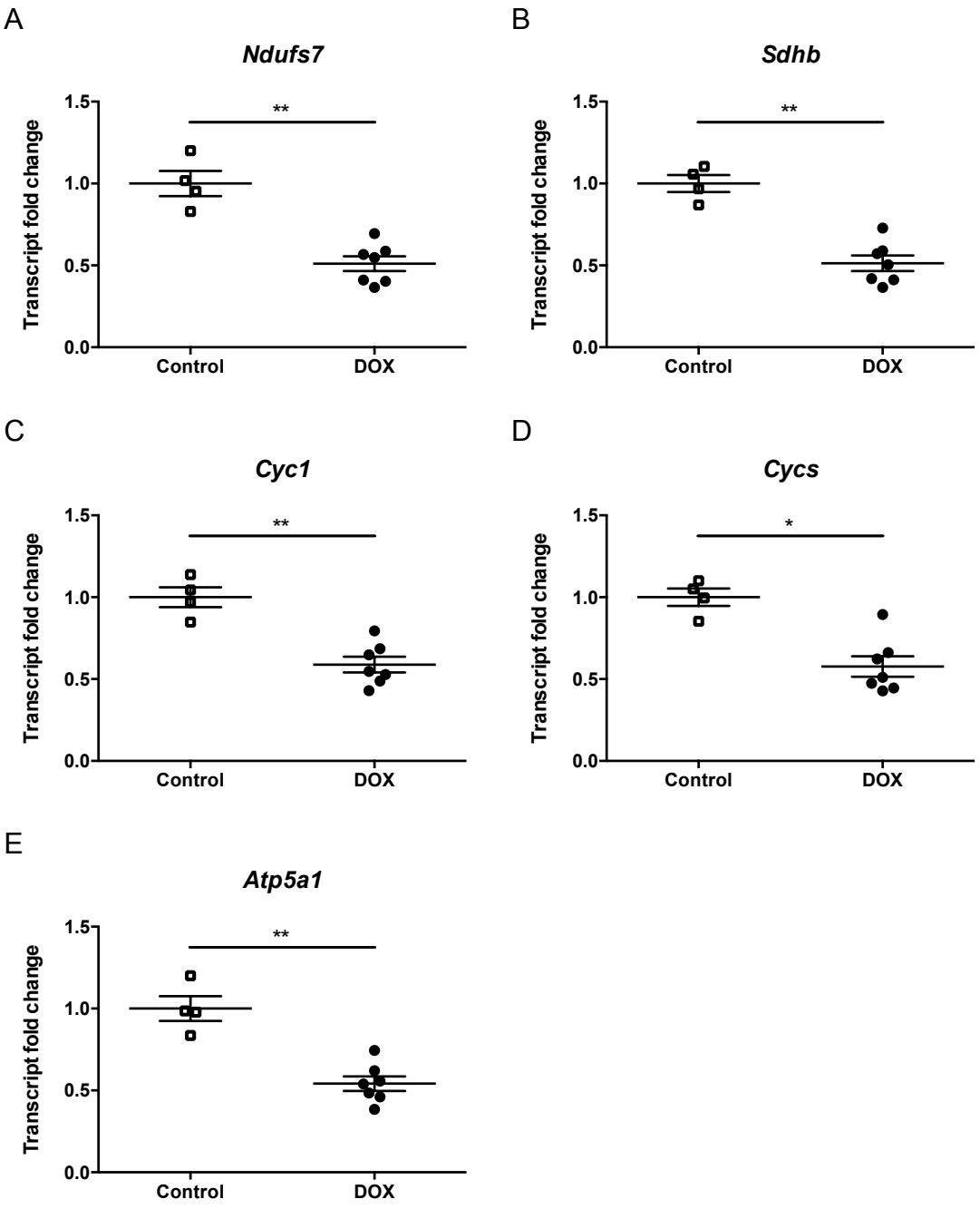


Fig. 4.6 qPCR analysis of transcript levels of genes related to the respiratory chain complexes that were decreased in DOX-induced cardiomyopathy.
qPCR analysis of (A) *Ndufs7* (B) *Sdhb* (C) *Cyc1* (D) *Cycs* (E) *Atp5a1* transcript levels. Scatter plot shows transcript levels obtained for individual rats control n = 4 (clear square) DOX n = 7 (circle), which were normalised to *Hsp90ab1* and expressed as fold change relative to average of control samples. Data is represented as mean ± *SEM*. Mann-Whitney *U* test **p* < 0.05 ***p* < 0.01.

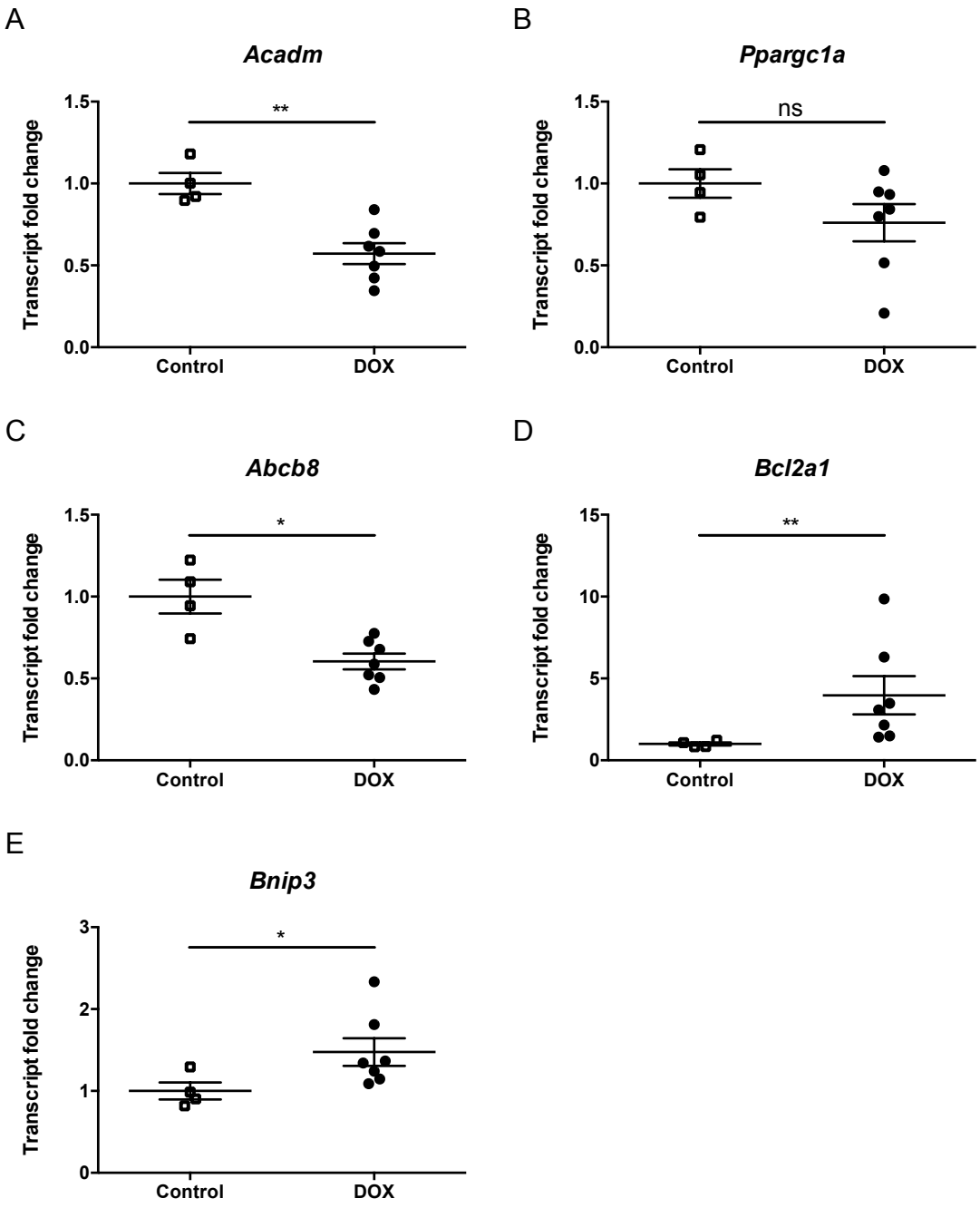


Fig. 4.7 qPCR analysis of transcript levels of genes related to mitochondrial function and cell death pathways in DOX-induced cardiomyopathy.
qPCR analysis of (A) *Acadm* (B) *Ppargc1a* (C) *Abcb8* (D) *Bcl2a1* (E) *Bnip3* transcript levels. Scatter plot shows transcript levels obtained for individual rats control n = 4 (clear square) DOX n = 7 (circle), which were normalised to *Hsp90ab1* and expressed as fold change relative to average of control samples. *Ppargc1a* transcript level changes between control and DOX-treated samples were not statistically significant when assessed by qPCR with a larger sample number suggesting variability in RNA-seq data. Data is represented as mean ± *SEM*. Mann-Whitney *U* test ns = not significant **p* < 0.05 ***p* < 0.01.

ROS related gene changes				
Gene	**↑↓**	**Log2(fold change)**	**FDR**	**Description of encoded protein function**
ROS generation				
Cybb	↑	2.42	0.001	NADPH oxidase 2, membrane-bound superoxide generating enzyme
Xdh	↑	1.60	0.003	Xanthine dehydrogenase, oxidative metabolism of purines. Role in ROS production
Cyba	↑	1.39	0.001	Cytochrome B-245 alpha, subunit of NADPH oxidase 2
Anti-oxidant function				
Hmox1	↑	3.26	0.001	Heme oxygenase mediates the first step of heme catabolism. Anti-oxidant, inducible stress response gene
Txnrd2	↓	-1.21	0.043	Thioredoxin reductase 2, ROS scavenger in mitochondria
Nqo1	↑	1.07	0.001	Anti-oxidant enzyme, protein's enzymatic activity prevents the one electron reduction of quinones
Prdx3	↓	-0.85	0.008	Peroxiredoxin 3, mitochondrial protein with anti-oxidant function

Table 5 Differential gene expression by RNA-seq of genes related to ROS production. Rows highlighted in yellow show genes that were validated using qPCR.

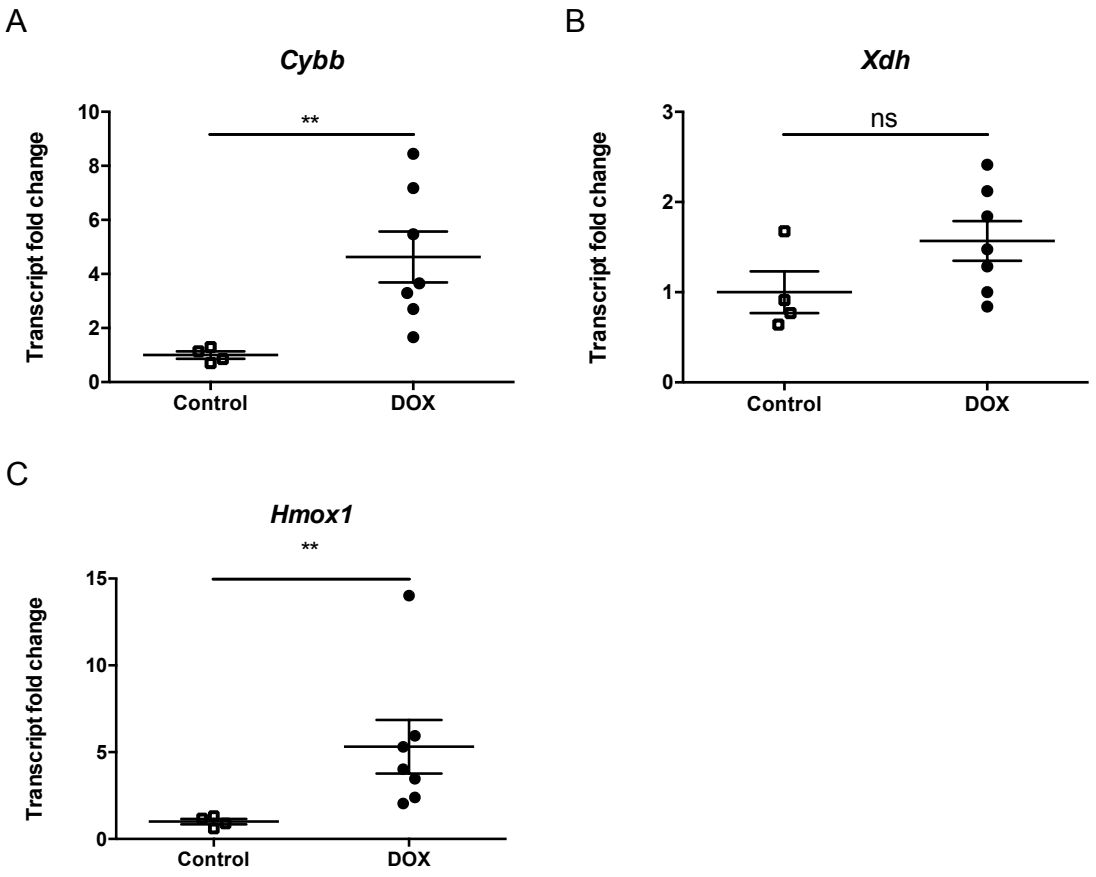


Fig. 4.8 qPCR analysis of transcript levels of genes related to ROS production in DOX-induced cardiomyopathy.
qPCR analysis of (A) *Cybb* (B) *Xdh* (C) *Hmox1* transcript levels. Scatter plot shows transcript levels obtained for individual rats control n = 4 (clear square) DOX n = 7 (circle), which were normalised to *Hsp90ab1* and expressed as fold change relative to average of control samples. *Xdh* transcript level changes between control and DOX-treated samples were not statistically significant when assessed by qPCR with a larger sample number suggesting variability in RNA-seq data. Data is represented as mean ± *SEM*. Mann-Whitney *U* test ns = not significant ***p* < 0.01.

Inflammation and cardiac remodelling

Differential inflammatory gene expression in DOX-treated myocardium showed DOX-induced tissue damage had caused a significant inflammatory and immune response. This is evident in the increase in transcript levels of major pro-inflammatory cytokines such as *Il1β*, *Tgfβ2*, *Ccl2, Il18* and *Il6r* (Table 6). There was an increase in transcript levels of other chemotactic cytokines such as *Cxcl1*, *Cxcl2*, *Cxcl16* and *Ccr5* (Table 6). Other inflammation related genes that had increased transcript levels included *Tlr9*, *Myd88*, *Nlrp3*, *Cd4*, *Cd80*, *Ifngr1* and *Postn* (Table 6). A number of genes involved in tissue remodelling and fibrotic processes had altered transcript levels in DOX-induced cardiotoxicity. These were for example *Serpine1*, *Fn1*, *Lgals3*, *Myl4*, *Lox*, *Myh6*, *Mmp2*, *Tgfb1* and *Myh7* (Table 7). Transcript levels of *Nppa* and *Nppb* were significantly increased in DOX-treated samples, whereas *Ryr2* and *Atp2a2* were both significantly decreased (Table 7). *Top2b* transcript levels were unchanged in this study (Table 7). Together, these data suggest that chronic DOX treatment induces a prolonged inflammatory state and adverse ventricular remodelling.

Inflammation and Immune Response				
Gene	**↑↓**	**Log2(fold change)**	**FDR**	**Description of encoded protein function**
Postn	↑	6.43	0.001	Periostin, extracellular matrix protein, upregulated in activated myofibroblasts, possible marker for activated fibroblasts. Associated with ventricular remodeling following myocardial infarction
Tgfβ2	↑	4.00	0.001	Transforming growth factor beta 2; multifunctional cytokine
Cd80	↑	3.52	0.034	Membrane receptor that when activated induces T-cell proliferation and cytokine production
Ccl2	↑	3.36	0.001	Cytokine, chemotactic activity for monocytes and basophils
Il1β	↑	3.07	0.001	Major inflammatory cytokine, produced by activated macrophages, induces prostaglandin synthesis, neutrophil influx and activation, T-cell activation and cytokine production, B-cell activation and antibody production, and fibroblast proliferation and collagen production
Cxcl1	↑	2.75	0.001	Chemokine expressed by macrophages, neutrophils and epithelial cells with chemotactic activity for neutrophils
Cxcl2	↑	2.72	0.019	Produced by activated monocytes and neutrophils, expressed at sites of inflammation
Cd86	↑	2.43	0.003	Protein necessary for T cell activation and survival
Il18	↑	2.28	0.007	Pro-inflammatory cytokine
Nlrp3	↑	2.26	0.001	In response to damage-associated signals, initiates the formation of the inflammasome polymeric complex. This complex functions as an upstream activator of NF-κB signaling, and it plays a role in the regulation of inflammation, the immune response, and apoptosis
Cxcl16	↑	2.04	0.001	Chemoattractant for inflammatory cells
Ccr5	↑	1.88	0.001	Macrophage chemoattractant
Tlr9	↑	1.84	0.003	Toll-like receptor 9; preferentially binds DNA present in bacteria and viruses and triggers pro-inflammatory signalling cascades
Myd88	↑	1.22	0.001	Adaptor molecule required for most TLR family activation
Il6r	↑	1.17	0.011	IL-6 receptor subunit alpha
Cd4	↑	1.14	0.001	A glycoprotein found on surface of T helper cells, monocytes, macrophages and dendritic cells
Ifngr1	↑	0.89	0.005	Interferon gamma receptor 1, receptor for cytokine interferon gamma

Table 6 Differential gene expression by RNA-seq of genes related to inflammation and the immune response.
Rows highlighted in yellow show genes that were validated using qPCR.

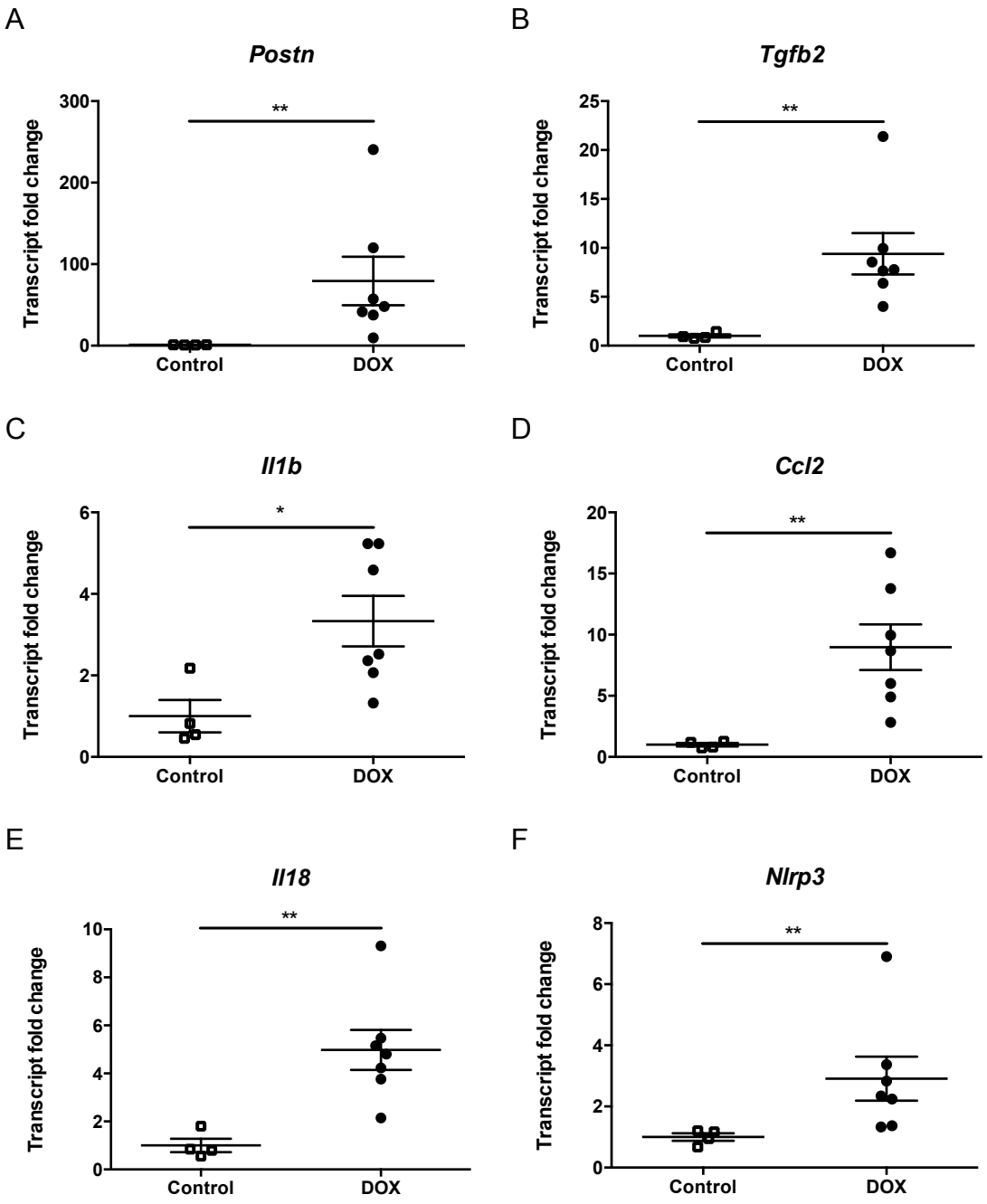


Fig. 4.9 qPCR analysis of transcript levels of genes related to inflammation and the immune response in DOX-induced cardiomyopathy.
qPCR analysis of (A) *Postn* (B) *Tgfb2* (C) *Il1b* (D) *Ccl2* (E) *Il18* (F) *Nlrp3* transcript levels. Scatter plot shows transcript levels obtained for individual rats control n = 4 (clear square) DOX n = 7 (circle), which were normalised to *Hsp90ab1* and expressed as fold change relative to average of control samples. Data is represented as mean ± *SEM*. Mann-Whitney *U* test **p* < 0.05 ***p* < 0.01.

Cardiac remodelling, fibrosis and dysfunction				
Gene	**↑↓**	**Log2(fold change)**	**FDR**	**Description of encoded protein function**
Cardiac remodelling and fibrosis				
Serpine1	↑	3.85	0.001	Inhibitor of fibrinolysis, may play a central role in acute cardiac remodelling
Fn1	↑	2.46	0.001	Fibronectin-1, found in cardiac ECM, involved in cardiac fibrosis
Lgals3	↑	2.46	0.001	Galectin-3, macrophage derived, induces cardiac fibroblast proliferation, collagen deposition and cardiac remodelling
Myl4	↑	2.46	0.001	Atrial light chain 1: expression is re-activated in human ventricular myocardium in cardiac muscle disease
Lox	↑	2.40	0.001	Collagen cross-linker. Indicative of fibrosis
Myh6	↓	-2.21	0.016	α-MHC, change from α-MHC to β-MHC is marker for cardiac remodelling and dysfunction
Mmp2	↑	1.31	0.001	Matrix metalloproteinase 2, increased levels indicate turnover of the ECM and fibrosis
Tgfb1	↑	0.96	0.008	Transforming growth factor beta 1, activates cardiac remodelling
Myh7	↑	0.94	0.529	β-MHC, change from α-MHC to β-MHC is marker for cardiac remodelling and dysfunction
Cardiac Dysfunction				
Nppa	↑	6.20	0.001	Atrial natriuretic peptide secreted by cardiomyocytes, used as a biomarker for cardiac dysfunction
Nppb	↑	1.76	0.001	Brain natriuretic peptide secreted by cardiomyocytes, used as a biomarker for cardiac dysfunction
Ryr2	↓	-1.74	0.009	Ryanodine receptor 2, calcium release from the sarcoplasmic reticulum
Atp2a2	↓	-0.98	0.610	Sarcoplasmic reticulum calcium ATPase 2, calcium uptake from the sarcoplasmic reticulum
Cst3	↑	0.76	0.021	Cystatin C inhibitor of cysteine proteinases, biomarker of kidney function, associated with cardiac dysfunction
Top2b	↓	-0.07	0.988	DNA topoisomerase-IIβ, cardiomyocyte-specific deletion protects against DOX-induced HF

Table 7 Differential gene expression by RNA-seq of genes related to cardiac remodelling, fibrosis and dysfunction.
Rows highlighted in yellow show genes that were validated using qPCR.

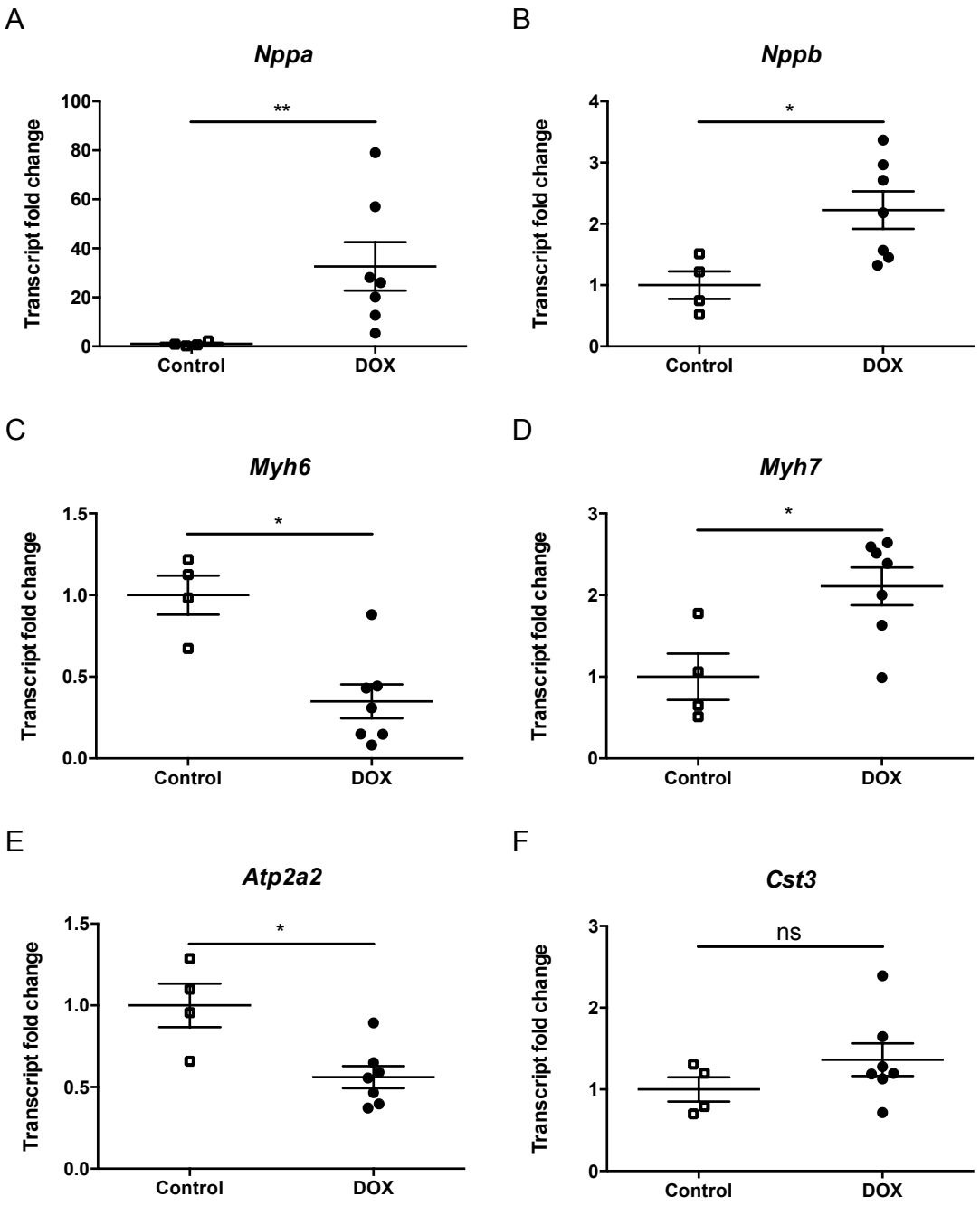


Fig. 4.10 qPCR analysis of transcript levels of genes related to cardiac remodelling and dysfunction in DOX-induced cardiomyopathy.
qPCR analysis of (A) *Nppa* (B) *Nppb* (C) *Myh6* (D) *Myh7* (E) *Atp2a2 (F) Cst3* transcript levels. Scatter plot shows transcript levels obtained for individual rats control n = 4 (clear square) DOX n = 7 (circle), which were normalised to *Hsp90ab1* and expressed as fold change relative to average of control samples. *Cst3* transcript level changes between control and DOX-treated samples were not statistically significant when assessed by qPCR with a larger sample number suggesting variability in RNA-seq data. Data is represented as mean ± *SEM*. Mann-Whitney *U* test ns = not significant **p* < 0.05 ***p* < 0.01.

4.3.5 A reduced mtDNA copy number in DOX-induced cardiotoxicity

The mitochondrial to nuclear DNA ratio was used as an estimation of mtDNA copy number (Rooney et al., 2015). This revealed a trend where relative mtDNA content decreased in DOX-treated compared to control (Fig. 4.11). However, the reduction was only statistically significant in *Mt-co3* but not in *Mt-co1* and *Mt-nd3*, possibly due to large variation in control samples and a low n number (Fig. 4.11). mtDNA encodes critical protein subunits of four out of the five mitochondrial respiratory complexes; Complex I, III, IV and V (Alexeyev et al., 2013). *Mt-co1* is the mitochondrially-encoded subunit I of cytochrome *c* oxidase (Complex IV) and Mt-co3 is the mitochondrially-encoded subunit III of cytochrome c oxidase, whereas *Cox412* is the nuclear encoded subunit IV of cytochrome *c* oxidase (Table 4). *Mt-nd3* is the mitochondrially-encoded subunit III of NADH:ubiquinone oxidoreductase (Complex I), whereas Ndufs7 is the nuclear encoded NADH:ubiquinone oxidoreductase core subunit S7 (Fig. 4.6A). Taken together, these results show a reduction in both nuclear and mitochondrially-encoded respiratory chain subunits in DOX-induced cardiotoxicity and suggest that mtDNA depletion contributes to respiratory chain defects in chronic DOX-induced cardiomyopathy. The ratio of mtDNA to myocyte DNA could also be affected by multinucleation which was not analysed in the present study. It was assumed that DOX treatment would have no effect on the number of nuclei per cell.

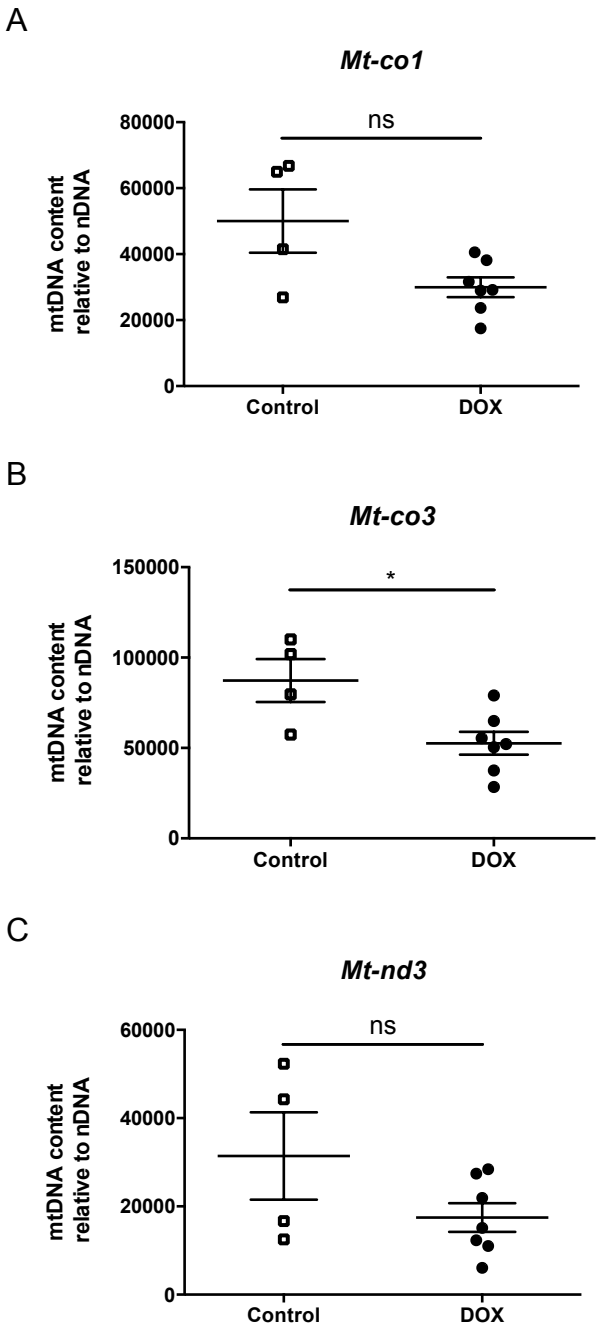


Fig. 4.11 qPCR analysis of the mitochondrial to nuclear DNA ratio which was used as an estimation of mtDNA copy number in DOX-induced cardiomyopathy.
mtDNA content relative to nuclear DNA (*Hsp90ab1*) for (A) *Mt-Co1* (B) *Mt-Co3* (C) *Mt-Nd3*. Scatter plot shows relative values obtained for individual rats control n = 4 (clear square) DOX n = 7 (circle). The mtDNA content relative to nuclear DNA for each sample was calculated as $2x2^{\Delta CT}$, where ΔCT = (nuclear DNA CT – mitochondrial DNA CT). Data is represented as mean ± *SEM*. Mann-Whitney *U* test ns = not significant **p* < 0.05.

4.4 Discussion

4.4.1 Transcriptome profiling of DOX-induced cardiomyopathy

RNA-seq of LV tissue was established as a robust tool to perform large-scale transcript profiling of a rat model of DOX-induced cardiomyopathy. All three *in silico* analyses on the RNA-seq data set indicated that in terms of gene expression, mitochondrial function and inflammation and the immune response were the most significantly affected pathways in this chronic DOX-induced cardiotoxicity model. *In silico* findings were validated using qPCR, on a larger sample size, which confirmed a significant decrease in transcript levels of genes related to mitochondrial structure and function and a significant increase in transcript levels of inflammation related genes. There appeared to be a correlation between the severity of contractile dysfunction, as assessed by the LVEF, and the Z-score of differentially expressed transcript levels. A correlation between transcript levels and the severity of contractile dysfunction suggests differential gene expression changes are affected by pathological progression or vice versa, consistent with clinical reports of the progressive nature of chronic DOX-induced cardiotoxicity (Lipshultz et al., 2005). *In silico* analysis and ontological evaluation of RNA-seq data consistently identified gene products involved in mitochondrial structure and function to be significantly decreased in DOX-induced cardiomyopathy, in agreement with well-established mitochondrial dysfunction with DOX and previous reports using microarrays to assess gene expression changes in response to chronic DOX treatment (Berthiaume and Wallace, 2007b; Zhang et al., 2012). Differential gene expression changes in both pro- and anti-apoptotic genes and ROS related genes is possibly due to a combination of induction by DOX-induced injury and a compensatory response to preserve optimal cellular function. Transcript levels of *Ryr2* and *Atp2a2*, which encode RyR2 and the SERCA2A respectively, were significantly decreased in DOX-treated samples compared to

control. DOX has been shown to have a direct effect on RyR2 and SERCA2A activity through ligand binding and redox modification resulting in a disruption to sarcoplasmic reticulum calcium handling (Hanna et al., 2014; Holmberg and Williams, 1990). Direct disruption of intracellular calcium handling leads to contractile dysfunction and is one of the proposed mechanisms of DOX-induced cardiotoxicity (Hanna et al., 2014).

4.4.2 Mitochondrial dysfunction in DOX-induced cardiomyopathy

RNA-seq analysis of LV tissue taken at sacrifice from DOX-treated animals revealed that a prominent feature of chronic DOX-induced cardiotoxicity and the onset of HF is a significant alteration in the abundance of a wide array of transcript levels of genes related to mitochondrial structure and function. A significant impact on mitochondrial performance was indicated by a decrease in transcript levels of genes associated with respiratory chain complexes, TCA cycle enzymes, inner and outer mitochondrial membrane proteins, energy metabolism and mitochondrial quality control and biogenesis, consistent with findings of functional mitochondrial impairment in murine models of chronic DOX-induced cardiotoxicity (Lebrecht et al., 2003; Zhang et al., 2012). Of note, the only genes linked to mitochondrial function that showed increased transcript levels were those involved in cell death and ROS related pathways. The transcript level results of this study and others (Berthiaume and Wallace, 2007b; Zhang et al., 2012) agree with the hypothesis of progressive uncompensated mitochondrial dysfunction in chronic DOX-induced cardiotoxicity, consistent with previous findings of progressive mitochondrial dysfunction with DOX treatment (Cove-Smith et al., 2014; Serrano et al., 1999; Zhou et al., 2001).

DOX has been shown to increase mitochondrial iron accumulation, further increasing ROS production via redox cycling within the mitochondria by directly regulating ABCB8 gene

expression (Ichikawa et al., 2014). Ichikawa *et al.* showed that DOX significantly reduced transcript and protein levels of ABCB8 and decreased or did not change levels of mitoferrin-2, a regulator of mitochondrial iron import, thereby increasing mitochondrial iron accumulation and increased ROS production in mitochondria (Ichikawa et al., 2014). In LV tissue from the present DOX-induced cardiotoxicity model transcript levels of the gene *Abcb8* were significantly decreased and transcript levels of *Slc25a28*, which encodes mitoferrin-2, were unaltered compared to control, consistent with Ichikawa *et al*.

The mtDNA copy number was reduced in DOX-treated samples compared to control in the present study, consistent with previous reports of reduced mtDNA copy with chronic DOX treatment (Adachi et al., 1993; Lebrecht et al., 2005; Lebrecht et al., 2003). Reduced Complex I activity has been reported with chronic DOX treatment (Lebrecht et al., 2003). Mitochondrial-encoded genes for subunits of Complex I and IV were both decreased in DOX-treated samples suggesting that mtDNA depletion contributes to respiratory chain defects in DOX-induced cardiomyopathy. The mechanisms involved in DOX-induced mtDNA damage remain unclear. It has been shown that DOX can directly interact with mtDNA (Ashley and Poulton, 2009b) and that intercalation causes nucleoid aggregation, inhibits mtDNA synthesis and causes mtDNA depletion (Ashley and Poulton, 2009a). It is postulated that inhibition of mitochondrial topoisomerase I (Top1mt) by DOX contributes to mtDNA damage and it has been shown that Top1mt knockdown mice are more sensitive to DOX-induced cardiotoxicity (Khiati et al., 2014). A high level of ROS within mitochondria due to redox cycling and ETC inhibition with DOX treatment is also likely to damage mtDNA. mtDNA damage leads to a decrease in the ETC proteins that are mtDNA encoded, exacerbating mitochondrial dysfunction and ROS production. Thus, DOX-induced mtDNA damage likely contributes to mitochondrial toxicity with DOX treatment.

DOX is postulated to cause cardiac mitochondrial dysfunction through its interaction with nuclear DNA topoisomerases. Cardiomyocyte-specific deletion of *Top2b* protects cardiomyocytes from DOX-induced DNA double-strand breaks and transcriptome changes that are thought to cause defective mitochondrial biogenesis and ROS formation (Zhang et al., 2012). In the present study no change in the transcript levels of *Top2b* was found.

Mitochondrial dysfunction as a result of chronic DOX treatment appears to progress from immediate biochemical disruption, via an unknown combination of multifactorial processes including redox cycling and ROS damage, direct ETC dysfunction, mtDNA damage and nuclear DNA damage via Top-2β, and accumulate in the absence of DOX with progressive dysfunction characterised by molecular changes and feedback on a transcriptional level that leads to decreased transcript levels of a variety of mitochondrial-related genes. Transcriptional changes may result in a further decline in mitochondrial integrity and cellular energy production, which ultimately results in energy compromise, a hallmark of HF (Ingwall and Weiss, 2004; Olson and Schwartz, 1951). Mitochondrial dysfunction is a critical component in the pathogenesis and phenotype of DOX-induced cardiomyopathy and is a promising therapeutic target for cardioprotection.

4.4.3 Chronic DOX treatment results in a pro-inflammatory state which triggers an immune response and ECM remodelling

RNA-seq analysis showed a significant increase in transcript levels associated with inflammation and the immune system as a result of chronic DOX treatment, consistent with findings by microarray in a chronic rat model of DOX-induced cardiotoxicity (Berthiaume and Wallace, 2007b). In the present study qPCR validation showed a significant increase in the transcript levels of *Tgfβ2*, *Il1β*, *Ccl2*, *Il18* and *Nlrp3*. DOX-induced IL-1β release has been

shown to be mediated by NLRP3 inflammasome activation in mice (Sauter et al., 2011). An increase in the transcript levels of *Myd88* and *Nlrp3* suggests TLR and NLRP3 inflammasome activation (Akira and Takeda, 2004; Schroder and Tschopp, 2010). Sauter *et al*. showed that the ability of DOX to provide pro-inflammatory "danger signals" was inhibited by co-treatment of murine bone marrow-derived macrophages with ROS inhibitors (Sauter et al., 2011). Indicating that DOX-induced inflammasome activation in macrophages is dependent on ROS production.

The NLRP3 inflammasome is a molecular platform activated upon cellular damage or infection that initiates the maturation of pro-inflammatory cytokines such as IL-1β and IL-18 which activate immune responses (Schroder and Tschopp, 2010). The NLRP3 inflammasome consists of NLRP3, the adaptor apoptosis-associated speck-like protein containing a caspase-recruitment domain (ASC) and pro-caspase-1 (Schroder and Tschopp, 2010). The protein NLRP3 contains a pyrin domain (PYD). Upon activation NLRP3 oligomerises with the PYD of ASC via a PYD-PYD interaction, which leads to the recruitment of pro-caspase-1 by ASC's caspase-recruitment domain (CARD) via CARD-CARD interaction, resulting in the active caspase-1 tetramer and successful assembly of the NLRP3 inflammasome. Inflammasome assembly and caspase-1 activation results in subsequent cleavage of pro-IL-1β and secretion of mature IL-1β (Schroder and Tschopp, 2010). The expression of pro-IL-1β requires induction via TLR-NF-κB signalling, signal 1 of the NLRP3 inflammasome activation (Bauernfeind et al., 2009). Therefore, NLRP3 inflammasome activation requires two events: the synthesis and accumulation of precursors proteins including NLRP3 and pro-IL-1β (signal 1) and the activation signal which leads to activation of caspase-1 and cleavage of pro-IL-1β to its active form (signal 2). RNA-seq analysis showed an increase in the transcript level of *Myd88,* which is necessary for TLR activation (Akira and Takeda, 2004). In addition, gene annotation analysis of RNA-seq data indicated TLR activation and an increase in NF-κB

signalling indicative of signal 1 of NLRP3 inflammasome activation. A wide array of “danger signals”, such as pathogen-associated molecular patterns and molecules that indicate cellular damage for example extracellular ATP and uric-acid crystals, activate the NLRP3 inflammasome (Franchi et al., 2010; Mariathasan et al., 2006; Schroder and Tschopp, 2010; Stutz et al., 2009). The mechanisms by which different stimuli trigger NLRP3 inflammasome activation are unknown. One model suggests that all NLRP3 agonists trigger ROS generation and this is a common pathway of NLRP3 inflammasome activation (Cassel et al., 2008; Cruz et al., 2007; Dostert et al., 2008). Mitochondria are a major site of ROS generation with DOX treatment. It has been shown that mitochondrial ROS can cause NLRP3 inflammasome activation and that agents that cause mitochondrial dysfunction enhance NLRP3 inflammasome activation (Jabaut et al., 2013; Zhou et al., 2011). Increased ROS production by cardiomyocytes during DOX treatment may trigger NLRP3 inflammasome activation in resident macrophages in the myocardium that leads to increased secretion of mature IL-1β.

Increased transcript levels of *Tgfβ2*, *Il1β*, *Ccl2*, *Il18* and *Nlrp3 and* other markers of cytokine production and an increase in transcript levels of chemotactic factors suggests chronic DOX treatment results in a prolonged inflammatory state with macrophage infiltration and fibroblast activation. Increased transcript levels of *Cd4*, *Cd80*, *Cd86* and *Ifngr1* suggest T cell activation and proliferation (Foreman et al., 1999), consistent with activation of the adaptive immune response. The initial trigger for an inflammatory response with DOX treatment is unknown. It is possible that DOX-induced ROS formation and membrane damage, mitochondrial dysfunction and/or myofibril damage triggers NLRP3 inflammasome activation and the release of pro-inflammatory cytokines. It is highly likely that myocyte necrosis and the release of ATP from dying cells as a result of DOX toxicity contributes to the stimulation of the NLRP3 inflammasome (Ghiringhelli et al., 2009; Li et al., 2009).

Although DOX-induced NLRP3 inflammasome activation likely contributes to myocardial inflammation with DOX treatment inflammasome activation may be essential for DOX's anti-tumour efficiency. Findings in mice indicate that some of DOX's efficacy against tumours relies on NLRP3 inflammasome activation (Ghiringhelli et al., 2009). ATP released from dying tumour cells, in response to DOX treatment, engages the $P2X_7$ purinergic receptors on dendritic cells to activate the NLRP3 inflammasome, which leads to the secretion of IL-1β as part of the innate immune system (Ghiringhelli et al., 2009). IL-1β is required for the priming of tumour-specific interferon-γ (IFN-γ)-producing CD8+ T cells (Ghiringhelli et al., 2009). Priming of tumour-specific IFN-γ-producing CD8+ T cells is necessary for the adaptive immune system to act against established tumours (Shankaran et al., 2001). The priming of IFN-γ-producing $CD8^+$ T cells by dying tumour cells fails in the absence of a functional IL-1 receptor 1 and in NLRP3-deficient or caspase-1-deficient mice unless exogenous IL-1β is provided (Ghiringhelli et al., 2009). Anthracycline-treated individuals with breast cancer carrying a loss-of-function allele of *P2RX7* developed metastatic disease more rapidly than individuals bearing the normal allele (Ghiringhelli et al., 2009). These results suggest that DOX-induced NLRP3 inflammasome activation induces IL-1β-dependent adaptive immunity against tumours.

RNA-seq results showed altered transcript levels of a number of genes involved in adverse tissue remodelling in DOX-treated samples including *Serpine1*, *Fn1*, *Lgals3*, *Myl4*, *Lox*, *Mmp2, Myh6, Myh7* and *Tgfb1*. An increase in transcript levels of pro-inflammatory and adverse remodelling related genes with inflammatory cell infiltration and fibroblast activation suggests chronic inflammation and adverse remodelling occur as a result of chronic DOX treatment. *Postn* transcript levels, which encode the ECM protein periostin, were significantly increased in DOX-treated compared to control in the present data set. An increase in periostin is associated with myocardial fibrosis and ventricular remodelling in human failing

hearts (Zhao et al., 2014). Periostin has also been reported to be increased in myofibroblasts in different states of cardiac injury such as myocardial infarction (Iekushi et al., 2007; Stanton et al., 2000) and in the pressure-overloaded heart (Oka et al., 2007) and may serve as a marker for activated fibroblasts following cardiac injury. Increased transcript levels of *Postn* in DOX-induced cardiotoxicity are consistent with the presence of myofibroblasts and ECM remodelling. To confirm the presence of myofibroblasts with chronic DOX treatment it would be necessary to stain for the presence of α-smooth muscle actin, a protein predominately expressed in smooth muscle cells, which is not found in "healthy" fibroblasts but is expressed in myofibroblasts in the infarcted and remodelling myocardium (Frangogiannis et al., 2000).

Together, these data confirm that chronic DOX treatment induces a prolonged inflammatory state and adverse ventricular remodelling. This is consistent with changes in transcript levels of inflammatory and immune genes, including ECM proteins involved in tissue remodelling, previously reported to be associated with the phenotype of progressive HF in gene array data (Sharma et al., 2005). Although inflammation is necessary for DOX's anti-tumour efficiency it is associated with adverse myocardial remodelling and impaired cardiac function. Therefore, any therapeutic interventions should focus on the inhibition of adverse consequences of pathological inflammation such as fibrosis rather than untargeted inhibition of inflammation.

4.4.4 Limitations and future directions

For transcriptome analysis whole tissue from the left ventricle of the heart was used for RNA extraction. The gene expression data and mtDNA copy number estimation may, therefore, be skewed by different cell types present in the myocardium and does not represent transcript changes in myocytes alone. To investigate myocyte specific changes in gene expression it would be necessary to isolate myocytes from DOX-treated whole hearts. Transcriptome

analysis is limited by the fact that it does not take into account regulation of gene expression or any post-translational modifications and, therefore, transcript levels do not represent protein expression. To further characterise and validate RNA-seq analysis it would be necessary to analysis protein expression in LV tissue. Performing transcriptome analysis only at the final time point means the progressive mechanistic gene changes are unknown and can only be inferred by previous findings. It would be interesting to see if the current findings of transcript changes related to mitochondrial dysfunction and inflammation are progressive and at what point during DOX administration they begin. To investigate gene expression and protein changes in depth it would be necessary to conduct the same chronic study but as a time course with gene expression analysis at different time points during the progression of DOX-induced cardiomyopathy. It would also be informative to explore if gene expression changes could be halted with fewer doses of DOX.

4.4.5 Conclusion

RNA-seq analysis identified a decrease in transcript levels of genes related to mitochondrial function and structure and an increase in transcript levels of genes related to inflammation, the immune response and ECM remodelling in DOX-induced cardiotoxicity. This data highlights the significant contribution of mitochondrial dysfunction and inflammation to the pathogenesis and phenotype of DOX-induced cardiomyopathy. These findings of significant mitochondrial dysfunction, that likely contributes to the HF seen with chronic DOX treatment, re-iterates the importance of direct mitochondrially-targeted protective strategies which may have the potential to protect the heart. However, it is highly likely that some of DOX's anti-tumour efficiency lies in its mitochondrial toxicity, therefore, mitochondrially-targeted protective strategies should be specifically targeted to cardiac mitochondria.

Chapter 5

The acute effect of DOX on cardiac mitochondria in isolated ARVM

Chapter 5 The acute effect of DOX on cardiac mitochondria in isolated ARVM

5.1 Introduction

The development and application of robust techniques to quantify and study mitochondrial function in real-time in intact cells is a major goal of bioenergetic research. Studying mitochondrial function in intact cells avoids artefacts due to mitochondrial isolation or cell permeabilisation and offers greater physiological relevance than isolated mitochondria. Generally, cells maintain a bioenergetic reserve capacity that is hypothesised to be required by cells to respond to stress and when this bioenergetic reserve is depleted by mitochondrial damage or dysfunction pathophysiological events occur (Hill et al., 2009). The bioenergetic reserve is, therefore, seen as an index of healthy mitochondrial populations. By assessing the bioenergetic reserve and stimulating “maximal” respiration of mitochondrial populations it can reflect differences between healthy and dysfunctional mitochondria.

To study mitochondrial function in intact cells methods have been developed to measure the OCR of cells in real-time. Assays that assess changes in the OCR in response to the addition of respiratory inhibitors can be used as an indirect measure of mitochondrial function. One such assay is the Mito Stress Test which makes use of sequential addition of pharmacological inhibitors of oxidative phosphorylation to assess mitochondrial function by measuring oxygen levels in the medium (Brand and Nicholls, 2011). Changes in oxygen concentration in the medium are assessed using oxygen-dependent fluorescence quenching (Gerencser et al., 2009). In the first series of measurements, usually performed over approximately 25 min depending on the machine used, the basal OCR of the cells is established. The basal OCR represents basal respiration; the net sum of all processes capable of consuming oxygen, including mitochondrial function and other oxidases.

Oligomycin is then injected. Oligomycin inhibits ATP synthase (Complex V) by blocking its proton channel. In most cell types oligomycin injection results in a decrease in the OCR correlated to the cellular ATP production by ATP synthase. Following oligomycin, FCCP is injected to estimate the "maximal" respiration of mitochondria (FCCP-stimulated maximal respiration) as an index of mitochondrial respiratory capacity. FCCP is a proton ionophore which permeabilises the IMM to hydrogen ions, destroying the proton gradient and disrupting the $\Delta\Psi_m$ (less polarised). Thus, electron flow through the ETC is uninhibited and oxygen is maximally consumed by Complex IV. Immediately upon exposure to the uncoupler, the OCR increases as the IMM becomes permeable to protons and electron transfer is no longer controlled by the proton gradient. Next, antimycin A in combination with rotenone is injected. Antimycin A blocks Complex III while rotenone blocks Complex I. Combined antimycin A and rotenone injection results in a drop in the OCR as the ETC can no longer function and mitochondrial respiration is inhibited.

The Mito Stress Test has previously been used to show a significantly lower basal respiration rate and FCCP-stimulated maximal respiration in patient-specific human induced pluripotent stem cell-derived cardiomyocytes (hiPSC-CMs) from breast cancer patients who suffered clinical DOX-induced cardiotoxicity compared to hiPSC-CMs from healthy control subjects (Burridge et al., 2016). hiPSC-CMs from patients who suffered DOX-induced cardiotoxicity showed decreased ATP activity and fewer mitochondria compared to hiPSC-CMs from control subjects, consistent with a decrease in mitochondrial function with DOX treatment (Burridge et al., 2016).

The typical Mito Stress Test profile differs between cell types (Hill et al., 2012). It has been previously reported that ARVM do not show a drop in the OCR following injection of oligomycin (Hill et al., 2012; Yancey et al., 2015). The reason why oligomycin has no effect on

the OCR of ARVM remains unknown. It is hypothesised that isolated cardiomyocytes in culture are not contracting as *in vivo* and, therefore, the activity of ATP synthase required to supply the ATP demand is very low and, thus, the effect of oligomycin on mitochondrial respiration is minimal (Hill et al., 2012).

MitoQ is a mitochondrially-targeted anti-oxidant which has been shown to be protective against DOX-induced cardiotoxicity *in vivo* (Chandran et al., 2009*)*. In isolated ARVM MitoQ pre-treatment at 50 nM was found to protect against stretch-induced mitochondrial dysfunction (Yancey et al., 2015). Given the extent of mitochondrial dysfunction reported in chronic models of DOX-induced cardiotoxicity and the proposed role of ROS in DOX-induced mitochondrial toxicity (Berthiaume and Wallace, 2007a; Davies and Doroshow, 1986; Doroshow and Davies, 1986; Min et al., 2015; Mukhopadhyay et al., 2009) in the present study the effect of 24 h DOX treatment with and without MitoQ on mitochondrial function in freshly isolated ARVM was investigated using the Mito Stress Test.

Reduced FCCP-stimulated maximal respiration compared to control is indicative of mitochondrial dysfunction. Early changes in mitochondrial function may lead to cellular signalling that stimulates altered transcription. Altered transcript levels of mitochondrial related genes may affect mitochondrial function over time with DOX treatment, therefore, transcript levels of mitochondrial related genes were investigated following 24 h DOX treatment of ARVM.

5.2 Hypothesis and aims

I hypothesis that acute 24 h DOX treatment of ARVM alters cardiac mitochondrial function and gene expression and that MitoQ may protect against changes in cardiac mitochondrial function induced by 24 h DOX treatment.

The aims of this chapter are as follows:

1. Establish an *in vitro* model to assess the effect of 24 h anti-cancer agent treatment on cardiac mitochondrial function in isolated ARVM using the Mito Stress Test
2. Examine the effect of 24 h DOX treatment with and without MitoQ on cardiac mitochondrial function in ARVM using the Mito Stress Test
3. Assess transcriptome changes related to cardiac and mitochondrial function in response to 24 h DOX treatment in ARVM

5.3 Results

5.3.1 *In vitro* assessment of cardiac mitochondrial function in isolated ARVM

To assess cardiac mitochondrial function in response to anti-cancer agent treatment over 24 h it was necessary to establish the cellular density necessary for the optimal basal respiration of ARVM in the Seahorse XFp Extracellular Flux Analyser. Freshly isolated ARVM were plated at different cell densities for 24 h prior to measurement of the basal OCR. The optimal basal OCR for the XFp analyser is reported to be between 20-150 pmol O_2/min (XFp Intro. Training Manual Cell Characterisation & Stress Tests, Agilent Technologies Inc., USA). 250 ARVM per well was found to be the optimal cellular density to produce an OCR within this range (Fig. 5.1A). To assess cardiac mitochondrial function the Mito Stress Test (Fig. 5.1B) was used with concentrations of oligomycin, FCCP, rotenone and antimycin A (1, 1, 1 and 10 μM, respectively) that had previously been optimised in isolated ARVM (Yancey et al., 2015). These concentrations were found to be sufficient to produce the expected profile of the Mito Stress Test with ARVM (Fig. 5.1C). Oligomycin had no effect on the OCR of ARVM, consistent with previous reports (Hill et al., 2012; Yancey et al., 2015). Cardiomyocytes plated at this cellular density were found to have a significant FCCP-stimulated maximal respiration compared to time-matched vehicle treated control (Fig. 5.1C). FCCP-stimulated maximal respiration was ceased by injection of antimycin A and rotenone, showing that the FCCP-stimulated maximal respiration reflects the mitochondrial respiratory capacity and can, therefore, be used as an assessment of cardiac mitochondrial function. The raw OCR was corrected for total protein present in each well to account for differences in cell number between wells (Fig. 5.1D). The total protein corrected OCR was normalised to basal respiration in order to examine differences between treated and control for FCCP-stimulated maximal respiration as a fold change from basal respiration (Fig. 5.1E). These findings

suggest that the Mito Stress Test performed in isolated ARVM using a XFp analyser can be used as a method to assess cardiac mitochondrial function. The OCR was not assessed on freshly isolated ARVM in the present study. It was only assessed followed culture for 24 h. Of note “n” in this chapter refers to the number of hearts used (number of isolations from which ARVM were obtained and used for the experimental protocol).

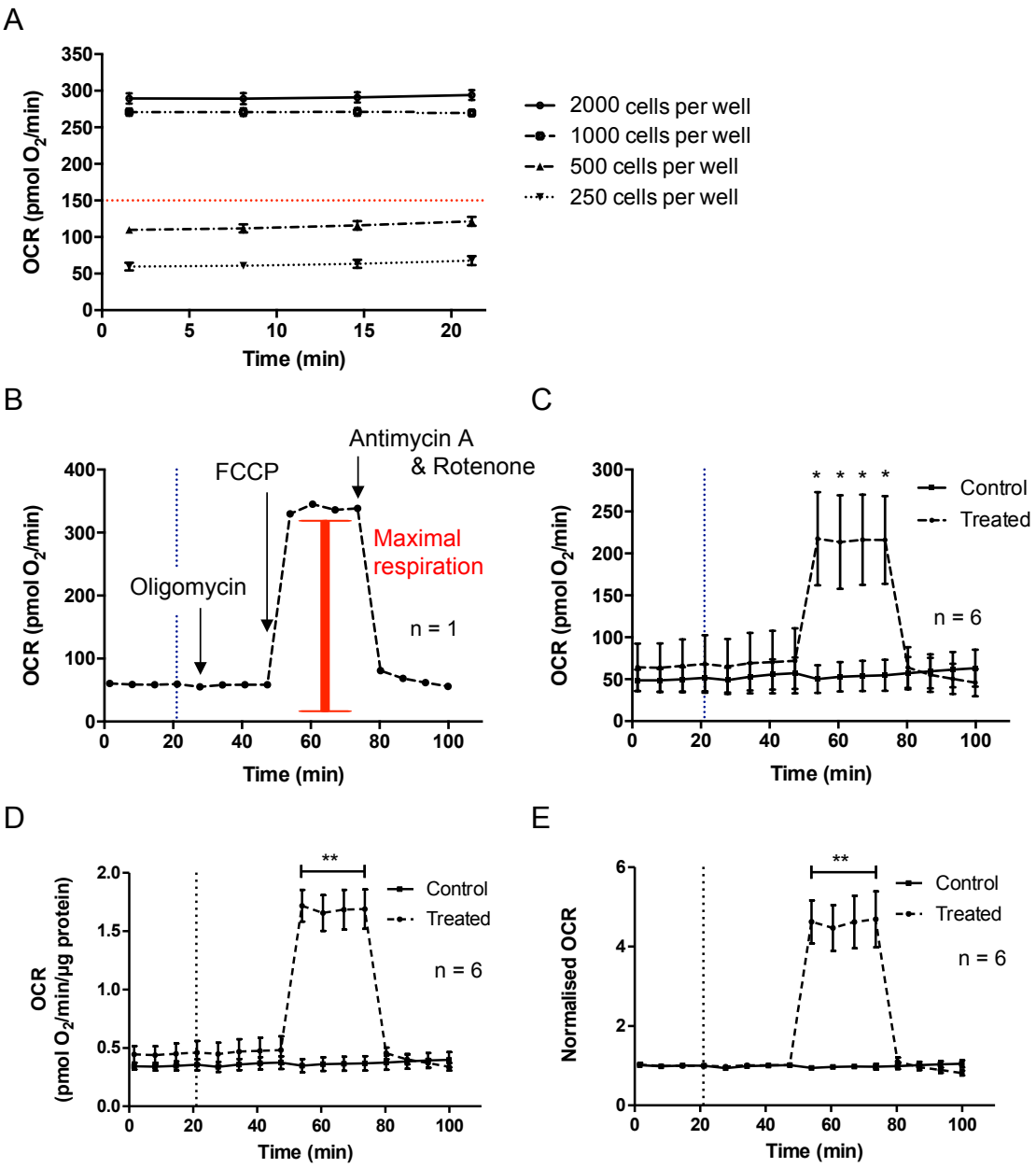


Fig. 5.1 The OCR of ARVM measured during the Mito Stress Test using a Seahorse XFp analyser. (A) The basal OCR (pmol O_2/min) of ARVM plated at 250, 500, 1000 and 2000 cells per well. Red dashed line indicates the maximum recommended basal OCR; 150 pmol O_2/min. Three technical replicates (B) The OCR of ARVM during the Mito Stress Test showing the FCCP-stimulated maximal respiration which was abolished by antimycin A and rotenone injection n = 1 (C) The OCR of ARVM during the Mito Stress Test showing a significant increase in the OCR during FCCP-stimulated maximal respiration (dashed line) compared to time-matched vehicle control (black line) n = 6 (D) The total protein corrected OCR of ARVM during the Mito Stress Test n = 6 (E) The normalised OCR of ARVM during the Mito Stress Test n = 6. Blue dashed line indicates baseline. Data is represented as mean ± *SEM*. Mann-Whitney *U* test *$p < 0.05$ **$p < 0.01$ compared to control.

The Seahorse XFp analyser uses fluorescence to measure the OCR of cells and since DOX itself is a fluorescent compound (Karukstis et al., 1998; Motlagh et al., 2016) it was necessary to assess the fluorescence of DOX in the XFp analyser. Initially, DOX itself was injected at 1, 3, 10 and 30 μM with no cells, as a control experiment. The OCR increased in a concentration-dependent manner showing that the fluorescence of DOX interfered with the measurement of oxygen in the XFp analyser (Fig. 5.2A). DOX 10 μM with and without MitoQ was incubated in wells with no cells for 24 h before the Mito Stress Test was performed, as a control experiment. Prior to the Mito Stress Test the medium was changed to DOX free XFp medium, as per the standard experimental protocol. The OCR between control and treatment with no cells showed that the fluorescence of DOX did not interfere with the assay when DOX was incubated in wells as a pre-treatment before conducting the Mito Stress Test (Fig. 5.2B). This data suggests that DOX's autofluorescence interferes with the measurement of oxygen in the XFp analyser when it is present in the assay medium but when DOX is incubated for 24 h and then removed before the Mito Stress Test it does not interfere with the OCR measurement. Therefore, the XFp analyser and the Mito Stress test can be used to assess cardiac mitochondrial function in isolated ARVM following 24 h DOX treatment with and without MitoQ.

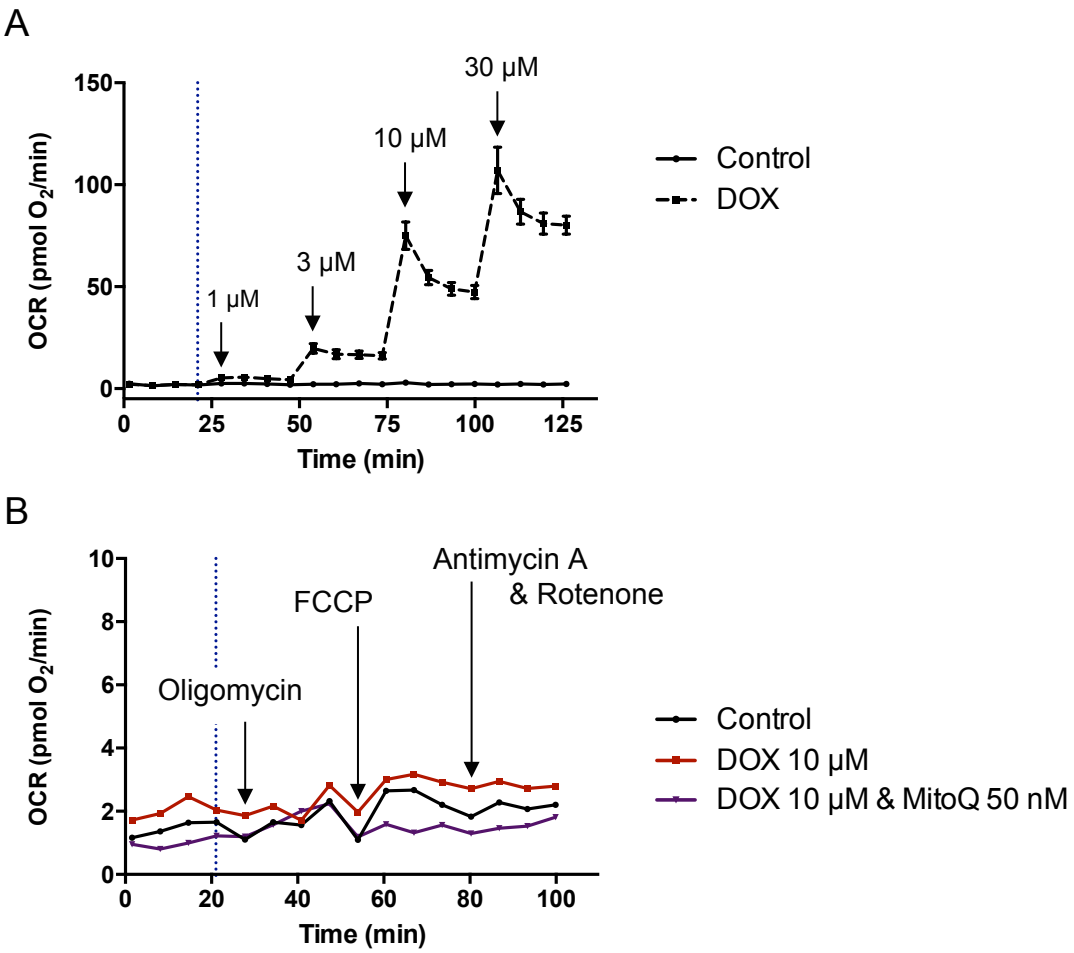


Fig. 5.2 The OCR in control experiments examining the effect of DOX's fluorescence on the measurement of oxygen by the Seahorse XFp analyser with no cells present.
(A) The OCR with injection of DOX at 1, 3, 10 and 30 µM (dashed line) compared to time-matched vehicle control (black line) with no cells present. Three technical replicates. Data is represented as mean ± *SEM*
(B) The OCR during the Mito Stress test of wells with no cells incubated with DOX 10 µM alone (cayenne line) or with MitoQ 50 nM (purple line) for 24 h prior to the Mito Stress Test compared to time-matched vehicle control. Two technical replicates. Data is represented as mean only. Blue dashed line indicates baseline.

5.3.2 The effect of 24 h DOX treatment on the mitochondrial respiratory capacity of ARVM

To assess the acute effect of DOX treatment on cardiac mitochondrial function freshly isolated ARVM were incubated for 24 h with DOX 3 μM alone, a concentration reflective of the peak plasma concentration in patients receiving DOX (approximately 1-3 μM) (Barpe et al., 2010; Muller et al., 1993), or DOX 3 μM with MitoQ 50 nM. In addition, as DOX-induced cardiotoxicity is reported to be dose-dependent in patients (Jensen et al., 2002; Lefrak et al., 1973; Mulrooney et al., 2009; Swain et al., 2003; Von Hoff et al., 1979) 10 μM of DOX was used for myocyte treatment over 24 h to assess concentration-dependent effects of DOX. Following 24 h DOX 3 μM alone or DOX 3 μM with MitoQ 50 nM treatment the medium was changed to DOX free medium and the Mito Stress test was performed. There was no significant difference in the FCCP-stimulated maximal respiration between DOX-treated and control ARVM, suggesting that DOX 3 μM over 24 h in this assay does not impair mitochondrial function (Fig. 5.3). Similarly, DOX 3 μM treatment in combination with MitoQ 50 nM had no significant effect on mitochondrial function compared to DOX-treated alone or control ARVM. Freshly isolated ARVM were incubated with DOX 10 μM alone or DOX 10 μM with MitoQ 50 nM for 24 h. After 24 h treatment the medium was changed to DOX free medium and the Mito Stress test was performed. There was a significant decrease in the FCCP-stimulated maximal respiration in DOX 10 μM alone and DOX 10 μM with MitoQ 50 nM treated ARVM compared to time-matched vehicle control (Fig. 5.4). There was no significant difference between DOX 10 μM alone and DOX 10 μM with MitoQ 50 nM treatment (Fig. 5.4D). Overall, these findings show that DOX 3 μM treatment over 24 h had no effect on the mitochondrial respiratory capacity of ARVM assessed using FCCP-stimulated maximal respiration. In contrast DOX 10 μM treatment over 24 h caused a significant decrease in the FCCP-stimulated maximal respiration of ARVM compared to time-matched vehicle control

suggesting mitochondrial dysfunction with DOX 10 μM treatment. MitoQ treatment at 50 nM with DOX 10 μM did not protect against DOX-induced mitochondrial dysfunction in the present study.

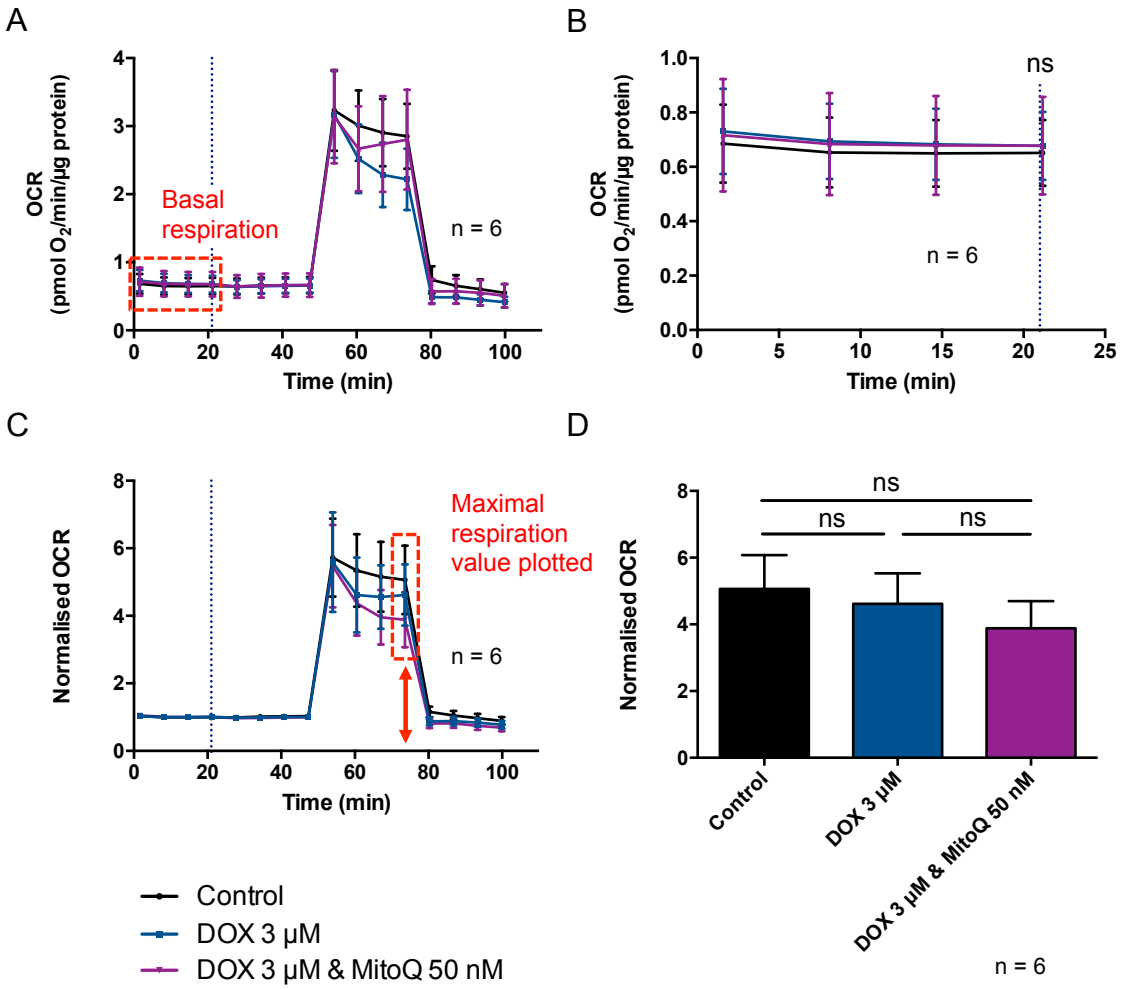


Fig. 5.3 Assessing cardiac mitochondrial function in isolated ARVM with 24 h DOX 3 µM treatment.
(A) The total protein corrected OCR of ARVM treated for 24 h with DOX 3 µM alone (blue line) or DOX 3 µM with MitoQ 50 nM (purple line) compared to control (black line) during the Mito Stress Test n = 6. Red dashed rectangle indicates basal respiration (B) The basal OCR showing no difference in oxygen consumption at baseline between groups n = 6 (C) The normalised OCR during the Mito Stress Test showing the FCCP-stimulated maximal respiration value as a fold change from basal respiration plotted between groups (red dashed rectangle) n = 6 (D) The normalised OCR of FCCP-stimulated maximal respiration between groups n = 6. Blue dashed line indicates baseline. Data is represented as mean ± *SEM*. Kruskal-Wallis test with Dunn's multiple comparisons test ns = not significant compared to control.

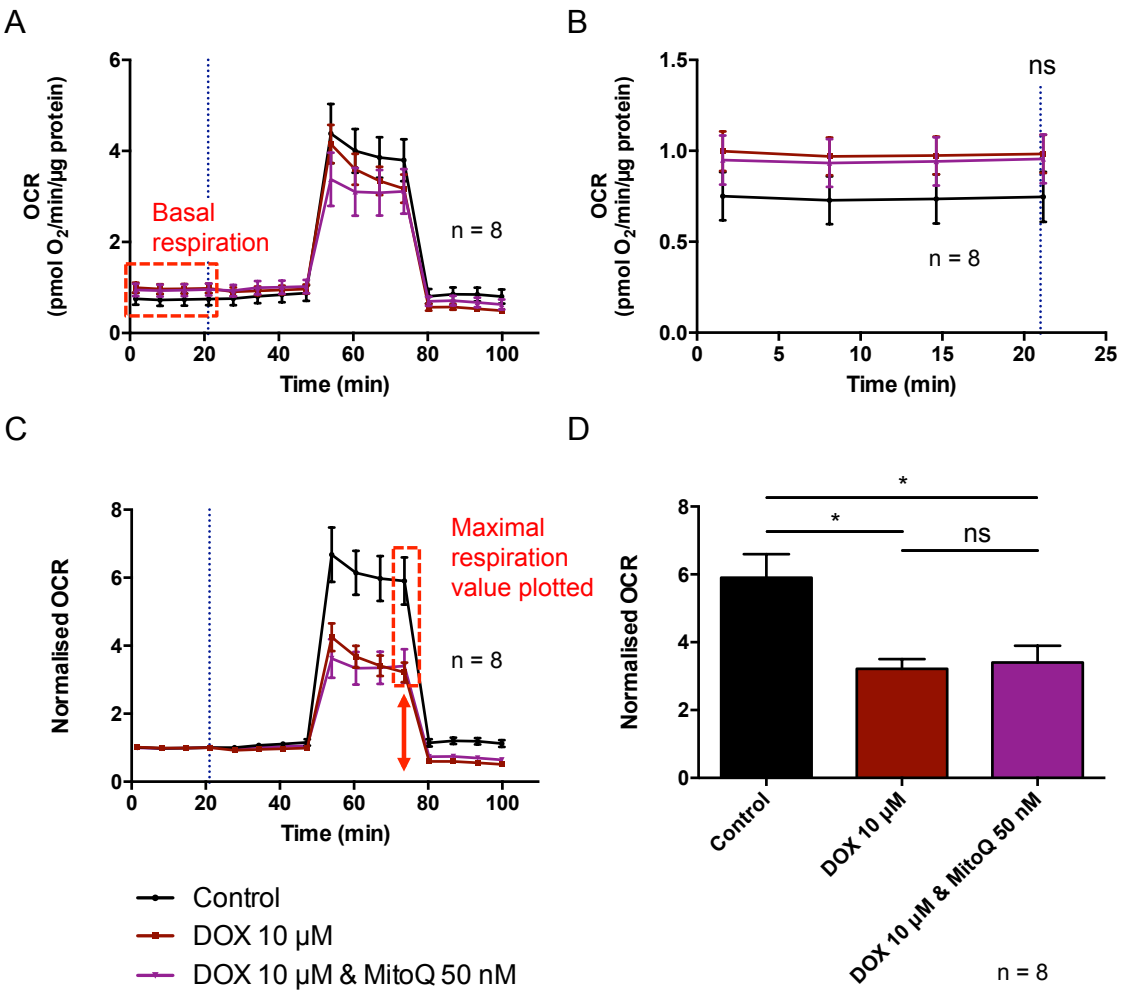


Fig. 5.4 Assessing cardiac mitochondrial function in isolated ARVM with 24 h DOX 10 µM treatment.
(A) The total protein corrected OCR of ARVM treated for 24 h with DOX 10 µM alone (cayenne line) or DOX 10 µM with MitoQ 50 nM (purple line) compared to control (black line) during the Mito Stress Test n = 8. Red dashed rectangle indicates basal respiration (B) The basal OCR showing no difference in oxygen consumption at baseline between groups n = 8 (C) The normalised OCR during the Mito Stress test showing the FCCP-stimulated maximal respiration value as a fold change from basal respiration plotted between groups (red dashed rectangle) n = 8 (D) The normalised OCR of FCCP-stimulated maximal respiration between groups n = 8. Blue dashed line indicates baseline. Data is represented as mean ± *SEM*. Kruskal-Wallis test with Dunn's multiple comparisons test ns = not significant **p* < 0.05 compared to control.

5.3.3 Differential gene expression following 24 h DOX treatment in ARVM

To investigate acute myocyte specific transcript changes in response to DOX treatment, ARVM were treated with DOX 3 or 10 μM for 24 h. The effect of DOX treatment on transcript levels of genes related to cardiac and mitochondrial function was assessed. The trend in transcript levels changes after 24 h DOX 3 or 10 μM treatment was similar, but for the majority of transcripts examined statistically significant changes were only observed with DOX 10 μM treatment (Fig. 5.5, Fig. 5.6 & Fig. 5.7) with the exception of *Cycs* transcript levels which showed significantly increased levels after 24 h DOX 3 or 10 μM treatment (Fig. 5.5D). Transcript levels of genes that encode components of the respiratory chain complexes necessary for oxidative phosphorylation including *Nduf7* (Complex I), *Sdhb* (Complex II), *Cyc1* (Complex III), *Cycs* (Cytochrome C) and *Atp5a1* (Complex V) were all significantly increased by 24 h DOX 10 μM treatment (Fig. 5.5). *Abcb8* transcript levels, encoding an ATP-dependent transporter protein necessary for mitochondrial iron export, were significantly increased by 24 h DOX 10 μM treatment (Fig. 5.6A). *Bnip3* transcript levels, encoding a mitochondrial pro-apoptotic protein, were increased, but not significantly, by 24 h DOX treatment (Fig. 5.6B). *Acadm* transcript levels were significantly increased by 24 h DOX 10 μM treatment (Fig. 5.6C). *Acadm* transcripts encode acyl-CoA dehydrogenase, which functions during the initial step of mitochondrial fatty acid β-oxidation. Mean *Ppargc1a* transcript levels were decreased, but not significantly, by DOX treatment (Fig. 5.6D). The protein encoded by *Ppargc1a* is a transcriptional co-activator involved in energy metabolism and mitochondrial biogenesis. Both *Xdh* (pro-ROS) and *Hmox1* (anti-oxidant) transcript levels were significantly decreased by 24 h DOX 10 μM treatment (Fig. 5.6E & F). *Xdh* encodes xanthine dehydrogenase which is involved in the oxidative metabolism of purine and is associated with ROS production (Maia et al., 2005). *Hmox1* encodes heme oxygenase 1 which functions during the oxidative degradation of heme and is proposed to be protective

against ROS (Gozzelino et al., 2010; Turkseven et al., 2005). *Nppa* transcript levels were significantly increased by 24 h DOX 10 μM treatment (Fig. 5.7A), however *Nppb* transcripts were not significantly altered by treatment (Fig. 5.7B). *Atp2a2* transcript levels were significantly increased by 24 h DOX 10 μM treatment (Fig. 5.7C). Overall, these findings suggest that a prominent feature of 24 h DOX 10 μM treatment is a significant increase in the abundance of transcripts related to their subcellular location and function within mitochondria. Significantly increased transcript levels of *Nppa* indicate DOX treatment over 24 h causes myocyte dysfunction with significantly altering transcript levels of genes that affect mitochondrial function, ROS and calcium homeostasis.

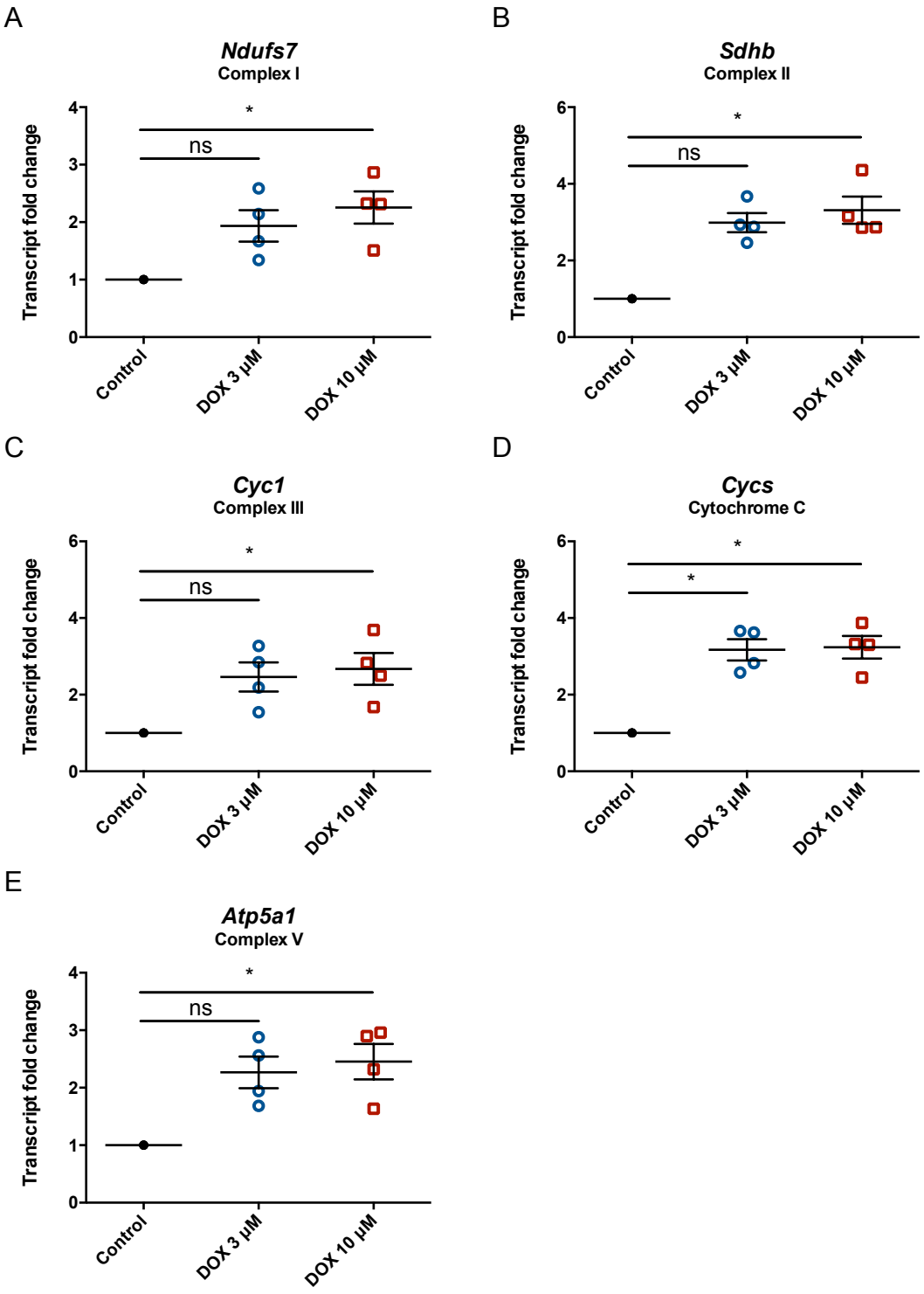


Fig. 5.5 qPCR analysis of transcript levels of genes related to the respiratory chain complexes following 24 h DOX treatment in ARVM.
qPCR analysis of (A) *Ndufs7* (B) *Sdhb* (C) *Cyc1* (D) *Cycs* (E) *Atp5a1* transcript levels. Scatter plot shows transcript levels obtained for n = 4 isolations following 24 h treatment which were normalised to *Hsp90ab1* and expressed as fold change relative to control for each isolation. Control (black circle), DOX 3 µM (blue circle outline) and DOX 10 µM (red square outline). Data is represented as mean ± *SEM*. Kruskal-Wallis test with Dunn's multiple comparisons test ns = not significant **p* < 0.05 compared to control.

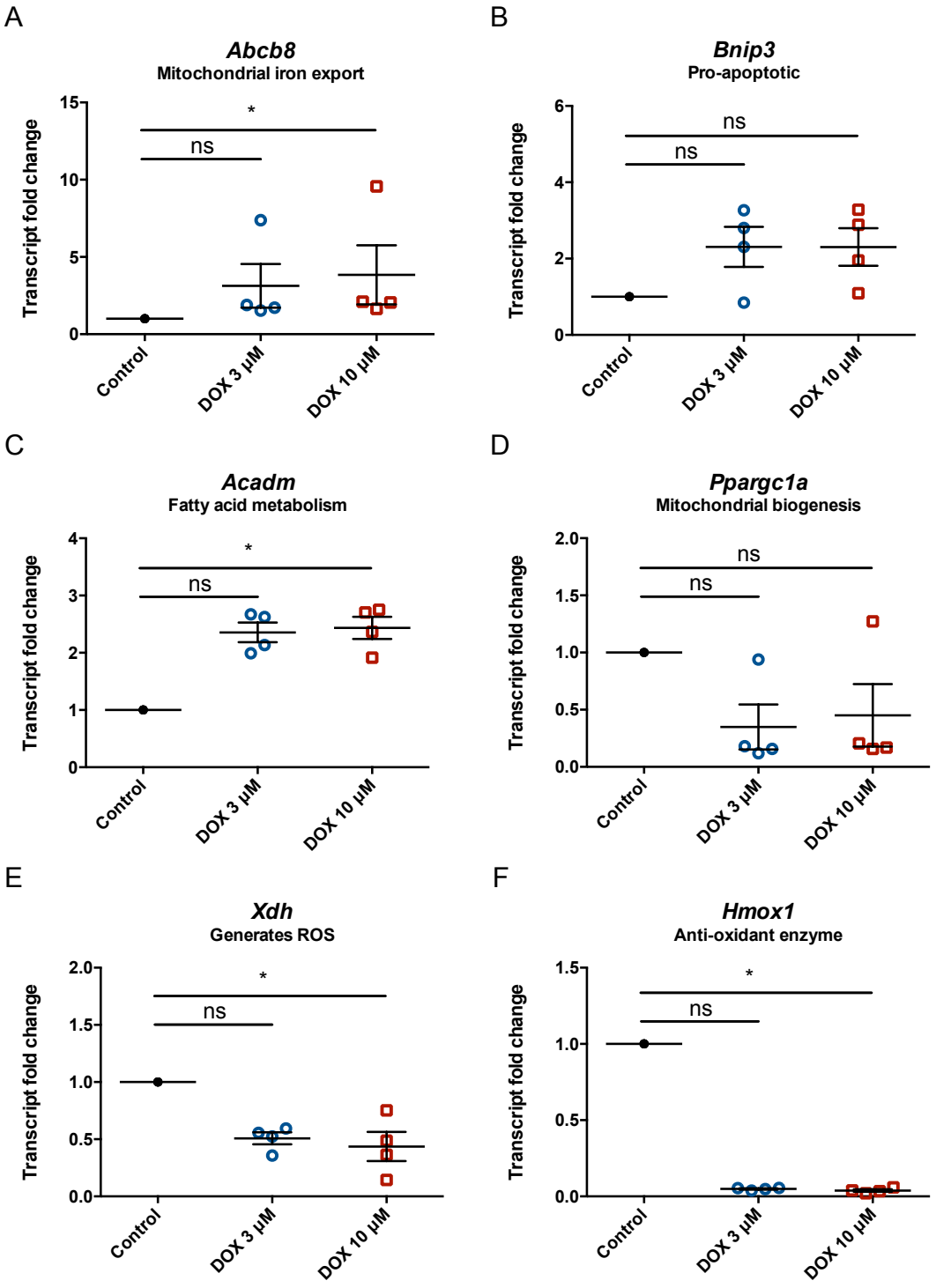


Fig. 5.6 qPCR analysis of transcript levels of genes related to the mitochondrial function and ROS production following 24 h DOX treatment in ARVM.
qPCR analysis of (A) *Abcb8* (B) *Bnip3* (C) *Acadm* (D) *Ppargc1a* (E) *Xdh* (F) *Hmox1* transcript levels. Scatter plot shows transcript levels obtained for n = 4 isolations following 24 h treatment which were normalised to *Hsp90ab1* and expressed as fold change relative to control for each isolation. Control (black circle), DOX 3 µM (blue circle outline) and DOX 10 µM (red square outline). Data is represented as mean ± *SEM*. Kruskal-Wallis test with Dunn's multiple comparisons test ns = not significant **p* < 0.05 compared to control.

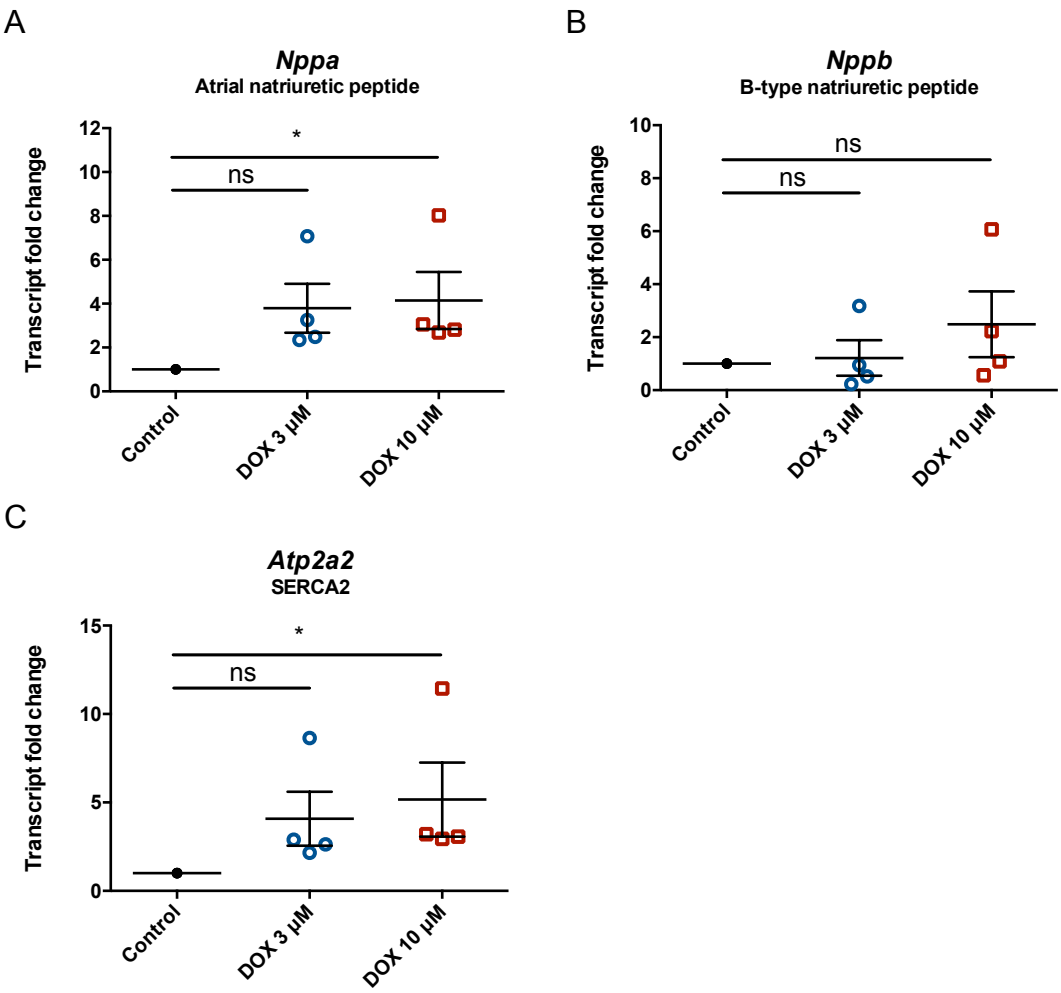


Fig. 5.7 qPCR analysis of transcript levels of genes related to cardiac dysfunction following 24 h DOX treatment in ARVM.
qPCR analysis of (A) *Nppa* (B) *Nppa* (C) *Atp2a2* transcript levels. Scatter plot shows transcript levels obtained for n = 4 isolations following 24 h treatment which were normalised to *Hsp90ab1* and expressed as fold change relative to control for each isolation. Control (black circle), DOX 3 µM (blue circle outline) and DOX 10 µM (red square outline). Data is represented as mean ± *SEM*. Kruskal-Wallis test with Dunn's multiple comparisons test ns = not significant **p* < 0.05 compared to control.

5.4 Discussion

5.4.1 *In vitro* assessment of cardiac mitochondrial function in isolated ARVM

Freshly isolated ARVM cultured over 24 h showed a significant FCCP-stimulated maximal respiration compared to time-matched vehicle control and a typical OCR profile during the Mito Stress Test. A significant increase in respiration in response to FCCP can be used as an index of mitochondrial respiratory capacity and a read-out of cardiac mitochondrial function in ARVM.

Control experiments, in the absence of cells, to examine the use of DOX in the XFp analyser showed DOX's fluorescence interfered with the OCR measurement when present in the assay medium. This suggests that when present in the medium DOX's fluorescence blocks the ability of the XFp analyser to measure oxygen, resulting in a false increase in the OCR. 24 h incubation of DOX, with and without MitoQ, followed by a change in the medium to DOX-free medium prior to the Mito Stress Test showed no difference in the OCR compared to control. This data suggests that pre-treatment with DOX does not affect the ability of the XFp analyser to measure oxygen. Therefore, the Mito Stress Test was used to assess cardiac mitochondrial function in isolated ARVM pre-treated with DOX for 24 h.

5.4.2 The effect of 24 h DOX treatment on the mitochondrial respiratory capacity of ARVM

DOX 3 μM treatment over 24 h had no effect on the mitochondrial respiratory capacity of ARVM, whereas 24 h treatment of DOX 10 μM resulted in a significant decrease in the FCCP-stimulated maximal respiration of ARVM compared to time-matched vehicle control.

This data suggests that 24 h DOX 10 μM treatment results in impaired cardiac mitochondrial function. A lower respiratory capacity compared to control indicates that mitochondrial mass and/or integrity is compromised in DOX 10 μM-treated ARVM. DOX 3 μM treatment over 24 h had no effect on the mitochondrial respiratory capacity of ARVM. This suggests that there is a threshold of mitochondrial damage that leads to the observed decrease in mitochondrial function with DOX 10 μM treatment. DOX treatment over 24 h may not cause mitochondrial dysfunction at 3 μM. DOX-treated cells are placed in DOX-free medium 1 h before the Mito Stress Test, therefore, it is possible that mitochondria exposed to and damaged by 24 h DOX treatment at 3 μM can recover. It is also possible that DOX 3 μM-treated cells can maintain normal function despite mitochondrial damage, whereas DOX 10 μM treatment damages mitochondria beyond the threshold of uncompromised function as assessed using the Mito Stress Test. Treatment of NRVM with DOX 10 μM for 16 h resulted in a significant reduction in the FCCP-stimulated maximal respiration compared to control (Ichikawa et al., 2014), consistent with the present findings. A decrease in cardiac mitochondrial function with acute DOX treatment suggests that energy compromise and mitochondrial dysfunction is an early characteristic of DOX-induced cardiotoxicity.

Twenty-four h DOX 10 μM treatment in combination with MitoQ 50 nM treatment did not protect against a significant decrease in the FCCP-stimulated maximal respiration compared to DOX treated alone in ARVM. This suggests that MitoQ at this concentration is not protective against DOX-induced mitochondrial dysfunction as assessed using the Mito Stress Test. MitoQ pre-treatment at the same concentration of 50 nM was found to prevent an increase in xanthine oxidase activity and mitochondrial swelling induced by 3 h cyclical stretching of isolated ARVM (Gladden et al., 2011). The uptake of MitoQ into mitochondria is dependent on the $\Delta\Psi_m$ (-150 to -180 mV) (Murphy, 1997; Smith et al., 2004). If DOX treatment causes an immediate and significant depolarisation of the $\Delta\Psi_m$ this will limit or even prevent

the uptake of MitoQ into mitochondria. To overcome depolarisation of the $\Delta\Psi_m$ it would be necessary to use a much higher concentration of MitoQ and to pre-treat cells with MitoQ before exposing them to DOX in order to see protection. Therefore, in the present study no protective effect with MitoQ may be due to $\Delta\Psi_m$ depolarisation which prevents the uptake of MitoQ into mitochondria.

5.4.3 Differential gene expression following 24 h DOX treatment in ARVM

Twenty-four h DOX 10 μM treatment resulted in a significant increase in transcript levels of mitochondrial related genes including those that function in the respiratory chain, fatty acid metabolism and cardiac mitochondrial iron export. Acute DOX 15 mg/kg administration *in vivo* in mice has previously been shown to cause a significant increase in transcript levels of myocardial ETC genes at early time points including 24 h after a single acute dose (Pointon et al., 2010), consistent with the present study in isolated cardiomyocytes. A significant increase in transcript levels of mitochondrial related genes was accompanied by a significant decrease in FCCP-stimulated maximal respiration at the same time point in isolated ARVM. This suggests that acute DOX treatment causes mitochondrial damage or loss that triggers a compensatory increase in transcript levels of genes related to mitochondrial function and the ETC.

Although 24 h DOX 3 μM treatment showed a similar trend in differential transcript levels compared to DOX 10 μM treatment, findings with DOX 3 μM treatment were not statistically significant compared to control with the exception of *Cycs* transcripts. This suggests that although 24 h DOX 3 μM treatment was not found to decrease cardiac mitochondrial function, as assessed using the Mito Stress Test, it does affect transcript levels related to mitochondrial function, ROS and calcium homeostasis and transcript levels of *Nppa*.

Significant differences between control and DOX 10 μM and a similar trend between control and DOX 3 μM is consistent with concentration-dependent myocyte dysfunction with acute DOX treatment. This is in agreement with clinical reports of the dose-dependent nature of DOX-induced cardiotoxicity (Jensen et al., 2002; Lefrak et al., 1973; Mulrooney et al., 2009; Swain et al., 2003; Von Hoff et al., 1979).

Twenty-four h DOX 10 μM treatment caused a significant decrease in both *Xdh* and *Hmox1* transcript levels. The reason why both pro- and anti-ROS related transcript levels would both be decreased with acute DOX treatment is unclear. It is possible that a reduction in *Xdh* transcript levels is due to increased ROS with DOX that stimulates a compensatory response to reduce ROS levels. Why *Hmox1* transcript levels, which encode the cardioprotective stress-inducible enzyme heme oxygenase 1 (HO-1), are decreased with acute DOX treatment is unknown. HO-1 expression is reported to be increased with oxidative stress (Hull et al., 2016; Otterbein and Choi, 2000). Cardiac-specific overexpression of HO-1 has been found to protect mice from DOX-induced dilated cardiomyopathy (Hull et al., 2016). HO-1 overexpression is reported to promote mitochondrial biogenesis and prevent mitochondrial fragmentation by increasing expression of mitochondrial fusion proteins and decreasing expression of the protein mitochondrial fission 1, a fission-related protein that is associated with mitophagy (Hull et al., 2016). How overexpression of HO-1 protects against DOX-induced mitochondrial damage and why it's expression was found to be decreased with acute DOX treatment is unclear.

Transcript levels of *Nppa* and *Atp2a2* were both significantly increased in response to 24 h DOX 10 μM treatment. An increase in transcript levels of *Atp2a2* is consistent with DOX's known interaction with the calcium pump of the sarcoplasmic reticulum (Hanna et al., 2014). SERCA2 damage or dysfunction with DOX treatment may lead to an initial increase in

transcript levels of *Atp2a2* as a compensatory response to damage. Increased *Nppa* transcript levels suggest myocyte dysfunction as a result of DOX treatment. Taken together, these findings show that acute DOX treatment has a significant effect on the transcript levels of genes related to mitochondrial function and structure, ROS, calcium handling and myocyte function, highlighting the acute effect of DOX on myocardial function.

5.4.4 Limitations and future directions

The XFp analyser uses fluorescence in order to measure oxygen in the medium surrounding cells. Therefore, it is important to assess the effect of fluorescent compounds in the absence of cells on the OCR and during the Mito Stress Test since fluorescent compounds may interfere with the ability of the XFp to assess oxygen consumption. Since the XFp analyser does not measure mitochondrial function directly it would be informative in future studies to use other assays to assess mitochondrial function such as an assay for quantitative determination of ATP.

No concentration response studies were performed with MitoQ in the present work. It is possible that no protection was seen with MitoQ because the concentration of MitoQ had not been optimised for this protocol and cell type.

The present findings do not examine if mitochondrial function or transcript level changes with 24 h DOX treatment are reversible. Future studies could examine the effect of acute DOX treatment followed by a period of “recovery” to see if DOX-induced changes are reversible.

Isolated myocytes lack *in vivo* context and deteriorate over time in culture. Future studies could examine mitochondrial function and gene changes following a low clinically relevant

dose of DOX at 24 h following administration. This type of study *in vivo* would allow a time course examination of cardiac mitochondrial function with DOX treatment to examine if cardiac mitochondrial damage and dysfunction is cumulative over time.

Transcript levels do not represent protein expression. Future studies could examine protein expression following DOX treatment of ARVM to further characterise acute DOX-induced mitochondrial and myocyte dysfunction.

The present study did not examine the effect of 24 h DOX treatment on mtDNA. Future studies may wish to examine the acute effect of DOX on the mtDNA copy number of ARVC.

5.4.5 Conclusion

Twenty-four h DOX 10 μM treatment of ARVM resulted in a significant decrease in cardiac mitochondrial function that was accompanied by a significant change in transcript levels of genes related to mitochondrial function, ROS, calcium homeostasis and myocyte damage. Although not statistically significant, with the except of *Cycs* transcript levels, 24 h DOX 3 μM treatment of ARVM resulted in a similar altered transcript expression pattern, suggesting a concentration-dependent effect of DOX on transcript level changes. Although DOX 3 μM treatment was not found to affect mitochondrial function in the present model, differential transcript expression with 24 h DOX 3 μM treatment suggests that even after an acute, clinically relevant dose of DOX, transcriptional changes are activated, possibly, to reduce DOX-induced myocyte damage.

Taken together the present findings in isolated ARVM highlight the acute effect of DOX over 24 h on mitochondrial and myocyte function.

Chapter 6

The acute effect of DOX on the $\Delta\Psi_m$ in the Langendorff-perfused rat heart

Chapter 6 The acute effect of DOX on the $\Delta\Psi_m$ in the Langendorff-perfused rat heart

6.1 Introduction

Energy produced by the movement of electrons along the respiratory chain is stored as a Δp across the inner membrane of mitochondria (Mitchell, 1961; Nicholls, 1982). The flow of electrons across the respiratory chain pumps H^+ across the inner membrane from the matrix to the intermembrane space. The movement of H^+ across the IMM results in two major consequences. Firstly, it generates a pH gradient (ΔpH) across the IMM with a higher pH of approximately seven in the matrix and, since, small molecules equilibrate freely across the OMM the pH of the intermembrane space is the same as the cytosol. Secondly, it results in a voltage gradient across the IMM referred to as the $\Delta\Psi_m$. The net outflow of positive ions produces a negative membrane potential in the matrix and a positive membrane potential in the intermembrane space. The ΔpH drives H^+ back into the matrix and OH^- out of the matrix and, thus, reinforces the $\Delta\Psi_m$ which attracts positive ions into the matrix and pushes negative ions out. Together, the ΔpH and the $\Delta\Psi_m$ constitute the Δp which exerts a proton-motive force that can be measured in units of millivolts (mV). The estimated Δp ranges from 180-220 mV with the $\Delta\Psi_m$ typically accounting for 150-180 mV and the ΔpH contributing 30-60 mV (Mitchell and Moyle, 1969; Nicholls, 1974; Nicholls and Ward, 2000). The Δp is harnessed to produce ATP from ADP and P_i and to transport metabolites and proteins such as ADP, phosphate and pyruvate and ions, for example calcium, into the matrix space (Durand et al., 1981; Hinkle and McCarty, 1978; LaNoue and Schoolwerth, 1979).

Early $\Delta\Psi_m$ depolarisation is a unifying and unavoidable pathophysiological event in a range of metabolic disorders affecting excitable tissues (Bhat et al., 2015; Gustafsson and Gottlieb,

2008). Investigating processes that result in $\Delta\Psi_m$ depolarisation is critical not only in order to try to prevent and treat these disorders but also to our understanding of mitochondrial biology.

Fluorescent lipophilic cationic compounds accumulate electrophoretically into polarised areas and can be used as semi-quantitative indicators of the $\Delta\Psi_m$ (Ehrenberg et al., 1988; Johnson et al., 1981; Lemasters and Ramshesh, 2007). The more negative the potential the greater the accumulation of positively charged compounds. Hence, these cationic fluorescent dyes equilibrate across membranes in individual cells and accumulate inside mitochondria in inverse proportion to the $\Delta\Psi_m$ because of their charge and solubility in both the inner mitochondrial membrane and matrix space (Scaduto and Grotyohann, 1999). A more negative (more polarised) $\Delta\Psi_m$ will accumulate more dye and a more positive (less polarised) $\Delta\Psi_m$ will accumulate less dye. Fluorescent cationic dyes such as TMRM and tetramethylrhodamine ethyl ester (TMRE), amongst others, are important tools used as semi-quantitative indicators of the $\Delta\Psi_m$.

Typically, cationic fluorescent dyes can be used in quenching or non-quenching modes (Duchen, 2004; Nicholls and Ward, 2000). Quenching mode of monochromatic fluorescent compounds utilises higher concentrations of dye than non-quenching mode such that the concentration of dye present in mitochondria leads to the formation of aggregates. These aggregates quench some of the fluorescent emissions of the dye. In quenching mode $\Delta\Psi_m$ depolarisation will lead to dissipation of the dye thus un-quenching fluorescence and, thereby, transiently increasing the fluorescence signal. In this fashion $\Delta\Psi_m$ depolarisation is associated with a transient increase in fluorescence (Bunting et al., 1989). Quenching mode is, for example, used to investigate opening of the mPTP as it results in a sensitive and transient

increase in TMRM fluorescence when the mPTP opens (Hausenloy et al., 2003; Ong et al., 2010). For the present study TMRM was used in non-quenching mode to examine changes in the $\Delta\Psi_m$ over time. TMRM was utilised because of low mitochondrial binding and a low risk of ETC inhibition at the concentration used compared to other fluorescent rhodamine derivatives, fast equilibration and previous investigation in the Langendorff-perfused rat heart (Jin et al., 2010; Lyon et al., 2010; Perry et al., 2011; Scaduto and Grotyohann, 1999).

Oskar Langendorff first established the isolated perfused mammalian heart preparation over a century ago (Langendorff, 1895; Skrzypiec-Spring et al., 2007). Langendorff's key contribution was to perfuse the ascending aorta retrogradedly via an aortic cannula. Retrograde perfusion down the ascending aorta closes the aortic valve leaflets and forces the perfusate to enter the coronary arteries via their ostia at the aortic root. The perfusion buffer then passes through the vascular bed before being drawn off via the coronary veins to the coronary sinus in the right atrium and is expelled from the heart via the pulmonary artery. The preparation can thus be maintained for several hours without any fluid filling the ventricular chambers. In the original description the preparation was perfused under constant pressure, a mode of perfusion that remains common to this day, but there is also the option for a constant flow perfusion. The constant pressure perfusion system has the advantage of letting auto-regulatory mechanisms alter and determine the coronary flow rate, either by coronary artery vasodilatation or vasoconstriction, depending on the physiological context. A constant flow perfusion makes use of a peristaltic pump to drive a constant flow rate of perfusate through the coronary arteries. This system overrides the auto-regulatory mechanisms and the amount of perfusate delivered is not altered in response to changes in heart rate or contraction. A constant flow perfusion was used in the optical mapping experiments described in this study.

Optical mapping of mitochondrial function in the Langendorff-perfused beating rat heart allows changes in the $\Delta\Psi_m$ to be examined in real-time in the functioning organ. Studies examining cardiac mitochondrial function in isolated cardiomyocytes rather than in intact functioning cardiac cells perfused via the coronary circulation have limitations due to the absence of other cardiac cell types and cardiomyocyte disruption and damage due to the isolation technique. Therefore, as a technique which bridges *in vitro* assays and *in vivo* models the Langendorff preparation was used for *ex vivo* optical mapping of cardiac mitochondria function in the present study.

DOX 1 μM perfusion in the Langendorff preparation has been previously shown to decrease the fluorescence intensity of the $\Delta\Psi_m$-sensitive dye 5, 5′, 6, 6′-tetrachloro-1, 1′, 3, 3′-tetra-ethyl benzimidazolyl carbocyanine iodide (JC-1) in a time-dependent manner in the functioning rat heart (Montaigne et al., 2010). JC-1 is a cationic fluorescent compound that accumulates inside mitochondria. When the concentration is sufficient green JC-1 monomers (485 nm excitation, 530 nm emission) form red J-aggregates (485 nm excitation, 590 nm emission). Thus, the ratio of red J-aggregate to green monomeric JC-1 emission is directly proportional to the $\Delta\Psi_m$ (Reers et al., 1995). Montaigne *et al*. showed a decrease in the JC-1 fluorescence ratio suggesting $\Delta\Psi_m$ dissipation with DOX 1 μM perfusion across five adjacent regions of interest of 2 mm^2 with 40x magnificent at the LV surface (Montaigne et al., 2010). The use of JC-1 for ratiometric semi-quantitative assessment of the $\Delta\Psi_m$ has limitations. JC-1 is very photosensitive (Nicholls and Ward, 2000) and as a ratiometric probe the use of JC-1 relies on dual-colour assessment of the $\Delta\Psi_m$. The two forms of JC-1 are differentially permeant based on their molecular structure. While the monomer (green) form of JC-1 is reported to equilibrate on a similar time scale to that of TMRM/TMRE (approximately 15 min) the aggregate (red) form of JC-1 has been reported to take approximately 90 min to reach

equilibration in cardiomyocytes (Mathur et al., 2000). Thus, results obtained using JC-1 must be evaluated with these issues in mind and interpreted with caution (Perry et al., 2011). Ideally, findings using JC-1 would be validated using a $\Delta\Psi_m$-sensitive complementary dye such as TMRM.

Dissipation of the $\Delta\Psi_m$ indicates that the IMM can no longer provide a barrier and that there is acute mitochondrial toxicity. The aim of this area of research was, therefore, to investigate the acute concentration-dependent effect of DOX-perfusion on epicardial whole heart $\Delta\Psi_m$ stability in the *ex vivo* functioning rat heart using optical mapping of the fluorescent lipophilic cationic dye TMRM.

6.2 Hypothesis and aims

I hypothesis that infusion of DOX in to the Langendorff-perfused beating rat heart will cause an immediate concentration-dependent $\Delta\Psi_m$ depolarisation, shown by a drop in TMRM fluorescence intensity, and that DOX infusion predispose the heart to metabolic dysfunction.

The aims of this chapter are as follows:

1. Establish an *ex vivo* optical mapping protocol to assess acute signs of mitochondrial dysfunction using TMRM in the Langendorff-perfused beating rat heart
2. Examine innate DOX fluorescence *in vitro* and in Langendorff-perfused rat hearts in comparison to TMRM fluorescence using the spectrum required for *ex vivo* optical mapping of mitochondrial function
3. Assess the acute concentration-dependent effect of DOX on mitochondrial function across the epicardial surface in the Langendorff-perfused beating rat heart using optical mapping
4. Examine the effect of a metabolic challenge on mitochondrial function in Langendorff-perfused rat hearts pre-perfused with DOX

6.3 Results

6.3.1 *Ex vivo* optical mapping of mitochondrial function in the Langendorff-perfused rat heart

To examine the acute effect of anti-cancer agents on cardiac mitochondrial function in the functioning rat heart in real-time it was necessary to establish a robust optical mapping protocol in the Langendorff-perfused beating heart.

Following ten min of stabilisation in an optical mapping chamber (Fig. 6.1A) fluorescence intensity data was acquired, with an excitation wavelength of 530 nm and an emission wavelength of 585 ± 20 nm (TMRM camera image), in order to subtract autofluorescence in the mapping field from TMRM fluorescence intensity. Hearts were then perfused for 20 min with Krebs-Henseleit solution containing TMRM (200 nM) (TMRM loading phase). This TMRM loading phase resulted in a robust increase in TMRM fluorescence across the whole epicardial surface of the heart (Fig. 6.1B). An occlusion to the left anterior descending artery shows TMRM fluorescence in healthy myocardial tissue perfused via the coronary circulation and no TMRM fluorescence intensity in the ischaemic zone (Fig. 6.1C &D). The concentration of TMRM 200 nM was previously optimised to avoid dye quenching while still producing a robust and stable TMRM fluorescence signal; data not shown as submitted as part of an MRes thesis authored by myself (Elder, 2013). To obtain a stable TMRM fluorescence intensity and avoid quenching of TMRM a series of calibration experiments were conducted in which a range of concentrations of TMRM (50, 100, 200, 250 or 300 nM) were used to establish the optimal concentration (Elder, 2013). Perfusion of TMRM 200 nM over 20 min resulted in a gradual increase in TMRM fluorescence across the whole epicardial surface of the heart (Fig. 6.2).

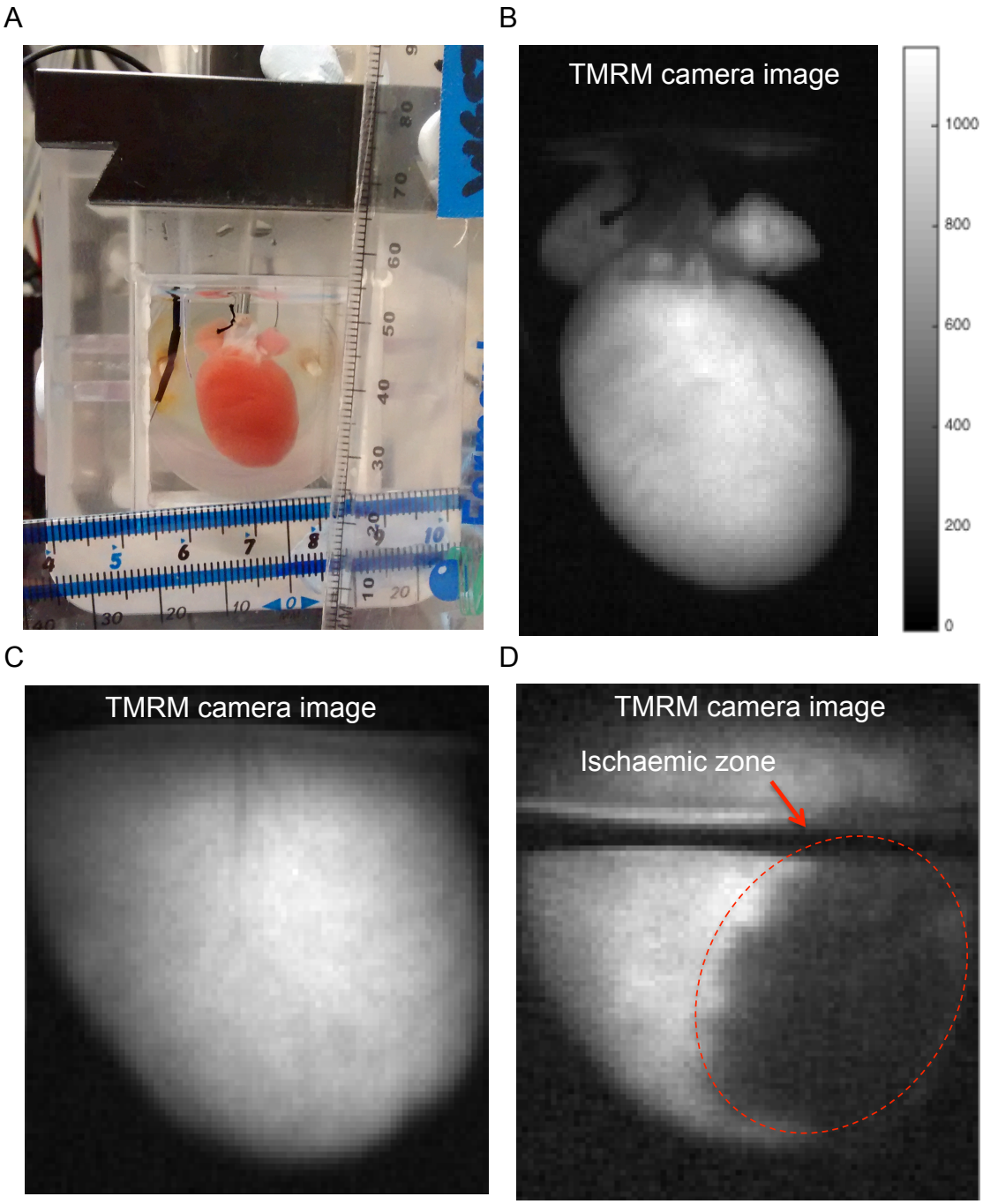


Fig. 6.1 Whole heart images of setup of *ex vivo* optical mapping of cardiac mitochondrial function in the Langendorff-perfused beating rat heart.
(A) Image of control rat heart in the optical mapping chamber surrounded by Krebs-Henseleit solution at 37°C (B) TMRM camera image (excitation wavelength 530 nm and emission wavelength 585 ± 20 nm) following a 20 min TMRM loading phase. Scale shows fluorescence in arbitrary fluorescence units (afu) (C) TMRM camera image of control rat heart following TMRM loading phase (D) TMRM camera image of rat heart with an occlusion in the left descending artery following TMRM loading phase. TMRM fluorescence is absent in the ischaemic zone.

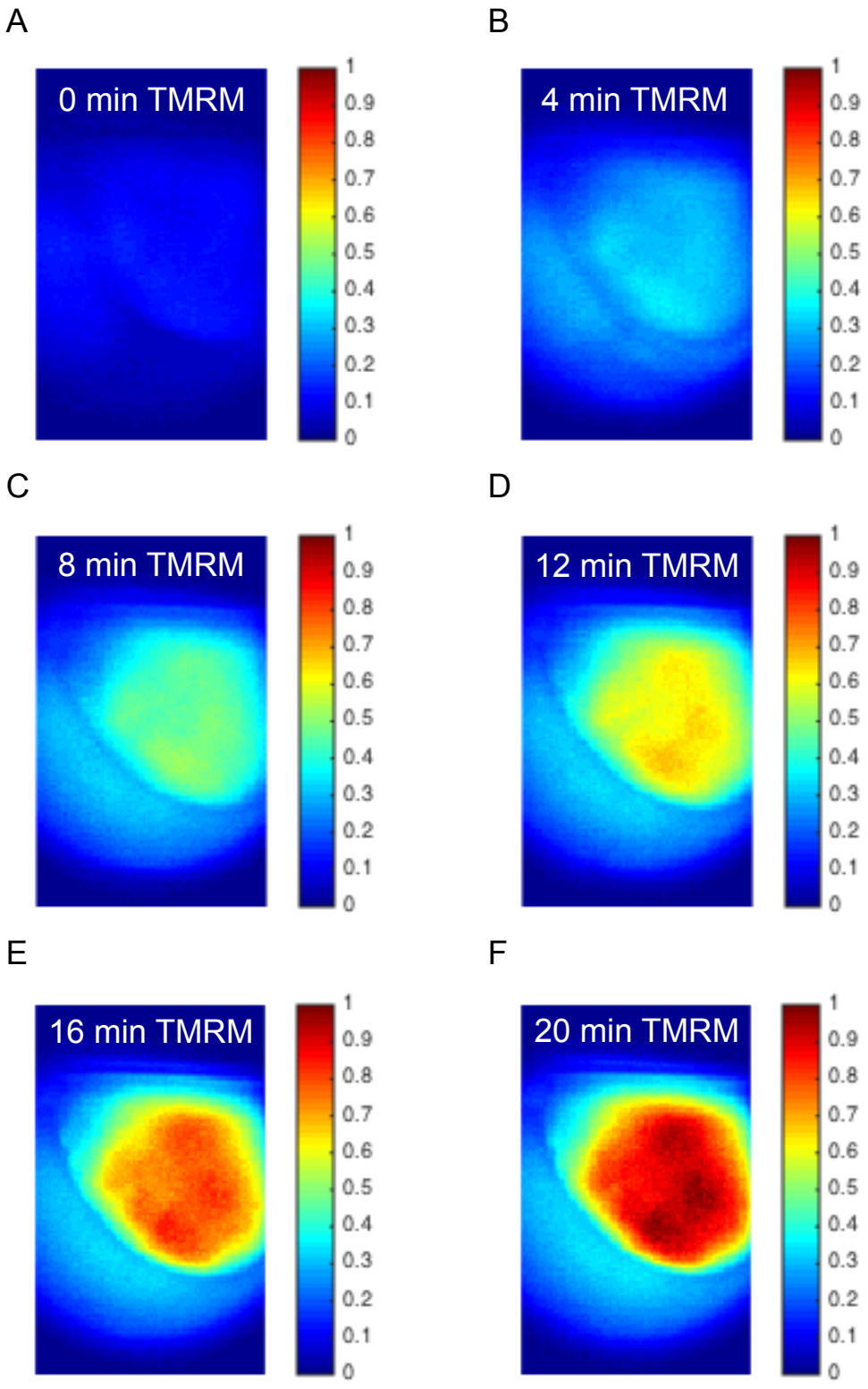


Fig. 6.2 Real-time imaging of normalised whole heart and background TMRM fluorescence during TMRM loading phase in the Langendorff-perfused rat heart.
Images show normalised TMRM fluorescence across the whole heart at (A) 0 min (B) 4 min (C) 8 min (D) 12 min (E) 16 min (F) 20 min of TMRM loading phase. Scale bar shows normalised TMRM fluorescence where 0 is the minimum and 1 is the maximum normalised fluorescence value.

A 20 min TMRM loading phase was followed by a 20-30 min fluorescence signal stabilisation period (stabilisation phase) during which perfusion was switched back to dye free Krebs-Henseleit solution. This stabilisation phase was used to “washout” any excess dye present in the perfusate and extracellular space and to develop a stable TMRM fluorescence intensity. To limit variation in TMRM fluorescence caused by the movement of the heart and differences in light intensity across the heart a region of interest (ROI) on the LV epicardial surface with consistent light intensity was mapped for quantification of TMRM fluorescence changes over time (Fig. 6.3A). Once a stable fluorescence intensity of TMRM, reflecting the $\Delta\Psi_m$, had been achieved this was used as the steady-state TMRM fluorescence value and data was normalised to this point (baseline; normalised $\Delta\Psi_m$) (Fig. 6.3B & C). As a preliminary experiment, following the stabilisation phase TMRM fluorescence was imaged every two min over three h (Fig. 6.3D). Normalised TMRM fluorescence was found to decline marginally with time after 100 min (Fig. 6.3D), possibly due to a decline in cardiac function on the Langendorff-perfusion system. Normalised TMRM fluorescence was found to be stable over 90 min exhibiting less than 3.5% variation in continuously perfused, non-ischaemic control hearts (Fig. 6.3E & F). Experiments examining cardiac mitochondrial function with anti-cancer agents on the Langendorff-perfusion system were, therefore, limited to 90 min after reaching steady-state TMRM fluorescence intensity.

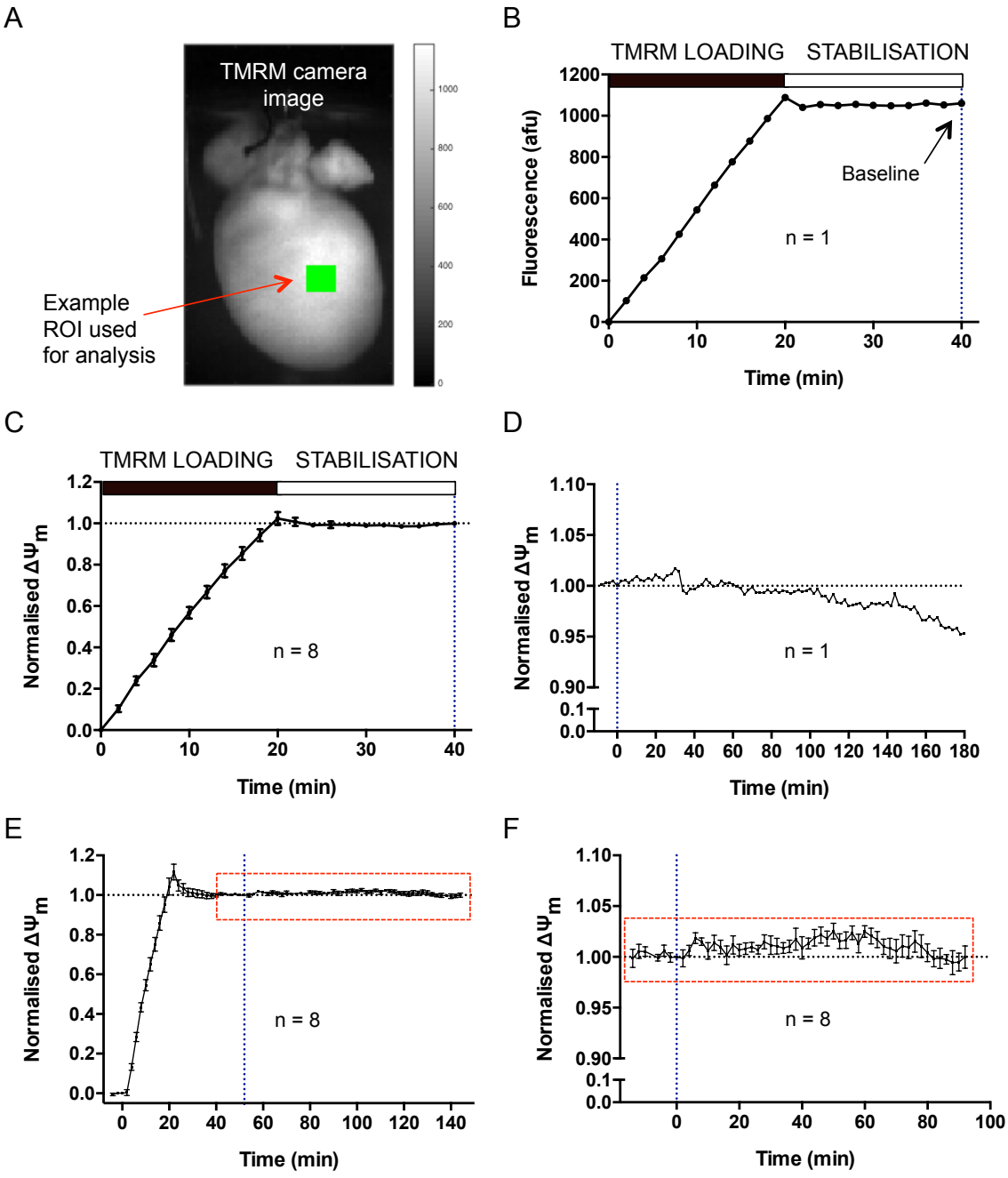


Fig. 6.3 Real-time imaging of epicardial TMRM fluorescence in control Langendorff-perfused rat hearts. (A) Representative TMRM fluorescence image showing an example ROI on the left ventricle used for analysis of TMRM fluorescence over time. Scale shows fluorescence in afu excited at a wavelength of 530 nm and with an emission wavelength of 585 ± 20 nm (B) Fluorescence (afu) imaged every 2 min during the TMRM loading phase followed by a 20 min stabilisation phase to allow TMRM fluorescence intensity to reach a steady-state which could be used as a baseline n = 1 (C) TMRM fluorescence ($\Delta\Psi_m$) during loading and stabilisation phases normalised to steady-state TMRM fluorescence for n = 8 (D) Normalised TMRM fluorescence over 3 h in the Langendorff-perfused rat heart n = 1 (E) Normalised TMRM fluorescence during TMRM loading and stabilisation phase followed by 90 min follow-up n = 8 (F) Stable normalised TMRM fluorescence over 90 min follow-up exhibiting less than 3.5% variation in control Langendorff-perfused rat hearts n = 8. Blue dashed line indicates baseline.

To validate that TMRM can be used as an accurate indicator of the $\Delta\Psi_m$ in Langendorff-perfused rat hearts the mitochondria-uncoupling agent FCCP was used as a positive control for *ex vivo* optical mapping of mitochondrial function (Fig. 6.4A). In a subset of experiments hearts were perfused with FCCP and oligomycin A to see if a combined insult would affect the rate of TMRM fluorescence loss. In the event of $\Delta\Psi_m$ depolarisation cells can re-establish the $\Delta\Psi_m$ by switching from ATP synthesis (H^+ pumped into the matrix) to ATP hydrolysis (H^+ pumped out of the matrix) by ATP synthase (Nicholls et al., 2002). Oligomycin A blocks the proton channel of the ATP synthase in the IMM, preventing $\Delta\Psi_m$ recovery by ATP hydrolysis (Nicholls et al., 2002). Perfusion of FCCP, with and without oligomycin A, resulted in an acute decrease in normalised TMRM fluorescence suggesting that as the mitochondria depolarise in response to FCCP TMRM diffuses out of the mitochondria resulting in a marked decrease in fluorescence intensity (Fig. 6.4A). Despite an acute decrease in fluorescence a steady-state fluorescence signal was not reached until approximately 1 h after the initial infusion of FCCP (Fig. 6.4A). Combined perfusion of FCCP and oligomycin A, in this system, did not cause a greater decrease in normalised TMRM fluorescence over time compared to FCCP alone, suggesting the concentration of FCCP used was sufficient to cause complete collapse of the $\Delta\Psi_m$ (Fig. 6.4A). Perfusion with FCCP 10 μM for 20 min decreased normalised TMRM fluorescence by 98% after 60 min (Fig. 6.4B). This data suggests that TMRM can be used as an accurate indicator of the $\Delta\Psi_m$ in Langendorff-perfused beating rat hearts. Therefore, mitochondrial dysfunction, manifesting as depolarisation of the $\Delta\Psi_m$, was observed as a drop in steady-state TMRM fluorescence.

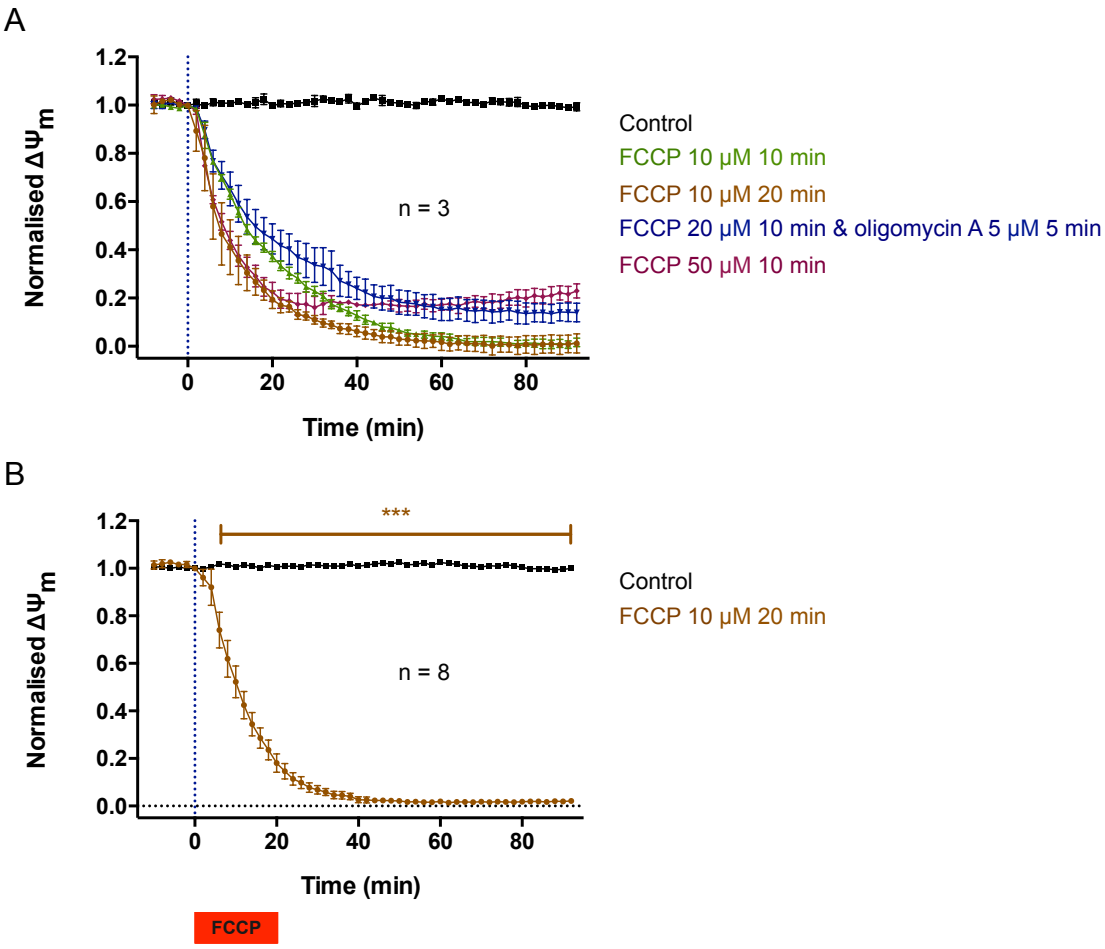


Fig. 6.4 Real-time changes in normalised epicardial TMRM fluorescence with infusion of the mitochondrial uncoupling agent FCCP and oligomycin A in Langendorff-perfused rat hearts.
(A) Normalised epicardial TMRM fluorescence with perfusion of FCCP alone or with oligomycin A n = 3. Perfusion of FCCP ± oligomycin A caused an acute decrease in TMRM fluorescence (B) Perfusion with FCCP 10 µM for 20 min decreased normalised TMRM fluorescence by 98% after 60 min n = 8. Blue dashed line indicates baseline. Data is represented as mean ± *SEM*. Two-way repeated measures ANOVA with Bonferroni's multiple comparison test ***$p < 0.001$ compared to control.

6.3.2 Assessing the feasibility of using DOX for *ex vivo* optical mapping of mitochondrial function in the Langendorff-perfused rat heart

It is known that DOX itself is a fluorescent compound (Karukstis et al., 1998; Motlagh et al., 2016), therefore, the feasibility of using DOX for *ex vivo* optical mapping in the spectrum required to assess mitochondrial function was examined. Initially, the fluorescence of DOX was assessed using a cuvette-based spectrofluorophotometer. Measurements of fluorescence emission spectra were carried out on samples of TMRM 200 nM with and without DOX 1 μM or DOX 10 μM and DOX 1 μM or 10 μM alone using a 530 nm excitation wavelength; emission spectra were recorded from 400 to 700 nm (Fig. 6.5A & B). DOX 1 μM at this excitation had a peak emission wavelength between 472-505 nm (Fig. 6.5A). DOX 10 μM at this excitation had a peak emission wavelength between 493-498 nm (Fig. 6.5B). Fluorescence of samples of TMRM 200 nM with and without DOX 1 μM or DOX 10 μM and DOX 1 μM or 10 μM alone were measured using 530 nm excitation and 585 nm emission wavelength at room temperature (Fig. 6.5C). DOX 1 and 10 μM were found to be fluorescent at the spectrum examined and showed a trend of increased fluorescence intensity with TMRM 200 nM compared to TMRM 200 nM alone (Fig. 6.5C).

To investigate DOX's fluorescence with an excitation wavelength of 530 nm and an emission wavelength of 585 ± 20 nm in Langendorff-perfused rat hearts control hearts were perfused with DOX 10 μM alone over 30 min with a ten min follow-up phase (Fig. 6.6A). Fluorescence increased to a mean (n = 3) peak value of 16 afu over 30 min DOX 10 μM perfusion in Langendorff-perfused rat hearts (Fig. 6.6A). Fig. 6.6B shows the increase in fluorescence to a mean (n = 8) peak value of 1165 afu over a 20 min TMRM 200 nM perfusion in Langendorff-perfused rat hearts. Overall, these findings demonstrate that DOX slightly increases the

fluorescence intensity of TMRM and may mask a decrease in TMRM fluorescence intensity in the *ex vivo* optical mapping system.

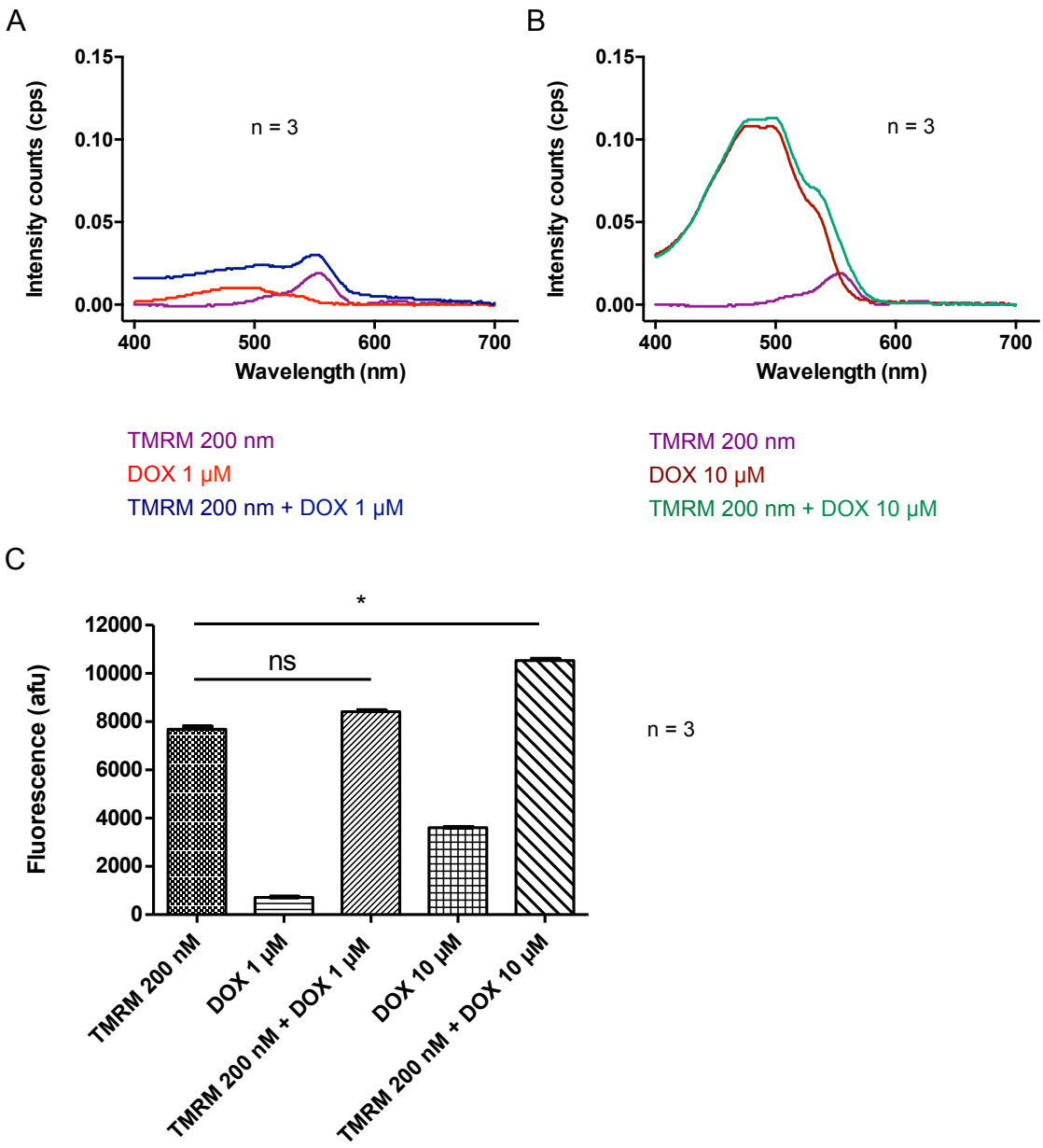


Fig. 6.5 Fluorescence at room temperature measured using a cuvette-based spectrofluorophotometer. (A) Intensity counts measured in counts per second (cps) of TMRM 200 nM alone, DOX 1 µM alone and TMRM 200 nM with DOX 1 µM over an emission spectra from 400 to 700 nm with 530 nm excitation wavelength (B) Intensity counts (cps) of TMRM 200 nM alone, DOX 10 µM alone and TMRM 200 nM with DOX 10 µM over an emission spectra from 400 to 700 nm with a 530 nm excitation wavelength (C) Fluorescence (afu) of TMRM 200 nM with and without DOX 1 µM or DOX 10 µM and DOX 1 µM or 10 µM alone using 530 nm excitation and 585 nm emission wavelength. Error bars represent *SEM*. Kruskal-Wallis test with Dunn's multiple comparisons test ns = not significant *$p < 0.05$ compared to control.

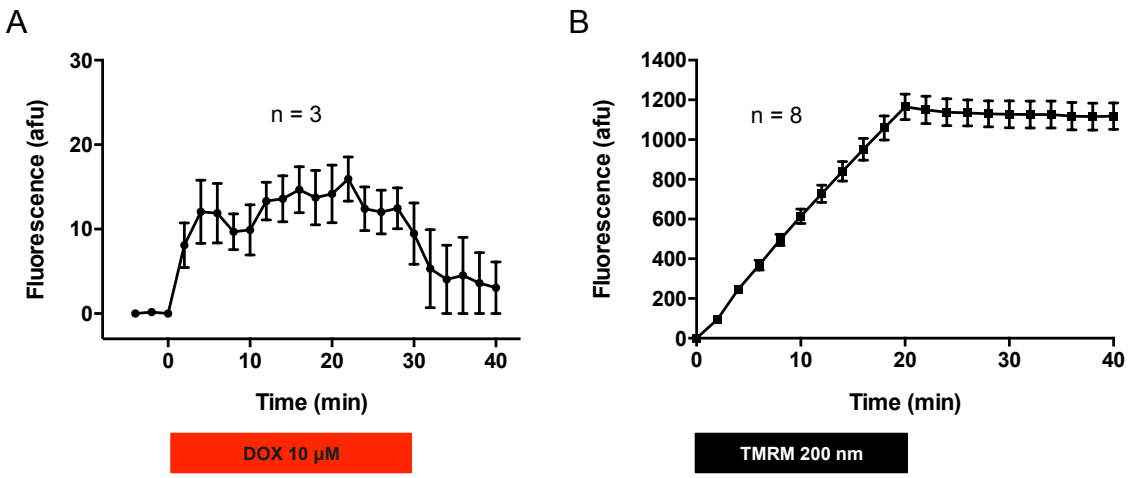


Fig. 6.6 Fluorescence imaged every 2 min with an excitation wavelength of 530 nm and an emission wavelength of 585 ± 20 nm in Langendorff-perfused rat hearts.
(A) Fluorescence (afu) imaged every 2 min during 30 min DOX 10 µM perfusion followed by 10 min follow-up n = 3 (B) Fluorescence (afu) imaged every 2 min during 20 min TMRM 200 nM perfusion followed by 20 min follow-up n = 8. Data is represented as mean ± *SEM*.

6.3.3 Acute concentration-dependent $\Delta\Psi_m$ dissipation with DOX in the Langendorff-perfused rat heart

To examine the acute effect of DOX on the $\Delta\Psi_m$ Langendorff-perfused beating rat hearts, loaded with TMRM, were perfused for 60 min with Krebs-Henseleit solution containing DOX 1 μM, a concentration reflective of the peak plasma drug concentration in patients receiving DOX (approximately 1-3 μM) (Barpe et al., 2010; Muller et al., 1993). Normalised TMRM fluorescence decreased by 13% in DOX 1 μM-treated hearts after 60 min (Fig. 6.7A). Hearts were perfused with DOX 1 μM for 60 min followed by a 20 min perfusion with FCCP 10 μM as a positive control (Fig. 6.7B). To investigate the concentration-dependent effects of acute DOX treatment hearts were perfused for 60 min with Krebs-Henseleit solution containing DOX 3 or 10 μM. Perfusion of DOX 1 or 3 μM showed a similar decrease in normalised TMRM fluorescence (Fig. 6.7C). Normalised TMRM fluorescence decreased by 24% in DOX 10 μM-treated hearts after 60 min (Fig. 6.7D). This data suggests that DOX causes progressive concentration-dependent $\Delta\Psi_m$ dissipation in the *ex vivo* beating rat heart suggesting acute mitochondrial dysfunction with DOX.

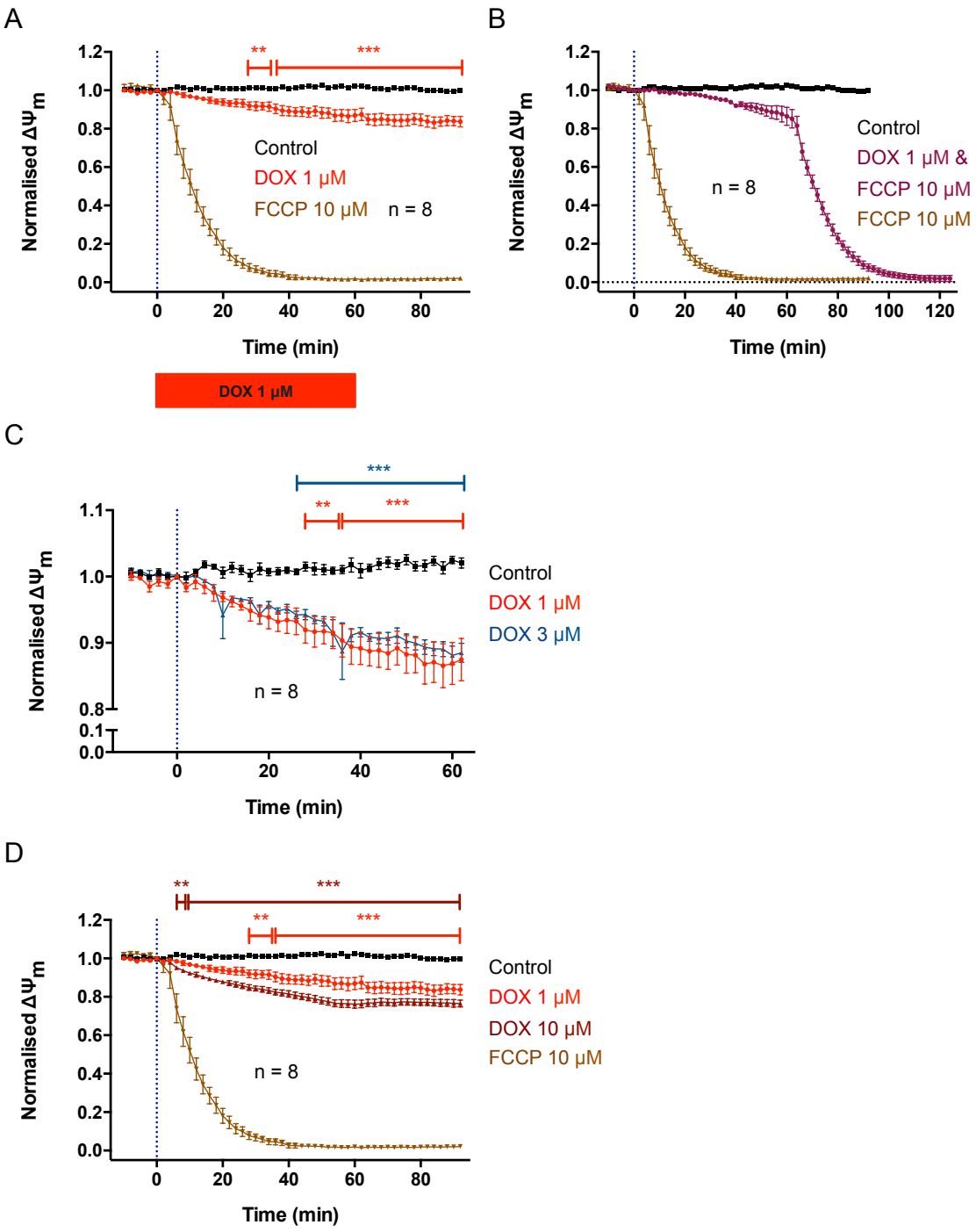


Fig. 6.7 Real-time changes in normalised epicardial TMRM fluorescence with DOX perfusion in the Langendorff-perfused rat heart.
(A) Epicardial TMRM fluorescence over 60 min perfusion of DOX 1 μM (red line) compared to control (black line) followed by 30 min follow-up n = 8. FCCP 10 μM was perfused over 20 min as a positive control (brown line) (B) Epicardial TMRM fluorescence changes in real-time over 60 min perfusion of DOX 1 μM followed by a 20 min perfusion of FCCP 10 μM (maroon line) n = 8 (C) Epicardial TMRM fluorescence over 60 min perfusion of DOX 1 or 3 (blue line) μM n = 8 (D) Epicardial TMRM fluorescence over 60 min perfusion of DOX 1 or 10 (cayenne) μM followed by 30 min follow-up n = 8. Blue dashed line indicates baseline. Data is represented as mean ± *SEM*. Two-way repeated measures ANOVA with Bonferroni's multiple comparisons test **$p < 0.01$ ***$p < 0.001$ compared to control.

To validate findings using a ROI on the LV epicardial surface for analysis of TMRM fluorescence normalised TMRM fluorescence across the whole epicardial surface was mapped for the DOX 10 μM perfusion protocol. Normalised TMRM fluorescence decreased across the epicardial surface over time with DOX 10 μM perfusion (Fig. 6.8) compared to control (Fig. 6.9). To exclude background fluorescence a "mask" was fitted to the data to show only fluorescence present on the epicardial surface of the heart. Non-epicardial regions of the mapping field were "masked out". To adjust for differences in light intensity across the heart all epicardial fluorescence was set to 1 at baseline (Fig. 6.10A). Using this technique it was possible to track all pixels present on the epicardial surface with DOX 10 μM perfusion without background fluorescence and as a change from baseline (Fig. 6.10) compared to control (Fig. 6.11). Pixels present on the epicardial surface were used to generate histograms showing the number of pixels on the epicardial surface and their normalised TMRM fluorescence value over time with DOX 10 μM perfusion (Fig. 6.12). Representative histograms for control and DOX 1 μM-perfused hearts showed consistent results with ROI analysis (Fig. 6.13 & Fig. 6.14, respectively).

Next a representative value of the fluorescence across the whole heart was calculated. Using the normalised TMRM fluorescence value for each pixel across the epicardial surface the average normalised fluorescence (ANF) value across the whole heart over time could be generated (Fig. 6.15). ANF values in control and hearts with DOX perfusion showed consistent results with ROI analysis (Fig. 6.15D & Fig. 6.7D). Normalised TMRM fluorescence decreased in an acute progressive concentration-dependent matter across the whole epicardial surface with DOX perfusion, validating findings using ROI analysis.

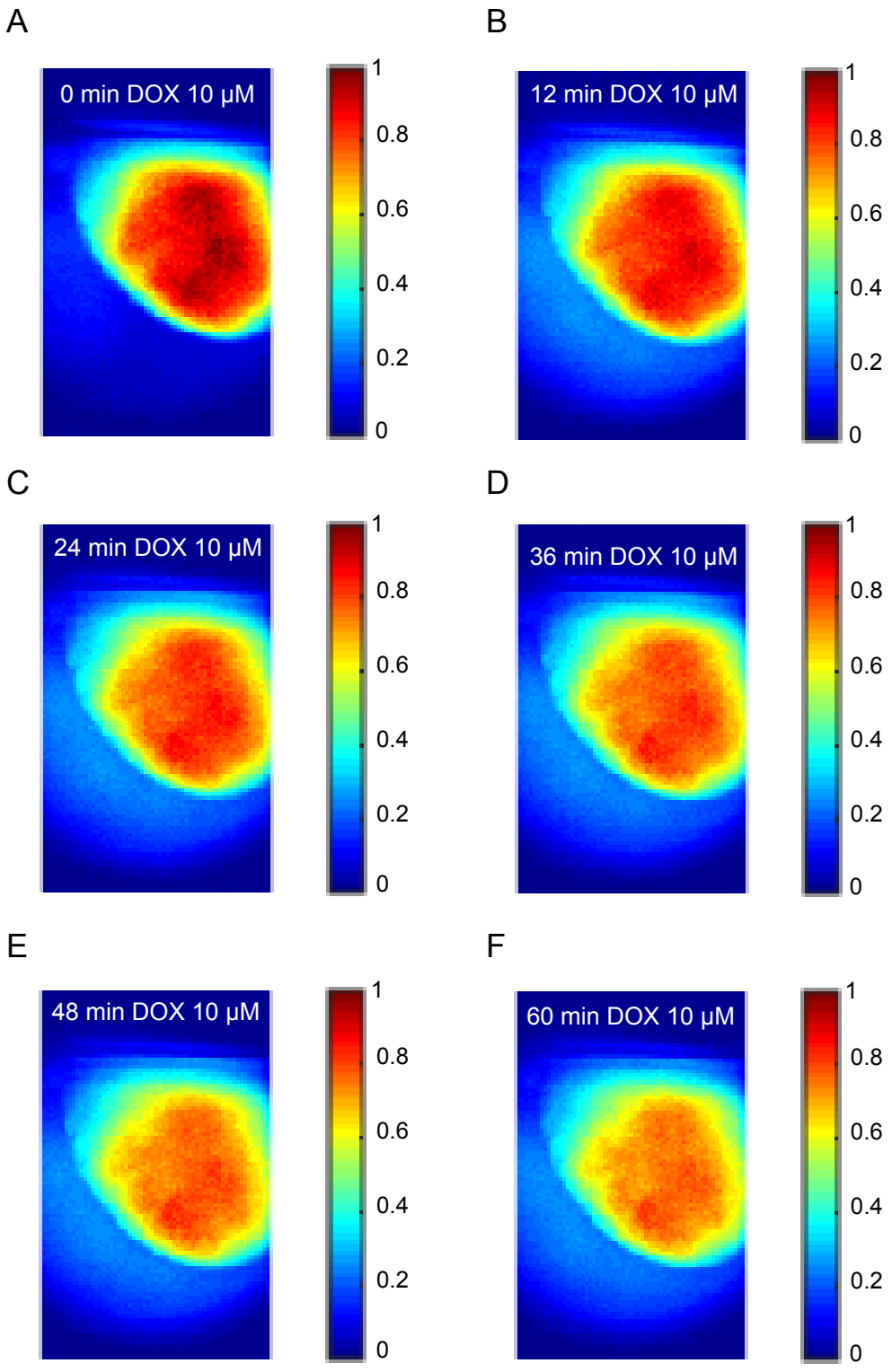


Fig. 6.8 Real-time imaging of normalised whole heart and background TMRM fluorescence during DOX 10 µM perfusion in the Langendorff-perfused rat heart. Images show normalised TMRM fluorescence across the whole heart at (A) 0 min (baseline) (B) 12 min (C) 24 min (D) 36 min (E) 48 min (F) 60 min of DOX 10 µM perfusion. Scale bar shows normalised TMRM fluorescence where 0 is the minimum and 1 is the maximum normalised fluorescence value.

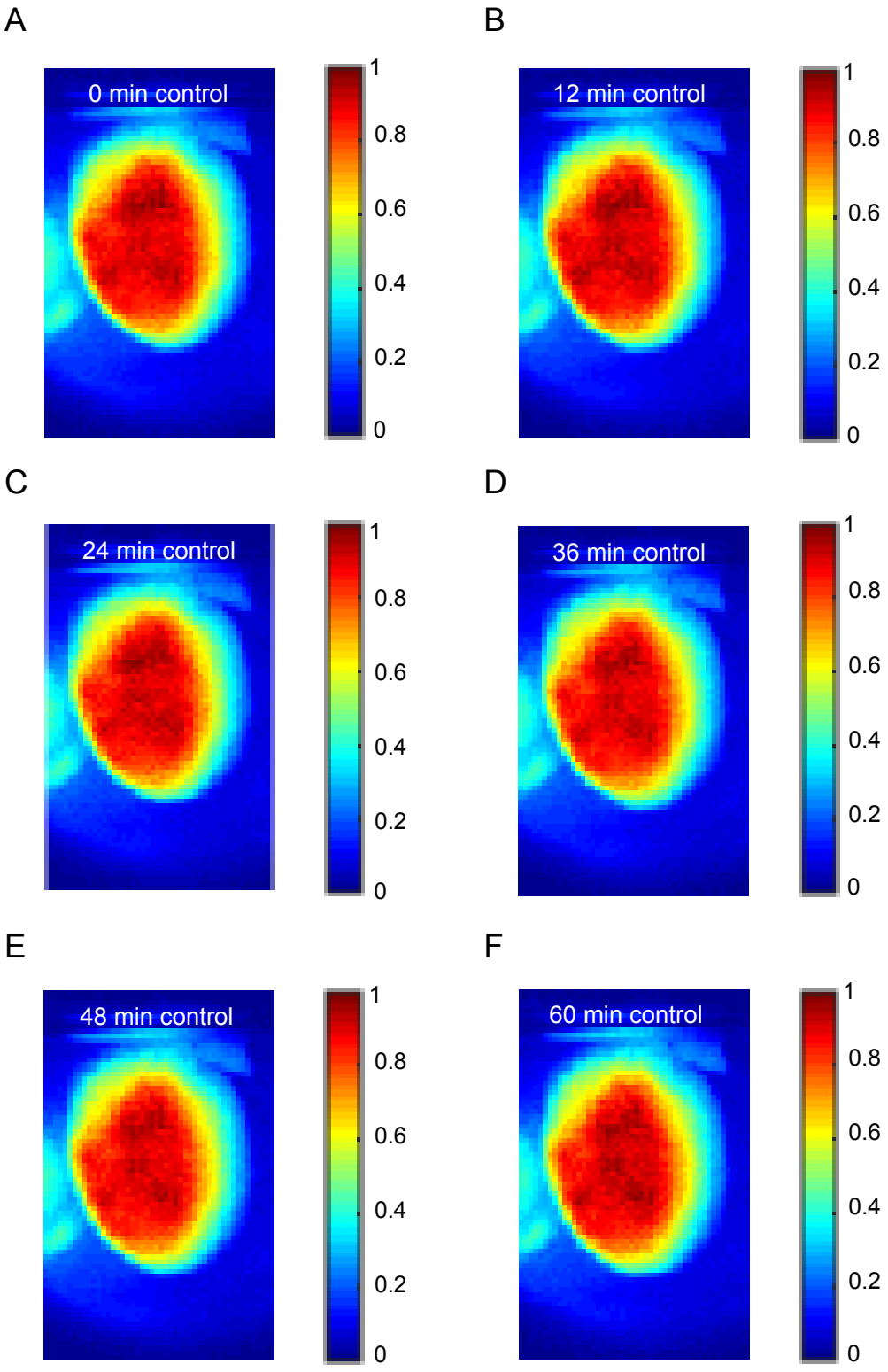


Fig. 6.9 Real-time imaging of normalised whole heart and background TMRM fluorescence during control perfusion in the Langendorff-perfused rat heart. Images show normalised TMRM fluorescence across the whole heart at (A) 0 min (baseline) (B) 12 min (C) 24 min (D) 36 min (E) 48 min (F) 60 min of perfusion. Scale bar shows normalised TMRM fluorescence where 0 is the minimum and 1 is the maximum normalised fluorescence value.

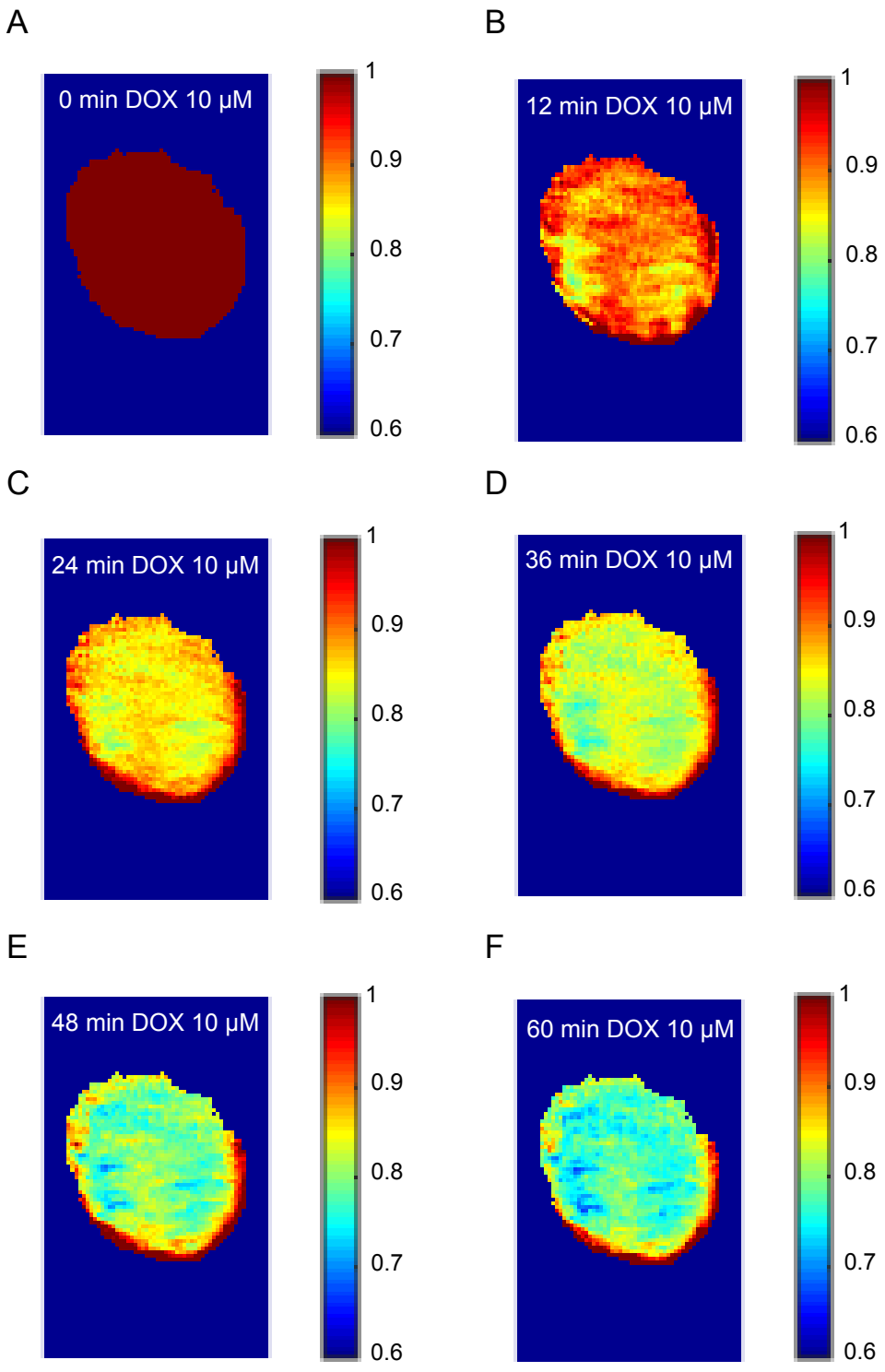


Fig. 6.10 Real-time imaging of normalised whole heart epicardial TMRM fluorescence during DOX 10 µM perfusion in the Langendorff-perfused rat heart.
Images show normalised TMRM fluorescence across the whole epicardial surface at (A) 0 min, the time point at which all epicardial pixel values were corrected to 1 in order to track epicardial TMRM fluorescence with DOX perfusion, (B) 12 min (C) 24 min (D) 36 min (E) 48 min (F) 60 min of DOX 10 µM perfusion. The dark blue area shows "masked out" background fluorescence. Scale bar shows normalised TMRM fluorescence where 0.6 is the minimum and 1 is the maximum normalised fluorescence value.

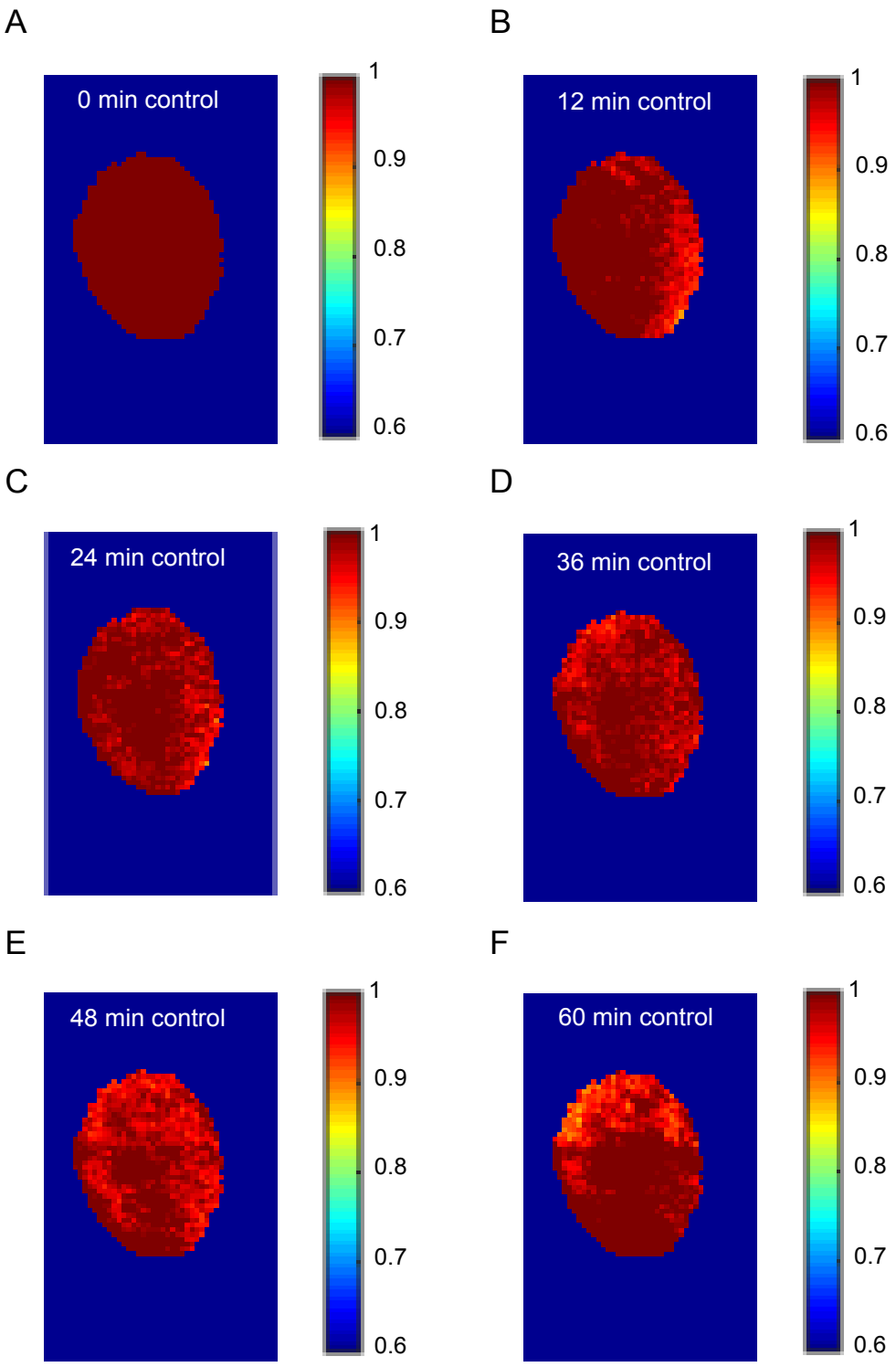


Fig. 6.11 Real-time imaging of normalised whole heart epicardial TMRM fluorescence during control perfusion in the Langendorff-perfused rat heart.
Images show normalised TMRM fluorescence across the whole epicardial surface at (A) 0 min, the time point at which all epicardial pixel values were corrected to 1 in order to track epicardial TMRM fluorescence with perfusion, (B) 12 min (C) 24 min (D) 36 min (E) 48 min (F) 60 min of perfusion. The dark blue area shows "masked out" background fluorescence. Scale bar shows normalised TMRM fluorescence where 0.6 is the minimum and 1 is the maximum normalised fluorescence value.

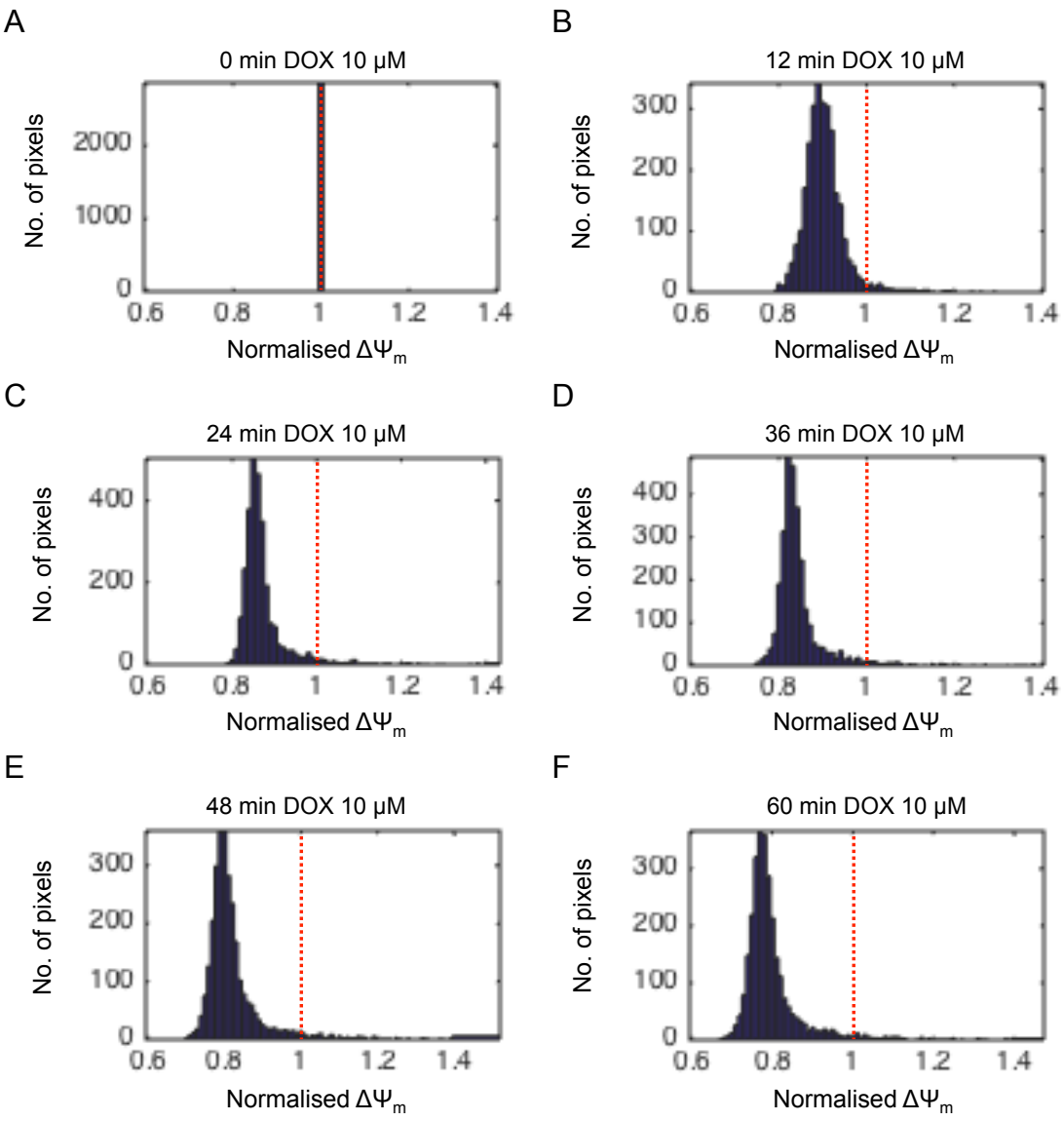


Fig. 6.12 Histograms of normalised TMRM fluorescence across the whole epicardial surface during DOX 10 μM perfusion in the Langendorff-perfused rat heart.
Histograms show normalised TMRM fluorescence across the whole epicardial surface at (A) 0 min, the time point at which all epicardial pixel values were corrected to 1 in order to track epicardial TMRM fluorescence with DOX perfusion, (B) 12 min (C) 24 min (D) 36 min (E) 48 min (F) 60 min of DOX 10 μM perfusion. Red dashed line on each histogram over time indicates baseline. Y-axis shows the number of pixels present at each normalised TMRM fluorescence intensity at each time point.

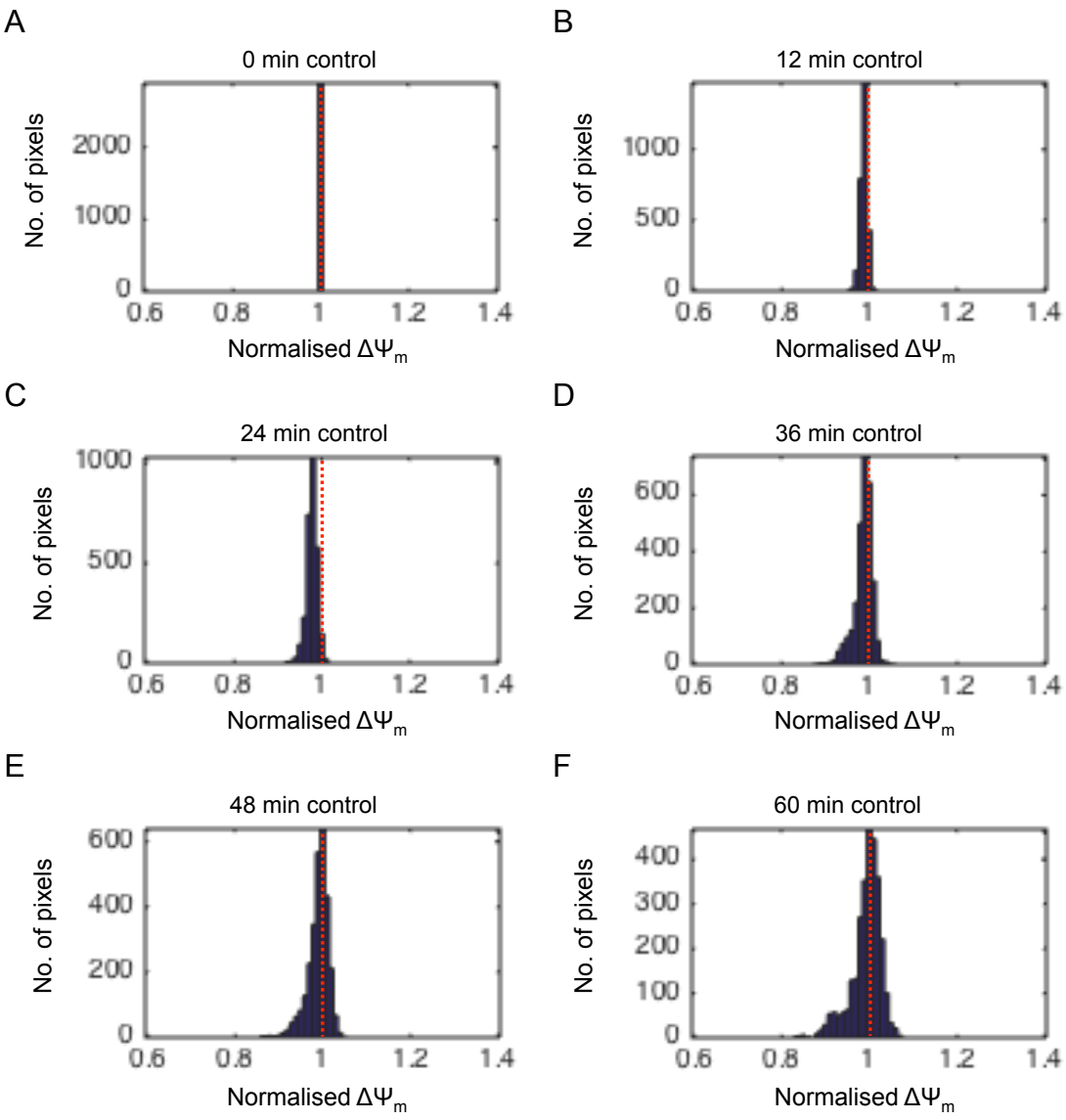


Fig. 6.13 Histograms of normalised TMRM fluorescence across the whole epicardial surface during vehicle control perfusion in the Langendorff-perfused rat heart.
Histograms show normalised TMRM fluorescence across the whole epicardial surface at (A) 0 min, the time point at which all epicardial pixel values were corrected to 1 in order to track epicardial TMRM fluorescence with vehicle control perfusion, (B) 12 min (C) 24 min (D) 36 min (E) 48 min (F) 60 min of vehicle control perfusion. Red dashed line on each histogram over time indicates baseline. Y-axis shows the number of pixels present at each normalised TMRM fluorescence intensity at each time point.

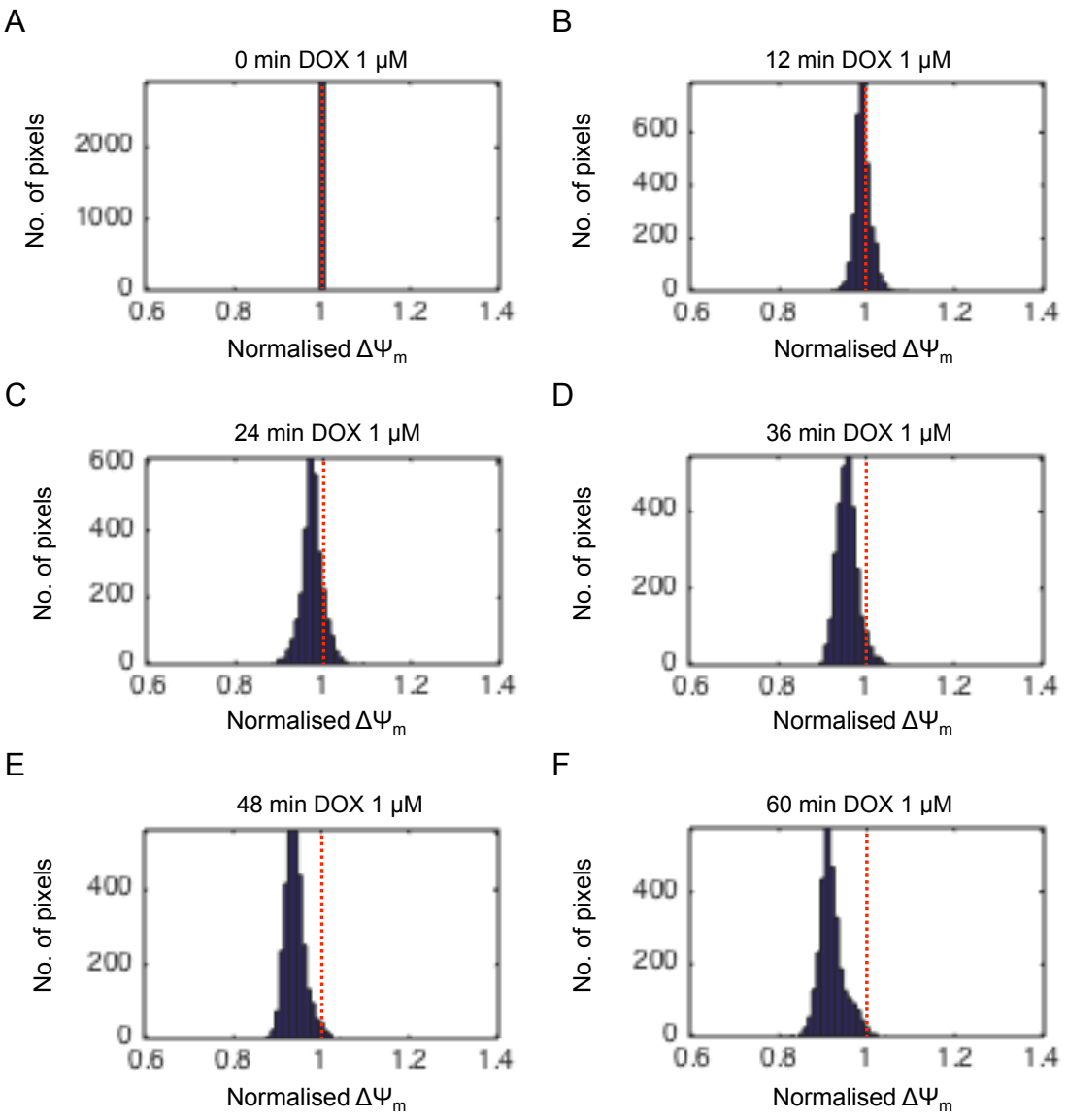


Fig. 6.14 Histograms of normalised TMRM fluorescence across the whole epicardial surface during DOX 1 μM perfusion in the Langendorff-perfused rat heart.
Histograms show normalised TMRM fluorescence across the whole epicardial surface at (A) 0 min, the time point at which all epicardial pixel values were corrected to 1 in order to track epicardial TMRM fluorescence with DOX perfusion, (B) 12 min (C) 24 min (D) 36 min (E) 48 min (F) 60 min of DOX 1 μM perfusion. Red dashed line on each histogram over time indicates baseline. Y-axis shows the number of pixels present at each normalised TMRM fluorescence intensity at each time point.

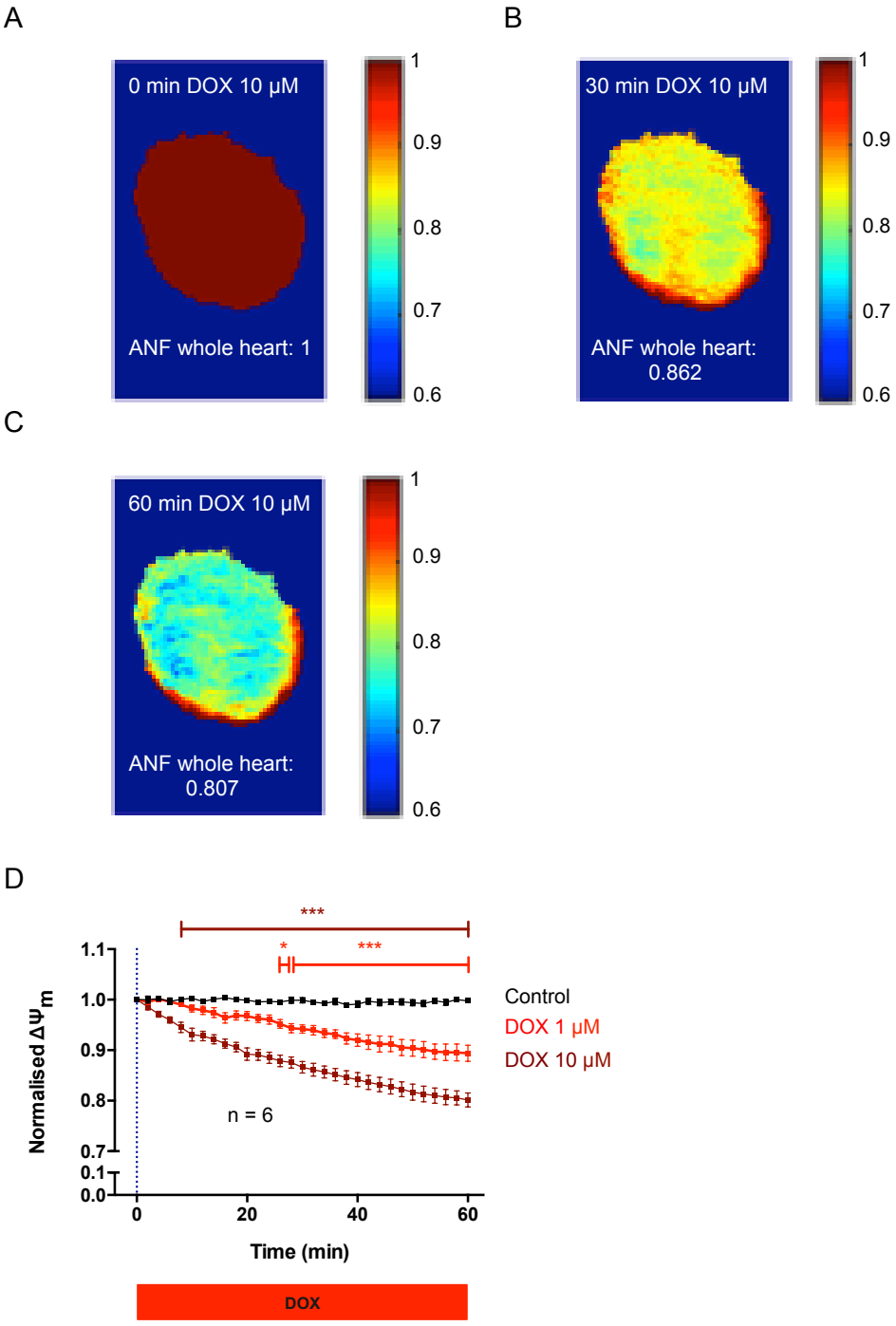


Fig. 6.15 Real-time imaging of normalised whole heart epicardial TMRM fluorescence and the ANF over time in Langendorff-perfused rat hearts.
Images show normalised TMRM fluorescence across the whole epicardial surface with the ANF value at (A) 0 min, the time point at which all epicardial pixel values were corrected to 1 in order to track epicardial TMRM fluorescence with DOX perfusion, (B) 30 min (C) 60 min of DOX 10 µM perfusion. The dark blue area shows "masked out" background fluorescence. Scale bar shows normalised TMRM fluorescence where 0.6 is the minimum and 1 is the maximum normalised fluorescence value (D) Whole heart epicardial ANF over 60 perfusion of DOX 1 (red line) or 10 µM (cayenne line) compared to control (black line) n = 6. Blue dashed line indicates baseline. Data is represented as mean ± *SEM*. Two-way repeated measures ANOVA with Bonferroni's multiple comparisons test **p* < 0.05 ****p* < 0.001 compared to control.

6.3.4 The effect of a metabolic challenge on mitochondrial function in Langendorff-perfused rat hearts pre-perfused with DOX

Left atrial pacing was used to investigate the effect of a metabolic challenge on mitochondrial function in Langendorff-perfused rat hearts pre-perfused with DOX. Before examining the effect of pacing on DOX-perfused hearts the maximum pacing threshold at which pacing would be captured by rat hearts and the effect of pacing alone on normalised TMRM fluorescence in control hearts was determined. As part of the Langendorff preparation for optical mapping of mitochondrial function all study hearts were paced at 400 BPM to keep the metabolic demand consistent between experiments. To examine the effect of a metabolic challenge of a HR above 400 BPM on mitochondrial function control rat hearts were paced for 20 min at 500 BPM following baseline (Fig. 6.16A). Once it was observed that hearts on this preparation would capture at 500 BPM, as evidenced by ECG traces, hearts were then paced at 600 BPM for 20 min (Fig. 6.16A). Normalised TMRM fluorescence decreased with ramped pacing over time by approximately 12% over 40 min (Fig. 6.16A). The maximum pacing threshold was found to be 600 BPM in Langendorff-perfused rat hearts and this HR was used as a metabolic challenge in hearts that had been pre-perfused with DOX 10 μM for 60 min (Fig. 6.16B). Rat hearts were perfused for 60 min with DOX 10 μM followed by pacing at 600 BPM for 20 min, as a metabolic challenge (Fig. 6.16B). No significant difference in normalised TMRM fluorescence was seen over 20 min pacing at 600 BPM compared to DOX 10 μM perfused alone (Fig. 6.16B). This finding suggests that DOX 10 μM pre-perfusion on this timescale does not render the heart more susceptible to pacing-induced mitochondrial dysfunction.

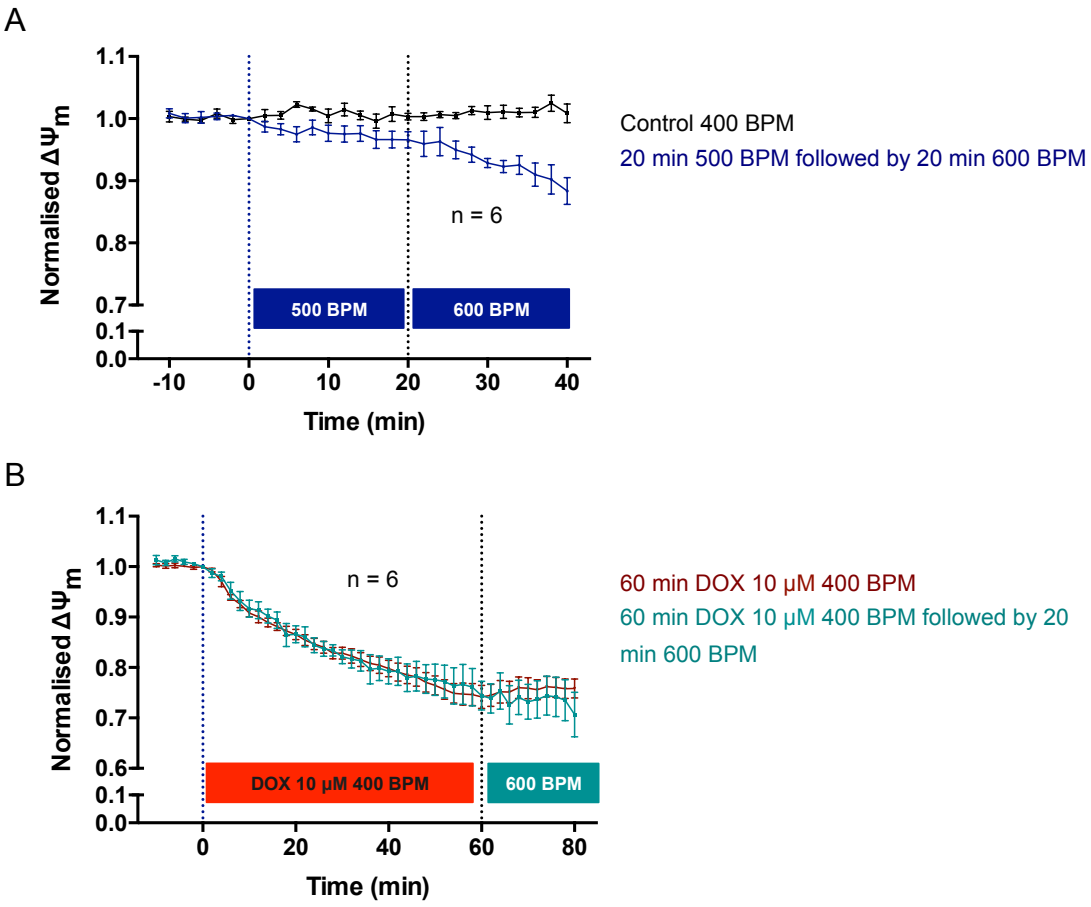


Fig. 6.16 The effect of a metabolic challenge on normalised TMRM fluorescence in Langendorff-perfused rat hearts.
(A) The effect of 20 min pacing at 500 BPM followed by 20 min pacing at 600 BPM (blue line) on normalised TMRM fluorescence in Langendorff-perfused rat hearts as a metabolic challenge compared to control hearts paced at 400 BPM (black line) n = 6 (B) The effect of 60 min perfusion of DOX 10 µM followed by 20 min pacing at 600 BPM (turquoise line) on normalised TMRM fluorescence in Langendorff-perfused rat hearts as a metabolic challenge following DOX perfusion compared to 60 min perfusion of DOX 10 µM alone (cyan line) n = 6. Blue dashed line indicates baseline. Black dashed line indicates (A) in treated an increase in pacing from 500 BPM to 600 BPM (B) in treated a switch from perfusion of DOX 10 µM to an increase in pacing from 400 BPM to 600 BPM.

6.4 Discussion

6.4.1 *Ex vivo* optical mapping of mitochondrial function in the Langendorff-perfused rat heart

TMRM loading resulted in a robust and stable increase in TMRM fluorescence across the whole epicardial surface in the functioning *ex vivo* rat heart. Perfusion of the mitochondrial-uncoupling agent FCCP resulted in an acute decrease in normalised TMRM fluorescence that did not reach a steady-state fluorescence signal until approximately 1 h after the initial perfusion of FCCP, suggesting that the movement of TMRM out of the mitochondria is a rate-limiting step in the present experimental model. A decrease in normalised TMRM fluorescence in response to FCCP suggests that TMRM can be used as an accurate indicator of the $\Delta\Psi_m$ in the Langendorff-perfused beating rat heart, consistent with previous reports using TMRE and TMRM (Jin et al., 2010; Kato et al., 2009; Lyon et al., 2010; Matsumoto-Ida et al., 2006). Real-time optical mapping of changes in the $\Delta\Psi_m$ allows the simultaneous study of approximately hundreds of millions of cardiac mitochondria and provides a unique insight into cardiac mitochondrial function in the *ex vivo* functioning rat heart.

6.4.2 DOX for *ex vivo* optical mapping of mitochondrial function in the Langendorff-perfused rat heart

DOX itself is a fluorescent compound. In the present study it was found that DOX, at the concentrations and at the excitation and emission wavelength used for *ex vivo* optical mapping of mitochondrial function, increases the fluorescence seen with TMRM alone *in vitro*. In Langendorff-perfused rat hearts DOX 10 μM infusion marginally increased fluorescence over 30 min perfusion in the spectrum examined. The degree of DOX's fluorescence is

dependent on the concentration and excitation light intensity used. The fluorescence of DOX was not assessed in previous *ex vivo* studies examining the effect of DOX on mitochondrial function in isolated rat hearts using JC-1 (Montaigne et al., 2010). The autofluorescence of DOX should be evaluated when using fluorescent compounds to examine the effect of DOX on cardiac function and findings should be interpreted with caution.

6.4.3 Acute progressive concentration-dependent $\Delta\Psi_m$ dissipation with DOX in the Langendorff-perfused rat heart

Normalised TMRM fluorescence decreased over time in DOX 1 µM-perfused rat hearts suggesting progressive $\Delta\Psi_m$ dissipation and acute mitochondrial dysfunction with DOX treatment at a clinically relevant concentration in the *ex vivo* functioning rat heart. No significant changes in normalised TMRM fluorescence were observed in time-matched vehicle-perfused controls. This finding is in agreement with previous reports in the isolated perfused rat heart where DOX 1 µM-perfusion over 60 min was shown to decrease JC-1 fluorescence intensity in a time-dependent manner indicating acute mitochondrial dysfunction with DOX in the *ex vivo* rat heart (Montaigne et al., 2010). Consistent with the present study, Montaigne *et al*. saw a significant decline in JC-1 fluorescence intensity after only 30 min of DOX 1 µM-perfusion, highlighting the reproducibility of the result and similarity between the two independent models. DOX-induced changes in JC-1 fluorescence were observed in the absence of major changes in coronary perfusion pressure (82 ± 2 mm Hg versus 85 ± 4 mm Hg at 60 min perfusion in control and DOX hearts, respectively) (Montaigne et al., 2010). DOX 3 µM-perfusion showed similar results to DOX 1 µM, however DOX 10 µM-perfusion showed a significant decrease in normalised TMRM fluorescence that was progressive over time suggesting that DOX perfusion in the *ex vivo* beating rat heart causes acute progressive concentration-dependent $\Delta\Psi_m$ dissipation and mitochondrial dysfunction. Concentration-

dependent mitochondrial dysfunction in the Langendorff-perfused rat heart is in agreement with clinical findings that the occurrence of anthracycline-induced cardiotoxicity increases with cumulative dose (Jensen et al., 2002; Lefrak et al., 1973; Mulrooney et al., 2009; Swain et al., 2003; Von Hoff et al., 1979).

A decrease rather than an increase in normalised TMRM fluorescence with DOX perfusion gives the possibility that the fluorescence of DOX may be masking a greater decrease in normalised TMRM fluorescence than was observed since

DOX with TMRM 200 nM *in vitro* increased fluorescence intensity in the spectrum examined. However in the present optical mapping system the magnitude of DOX fluorescence is so small compared to the TMRM fluorescence that it is unlikely to have any significant effect on the results. Ideally, one would use a non-active yet still fluorescent control compound to determine the contribution of DOX's autofluorescence to fluorescence intensity in the optical mapping system.

Progressive dissipation of the $\Delta\Psi_m$ in Langendorff-perfused rat hearts suggests acute mitochondrial dysfunction with DOX perfusion. Montaigne *et al*. found that cardiac skinned fibres prepared from DOX 1 μM-perfused heart for 60 min displayed decreased phosphorylation-linked oxygen consumption and increased non-phosphorylation-linked oxygen consumption consistent with DOX's known inhibitory effects on specific elements of the ETC and respiratory enzymes (Davies and Doroshow, 1986; Lebrecht et al., 2003; Nicolay and de Kruijff, 1987). NADH fluorescence intensity has been shown to increase over 60 min in DOX 1 μM-perfused hearts compared to controls (Montaigne et al., 2010). Heart surface NADH autofluorescence reflects mitochondrial NADH/NAD^+ ratio and the mitochondrial energy state (Ashruf et al., 1999). An increase in NADH autofluorescence with

DOX-perfusion suggests dysfunctional electron flux through the ETC and an accumulation of NADH (Montaigne et al., 2010). CsA and the non-immunosuppressive analogue N-Methyl-4-isoleucine cyclosporine reduced DOX-induced $\Delta\Psi_m$ dissipation and NADH autofluorescence in the isolated rat heart suggesting that the mPTP plays a role in acute DOX-induced mitochondrial dysfunction (Montaigne et al., 2010).

6.4.4 The effect of a metabolic challenge on mitochondrial function in Langendorff-perfused rat hearts pre-perfused with DOX

In the present model no significant difference in normalised TMRM fluorescence was seen over 20 min pacing at 600 BPM following 60 min perfusion of DOX 10 μM compared to DOX 10 μM perfused alone. It is possible that a 60 min perfusion of DOX at 10 μM is not sufficient to cause a compromised energy reserve in Langendorff-perfused rat hearts. Since normalised TMRM fluorescence in this model cannot show a recovery in mitochondrial function following insult it is possible that the mitochondria recover once DOX is no longer perfused. In clinical practice exercise testing is often used to induce cardiac dysfunction. Patients with DOX-induced HF are intolerant of a high HR. A reduced energy reserve with DOX-induced cardiotoxicity suggests DOX-treated hearts are more susceptible to metabolic stress (Dekker et al., 1991; Eidenschink et al., 2000). It is possible that a reduced metabolic reserve only occurs over time with DOX treatment, as mitochondrial damage accumulates.

6.4.5 Limitations and future directions

Findings in the isolated unloaded crystalloid perfused heart preparation may not accurately reflect the effects of DOX in the blood-perfused heart and only provide an insight into the possible mechanisms and processing occurring *in vivo*. Since the heart is unloaded the

metabolic requirements of the heart are less; so the metabolic reserve in the Langendorff-perfused rat heart may be greater than the *in vivo* heart. Another disadvantage of the *ex vivo* isolated heart preparation is the lack of neuronal and humoral influence. In addition, it is highly likely that the Langendorff-perfused heart is on the boarder of ischaemia since it has been unperfused during removal from the body. Despite these limitations the established technique allows real-time imaging of changes in the $\Delta\Psi_m$ in the functioning *ex vivo* rat heart. However, measurements of fluorescence in the present model are limited to the epicardial surface of the heart. To measure mitochondrial function in a functioning rat heart in real-time throughout the heart it would be necessary to use $\Delta\Psi_m$-sensitive positron emitting lipophilic cations and positron emission tomography. This would allow the study of mitochondrial function in real-time in the intact whole heart.

6.4.6 Conclusion

DOX perfusion resulted in progressive concentration-dependent $\Delta\Psi_m$ dissipation in the Langendorff-perfused beating rat heart suggesting acute mitochondrial dysfunction with a clinically relevant concentration of DOX. This acute effect indicates that mitochondrial dysfunction may be an early indicator of cardiotoxicity and a potential therapeutic target. Optical mapping of cardiac mitochondrial function in real-time in response to anti-cancer agents provides a unique insight into subcellular physiology in the *ex vivo* functioning heart. This technique may function as a potential screening assay allowing the risk of cardiotoxicity to be established in the functioning heart.

Chapter 7

The acute effect of TKIs on cardiac mitochondrial function

Chapter 7 The acute effect of TKIs on cardiac mitochondrial function

7.1 Introduction

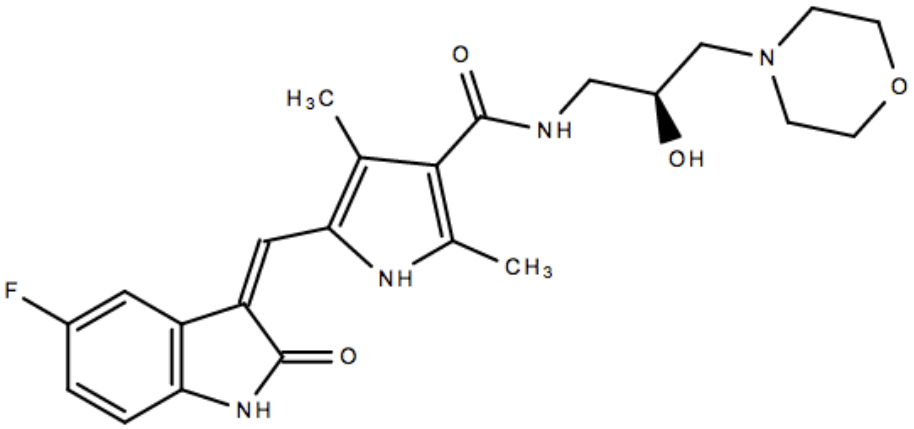
Traditional chemotherapy agents, like DOX, target all rapidly dividing cells whereas modern "targeted therapy" is aimed at cancer cell specific proteins involved in tumour angiogenesis and proliferation. However, despite their name, it has become apparent that targeted therapies have the potential to cause cardiotoxicity (Chu et al., 2007; Kerkela et al., 2006; Kerkela et al., 2009; Schmidinger et al., 2008; Seidman et al., 2002). One such compound reported to cause cardiotoxicity is STB, a receptor TKI approved for the treatment of renal cell carcinoma, pancreatic neuroendocrine tumours and gastrointestinal stromal tumours. Previous studies have examined the effect of STB treatment on cardiac mitochondrial function in NRVM (Chu et al., 2007; Kerkela et al., 2009). Kerkela *et al*. found that NRVM treated with STB 1 μM for 12 h resulted in a reduction in the $\Delta\Psi_m$ and 8 h STB 1 μM treatment resulted in a reduction in cellular ATP concentration (Kerkela et al., 2009). NRVM treated with STB 1 μM for 30 h and 48 h showed diffuse cytochrome c staining, suggesting cytochrome c release from the mitochondria and the initiation of mitochondrial-induced cell death pathways (Chu et al., 2007). Therefore, to further investigate the effect of STB treatment on mitochondrial function the present study examined the effect of 24 h STB treatment on cardiac mitochondrial function using the Mito Stress Test. The Mito Stress Test was used to see if STB treatment over 24 h would have a negative impact on cardiac mitochondrial function. A decrease in the FCCP-stimulated maximal respiration would suggest acute cardiac mitochondrial dysfunction following 24 h STB treatment resulting from STB-induced mitochondrial damage or lose.

STB has previously been investigated in the isolated rat heart preparation (Henderson et al., 2013). Perfusion of STB at increasing concentrations, including 0.01, 0.1, 1 and 10 μM, was found to result in diminished isolated heart function compared to control (Henderson et al., 2013). STB caused statistically significant reductions in the rate of contraction and relaxation and the developed pressure, starting at 0.01 μM through to 10 μM, compared to control (Henderson et al., 2013). End diastolic pressure values were significantly higher with perfusion of 1 μM and 10 μM STB compared to control and HR significantly reduced during perfusion of 1 μM (Henderson et al., 2013). In addition, effluent collected from the heart during the last 5 min of each STB concentration perfusion showed significant increases in troponin T (1 and 10 μM concentrations) and TNFα (0.1, 1 and 10 μM concentrations) compared to control (Henderson et al., 2013). Coronary flow rates declined with STB perfusion, however, the changes in contractility occurred prior to significant reductions in heart perfusion. This indicates reduced contractility, which is not related to coronary flow (Henderson et al., 2013). The contractility effects occurred prior to increases in TNFα (0.01 versus 0.1 μM, respectively) and troponin T (1 μM). Overall, this indicates that the cause of reduced contractility at 0.1 μM may not be attributed to myocyte damage and/or ischaemia and further investigation into STB's effects on ion channels, sarcoplasmic reticulum calcium stores or mitochondrial function is necessary (Henderson et al., 2013). Therefore, in the present study the effect of STB perfusion on cardiac mitochondrial function in the Langendorff-perfused rat heart was examined. In addition, given the known effect of DOX on cardiac mitochondrial function and the proposed effect of STB on cardiac mitochondrial function the effect of combined STB and DOX perfusion on mitochondrial function was examined in the Langendorff-perfused rat heart using optical mapping.

SU is a small molecule with a broad-spectrum receptor TKI activity. SU exerts its inhibitory effects through binding to and inhibition of VEGFR1-VEGFR3, PDGFRα and PDGFRβ, Kit

and Flt-3; receptor tyrosine kinases also inhibited by STB (Force et al., 2007; Patyna et al., 2006). SU was identified from the same chemical library used to isolate STB and has a similar chemical structure (Fig. 7.1) and target profile to STB (Mendel et al., 2003; O'Farrell et al., 2003; Patyna et al., 2006). SU was developed as a next-generation TKI following STB (Hu-Lowe et al., 2011). In a phase I dose-escalation study to investigate SU in adults with solid tumours a patient pre-treated with anthracyclines died due to cardiac failure and myocardial infarction (Fiedler et al., 2011). This was considered to be potentially related to SU treatment; the patient had a particularly high SU plasma concentration (1020-1600 ng/ml; target concentration 100-200 ng/ml). The patient was treated with 150 mg/day continuous daily dosing (CDD). For future studies the maximum tolerated dose and recommended phase II dose was established as 100 mg/day CDD with the possibility of increasing to 150 mg/day. Two further trials with SU were conducted: a phase I trial in patients with solid tumours in combination with docetaxel (de Jonge et al., 2011); and a phase II single-agent trial in patients with metastatic breast carcinoma (clinicaltrials.gov: NCT00322517). An inclusion criterion for the phase II trial included prior treatment with an anthracycline either concurrently or sequentially in the adjuvant and/or advanced disease treatment setting. Following completion of the phase II trial the development of SU was terminated. The compound SU was provided to the Lyon lab as part of a research collaboration with Pfizer Inc. examining the effect of TKIs on mitochondrial function *ex vivo*. Therefore, in the present study the effect of SU infusion on mitochondrial function in the intact heart was examined.

Sunitinib



SU14813

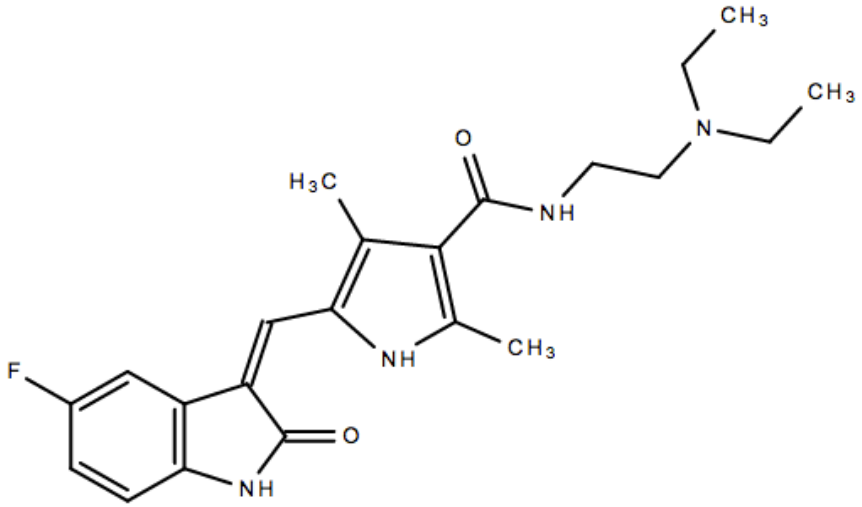


Fig. 7.1 The chemical structure of the TKIs STB and SU.

7.2 Hypothesis and aims

I hypothesis that 24 h STB treatment of ARVM alters cardiac mitochondrial function and that infusion of TKIs in the Langendorff preparation will cause an immediate concentration-dependent $\Delta\Psi_m$ depolarisation that is more significant in combination with DOX.

The aims of this chapter are as follows:

1. Examine the effect of 24 h STB treatment on cardiac mitochondrial function in ARVM using the Mito Stress Test
2. Assess the acute concentration-dependent effect of infusion of TKIs alone and in combination with DOX on mitochondrial function in the Langendorff-perfused beating rat heart using optical mapping

7.3 Results

7.3.1 The effect of 24 h STB treatment on the mitochondrial respiratory capacity of ARVM

To assess the acute effect of STB treatment on cardiac mitochondrial function freshly isolated ARVM were incubated for 24 h with STB 1 μM. Following 24 h STB 1 μM treatment the medium was changed to STB free medium and the Mito Stress test was performed. There was no significant difference in the FCCP-stimulated maximal respiration between STB-treated and control ARVM (Fig. 7.2), suggesting that STB 1 μM treatment over 24 h in this assay does not impair cardiac mitochondrial function.

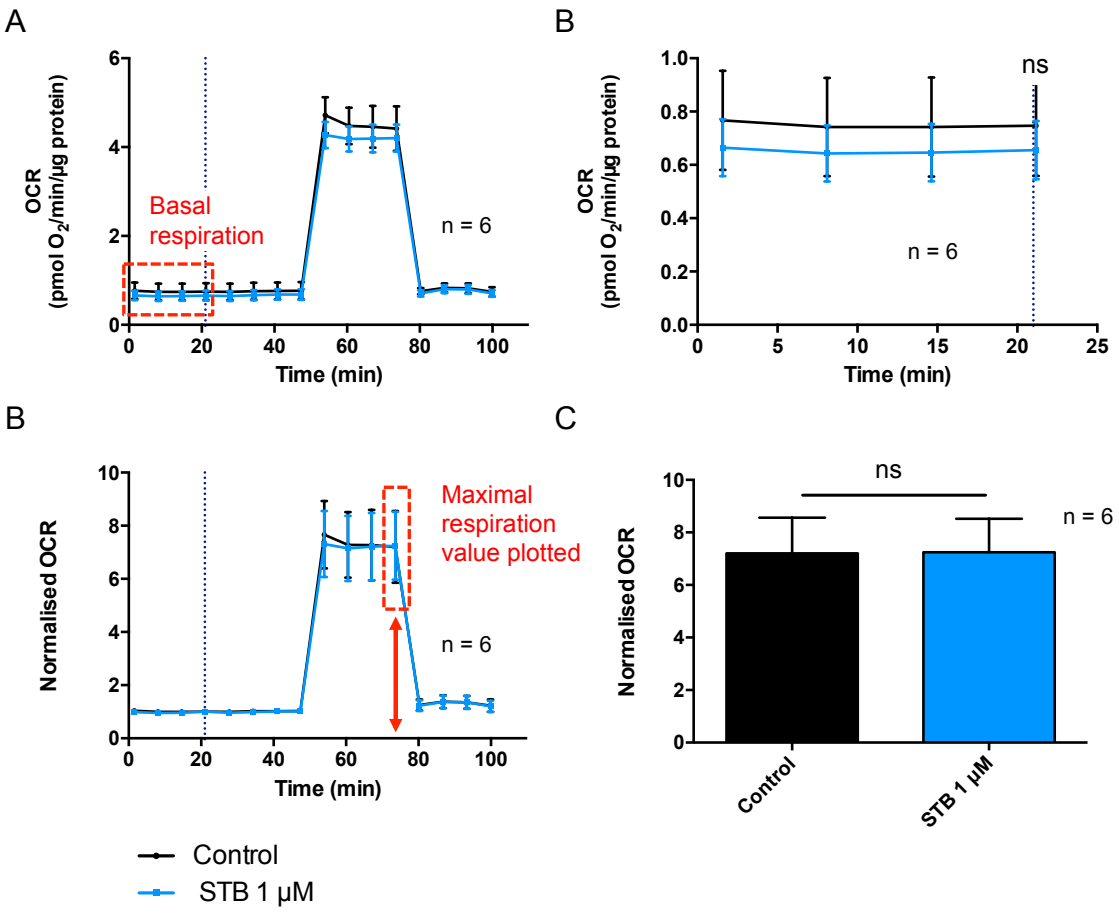


Fig. 7.2 Assessing cardiac mitochondrial function in isolated ARVM with 24 h STB 1 µM treatment.
(A) The total protein corrected OCR of ARVM treated for 24 h with STB 1 µM (blue line) compared to control (black line) during the Mito Stress Test n = 6. Red dashed rectangle indicates basal respiration (B) The basal OCR showing no difference in oxygen consumption at baseline between groups n = 6 (C) The normalised OCR during the Mito Stress Test showing the FCCP-stimulated maximal respiration value as a fold change from basal respiration plotted between groups (red dashed rectangle) n = 6 (D) The normalised OCR of FCCP-stimulated maximal respiration between groups n = 6. Blue dashed line indicates baseline. Data is represented as mean ± *SEM*. Mann-Whitney *U* test ns = not significant compared to control.

7.3.2 The acute effect of TKIs on the $\Delta\Psi_m$ in the Langendorff-perfused rat heart

To examine the acute effect of TKIs on the $\Delta\Psi_m$ Langendorff-perfused beating rat hearts loaded with TMRM were perfused for 60 min with Krebs-Henseleit solution containing SU or STB. The SU plasma concentration required for *in vivo* target inhibition has been previously estimated to be between 100-200 ng/mL (Patyna et al., 2006), which is equivalent to 0.18-0.36 µM. For this reason 0.18 or 0.36 µM of SU was infused over 60 min followed by a 30 min follow-up period in which perfusate was switched to SU-free Krebs-Henseleit solution. Normalised TMRM fluorescence was found to decrease slightly by 4% in SU 0.18 µM-treated hearts and by 10% in SU 0.36 µM-treated hearts after 60 min (Fig. 6.7A). Normalised TMRM fluorescence decreased in a concentration-dependent manner with SU infusion at 0.09, 0.18, 0.36 and 0.54 µM over 60 min (Fig. 6.7B). This data suggests that SU infusion causes a slight concentration-dependent $\Delta\Psi_m$ dissipation in the *ex vivo* beating rat heart.

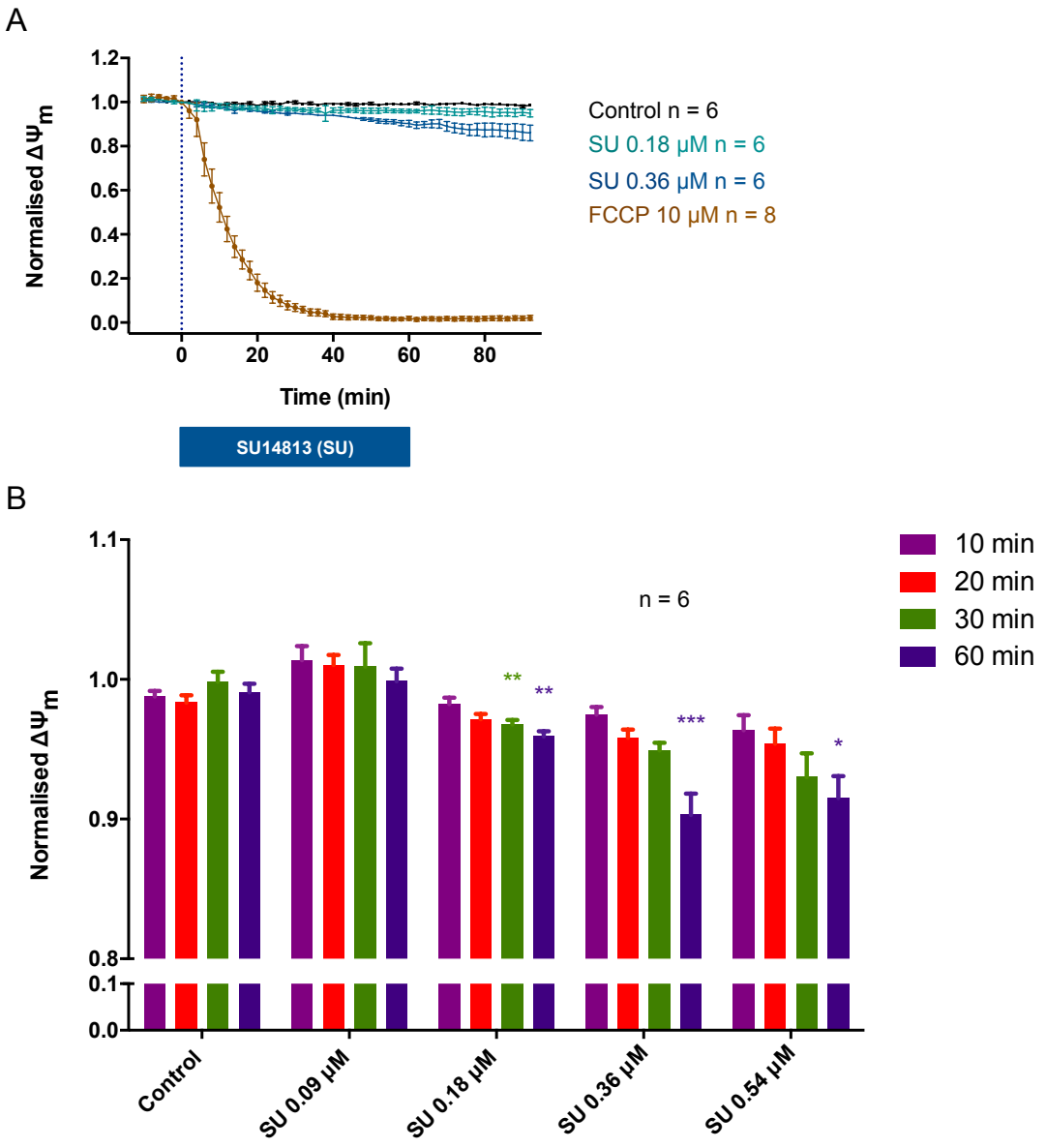


Fig. 7.3 Real-time changes in normalised epicardial TMRM fluorescence with SU perfusion in the Langendorff-perfused rat heart.
(A) Epicardial TMRM fluorescence over 60 min perfusion of SU 0.18 (turquoise line) or 0.36 µM (blue line) compared to time-matched vehicle control (black line) followed by a 30 min follow-up. FCCP 10 µM was perfused over 20 min as a positive control (brown line) n = 8. Blue dashed line indicates baseline (B) Epicardial TMRM fluorescence at 10 (plum), 20 (red), 30 (green) and 60 (blue) min of perfusion of SU at 0.09, 0.18, 0.36 and 0.54 µM compared to time-matched vehicle control n = 6. Data is represented as mean ± *SEM*. Two-way repeated measures ANOVA with Bonferroni's multiple comparisons test **p* < 0.05 ***p* < 0.01 ****p* < 0.001 compared to control.

Blood levels of STB in patients taking the FDA-approved dosage regimen are reported to be between 0.1 - 0.25 μM (Fiedler et al., 2005; Goodman et al., 2007; Motzer et al., 2006), however, the high volume of distribution of STB (2230 L) suggests tissue levels would be higher than those in the blood (Kerkela et al., 2009). Previous *in vitro* and *ex vivo* studies have used between 0.5 - 1 μM of STB as concentrations relevant to the clinical steady-state (Chu et al., 2007; Henderson et al., 2013; Kerkela et al., 2009). Therefore, in the present study 1 μM STB was infused over 60 min followed by a 30 min follow-up period. Normalised TMRM fluorescence was found to decrease slightly by 5% in STB 1 μM-treated hearts after 60 min (Fig. 7.4A). To compare the effect of combined STB and DOX infusion to STB or DOX infusion alone Langendorff-perfused beating rat hearts were perfused with anti-cancer agents in combination or alone over 60 min (Fig. 7.4). Combined 1 μM STB and DOX infusion did not significantly decrease normalised TMRM fluorescence compared to DOX 1 μM infusion alone (Fig. 7.4B).

Overall, these findings suggest that the TKIs SU and STB cause a slight decrease in the $\Delta\Psi_m$ in the Langendorff-perfused rat heart suggesting some mitochondrial dysfunction acutely with SU or STB infusion in the isolated heart. Combined STB and DOX infusion, however, did not result in a greater decrease in normalised TMRM fluorescence compared to DOX alone suggesting a combined infusion, in the present model, does not result in greater mitochondrial dysfunction at the concentrations studied.

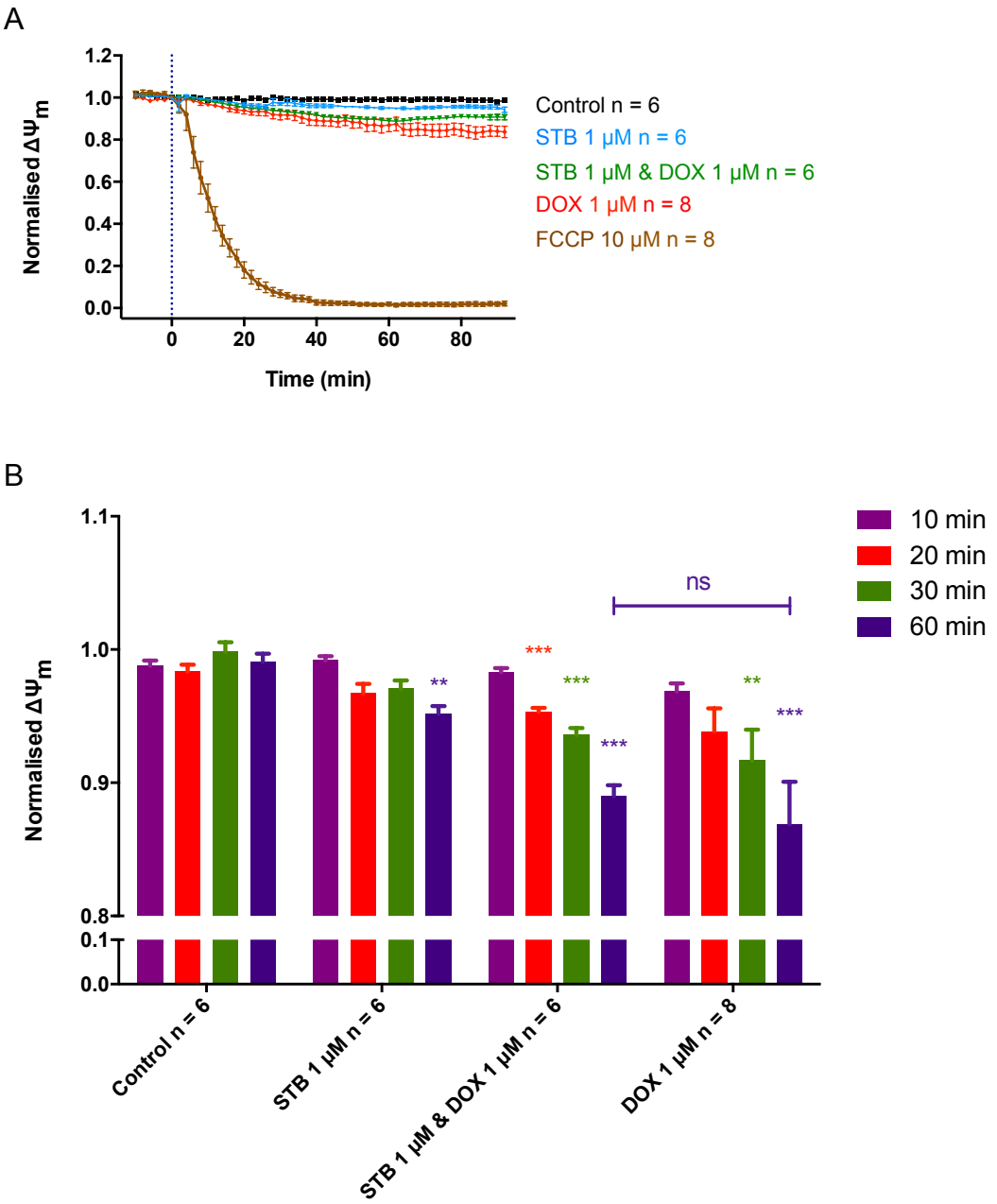


Fig. 7.4 Real-time changes in normalised epicardial TMRM fluorescence with STB perfusion with and without DOX in comparison to DOX alone in the Langendorff-perfused rat heart.
(A) Epicardial TMRM fluorescence over 60 min perfusion of STB 1 μM alone (blue line, n = 6) or STB 1 μM in combination with DOX 1 μM (green line n = 6) or DOX 1 μM alone (red line n = 8) compared to time-matched vehicle control (black line n = 6) followed by a 30 min follow-up. FCCP 10 μM was perfused over 20 min as a positive control (brown line) n = 8. Blue dashed line indicates baseline (B) Epicardial TMRM fluorescence at 10 (plum), 20 (red), 30 (green) and 60 (blue) min of perfusion of STB 1 μM alone (n = 6) or STB 1 μM in combination with DOX 1 μM (n = 6) or DOX 1 μM alone (n = 8) compared to time-matched vehicle control (n = 6). Data is represented as mean ± *SEM*. Two-way repeated measures ANOVA with Bonferroni's multiple comparisons test ns = not significant **$p < 0.01$ ***$p < 0.001$ compared to control.

7.4 Discussion

7.4.1 The effect of 24 h STB treatment on the mitochondrial respiratory capacity of ARVM

STB 1 μM treatment over 24 h had no effect on the FCCP-stimulated maximal respiration of ARVM compared to control. This suggests that STB at this concentration over 24 h has no effect on mitochondrial function as assessed using the Mito Stress Test. Previously findings reported a loss of the $\Delta\Psi_m$ in NRVM treated with STB 1 μM for 12 h (Kerkela et al., 2009). It is possible that early mitochondrial dysfunction with STB treatment cannot be detected using the Mito Stress Test and it is necessary to assess mitochondrial function following a longer treatment period.

Studies performed in isolated rat heart mitochondria have found that STB only impairs mitochondrial function at concentrations greater than 1 μM (Will et al., 2008). STB has been shown to reduce sarcoplasmic reticulum calcium stores and calcium transients at 0.3 μM in isolated cultured guinea pig myocytes (Qian and Guo, 2010). Reduced sarcoplasmic reticulum calcium stores and calcium transients could be responsible for the reduced rate of contraction, relaxation and magnitude of contraction seen in the isolated rat heart with STB infusion (Henderson et al., 2013). Dysfunctional calcium homeostasis and mitochondrial calcium overload may affect mitochondrial function with STB treatment over time. The precise sequence of events leading to mitochondrial injury observed with STB treatment remains unclear and is probably multifactorial. However, given findings in isolated mitochondria, it seems that STB-induced mitochondrial dysfunction is not direct and findings in the present study suggest that changes in mitochondrial function in isolated myocytes are not present acutely with a clinically relevant concentration of STB.

7.4.2 The acute effect of TKIs on the $\Delta\Psi_m$ in the Langendorff-perfused rat heart

Normalised TMRM fluorescence decreased in a concentration-dependent manner with SU infusion at 0.09, 0.18, 0.36 and 0.54 μM over 60 min. This data suggests that SU infusion causes a slight concentration-dependent $\Delta\Psi_m$ dissipation in the *ex vivo* beating rat heart. The compound SU is closely related to STB (Patyna et al., 2006). Normalised TMRM fluorescence was found to decrease slightly in STB 1 μM-treated hearts after 60 min. Previously, STB 1 μM infusion in the isolated rat heart has been found to result in reduced coronary flow rates (Henderson et al., 2013). Therefore, it is possible that the effects of SU and STB on normalised TMRM fluorescence in the present study may reflect changes in coronary perfusion rather than direct mitochondrial dysfunction. Previous studies in the Langendorff-perfused rat found that STB-treated hearts had an impaired response to the endothelium-dependent vasodilator bradykinin, the endothelium-independent vasodilator sodium nitroprusside and the vasoconstrictor angiotensin II and that all of the responses normalised after discontinuation of STB treatment (Kappers et al., 2010). These findings suggest that exposure to STB is associated with impaired function of vascular smooth muscle (Kappers et al., 2010), however it is unclear whether this is due to inhibition of VEGF signalling and/or interaction of STB with other target receptors such as PDGFRβ. VEGF has been shown to activate endothelial NO synthase which leads to increased vasodilatory NO production in coronary arteries (Ku et al., 1993; Robinson et al., 2010). VEGF signalling inhibition by STB may result in vasoconstriction of the coronary circulation resulting in reduced coronary flow rates. Vasoconstriction may cause ischaemia which is known to cause depolarisation of the $\Delta\Psi_m$ and a decrease in normalised TMRM fluorescence in the Langendorff-perfused rat heart (Jin et al., 2010; Lyon et al., 2010). It is possible that TKI infusion results in changes in coronary flow that may cause slight ischaemia resulting in mitochondrial damage and $\Delta\Psi_m$

dissipation. Therefore, a slight decrease in normalised TMRM fluorescence with TKI infusion may be indicative of vasoconstriction rather than direct TKI-induced mitochondrial toxicity. As the heart was submerged in the optical mapping chamber for these studies it was not possible to measure the coronary flow rate via the effluent. The Langendorff perfusion setup was also a flow driven system, therefore, to assess the coronary flow rate future studies would need to assess the aortic cannular pressure with TKI infusion.

Combined 1 μM STB and DOX infusion over 60 min in the Langendorff-perfused rat heart did not significantly decrease normalised TMRM fluorescence compared to DOX 1 μM infusion alone. This data suggests that a combined infusion, in the present model, does not result in greater mitochondrial dysfunction or that it is not possible to detect a cumulative effect of STB and DOX on mitochondrial function in the present model.

7.4.3 Limitations and future directions

The present study only examined the acute effect of STB treatment on cardiac mitochondrial function. It is likely that mitochondrial dysfunction accumulates with STB treatment. Therefore, it would be informative in future studies to access mitochondrial function with chronic STB treatment in the presence of mitochondrially-targeted protective agents.

Clinically patients who receive anti-cancer treatment and present with cardiotoxicity usually receive DOX treatment prior to STB. To examine the effect of combined therapy in the isolated heart in future studies it may be informative to pre-treat with DOX before treating with STB.

7.4.4 Conclusion

Twenty-four h STB 1 μM treatment had no effect on the FCCP-stimulated maximal respiration of ARVM compared to control suggesting that STB, in the present assay, does not directly effect cardiac mitochondrial function in isolated myocytes over 24 h. Infusion of the TKI SU resulted in a slight concentration-dependent decrease in normalised TMRM fluorescence, at clinically relevant concentrations, over time in the Langendorff-perfused beating rat heart. Similarly, STB 1 μM infusion resulted in a small decrease in normalised TMRM fluorescence. This data suggests that there is some mitochondrial dysfunction in the intact functioning rat heart with acute TKI infusion. Whether this mitochondrial dysfunction results from effects of the TKI on coronary perfusion or other pathophysiological processes or direct mitochondrial damage remains unknown.

Chapter 8

Final discussion

Chapter 8 Final discussion

8.1 Overview

A growing cancer survivorship population means cardiac dysfunction as a result of the agents used to treat cancer is becoming increasingly clinically relevant. The clinical success of anti-cancer agents against a wide array of cancers means the use and development of these therapies will continue for the foreseeable future. At present the strategies to limit and treat cardiac dysfunction include restricting anti-cancer agent dose, withdrawing treatment upon presentation of cardiotoxicity, both of which damage cancer prognosis, and institution of standard HF therapy. The use of anti-oxidants to protect against cardiotoxicity has proved ineffective, at least in part, because ROS-induced cytotoxicity is a mechanism for both cardiotoxicity and tumoricidal activity resulting in an association of secondary malignancies with a combination of anti-oxidant and chemotherapeutic treatment (Salzer et al., 2010; Tebbi et al., 2007). The development of therapeutic strategies that limit cardiotoxicity while maintaining anti-cancer efficiency is critical to the long-term comorbidity of cancer patients and requires a greater understanding of the processes that lead to cardiac dysfunction. A common final organelle which is frequently affected by this toxicity and which is crucial to healthy myocardial function is the mitochondrion. This thesis presents data that supports the intrinsic role of mitochondrial dysfunction to the pathogenesis of anti-cancer agent-induced cardiotoxicity and highlights cardiac mitochondria as a target for cardioprotection.

8.2 The chronic effect of DOX treatment on the myocardium and cardiac mitochondria

Eight weekly doses of a clinically relevant concentration of DOX resulted in reproducible and progressive LV dysfunction in male SD rats, consistent with a previous study using the same dosing regimen in Hannover Wistar rats (Cove-Smith et al., 2014). RNA-seq of LV tissue showed a significant decrease in the abundance of transcripts related to mitochondrial structure and function including those that function within the ETC and fatty acid oxidation. Transmission electron micrographs of LV tissue showed disrupted and abnormal mitochondrial morphology with chronic DOX treatment indicating mitochondrial damage and dysfunction. Relative mtDNA content was found to be decreased with chronic DOX treatment suggesting that mtDNA depletion contributes to respiratory chain defects in chronic DOX-induced cardiomyopathy (Lebrecht et al., 2003). A significant decrease in mitochondrial-related transcripts, mtDNA depletion and abnormal mitochondrial morphology is consistent with severe mitochondrial dysfunction and suggests compromised energy production with chronic DOX treatment. Previously reports have shown that the ATP content in the heart is depleted after treatment of animals with DOX (Dekker et al., 1991; Ferrero et al., 1976; Kawasaki et al., 1996).

The mechanisms involved in chronic DOX-induced mitochondrial dysfunction are multifactorial and appear to progress from direct ETC inhibition and redox cycling within the IMM to mtDNA and nuclear DNA damage. The findings in the present study are consistent with multifactorial processes taking place, such as mitochondrial iron accumulation and mtDNA and nuclear DNA damage, that accumulate to result in a phenotype of compromised mitochondrial function. The fact that cardiac dysfunction can appear decades after therapy, particularly in childhood survivors of cancer (Lipshultz et al., 2005; Mulrooney et al., 2009;

Steinherz et al., 1991), suggests that damage accumulates in the absence of DOX treatment with progressive irreversible dysfunction likely as a result of DNA damage, consistent with findings in the present *in vivo* model.

As well as mitochondrial dysfunction, RNA-seq data highlights other pathways through which DOX induces cardiotoxicity. RNA-seq data showed a significant increase in transcript levels related to inflammation and the immune response in DOX-induced cardiomyopathy. An upregulation in pro-inflammatory factors is consistent with histological findings suggesting macrophage infiltration and fibroblast activation in DOX-treated tissue compared to control. Functional annotation analysis showed an upregulation of leukocyte activation. Leukocyte activation is consistent with pathological observations of infiltration of mononuclear cells. Similarly, the increased transcript levels of genes involved in ECM remodelling and cell adhesion suggests remodelling and fibrosis which is consistent with increased vimentin staining in DOX-treated compared to control suggesting fibroblast activation. Together, this data highlights the role of inflammation and fibrosis in the pathogenesis of chronic DOX-induced myocardial dysfunction and HF.

Transcript levels of *Ryr2* and *Atp2a2* were significantly decreased in DOX-treated samples. DOX has previously been shown to have a direct effect on RyR2 and SERCA2A activity resulting in a disruption to calcium handling (Hanna et al., 2014). Direct disruption of intracellular calcium handling may lead to calcium overload, contractile dysfunction and myofibrillar deterioration as seen in transmission electron micrographs from DOX-treated rats. Calcium overload is known to contribute to mitochondrial dysfunction and may play a role in DOX-induced mPTP opening.

8.3 The acute effect of anti-cancer agents on cardiac mitochondrial function

Ex vivo optical mapping of mitochondrial function showed a progressive decrease in normalised TMRM fluorescence in real-time upon infusion of DOX, at a clinically relevant concentration, suggesting acute mitochondrial dysfunction with DOX treatment in the intact functioning rat heart. Of the proposed mechanisms of acute DOX-induced mitochondrial dysfunction, ETC inhibition by interaction with cardiolipin and redox cycling of DOX within mitochondria seem the most likely cause of direct mitochondrial damage that would result in dissipation of the $\Delta\Psi_m$ immediately upon DOX infusion. Twenty-four h 10 μM DOX treatment of ARVM resulted in a significant decrease in cardiac mitochondrial function that was accompanied by a significant increase in transcript levels of mitochondrial related genes including those that function in the respiratory chain, fatty acid metabolism and cardiac mitochondrial iron export. Although 24 h 3 μM DOX treatment of ARVM did not affect cardiac mitochondrial function it did increase transcript levels of mitochondrial-related genes suggesting DOX at this concentration does trigger compensatory mechanisms to preserve mitochondrial function. Together this data suggests that DOX has an acute effect on cardiac mitochondria that can limit their function at high doses and at clinically relevant concentrations triggers a compensatory increase in transcript levels of genes related to mitochondrial function.

In addition to mitochondrial dysfunction, 24 h DOX treatment of ARVM resulted in an increase in transcript levels of *Nppa* and *Atp2a2* and a decrease in transcript levels of *Xdh* and *Hmox*. An increase in *Atp2a2* transcript levels may reflect a compensatory response to increase SERCA2A expression since DOX's metabolic product, doxorubicinol, has been reported to disrupt SERCA2A activity (Hanna et al., 2014).

The TKIs STB and SU were found to cause a smaller decrease in normalised TMRM fluorescence in the intact heart. This decrease may result from “on target” toxicity possibly via inhibition of VEGFR2 and vasoconstriction rather than direct mitochondrial damage. Twenty-four h STB treatment of ARVM had no effect on cardiac mitochondrial function consistent with previous reports that STB had no direct effect on isolated mitochondria (Will et al., 2008). This data suggests that STB-induced mitochondrial structural abnormalities result from indirect mitochondrial toxicity via on-target angiogenesis pathway inhibition and/or from off-target effects such as inhibition of AMPK or RSK.

8.4 The acute versus chronic effect of DOX treatment on myocardial and cardiac mitochondrial function

Twenty-four h DOX treatment of ARVM resulted in an increase in mitochondrial-related transcript levels, a decrease in ROS-related transcript levels (*Xdh* and *Hmox1*) and an increase in *Atp2a2* transcript levels. In contrast, with chronic DOX administration followed by a period of off-dosing mitochondrial-related transcript levels were significantly decreased, ROS-related transcript levels were increased (*Cybb*, *Xdh* and *Hmox1*) and *Atp2a2* and *Ryr2* transcript levels were decreased. Of the transcript levels examined with acute and chronic DOX treatment only *Nppa* showed increased levels consistently. This suggests that acutely, at least on a transcriptional level, DOX-induced damage triggers a compensatory response, whereas, after chronic exposure to DOX the reduction in transcript levels related to mitochondrial function and calcium handling suggest that dysfunction is progressive. This data may also indicate different mechanisms involved in acute and chronic DOX-induced mitochondrial dysfunction.

A biophysical systems approach has been used to study the mechanisms of DOX-induced mitochondrial cardiotoxicity to quantify the contributions of alterations in ETC activity, ROS production and mtDNA damage to acute and chronic mitochondrial dysfunction with DOX treatment (de Oliveira and Niederer, 2016). Using a computational model based on experimental data it was observed that ETC inhibition and redox cycling were not sufficient to explain long-term and progressive mitochondrial dysfunction associated with DOX treatment (de Oliveira and Niederer, 2016). Mitochondrial function returned to baseline following DOX withdrawal suggesting different mechanisms in acute and chronic DOX-induced mitochondrial dysfunction (de Oliveira and Niederer, 2016). It was found that introducing direct mtDNA damage was necessary to model progressive and irreversible long-term mitochondrial dysfunction for therapeutic doses of DOX (de Oliveira and Niederer, 2016). A limitation of this *in silico* study was that it only modelled ETC activity, ROS production and mtDNA damage which does not represent the *in vivo* context of DOX-induced dysfunction. This means experimental conditions are simplified and may omit other mechanisms involved in DOX-induced mitochondrial toxicity. It remains to be seen if by protecting cardiac mtDNA and most likely also nuclear encoded mitochondrial related transcripts it is possible to preserve mitochondrial function and ameliorate some LV dysfunction with DOX treatment.

8.5 Model limitations

The current *in vivo* model offers a clinically relevant rat model of DOX-induced cardiomyopathy. However, this model does not take into account the effect of cancer itself on myocardial function. DOX was administered to cancer-free rats. Cancer itself has been reported to have adverse effects on cardiac function (Cramer et al., 2014; Pavo et al., 2015; Springer et al., 2014). Future studies may wish to model the combined effect of cancer and anti-cancer therapy on myocardial function.

In vitro work offers the potential to study the mechanisms of anti-cancer agent induced dysfunction on a cellular level. However, the present model was limited in that adult rat cardiomyocytes, although more clinically relevant than immortal cardiac cell lines, do not survive well in culture. This meant *in vitro* studies were limited to 24 h following isolation. Using this cell type and experimental protocol it was not possible to examine cardiac mitochondrial function over longer periods of time.

Ex vivo optical mapping of mitochondrial function allows the examination of the real-time changes in the Ψ_m in the functioning rat heart. However, a limitation of this model is that it uses fluorescence to assess changes in the Ψ_m. This means that the effect of fluorescent compounds need to be considered when interpreting results. In addition, the Langendorff-perfused rat heart deteriorates over time and studies are limited to 3 h following heart extraction. Although this model provides an insight into the acute effects of anti-cancer agents on cardiac mitochondrial function it cannot be used to study reversibility of damage caused or the effects of a duration of greater than 3 h of perfusion.

8.6 Future directions

Anthracycline-induced chemotherapy cardiomyopathy remains a huge challenge in oncology. The multifactorial nature of DOXs effects and the domino effect that each molecular event may trigger (Fig. 8.1) may explain why there is a lack of effective cardioprotective agents available. DOX causes a progressive deterioration of mitochondrial metabolism (Carvalho et al., 2014). Energy compromise is a unifying mechanism of HF yet interventions designed to alter energetics in the failing heart or improve mitochondrial function in HF are limited. The HF medication and β-blocker carvedilol has been reported to protect against DOX-induced cardiotoxicity in clinical practice (Kalay et al., 2006; Spallarossa et al., 2004; Tashakori

Beheshti et al., 2016). Carvedilol's protective effect in DOX-induced cardiotoxicity is postulated to be due to anti-oxidant activity that protects cardiac mitochondria from oxidative injury (Feuerstein and Ruffolo, 1995; Oliveira et al., 2001). The mitochondrial-targeted peptide elamipretide (Bendavia or MTP-131) is proposed to enhance ATP synthesis by stabilising cardiolipin, however the mechanism of action of elamipretide remains unclear (Birk et al., 2013; Brown et al., 2016; Zhao et al., 2004). It has been proposed that elamipretide binds to cardiolipin via electrostatic interaction inhibiting the peroxidase activity of cytochrome c and optimising the ability of the cytochrome c/cardiolipin complex to serve as an electron carrier (Birk et al., 2014; Birk et al., 2013). Elamipretide has been shown to improve LV and mitochondrial function in dogs with advanced HF (Sabbah et al., 2016). These improvements were associated with normalisation of mitochondrial respiration, membrane potential, complex activities and rate of ATP synthesis (Sabbah et al., 2016). As it is known that DOX can inhibit the ETC by binding to cardiolipin in the IMM and that DOX-induced mitochondrial damage results in ATP depletion elamipretide may be protective against DOX-induced mitochondrial dysfunction and cardiac dysfunction. By specifically targeting mitochondrial function for protection in DOX-induced cardiomyopathy it may be possible to tell if mitochondrial dysfunction is a consequence or a primary cause of cardiomyocyte dysfunction.

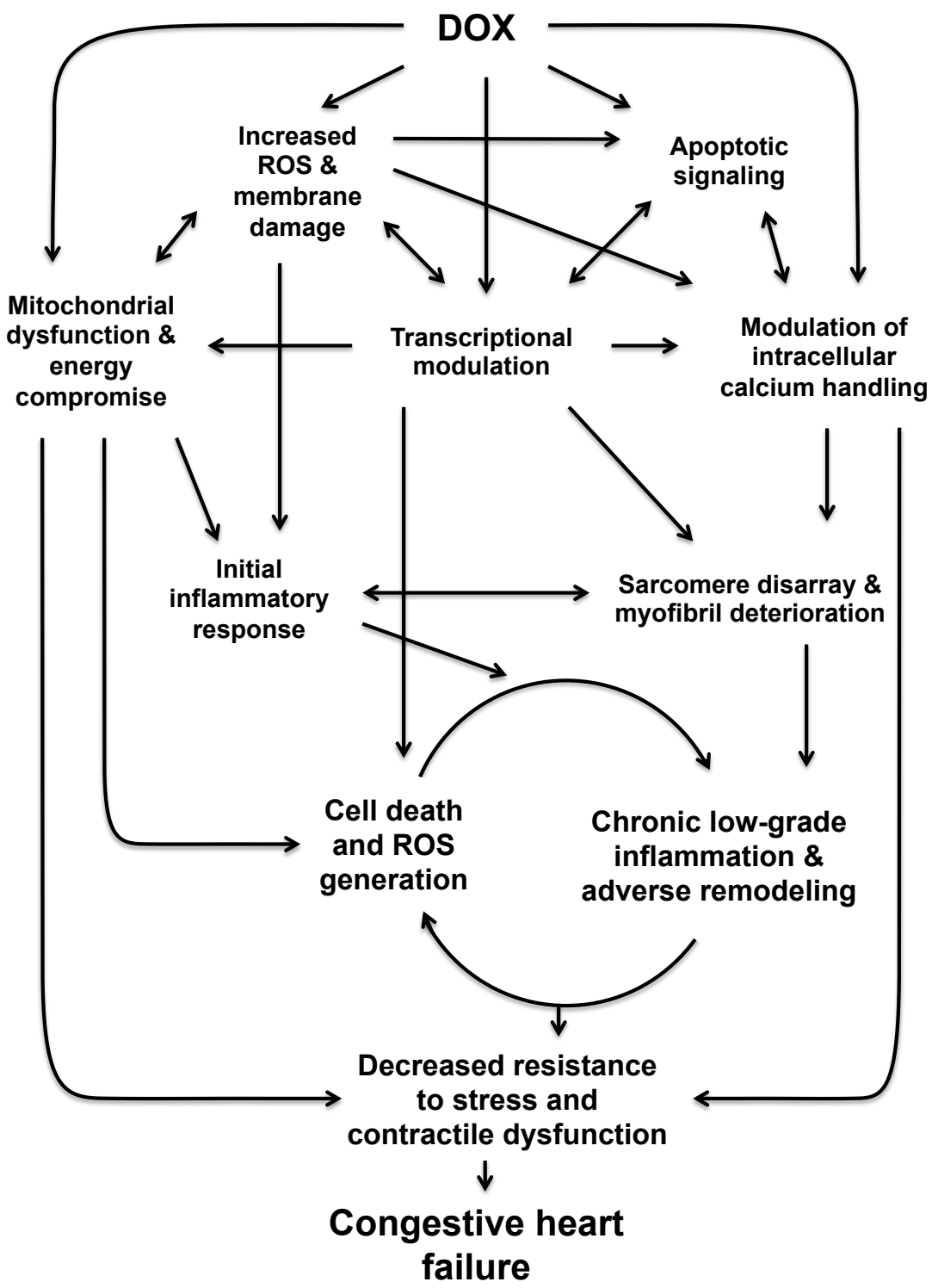


Fig. 8.1 Doxorubicin (DOX): the cellular, molecular and clinical progression of events that leads to DOX-induced chemotherapy cardiomyopathy. The present schematic exemplifies the complexity of the progression of DOX-induced cardiotoxicity from acute events to the delayed toxicity which leads to the development of congestive heart failure. Adapted from Carvalho *et al*.

The mitochondrially-targeted anti-oxidant MitoQ has been shown to be cardioprotective in a rat model of DOX-induced cardiomyopathy (Chandran et al., 2009). Mitochondrially-targeted anti-oxidants could be an important part of the quest for a treatment for DOX-induced HF. ROS scavengers have the potential to prevent the accumulation of mtDNA and respiratory chain defects in chronic DOX cardiomyopathy (Lebrecht et al., 2003). Physical activity has been suggested as a protective strategy used in the treatment and prevention of DOX-induced cardiotoxicity to boost cardiac mitochondrial capacity and upregulate the anti-oxidant systems of the heart (Ascensao et al., 2012; Carvalho et al., 2014; Shimauchi et al., 2017). Targeted agents that could preserve cardiac mitochondrial function without affecting anti-cancer efficiency have the potential to prevent DOX-induced cardiotoxicity.

The prevalence of mitochondrial dysfunction in a number of pathological disorders affecting excitable tissues means a better understanding of the progression of dysfunction would aid the design of interventions. The current *in vivo* rat model of DOX-induced cardiomyopathy could be used to study changes in mitochondrial function over time with intervention aimed at protecting cardiac mitochondria. Although DOX's mechanism of action against cancer is not specifically targeted at mitochondrial function it may be important to DOX's tumoricidal activity.

The present work focuses on DOX-induced mitochondrial dysfunction in the rat. Future studies may wish to examine if similar changes in gene expression are present and as prevalent in human DOX-induced cardiomyopathy. This would allow species differences to be examined.

Early diagnosis and intervention seems crucial to prevent severe cardiac decompensation with DOX treatment. Patients with anthracycline-induced cardiotoxicity who were treated with

HF therapy promptly after detection of cardiac dysfunction showed a significant response to HF treatment. Forty two percent of patients (85 patients out of 201) who received prompt HF treatment had a complete recovery of LVEF and 13% (26 patients out of 201) had a partial recovery of LVEF (Cardinale et al., 2010a). No complete recovery of LVEF was observed when HF treatment was initiated more than 6 months after chemotherapy (Cardinale et al., 2010a). This suggests that early intervention can prevent severe disease progression. Therapies designed to improve mitochondrial dysfunction should, therefore, be administered as soon as possible without compromising cancer treatment.

Early detention of cardiac dysfunction is crucial to outcome. Standard monitoring during treatment with known cardiotoxic agents involves LVEF measurements at baseline and every 3-6 months during therapy and every 6-12 months for at least 2 years thereafter. However, due to the late changes in LVEF with cardiotoxicity, the development of HF with a preserved LVEF and the variability in the measurement of LVEF other strategies to detect dysfunction are required. Since subcellular cardiomyocyte degeneration and mitochondrial dysfunction seem to be the earliest markers of cardiotoxicity (Cove-Smith et al., 2014) serum markers for mitochondrial dysfunction may allow early detection of damage. In addition, patients with more mitochondrial damage may be more susceptible to cardiac dysfunction. Serum markers for mitochondrial dysfunction and cell death have been reported to be possible predictive indicators for drug-induced liver injury (Kakisaka et al., 2017). Therefore, future studies could examine serum markers for mitochondrial dysfunction in the blood of rats receiving DOX.

8.7 Conclusion

Here, I present experiments where a clinically relevant and robust model of DOX-induced cardiomyopathy was used to further understand the pathogenesis and processes involved in

chemotherapy cardiomyopathy. It was found that mitochondrial dysfunction and inflammation play a significant role in the pathogenesis and phenotype of DOX-induced HF. The present *in vivo* rat model could be used to assess treatment strategies aimed at minimising DOX-induced myocardial dysfunction in clinical practice. *In vitro* and *ex vivo* models were further developed in order to examine the acute effect of anti-cancer agents on cardiac mitochondrial function. An *ex vivo* optical mapping system was developed in order to understand the acute processes involved in early dysfunction and could be used in future work to examine mitochondrial function with prior anti-cancer agent treatment. *In vitro* work highlighted the acute effect of DOX on adult cardiomyocytes. Acute models developed in the present work could be used to screen novel anti-cancer agents to allow the risk of mitochondrial dysfunction to be determined prior to clinical use of agents.

References

References

Adachi, K., Y. Fujiura, F. Mayumi, A. Nozuhara, Y. Sugiu, T. Sakanashi, T. Hidaka, and H. Toshima. 1993. A deletion of mitochondrial DNA in murine doxorubicin-induced cardiotoxicity. *Biochem Biophys Res Commun*. 195:945-951.

Adams, M.J., and S.E. Lipshultz. 2005. Pathophysiology of anthracycline- and radiation-associated cardiomyopathies: implications for screening and prevention. *Pediatr Blood Cancer*. 44:600-606.

Agen, C., N. Bernardini, R. Danesi, P. Della Torre, M. Costa, and M. Del Tacca. 1992. Reducing doxorubicin cardiotoxicity in the rat using deferred treatment with ADR-529. *Cancer Chemother Pharmacol*. 30:95-99.

Agrawal, A., and U. Mabalirajan. 2016. Rejuvenating cellular respiration for optimizing respiratory function: targeting mitochondria. *Am J Physiol Lung Cell Mol Physiol*. 310:L103-113.

Akira, S., and K. Takeda. 2004. Toll-like receptor signalling. *Nat Rev Immunol*. 4:499-511.

Alberts, B. 2002. Molecular biology of the cell. Garland Science, New York.

Albini, A., G. Pennesi, F. Donatelli, R. Cammarota, S. De Flora, and D.M. Noonan. 2010. Cardiotoxicity of anticancer drugs: the need for cardio-oncology and cardio-oncological prevention. *J Natl Cancer Inst*. 102:14-25.

Alexeyev, M., I. Shokolenko, G. Wilson, and S. LeDoux. 2013. The maintenance of mitochondrial DNA integrity--critical analysis and update. *Cold Spring Harb Perspect Biol*. 5:a012641.

Andoh, T. 1998. Bis(2,6-dioxopiperazines), catalytic inhibitors of DNA topoisomerase II, as molecular probes, cardioprotectors and antitumor drugs. *Biochimie*. 80:235-246.

Anjum, R., and J. Blenis. 2008. The RSK family of kinases: emerging roles in cellular signalling. *Nat Rev Mol Cell Biol*. 9:747-758.

Arai, M., K. Tomaru, T. Takizawa, K. Sekiguchi, T. Yokoyama, T. Suzuki, and R. Nagai. 1998. Sarcoplasmic reticulum genes are selectively down-regulated in cardiomyopathy produced by doxorubicin in rabbits. *Journal of molecular and cellular cardiology*. 30:243-254.

Arola, O.J., A. Saraste, K. Pulkki, M. Kallajoki, M. Parvinen, and L.M. Voipio-Pulkki. 2000. Acute doxorubicin cardiotoxicity involves cardiomyocyte apoptosis. *Cancer Res*. 60:1789-1792.

Ascensao, A., J. Magalhaes, J.M. Soares, R. Ferreira, M.J. Neuparth, F. Marques, P.J. Oliveira, and J.A. Duarte. 2005. Moderate endurance training prevents doxorubicin-induced in vivo mitochondriopathy and reduces the development of cardiac apoptosis. *Am J Physiol Heart Circ Physiol*. 289:H722-731.

Ascensao, A., P.J. Oliveira, and J. Magalhaes. 2012. Exercise as a beneficial adjunct therapy during Doxorubicin treatment--role of mitochondria in cardioprotection. *Int J Cardiol*. 156:4-10.

Ashley, N., and J. Poulton. 2009a. Anticancer DNA intercalators cause p53-dependent mitochondrial DNA nucleoid re-modelling. *Oncogene*. 28:3880-3891.

Ashley, N., and J. Poulton. 2009b. Mitochondrial DNA is a direct target of anti-cancer anthracycline drugs. *Biochem Biophys Res Commun*. 378:450-455.

Ashruf, J.F., C. Ince, and H.A. Bruining. 1999. Regional ischemia in hypertrophic Langendorff-perfused rat hearts. *Am J Physiol*. 277:H1532-1539.

Asin-Cayuela, J., A.R. Manas, A.M. James, R.A. Smith, and M.P. Murphy. 2004. Fine-tuning the hydrophobicity of a mitochondria-targeted antioxidant. *FEBS Lett*. 571:9-16.

Asselin, B.L., M. Devidas, L. Chen, V.I. Franco, J. Pullen, M.J. Borowitz, R.E. Hutchison, Y. Ravindranath, S.H. Armenian, B.M. Camitta, and S.E. Lipshultz. 2016. Cardioprotection and Safety of Dexrazoxane in Patients Treated for Newly Diagnosed T-Cell Acute Lymphoblastic Leukemia or Advanced-Stage Lymphoblastic Non-Hodgkin Lymphoma: A Report of the Children's Oncology Group Randomized Trial Pediatric Oncology Group 9404. *J Clin Oncol*. 34:854-862.

Aukrust, P., T. Ueland, E. Lien, K. Bendtzen, F. Muller, A.K. Andreassen, I. Nordoy, H. Aass, T. Espevik, S. Simonsen, S.S. Froland, and L. Gullestad. 1999. Cytokine network in congestive heart failure secondary to ischemic or idiopathic dilated cardiomyopathy. *Am J Cardiol*. 83:376-382.

Bachmann, E., E. Weber, and G. Zbinden. 1975. Effects of seven anthracycline antibiotics on electrocardiogram and mitochondrial function of rat hearts. *Agents Actions*. 5:383-393.

Balaban, R.S. 2002. Cardiac energy metabolism homeostasis: role of cytosolic calcium. *Journal of molecular and cellular cardiology*. 34:1259-1271.

Banfor, P.N., P.A. Franklin, J.A. Segreti, D.L. Widomski, S.K. Davidsen, D.H. Albert, B.F. Cox, R.M. Fryer, and G.A. Gintant. 2009. ETA receptor blockade with atrasentan prevents hypertension with the multitargeted tyrosine kinase inhibitor ABT-869 in telemetry-instrumented rats. *J Cardiovasc Pharmacol*. 53:173-178.

Barpe, D.R., D.D. Rosa, and P.E. Froehlich. 2010. Pharmacokinetic evaluation of doxorubicin plasma levels in normal and overweight patients with breast cancer and simulation of dose adjustment by different indexes of body mass. *Eur J Pharm Sci*. 41:458-463.

Barth, E., G. Stammler, B. Speiser, and J. Schaper. 1992. Ultrastructural quantitation of mitochondria and myofilaments in cardiac muscle from 10 different animal species including man. *Journal of molecular and cellular cardiology*. 24:669-681.

Bauernfeind, F.G., G. Horvath, A. Stutz, E.S. Alnemri, K. MacDonald, D. Speert, T. Fernandes-Alnemri, J. Wu, B.G. Monks, K.A. Fitzgerald, V. Hornung, and E. Latz. 2009. Cutting edge: NF-kappaB activating pattern recognition and cytokine receptors license NLRP3 inflammasome activation by regulating NLRP3 expression. *J Immunol*. 183:787-791.

Baughman, J.M., F. Perocchi, H.S. Girgis, M. Plovanich, C.A. Belcher-Timme, Y. Sancak, X.R. Bao, L. Strittmatter, O. Goldberger, R.L. Bogorad, V. Koteliansky, and V.K. Mootha. 2011. Integrative genomics identifies MCU as an essential component of the mitochondrial calcium uniporter. *Nature*. 476:341-345.

Baum, J., and H.S. Duffy. 2011. Fibroblasts and myofibroblasts: what are we talking about? *J Cardiovasc Pharmacol*. 57:376-379.

Bellinger, A.M., C.L. Arteaga, T. Force, B.D. Humphreys, G.D. Demetri, B.J. Druker, and J.J. Moslehi. 2015. Cardio-Oncology: How New Targeted Cancer Therapies and Precision Medicine Can Inform Cardiovascular Discovery. *Circulation*. 132:2248-2258.

Berndt, A., R. Buttner, S. Guhne, A. Gleinig, P. Richter, Y. Chen, M. Franz, and C. Liebmann. 2014. Effects of activated fibroblasts on phenotype modulation, EGFR signalling and cell cycle regulation in OSCC cells. *Exp Cell Res*. 322:402-414.

Berthiaume, J.M., P.J. Oliveira, M.W. Fariss, and K.B. Wallace. 2005. Dietary vitamin E decreases doxorubicin-induced oxidative stress without preventing mitochondrial dysfunction. *Cardiovasc Toxicol*. 5:257-267.

Berthiaume, J.M., and K.B. Wallace. 2007a. Adriamycin-induced oxidative mitochondrial cardiotoxicity. *Cell Biol Toxicol*. 23:15-25.

Berthiaume, J.M., and K.B. Wallace. 2007b. Persistent alterations to the gene expression profile of the heart subsequent to chronic Doxorubicin treatment. *Cardiovasc Toxicol*. 7:178-191.

Bhat, A.H., K.B. Dar, S. Anees, M.A. Zargar, A. Masood, M.A. Sofi, and S.A. Ganie. 2015. Oxidative stress, mitochondrial dysfunction and neurodegenerative diseases; a mechanistic insight. *Biomed Pharmacother*. 74:101-110.

Bianchi, C., A. Bagnato, M.G. Paggi, and A. Floridi. 1987. Effect of adriamycin on electron transport in rat heart, liver, and tumor mitochondria. *Exp Mol Pathol*. 46:123-135.

Birk, A.V., W.M. Chao, C. Bracken, J.D. Warren, and H.H. Szeto. 2014. Targeting mitochondrial cardiolipin and the cytochrome c/cardiolipin complex to promote electron transport and optimize mitochondrial ATP synthesis. *Br J Pharmacol*. 171:2017-2028.

Birk, A.V., S. Liu, Y. Soong, W. Mills, P. Singh, J.D. Warren, S.V. Seshan, J.D. Pardee, and H.H. Szeto. 2013. The mitochondrial-targeted compound SS-31 re-energizes ischemic mitochondria by interacting with cardiolipin. *J Am Soc Nephrol*. 24:1250-1261.

Bjelogrlic, S.K., J. Radic, V. Jovic, and S. Radulovic. 2005. Activity of d,l-alpha-tocopherol (vitamin E) against cardiotoxicity induced by doxorubicin and doxorubicin with cyclophosphamide in mice. *Basic Clin Pharmacol Toxicol*. 97:311-319.

Bodai, B.I., and P. Tuso. 2015. Breast cancer survivorship: a comprehensive review of long-term medical issues and lifestyle recommendations. *Perm J*. 19:48-79.

Bolter, C.P., and K.J. Atkinson. 1988. Maximum heart rate responses to exercise and isoproterenol in the trained rat. *Am J Physiol*. 254:R834-839.

Bonadonna, G., S. Monfardini, M. De Lena, F. Fossati-Bellani, and G. Beretta. 1970. Phase I and preliminary phase II evaluation of adriamycin (NSC 123127). *Cancer Res*. 30:2572-2582.

Bowles, E.J., R. Wellman, H.S. Feigelson, A.A. Onitilo, A.N. Freedman, T. Delate, L.A. Allen, L. Nekhlyudov, K.A. Goddard, R.L. Davis, L.A. Habel, M.U. Yood, C. McCarty, D.J. Magid, E.H. Wagner, and T. Pharmacovigilance Study. 2012. Risk of heart failure in breast cancer patients after anthracycline and trastuzumab treatment: a retrospective cohort study. *J Natl Cancer Inst*. 104:1293-1305.

Bozkurt, B., S.B. Kribbs, F.J. Clubb, Jr., L.H. Michael, V.V. Didenko, P.J. Hornsby, Y. Seta, H. Oral, F.G. Spinale, and D.L. Mann. 1998. Pathophysiologically relevant concentrations of tumor necrosis factor-alpha promote progressive left ventricular dysfunction and remodeling in rats. *Circulation*. 97:1382-1391.

Brand, M.D., and D.G. Nicholls. 2011. Assessing mitochondrial dysfunction in cells. *Biochem J*. 435:297-312.

Bristow, M.R., P.D. Thompson, R.P. Martin, J.W. Mason, M.E. Billingham, and D.C. Harrison. 1978. Early anthracycline cardiotoxicity. *Am J Med*. 65:823-832.

Brown, D.A., J.B. Perry, M.E. Allen, H.N. Sabbah, B.L. Stauffer, S.R. Shaikh, J.G. Cleland, W.S. Colucci, J. Butler, A.A. Voors, S.D. Anker, B. Pitt, B. Pieske, G. Filippatos, S.J. Greene, and M. Gheorghiade. 2016. Expert consensus document: Mitochondrial function as a therapeutic target in heart failure. *Nat Rev Cardiol*.

Bugaisky, L.B., P.G. Anderson, R.S. Hall, and S.P. Bishop. 1990. Differences in myosin isoform expression in the subepicardial and subendocardial myocardium during cardiac hypertrophy in the rat. *Circ Res*. 66:1127-1132.

Bujak, M., and N.G. Frangogiannis. 2009. The role of IL-1 in the pathogenesis of heart disease. *Arch Immunol Ther Exp (Warsz)*. 57:165-176.

Bunting, J.R., T.V. Phan, E. Kamali, and R.M. Dowben. 1989. Fluorescent cationic probes of mitochondria. Metrics and mechanism of interaction. *Biophys J*. 56:979-993.

Burridge, P.W., Y.F. Li, E. Matsa, H. Wu, S.G. Ong, A. Sharma, A. Holmstrom, A.C. Chang, M.J. Coronado, A.D. Ebert, J.W. Knowles, M.L. Telli, R.M. Witteles, H.M. Blau, D. Bernstein, R.B. Altman, and J.C. Wu. 2016. Human induced pluripotent stem cell-derived cardiomyocytes recapitulate the predilection of breast cancer patients to doxorubicin-induced cardiotoxicity. *Nat Med*. 22:547-556.

Cappelli, V., R. Moggio, E. Monti, L. Paracchini, F. Piccinini, and C. Reggiani. 1989. Reduction of myofibrillar ATPase activity and isomyosin shift in delayed doxorubicin cardiotoxicity. *Journal of molecular and cellular cardiology*. 21:93-101.

Capranico, G., S. Tinelli, C.A. Austin, M.L. Fisher, and F. Zunino. 1992. Different patterns of gene expression of topoisomerase II isoforms in differentiated tissues during murine development. *Biochim Biophys Acta*. 1132:43-48.

Cardinale, D., A. Colombo, G. Bacchiani, I. Tedeschi, C.A. Meroni, F. Veglia, M. Civelli, G. Lamantia, N. Colombo, G. Curigliano, C. Fiorentini, and C.M. Cipolla. 2015. Early detection of anthracycline cardiotoxicity and improvement with heart failure therapy. *Circulation*. 131:1981-1988.

Cardinale, D., A. Colombo, G. Lamantia, N. Colombo, M. Civelli, G. De Giacomi, M. Rubino, F. Veglia, C. Fiorentini, and C.M. Cipolla. 2010a. Anthracycline-induced cardiomyopathy: clinical relevance and response to pharmacologic therapy. *J Am Coll Cardiol*. 55:213-220.

Cardinale, D., A. Colombo, M.T. Sandri, G. Lamantia, N. Colombo, M. Civelli, G. Martinelli, F. Veglia, C. Fiorentini, and C.M. Cipolla. 2006. Prevention of high-dose chemotherapy-induced cardiotoxicity in high-risk patients by angiotensin-converting enzyme inhibition. *Circulation*. 114:2474-2481.

Cardinale, D., A. Colombo, R. Torrisi, M.T. Sandri, M. Civelli, M. Salvatici, G. Lamantia, N. Colombo, S. Cortinovis, M.A. Dessanai, F. Nole, F. Veglia, and C.M. Cipolla. 2010b. Trastuzumab-induced cardiotoxicity: clinical and prognostic implications of troponin I evaluation. *J Clin Oncol*. 28:3910-3916.

Carvalho, C., R.X. Santos, S. Cardoso, S. Correia, P.J. Oliveira, M.S. Santos, and P.I. Moreira. 2009. Doxorubicin: the good, the bad and the ugly effect. *Curr Med Chem*. 16:3267-3285.

Carvalho, F.S., A. Burgeiro, R. Garcia, A.J. Moreno, R.A. Carvalho, and P.J. Oliveira. 2014. Doxorubicin-induced cardiotoxicity: from bioenergetic failure and cell death to cardiomyopathy. *Med Res Rev*. 34:106-135.

Casali, C., F.M. Santorelli, G. D'Amati, P. Bernucci, L. DeBiase, and S. DiMauro. 1995. A novel mtDNA point mutation in maternally inherited cardiomyopathy. *Biochem Biophys Res Commun*. 213:588-593.

Cassel, S.L., S.C. Eisenbarth, S.S. Iyer, J.J. Sadler, O.R. Colegio, L.A. Tephly, A.B. Carter, P.B. Rothman, R.A. Flavell, and F.S. Sutterwala. 2008. The Nalp3 inflammasome is essential for the development of silicosis. *Proc Natl Acad Sci U S A*. 105:9035-9040.

Champoux, J.J. 2001. DNA topoisomerases: structure, function, and mechanism. *Annu Rev Biochem*. 70:369-413.

Chance, B., H. Sies, and A. Boveris. 1979. Hydroperoxide metabolism in mammalian organs. *Physiol Rev*. 59:527-605.

Chandran, K., D. Aggarwal, R.Q. Migrino, J. Joseph, D. McAllister, E.A. Konorev, W.E. Antholine, J. Zielonka, S. Srinivasan, N.G. Avadhani, and B. Kalyanaraman. 2009. Doxorubicin inactivates myocardial cytochrome c oxidase in rats: cardioprotection by Mito-Q. *Biophys J*. 96:1388-1398.

Chatham, J.C., J.P. Cousins, and J.D. Glickson. 1990. The relationship between cardiac function and metabolism in acute adriamycin-treated perfused rat hearts studied by 31P and 13C NMR spectroscopy. *Journal of molecular and cellular cardiology*. 22:1187-1197.

Chaudhary, K.W., E.I. Rossman, V. Piacentino, 3rd, A. Kenessey, C. Weber, J.P. Gaughan, K. Ojamaa, I. Klein, D.M. Bers, S.R. Houser, and K.B. Margulies. 2004. Altered myocardial Ca2+ cycling after left ventricular assist device support in the failing human heart. *J Am Coll Cardiol*. 44:837-845.

Chen, J., J.B. Long, A. Hurria, C. Owusu, R.M. Steingart, and C.P. Gross. 2012. Incidence of heart failure or cardiomyopathy after adjuvant trastuzumab therapy for breast cancer. *J Am Coll Cardiol*. 60:2504-2512.

Chen, W., and N.G. Frangogiannis. 2013. Fibroblasts in post-infarction inflammation and cardiac repair. *Biochim Biophys Acta*. 1833:945-953.

Chintalgattu, V., D. Ai, R.R. Langley, J. Zhang, J.A. Bankson, T.L. Shih, A.K. Reddy, K.R. Coombes, I.N. Daher, S. Pati, S.S. Patel, J.S. Pocius, G.E. Taffet, L.M. Buja, M.L. Entman, and A.Y. Khakoo. 2010. Cardiomyocyte PDGFR-beta signaling is an essential component of the mouse cardiac response to load-induced stress. *J Clin Invest*. 120:472-484.

Chiong, M., Z.V. Wang, Z. Pedrozo, D.J. Cao, R. Troncoso, M. Ibacache, A. Criollo, A. Nemchenko, J.A. Hill, and S. Lavandero. 2011. Cardiomyocyte death: mechanisms and translational implications. *Cell Death Dis*. 2:e244.

Chu, T.F., M.A. Rupnick, R. Kerkela, S.M. Dallabrida, D. Zurakowski, L. Nguyen, K. Woulfe, E. Pravda, F. Cassiola, J. Desai, S. George, J.A. Morgan, D.M. Harris, N.S. Ismail, J.H. Chen, F.J. Schoen, A.D. Van den Abbeele, G.D. Demetri, T. Force, and M.H. Chen. 2007. Cardiotoxicity associated with tyrosine kinase inhibitor sunitinib. *Lancet*. 370:2011-2019.

Chugun, A., K. Temma, T. Oyamada, N. Suzuki, Y. Kamiya, Y. Hara, T. Sasaki, H. Kondo, and T. Akera. 2000. Doxorubicin-induced late cardiotoxicity: delayed impairment of Ca2+-handling mechanisms in the sarcoplasmic reticulum in the rat. *Can J Physiol Pharmacol*. 78:329-338.

Classen, S., S. Olland, and J.M. Berger. 2003. Structure of the topoisomerase II ATPase region and its mechanism of inhibition by the chemotherapeutic agent ICRF-187. *Proc Natl Acad Sci U S A*. 100:10629-10634.

Cobleigh, M.A., V.K. Langmuir, G.W. Sledge, K.D. Miller, L. Haney, W.F. Novotny, J.D. Reimann, and A. Vassel. 2003. A phase I/II dose-escalation trial of bevacizumab in previously treated metastatic breast cancer. *Semin Oncol*. 30:117-124.

Coiffier, B., C. Thieblemont, E. Van Den Neste, G. Lepeu, I. Plantier, S. Castaigne, S. Lefort, G. Marit, M. Macro, C. Sebban, K. Belhadj, D. Bordessoule, C. Ferme, and H. Tilly. 2010. Long-term outcome of patients in the LNH-98.5 trial, the first randomized study comparing rituximab-CHOP to standard CHOP chemotherapy in DLBCL patients: a study by the Groupe d'Etudes des Lymphomes de l'Adulte. *Blood*. 116:2040-2045.

Cove-Smith, L., N. Woodhouse, A. Hargreaves, J. Kirk, S. Smith, S.A. Price, M. Galvin, C.J. Betts, S. Brocklehurst, A. Backen, J. Radford, K. Linton, R.A. Roberts, M. Schmitt, C. Dive, J.D. Tugwood, P.D. Hockings, and H.R. Mellor. 2014. An integrated characterization of serological, pathological, and functional events in doxorubicin-induced cardiotoxicity. *Toxicol Sci*. 140:3-15.

Cramer, L., B. Hildebrandt, T. Kung, K. Wichmann, J. Springer, W. Doehner, A. Sandek, M. Valentova, T. Stojakovic, H. Scharnagl, H. Riess, S.D. Anker, and S. von Haehling. 2014. Cardiovascular function and predictors of exercise capacity in patients with colorectal cancer. *J Am Coll Cardiol*. 64:1310-1319.

Crompton, M., and A. Costi. 1988. Kinetic evidence for a heart mitochondrial pore activated by Ca2+, inorganic phosphate and oxidative stress. A potential mechanism for mitochondrial dysfunction during cellular Ca2+ overload. *Eur J Biochem*. 178:489-501.

Crompton, M., and A. Costi. 1990. A heart mitochondrial Ca2(+)-dependent pore of possible relevance to re-perfusion-induced injury. Evidence that ADP facilitates pore interconversion between the closed and open states. *Biochem J*. 266:33-39.

Crompton, M., A. Costi, and L. Hayat. 1987. Evidence for the presence of a reversible Ca2+-dependent pore activated by oxidative stress in heart mitochondria. *Biochem J*. 245:915-918.

Crompton, M., H. Ellinger, and A. Costi. 1988. Inhibition by cyclosporin A of a Ca2+-dependent pore in heart mitochondria activated by inorganic phosphate and oxidative stress. *Biochem J*. 255:357-360.

Cruz, C.M., A. Rinna, H.J. Forman, A.L. Ventura, P.M. Persechini, and D.M. Ojcius. 2007. ATP activates a reactive oxygen species-dependent oxidative stress response and secretion of proinflammatory cytokines in macrophages. *J Biol Chem*. 282:2871-2879.

Cung, T.T., O. Morel, G. Cayla, G. Rioufol, D. Garcia-Dorado, D. Angoulvant, E. Bonnefoy-Cudraz, P. Guerin, M. Elbaz, N. Delarche, P. Coste, G. Vanzetto, M. Metge, J.F. Aupetit, B. Jouve, P. Motreff, C. Tron, J.N. Labeque, P.G. Steg, Y. Cottin, G. Range, J. Clerc, M.J. Claeys, P. Coussement, F. Prunier, F. Moulin, O. Roth, L. Belle, P. Dubois, P. Barragan, M. Gilard, C. Piot, P. Colin, F. De Poli, M.C. Morice, O. Ider, J.L. Dubois-Rande, T. Unterseeh, H. Le Breton, T. Beard, D. Blanchard, G. Grollier, V. Malquarti, P. Staat, A. Sudre, E. Elmer, M.J. Hansson, C. Bergerot, I. Boussaha, C. Jossan, G. Derumeaux, N. Mewton, and M. Ovize. 2015. Cyclosporine before PCI in Patients with Acute Myocardial Infarction. *N Engl J Med*. 373:1021-1031.

Czabotar, P.E., G. Lessene, A. Strasser, and J.M. Adams. 2014. Control of apoptosis by the BCL-2 protein family: implications for physiology and therapy. *Nat Rev Mol Cell Biol*. 15:49-63.

Davies, K.J., and J.H. Doroshow. 1986. Redox cycling of anthracyclines by cardiac mitochondria. I. Anthracycline radical formation by NADH dehydrogenase. *J Biol Chem*. 261:3060-3067.

Dazzi, H., K. Kaufmann, and F. Follath. 2001. Anthracycline-induced acute cardiotoxicity in adults treated for leukaemia. Analysis of the clinico-pathological aspects of documented acute anthracycline-induced cardiotoxicity in patients treated for acute leukaemia at the University Hospital of Zurich, Switzerland, between 1990 and 1996. *Ann Oncol*. 12:963-966.

De Angelis, A., E. Piegari, D. Cappetta, L. Marino, A. Filippelli, L. Berrino, J. Ferreira-Martins, H. Zheng, T. Hosoda, M. Rota, K. Urbanek, J. Kajstura, A. Leri, F. Rossi, and P. Anversa. 2010. Anthracycline cardiomyopathy is mediated by depletion of the cardiac stem cell pool and is rescued by restoration of progenitor cell function. *Circulation*. 121:276-292.

de Beer, E.L., A.E. Bottone, J. van Der Velden, and E.E. Voest. 2000. Doxorubicin impairs crossbridge turnover kinetics in skinned cardiac trabeculae after acute and chronic treatment. *Mol Pharmacol*. 57:1152-1157.

de Jonge, M.J., H. Dumez, J.J. Kitzen, B. Beuselinck, J. Verweij, R. Courtney, A. Battista, N. Brega, and P. Schoffski. 2011. Phase I safety and pharmacokinetic study of SU-014813 in combination with docetaxel in patients with advanced solid tumours. *Eur J Cancer*. 47:1328-1335.

de Oliveira, B.L., and S. Niederer. 2016. A Biophysical Systems Approach to Identifying the Pathways of Acute and Chronic Doxorubicin Mitochondrial Cardiotoxicity. *PLoS Comput Biol*. 12:e1005214.

De Stefani, D., A. Raffaello, E. Teardo, I. Szabo, and R. Rizzuto. 2011. A forty-kilodalton protein of the inner membrane is the mitochondrial calcium uniporter. *Nature*. 476:336-340.

Deavall, D.G., E.A. Martin, J.M. Horner, and R. Roberts. 2012. Drug-induced oxidative stress and toxicity. *J Toxicol*. 2012:645460.

Dekker, T., C.J. van Echteld, J.H. Kirkels, T.J. Ruigrok, Q.G. van Hoesel, W.H. de Jong, and J.H. Schornagel. 1991. Chronic cardiotoxicity of adriamycin studied in a rat model by 31P NMR. *NMR Biomed*. 4:16-24.

Demetrius, L. 2005. Of mice and men. When it comes to studying ageing and the means to slow it down, mice are not just small humans. *EMBO Rep*. 6 Spec No:S39-44.

Denton, R.M., J.G. McCormack, and N.J. Edgell. 1980. Role of calcium ions in the regulation of intramitochondrial metabolism. Effects of Na+, Mg2+ and ruthenium red on the Ca2+-stimulated oxidation of oxoglutarate and on pyruvate dehydrogenase activity in intact rat heart mitochondria. *Biochem J*. 190:107-117.

Di Marco, A., M. Gaetani, and B. Scarpinato. 1969. Adriamycin (NSC-123,127): a new antibiotic with antitumor activity. *Cancer Chemother Rep*. 53:33-37.

Dimarco, A., M. Gaetani, L. Dorigotti, M. Soldati, and O. Bellini. 1963. [Experimental Studies of the Antineoplastic Activity of a New Antibiotic, Daunomycin]. *Tumori*. 49:203-217.

Dirks-Naylor, A.J., S.A. Kouzi, J.D. Bero, D.T. Phan, H.N. Taylor, S.D. Whitt, and R. Mabolo. 2014. Doxorubicin alters the mitochondrial dynamics machinery and mitophagy in the liver of treated animals. *Fundam Clin Pharmacol*. 28:633-642.

Dodos, F., T. Halbsguth, E. Erdmann, and U.C. Hoppe. 2008. Usefulness of myocardial performance index and biochemical markers for early detection of anthracycline-induced cardiotoxicity in adults. *Clin Res Cardiol*. 97:318-326.

Doroshow, J.H., and K.J. Davies. 1986. Redox cycling of anthracyclines by cardiac mitochondria. II. Formation of superoxide anion, hydrogen peroxide, and hydroxyl radical. *J Biol Chem*. 261:3068-3074.

Doroshow, J.H., G.Y. Locker, and C.E. Myers. 1980. Enzymatic defenses of the mouse heart against reactive oxygen metabolites: alterations produced by doxorubicin. *J Clin Invest*. 65:128-135.

Dostert, C., V. Petrilli, R. Van Bruggen, C. Steele, B.T. Mossman, and J. Tschopp. 2008. Innate immune activation through Nalp3 inflammasome sensing of asbestos and silica. *Science*. 320:674-677.

Dubost, M., P. Ganter, R. Maral, L. Ninet, S. Pinnert, J. Preudhomme, and G.H. Werner. 1964. Rubidomycin: A New Antibiotic with Cytostatic Properties. *Cancer Chemother Rep*. 41:35-36.

Duchen, M.R. 1992. Ca(2+)-dependent changes in the mitochondrial energetics in single dissociated mouse sensory neurons. *Biochem J*. 283 (Pt 1):41-50.

Duchen, M.R. 2004. Mitochondria in health and disease: perspectives on a new mitochondrial biology. *Mol Aspects Med*. 25:365-451.

Duchen, M.R., O. McGuinness, L.A. Brown, and M. Crompton. 1993. On the involvement of a cyclosporin A sensitive mitochondrial pore in myocardial reperfusion injury. *Cardiovasc Res*. 27:1790-1794.

Dunkelberger, J.R., and W.C. Song. 2010. Complement and its role in innate and adaptive immune responses. *Cell Res*. 20:34-50.

Durand, R., Y. Briand, S. Touraille, and S. Alziari. 1981. Molecular approaches to phosphate transport in mitochondria. *Trends in Biochemical Sciences*. 6:211-214.

Ehrenberg, B., V. Montana, M.D. Wei, J.P. Wuskell, and L.M. Loew. 1988. Membrane potential can be determined in individual cells from the nernstian distribution of cationic dyes. *Biophys J*. 53:785-794.

Eidenschink, A.B., G. Schroter, S. Muller-Weihrich, and H. Stern. 2000. Myocardial high-energy phosphate metabolism is altered after treatment with anthracycline in childhood. *Cardiol Young*. 10:610-617.

Eiken, H.G., E. Oie, J.K. Damas, A. Yndestad, V. Bjerkeli, H. Aass, S. Simonsen, O.R. Geiran, T. Tonnessen, G. Christensen, S.S. Froland, L. Gullestad, H. Attramadal, and P. Aukrust. 2001. Myocardial gene expression of leukaemia inhibitory factor, interleukin-6 and glycoprotein 130 in end-stage human heart failure. *Eur J Clin Invest*. 31:389-397.

Eisenberg, S.P., R.J. Evans, W.P. Arend, E. Verderber, M.T. Brewer, C.H. Hannum, and R.C. Thompson. 1990. Primary structure and functional expression from complementary DNA of a human interleukin-1 receptor antagonist. *Nature*. 343:341-346.

Elder, J.M. 2013. Regional differences in mitochondrial membrane potential dynamics in ex vivo perfused rat hearts.

Eppler, S.M., D.L. Combs, T.D. Henry, J.J. Lopez, S.G. Ellis, J.H. Yi, B.H. Annex, E.R. McCluskey, and T.F. Zioncheck. 2002. A target-mediated model to describe the pharmacokinetics and hemodynamic effects of recombinant human vascular endothelial growth factor in humans. *Clin Pharmacol Ther*. 72:20-32.

Evans, C.J., and R.J. Aguilera. 2003. DNase II: genes, enzymes and function. *Gene*. 322:1-15.

Ewer, M.S., D.D. Von Hoff, and R.S. Benjamin. 2011. A historical perspective of anthracycline cardiotoxicity. *Heart Fail Clin*. 7:363-372.

Fabian, M.A., W.H. Biggs, 3rd, D.K. Treiber, C.E. Atteridge, M.D. Azimioara, M.G. Benedetti, T.A. Carter, P. Ciceri, P.T. Edeen, M. Floyd, J.M. Ford, M. Galvin, J.L. Gerlach, R.M. Grotzfeld, S. Herrgard, D.E. Insko, M.A. Insko, A.G. Lai, J.M. Lelias, S.A. Mehta, Z.V. Milanov, A.M. Velasco, L.M. Wodicka, H.K. Patel, P.P. Zarrinkar, and D.J. Lockhart. 2005. A small molecule-kinase interaction map for clinical kinase inhibitors. *Nat Biotechnol*. 23:329-336.

Falcao, L.M., F. Pinto, L. Ravara, and P.A. van Zwieten. 2004. BNP and ANP as diagnostic and predictive markers in heart failure with left ventricular systolic dysfunction. *Journal of the renin-angiotensin-aldosterone system : JRAAS*. 5:121-129.

Feldman, A.M., B.H. Lorell, and S.E. Reis. 2000. Trastuzumab in the treatment of metastatic breast cancer : anticancer therapy versus cardiotoxicity. *Circulation*. 102:272-274.

Ferdinandy, P., R. Schulz, and G.F. Baxter. 2007. Interaction of cardiovascular risk factors with myocardial ischemia/reperfusion injury, preconditioning, and postconditioning. *Pharmacol Rev*. 59:418-458.

Ferrara, N., K.J. Hillan, H.P. Gerber, and W. Novotny. 2004. Discovery and development of bevacizumab, an anti-VEGF antibody for treating cancer. *Nat Rev Drug Discov*. 3:391-400.

Ferrero, M.E., E. Ferrero, G. Gaja, and A. Bernelli-Zazzera. 1976. Adriamycin: energy metabolism and mitochondrial oxidations in the heart of treated rabbits. *Biochem Pharmacol*. 25:125-130.

Feuerstein, G.Z., and R.R. Ruffolo, Jr. 1995. Carvedilol, a novel multiple action antihypertensive agent with antioxidant activity and the potential for myocardial and vascular protection. *Eur Heart J*. 16 Suppl F:38-42.

Fiedler, W., G. Giaccone, P. Lasch, I. van der Horst, N. Brega, R. Courtney, A. Abbattista, D.R. Shalinsky, C. Bokemeyer, and E. Boven. 2011. Phase I trial of SU14813 in patients with advanced solid malignancies. *Ann Oncol*. 22:195-201.

Fiedler, W., H. Serve, H. Dohner, M. Schwittay, O.G. Ottmann, A.M. O'Farrell, C.L. Bello, R. Allred, W.C. Manning, J.M. Cherrington, S.G. Louie, W. Hong, N.M. Brega, G. Massimini, P. Scigalla, W.E. Berdel, and D.K. Hossfeld. 2005. A phase 1 study of SU11248 in the treatment of patients with refractory or resistant acute myeloid leukemia (AML) or not amenable to conventional therapy for the disease. *Blood*. 105:986-993.

Flamm, S.D., J. Taki, R. Moore, S.F. Lewis, F. Keech, F. Maltais, M. Ahmad, R. Callahan, S. Dragotakes, N. Alpert, and et al. 1990. Redistribution of regional and organ blood volume and effect on cardiac function in relation to upright exercise intensity in healthy human subjects. *Circulation*. 81:1550-1559.

Flewelling, R.F., and W.L. Hubbell. 1986. Hydrophobic ion interactions with membranes. Thermodynamic analysis of tetraphenylphosphonium binding to vesicles. *Biophys J*. 49:531-540.

Florescu, M., M. Cinteza, and D. Vinereanu. 2013. Chemotherapy-induced Cardiotoxicity. *Maedica (Buchar)*. 8:59-67.

Folkman, J. 2007. Angiogenesis: an organizing principle for drug discovery? *Nat Rev Drug Discov*. 6:273-286.

Force, T., and K.L. Kolaja. 2011. Cardiotoxicity of kinase inhibitors: the prediction and translation of preclinical models to clinical outcomes. *Nat Rev Drug Discov*. 10:111-126.

Force, T., D.S. Krause, and R.A. Van Etten. 2007. Molecular mechanisms of cardiotoxicity of tyrosine kinase inhibition. *Nat Rev Cancer*. 7:332-344.

Foreman, K.E., T. Wrone-Smith, A.E. Krueger, and B.J. Nickoloff. 1999. Expression of costimulatory molecules CD80 and/or CD86 by a Kaposi's sarcoma tumor cell line induces differential T-cell activation and proliferation. *Clin Immunol*. 91:345-353.

Franchi, L., R. Munoz-Planillo, T. Reimer, T. Eigenbrod, and G. Nunez. 2010. Inflammasomes as microbial sensors. *Eur J Immunol*. 40:611-615.

Frangogiannis, N.G., L.H. Michael, and M.L. Entman. 2000. Myofibroblasts in reperfused myocardial infarcts express the embryonic form of smooth muscle myosin heavy chain (SMemb). *Cardiovasc Res*. 48:89-100.

Friedman, M.A., M.J. Bozdech, M.E. Billingham, and A.K. Rider. 1978. Doxorubicin cardiotoxicity. Serial endomyocardial biopsies and systolic time intervals. *JAMA*. 240:1603-1606.

Fukai, T., and M. Ushio-Fukai. 2011. Superoxide dismutases: role in redox signaling, vascular function, and diseases. *Antioxid Redox Signal*. 15:1583-1606.

Furness, L.J., and J.R. Speakman. 2008. Energetics and longevity in birds. *Age (Dordr)*. 30:75-87.

Ganz, P.A. 2009. Survivorship: adult cancer survivors. *Prim Care*. 36:721-741.

Gelinas, D.S., P.N. Bernatchez, S. Rollin, N.G. Bazan, and M.G. Sirois. 2002. Immediate and delayed VEGF-mediated NO synthesis in endothelial cells: role of PI3K, PKC and PLC pathways. *Br J Pharmacol*. 137:1021-1030.

Gerencser, A.A., A. Neilson, S.W. Choi, U. Edman, N. Yadava, R.J. Oh, D.A. Ferrick, D.G. Nicholls, and M.D. Brand. 2009. Quantitative microplate-based respirometry with correction for oxygen diffusion. *Anal Chem*. 81:6868-6878.

Gewirtz, D.A. 1999. A critical evaluation of the mechanisms of action proposed for the antitumor effects of the anthracycline antibiotics adriamycin and daunorubicin. *Biochem Pharmacol*. 57:727-741.

Ghiringhelli, F., L. Apetoh, A. Tesniere, L. Aymeric, Y. Ma, C. Ortiz, K. Vermaelen, T. Panaretakis, G. Mignot, E. Ullrich, J.L. Perfettini, F. Schlemmer, E. Tasdemir, M. Uhl, P. Genin, A. Civas, B. Ryffel, J. Kanellopoulos, J. Tschopp, F. Andre, R. Lidereau, N.M. McLaughlin, N.M. Haynes, M.J. Smyth, G. Kroemer, and L. Zitvogel. 2009. Activation of the NLRP3 inflammasome in dendritic cells induces IL-1beta-dependent adaptive immunity against tumors. *Nat Med*. 15:1170-1178.

Gladden, J.D., B.R. Zelickson, C.C. Wei, E. Ulasova, J. Zheng, M.I. Ahmed, Y. Chen, M. Bamman, S. Ballinger, V. Darley-Usmar, and L.J. Dell'Italia. 2011. Novel insights into interactions between mitochondria and xanthine oxidase in acute cardiac volume overload. *Free Radic Biol Med*. 51:1975-1984.

Glancy, B., W.T. Willis, D.J. Chess, and R.S. Balaban. 2013. Effect of calcium on the oxidative phosphorylation cascade in skeletal muscle mitochondria. *Biochemistry*. 52:2793-2809.

Gliki, G., R. Abu-Ghazaleh, S. Jezequel, C. Wheeler-Jones, and I. Zachary. 2001. Vascular endothelial growth factor-induced prostacyclin production is mediated by a protein kinase C (PKC)-dependent activation of extracellular signal-regulated protein kinases 1 and 2 involving PKC-delta and by mobilization of intracellular Ca2+. *Biochem J*. 353:503-512.

Goodman, V.L., E.P. Rock, R. Dagher, R.P. Ramchandani, S. Abraham, J.V. Gobburu, B.P. Booth, S.L. Verbois, D.E. Morse, C.Y. Liang, N. Chidambaram, J.X. Jiang, S. Tang, K. Mahjoob, R. Justice, and R. Pazdur. 2007. Approval summary: sunitinib for the treatment of imatinib refractory or intolerant gastrointestinal stromal tumors and advanced renal cell carcinoma. *Clin Cancer Res*. 13:1367-1373.

Goormaghtigh, E., R. Brasseur, P. Huart, and J.M. Ruysschaert. 1987. Study of the adriamycin-cardiolipin complex structure using attenuated total reflection infrared spectroscopy. *Biochemistry*. 26:1789-1794.

Gozzelino, R., V. Jeney, and M.P. Soares. 2010. Mechanisms of cell protection by heme oxygenase-1. *Annu Rev Pharmacol Toxicol*. 50:323-354.

Gray, M.W., G. Burger, and B.F. Lang. 1999. Mitochondrial evolution. *Science*. 283:1476-1481.

Griffiths, E.J., and A.P. Halestrap. 1995. Mitochondrial non-specific pores remain closed during cardiac ischaemia, but open upon reperfusion. *Biochem J*. 307 (Pt 1):93-98.

Gustafsson, A.B., and R.A. Gottlieb. 2008. Heart mitochondria: gates of life and death. *Cardiovasc Res*. 77:334-343.

Halestrap, A.P., S.J. Clarke, and S.A. Javadov. 2004. Mitochondrial permeability transition pore opening during myocardial reperfusion--a target for cardioprotection. *Cardiovasc Res*. 61:372-385.

Halestrap, A.P., P.M. Kerr, S. Javadov, and K.Y. Woodfield. 1998. Elucidating the molecular mechanism of the permeability transition pore and its role in reperfusion injury of the heart. *Biochim Biophys Acta*. 1366:79-94.

Halestrap, A.P., and P. Pasdois. 2009. The role of the mitochondrial permeability transition pore in heart disease. *Biochim Biophys Acta*. 1787:1402-1415.

Halestrap, A.P., K.Y. Woodfield, and C.P. Connern. 1997. Oxidative stress, thiol reagents, and membrane potential modulate the mitochondrial permeability transition by affecting nucleotide binding to the adenine nucleotide translocase. *J Biol Chem*. 272:3346-3354.

Hanna, A.D., A. Lam, S. Tham, A.F. Dulhunty, and N.A. Beard. 2014. Adverse effects of doxorubicin and its metabolic product on cardiac RyR2 and SERCA2A. *Mol Pharmacol*. 86:438-449.

Hasinoff, B.B., K. Hellmann, E.H. Herman, and V.J. Ferrans. 1998. Chemical, biological and clinical aspects of dexrazoxane and other bisdioxopiperazines. *Curr Med Chem*. 5:1-28.

Hausenloy, D.J., M.R. Duchen, and D.M. Yellon. 2003. Inhibiting mitochondrial permeability transition pore opening at reperfusion protects against ischaemia-reperfusion injury. *Cardiovasc Res*. 60:617-625.

Hayakawa, H., Y. Komada, M. Hirayama, H. Hori, M. Ito, and M. Sakurai. 2001. Plasma levels of natriuretic peptides in relation to doxorubicin-induced cardiotoxicity and cardiac function in children with cancer. *Med Pediatr Oncol*. 37:4-9.

Hayek, E.R., E. Speakman, and E. Rehmus. 2005. Acute doxorubicin cardiotoxicity. *N Engl J Med*. 352:2456-2457.

He, H., V.J. Venema, X. Gu, R.C. Venema, M.B. Marrero, and R.B. Caldwell. 1999. Vascular endothelial growth factor signals endothelial cell production of nitric oxide and prostacyclin through flk-1/KDR activation of c-Src. *J Biol Chem*. 274:25130-25135.

Hemmi, H., O. Takeuchi, T. Kawai, T. Kaisho, S. Sato, H. Sanjo, M. Matsumoto, K. Hoshino, H. Wagner, K. Takeda, and S. Akira. 2000. A Toll-like receptor recognizes bacterial DNA. *Nature*. 408:740-745.

Henderson, K.A., R.B. Borders, J.B. Ross, T.B. Huwar, C.O. Travis, B.J. Wood, Z.J. Ma, S.P. Hong, T.M. Vinci, and B.M. Roche. 2013. Effects of tyrosine kinase inhibitors on rat

isolated heart function and protein biomarkers indicative of toxicity. *J Pharmacol Toxicol Methods*. 68:150-159.

Henson, K.E., P. McGale, C. Taylor, and S.C. Darby. 2013. Radiation-related mortality from heart disease and lung cancer more than 20 years after radiotherapy for breast cancer. *Br J Cancer*. 108:179-182.

Hequet, O., Q.H. Le, I. Moullet, E. Pauli, G. Salles, D. Espinouse, C. Dumontet, C. Thieblemont, P. Arnaud, D. Antal, F. Bouafia, and B. Coiffier. 2004. Subclinical late cardiomyopathy after doxorubicin therapy for lymphoma in adults. *J Clin Oncol*. 22:1864-1871.

Herman, E., B. Ardalan, C. Bier, V. Waravdekar, and S. Krop. 1979. Reduction of daunorubicin lethality and myocardial cellular alterations by pretreatment with ICRF-187 in Syrian golden hamsters. *Cancer Treat Rep*. 63:89-92.

Hill, B.G., G.A. Benavides, J.R. Lancaster, Jr., S. Ballinger, L. Dell'Italia, Z. Jianhua, and V.M. Darley-Usmar. 2012. Integration of cellular bioenergetics with mitochondrial quality control and autophagy. *Biol Chem*. 393:1485-1512.

Hill, B.G., B.P. Dranka, L. Zou, J.C. Chatham, and V.M. Darley-Usmar. 2009. Importance of the bioenergetic reserve capacity in response to cardiomyocyte stress induced by 4-hydroxynonenal. *Biochem J*. 424:99-107.

Hinkle, P.C., and R.E. McCarty. 1978. How cells make ATP. *Scientific American*. 238:104-117, 121-103.

Holmberg, S.R., and A.J. Williams. 1990. Patterns of interaction between anthraquinone drugs and the calcium-release channel from cardiac sarcoplasmic reticulum. *Circ Res*. 67:272-283.

Holmgren, D., H. Wahlander, B.O. Eriksson, A. Oldfors, E. Holme, and M. Tulinius. 2003. Cardiomyopathy in children with mitochondrial disease; clinical course and cardiological findings. *Eur Heart J*. 24:280-288.

Hood, J.D., C.J. Meininger, M. Ziche, and H.J. Granger. 1998. VEGF upregulates ecNOS message, protein, and NO production in human endothelial cells. *Am J Physiol*. 274:H1054-1058.

Horowitz, J.R., A. Rivard, R. van der Zee, M. Hariawala, D.D. Sheriff, D.D. Esakof, G.M. Chaudhry, J.F. Symes, and J.M. Isner. 1997. Vascular endothelial growth factor/vascular permeability factor produces nitric oxide-dependent hypotension. Evidence for a maintenance role in quiescent adult endothelium. *Arterioscler Thromb Vasc Biol*. 17:2793-2800.

Howlader, N., L.A. Ries, A.B. Mariotto, M.E. Reichman, J. Ruhl, and K.A. Cronin. 2010. Improved estimates of cancer-specific survival rates from population-based data. *J Natl Cancer Inst*. 102:1584-1598.

Hu-Lowe, D., N. Brega, and S. Patyna. 2011. The discovery and development of SU14813, a next-generation multitargeted tyrosine kinase inhibitor for the treatment of human malignancies. *Mol Cancer Ther*. 10:2015.

Huang da, W., B.T. Sherman, and R.A. Lempicki. 2009. Systematic and integrative analysis of large gene lists using DAVID bioinformatics resources. *Nat Protoc*. 4:44-57.

Hull, T.D., R. Boddu, L. Guo, C.C. Tisher, A.M. Traylor, B. Patel, R. Joseph, S.D. Prabhu, H.B. Suliman, C.A. Piantadosi, A. Agarwal, and J.F. George. 2016. Heme oxygenase-1 regulates mitochondrial quality control in the heart. *JCI Insight*. 1:e85817.

Hunter, D.R., and R.A. Haworth. 1979. The Ca2+-induced membrane transition in mitochondria. I. The protective mechanisms. *Arch Biochem Biophys*. 195:453-459.

Hunter, D.R., R.A. Haworth, and J.H. Southard. 1976. Relationship between configuration, function, and permeability in calcium-treated mitochondria. *J Biol Chem*. 251:5069-5077.

Ichikawa, Y., M. Bayeva, M. Ghanefar, V. Potini, L. Sun, R.K. Mutharasan, R. Wu, A. Khechaduri, T. Jairaj Naik, and H. Ardehali. 2012. Disruption of ATP-binding cassette B8 in mice leads to cardiomyopathy through a decrease in mitochondrial iron export. *Proc Natl Acad Sci U S A*. 109:4152-4157.

Ichikawa, Y., M. Ghanefar, M. Bayeva, R. Wu, A. Khechaduri, S.V. Naga Prasad, R.K. Mutharasan, T.J. Naik, and H. Ardehali. 2014. Cardiotoxicity of doxorubicin is mediated through mitochondrial iron accumulation. *J Clin Invest*. 124:617-630.

Iekushi, K., Y. Taniyama, J. Azuma, N. Katsuragi, N. Dosaka, F. Sanada, N. Koibuchi, K. Nagao, T. Ogihara, and R. Morishita. 2007. Novel mechanisms of valsartan on the treatment of acute myocardial infarction through inhibition of the antiadhesion molecule periostin. *Hypertension*. 49:1409-1414.

Ingwall, J.S., and R.G. Weiss. 2004. Is the failing heart energy starved? On using chemical energy to support cardiac function. *Circ Res*. 95:135-145.

Izumiya, Y., I. Shiojima, K. Sato, D.B. Sawyer, W.S. Colucci, and K. Walsh. 2006. Vascular endothelial growth factor blockade promotes the transition from compensatory cardiac hypertrophy to failure in response to pressure overload. *Hypertension*. 47:887-893.

Jabaut, J., J.L. Ather, A. Taracanova, M.E. Poynter, and K. Ckless. 2013. Mitochondria-targeted drugs enhance Nlrp3 inflammasome-dependent IL-1beta secretion in association with alterations in cellular redox and energy status. *Free Radic Biol Med*. 60:233-245.

Jabbour, A., C.S. Hayward, A.M. Keogh, E. Kotlyar, J.A. McCrohon, J.F. England, R. Amor, X. Liu, X.Y. Li, M.D. Zhou, R.M. Graham, and P.S. Macdonald. 2011. Parenteral administration of recombinant human neuregulin-1 to patients with stable chronic heart failure produces favourable acute and chronic haemodynamic responses. *Eur J Heart Fail*. 13:83-92.

Jaenke, R.S. 1974. An anthracycline antibiotic-induced cardiomyopathy in rabbits. *Lab Invest*. 30:292-304.

Jemal, A., E. Ward, and M. Thun. 2010. Declining death rates reflect progress against cancer. *PLoS One*. 5:e9584.

Jensen, B.V., T. Skovsgaard, and S.L. Nielsen. 2002. Functional monitoring of anthracycline cardiotoxicity: a prospective, blinded, long-term observational study of outcome in 120 patients. *Ann Oncol*. 13:699-709.

Jensen, P.K. 1966. Antimycin-insensitive oxidation of succinate and reduced nicotinamide-adenine dinucleotide in electron-transport particles. I. pH dependency and hydrogen peroxide formation. *Biochim Biophys Acta*. 122:157-166.

Jin, H., R.D. Nass, P.J. Joudrey, A.R. Lyon, E.R. Chemaly, K. Rapti, and F.G. Akar. 2010. Altered spatiotemporal dynamics of the mitochondrial membrane potential in the hypertrophied heart. *Biophys J*. 98:2063-2071.

Johnson, L.V., M.L. Walsh, B.J. Bockus, and L.B. Chen. 1981. Monitoring of relative mitochondrial membrane potential in living cells by fluorescence microscopy. *J Cell Biol*. 88:526-535.

Jones, L.W., M.J. Haykowsky, J.J. Swartz, P.S. Douglas, and J.R. Mackey. 2007. Early breast cancer therapy and cardiovascular injury. *J Am Coll Cardiol*. 50:1435-1441.

Jouaville, L.S., P. Pinton, C. Bastianutto, G.A. Rutter, and R. Rizzuto. 1999. Regulation of mitochondrial ATP synthesis by calcium: evidence for a long-term metabolic priming. *Proc Natl Acad Sci U S A*. 96:13807-13812.

Kahn, B.B., T. Alquier, D. Carling, and D.G. Hardie. 2005. AMP-activated protein kinase: ancient energy gauge provides clues to modern understanding of metabolism. *Cell Metab*. 1:15-25.

Kaiserova, H., T. Simunek, M. Sterba, G.J. den Hartog, L. Schroterova, O. Popelova, V. Gersl, E. Kvasnickova, and A. Bast. 2007. New iron chelators in anthracycline-induced cardiotoxicity. *Cardiovasc Toxicol*. 7:145-150.

Kakisaka, K., Y. Yoshida, Y. Suzuki, T. Sato, H. Kuroda, A. Miyasaka, and Y. Takikawa. 2017. Serum markers for mitochondrial dysfunction and cell death are possible predictive indicators for drug-induced liver injury by direct acting antivirals. *Hepatol Res*.

Kalay, N., E. Basar, I. Ozdogru, O. Er, Y. Cetinkaya, A. Dogan, T. Inanc, A. Oguzhan, N.K. Eryol, R. Topsakal, and A. Ergin. 2006. Protective effects of carvedilol against anthracycline-induced cardiomyopathy. *J Am Coll Cardiol*. 48:2258-2262.

Kappers, M.H., J.H. van Esch, W. Sluiter, S. Sleijfer, A.H. Danser, and A.H. van den Meiracker. 2010. Hypertension induced by the tyrosine kinase inhibitor sunitinib is associated with increased circulating endothelin-1 levels. *Hypertension*. 56:675-681.

Karukstis, K.K., E.H. Thompson, J.A. Whiles, and R.J. Rosenfeld. 1998. Deciphering the fluorescence signature of daunomycin and doxorubicin. *Biophys Chem*. 73:249-263.

Kato, M., M. Akao, M. Matsumoto-Ida, T. Makiyama, M. Iguchi, T. Takeda, S. Shimizu, and T. Kita. 2009. The targeting of cyclophilin D by RNAi as a novel cardioprotective therapy: evidence from two-photon imaging. *Cardiovasc Res*. 83:335-344.

Kawane, K., M. Ohtani, K. Miwa, T. Kizawa, Y. Kanbara, Y. Yoshioka, H. Yoshikawa, and S. Nagata. 2006. Chronic polyarthritis caused by mammalian DNA that escapes from degradation in macrophages. *Nature*. 443:998-1002.

Kawasaki, N., J.D. Lee, H. Shimizu, Y. Ishii, and T. Ueda. 1996. Cardiac energy metabolism at several stages of adriamycin-induced heart failure in rats. *Int J Cardiol*. 55:217-225.

Keizer, H.G., H.M. Pinedo, G.J. Schuurhuis, and H. Joenje. 1990. Doxorubicin (adriamycin): a critical review of free radical-dependent mechanisms of cytotoxicity. *Pharmacol Ther*. 47:219-231.

Kelso, G.F., C.M. Porteous, C.V. Coulter, G. Hughes, W.K. Porteous, E.C. Ledgerwood, R.A. Smith, and M.P. Murphy. 2001. Selective targeting of a redox-active ubiquinone to mitochondria within cells: antioxidant and antiapoptotic properties. *J Biol Chem*. 276:4588-4596.

Kerkela, R., L. Grazette, R. Yacobi, C. Iliescu, R. Patten, C. Beahm, B. Walters, S. Shevtsov, S. Pesant, F.J. Clubb, A. Rosenzweig, R.N. Salomon, R.A. Van Etten, J. Alroy, J.B. Durand, and T. Force. 2006. Cardiotoxicity of the cancer therapeutic agent imatinib mesylate. *Nat Med*. 12:908-916.

Kerkela, R., K.C. Woulfe, J.B. Durand, R. Vagnozzi, D. Kramer, T.F. Chu, C. Beahm, M.H. Chen, and T. Force. 2009. Sunitinib-induced cardiotoxicity is mediated by off-target inhibition of AMP-activated protein kinase. *Clin Transl Sci*. 2:15-25.

Khiati, S., I. Dalla Rosa, C. Sourbier, X. Ma, V.A. Rao, L.M. Neckers, H. Zhang, and Y. Pommier. 2014. Mitochondrial topoisomerase I (top1mt) is a novel limiting factor of doxorubicin cardiotoxicity. *Clin Cancer Res*. 20:4873-4881.

Koh, J.T., H.H. Choi, K.Y. Ahn, J.U. Kim, J.H. Kim, J.Y. Chun, Y.H. Baik, and K.K. Kim. 2001. Cardiac Characteristics of Transgenic Mice Overexpressing Refsum Disease Gene-Associated Protein within the Heart. *Biochem Biophys Res Commun*. 286:1107-1116.

Kohlhaas, M., T. Liu, A. Knopp, T. Zeller, M.F. Ong, M. Bohm, B. O'Rourke, and C. Maack. 2010. Elevated cytosolic Na+ increases mitochondrial formation of reactive oxygen species in failing cardiac myocytes. *Circulation*. 121:1606-1613.

Kremer, L.C., H.J. van der Pal, M. Offringa, E.C. van Dalen, and P.A. Voute. 2002. Frequency and risk factors of subclinical cardiotoxicity after anthracycline therapy in children: a systematic review. *Ann Oncol*. 13:819-829.

Krown, K.A., M.T. Page, C. Nguyen, D. Zechner, V. Gutierrez, K.L. Comstock, C.C. Glembotski, P.J. Quintana, and R.A. Sabbadini. 1996. Tumor necrosis factor alpha-

induced apoptosis in cardiac myocytes. Involvement of the sphingolipid signaling cascade in cardiac cell death. *J Clin Invest*. 98:2854-2865.

Ku, D.D., J.K. Zaleski, S. Liu, and T.A. Brock. 1993. Vascular endothelial growth factor induces EDRF-dependent relaxation in coronary arteries. *Am J Physiol*. 265:H586-592.

Kubota, T., C.F. McTiernan, C.S. Frye, S.E. Slawson, B.H. Lemster, A.P. Koretsky, A.J. Demetris, and A.M. Feldman. 1997. Dilated cardiomyopathy in transgenic mice with cardiac-specific overexpression of tumor necrosis factor-alpha. *Circ Res*. 81:627-635.

Ky, B., S.E. Kimmel, R.N. Safa, M.E. Putt, N.K. Sweitzer, J.C. Fang, D.B. Sawyer, and T.P. Cappola. 2009. Neuregulin-1 beta is associated with disease severity and adverse outcomes in chronic heart failure. *Circulation*. 120:310-317.

Ky, B., P. Vejpongsa, E.T. Yeh, T. Force, and J.J. Moslehi. 2013. Emerging paradigms in cardiomyopathies associated with cancer therapies. *Circ Res*. 113:754-764.

Lagarto, J., B.T. Dyer, C. Talbot, M.B. Sikkel, N.S. Peters, P.M. French, A.R. Lyon, and C. Dunsby. 2015. Application of time-resolved autofluorescence to label-free in vivo optical mapping of changes in tissue matrix and metabolism associated with myocardial infarction and heart failure. *Biomed Opt Express*. 6:324-346.

Langendorff, O. 1895. Untersuchungen am uberlebenden Saugethierherzen. *Pflugers Arch*. 61:291-332.

Langfelder, P., and S. Horvath. 2008. WGCNA: an R package for weighted correlation network analysis. *BMC Bioinformatics*. 9:559.

LaNoue, K.F., and A.C. Schoolwerth. 1979. Metabolite transport in mitochondria. *Annu Rev Biochem*. 48:871-922.

Lebrecht, D., A. Kokkori, U.P. Ketelsen, B. Setzer, and U.A. Walker. 2005. Tissue-specific mtDNA lesions and radical-associated mitochondrial dysfunction in human hearts exposed to doxorubicin. *J Pathol*. 207:436-444.

Lebrecht, D., B. Setzer, U.P. Ketelsen, J. Haberstroh, and U.A. Walker. 2003. Time-dependent and tissue-specific accumulation of mtDNA and respiratory chain defects in chronic doxorubicin cardiomyopathy. *Circulation*. 108:2423-2429.

Lebrecht, D., B. Setzer, R. Rohrbach, and U.A. Walker. 2004. Mitochondrial DNA and its respiratory chain products are defective in doxorubicin nephrosis. *Nephrol Dial Transplant*. 19:329-336.

Lefrak, E.A., J. Pitha, S. Rosenheim, and J.A. Gottlieb. 1973. A clinicopathologic analysis of adriamycin cardiotoxicity. *Cancer*. 32:302-314.

Lemasters, J.J., T. Qian, C.A. Bradham, D.A. Brenner, W.E. Cascio, L.C. Trost, Y. Nishimura, A.L. Nieminen, and B. Herman. 1999. Mitochondrial dysfunction in the pathogenesis of necrotic and apoptotic cell death. *J Bioenerg Biomembr*. 31:305-319.

Lemasters, J.J., and V.K. Ramshesh. 2007. Imaging of mitochondrial polarization and depolarization with cationic fluorophores. *Methods Cell Biol*. 80:283-295.

Lemmens, K., K. Doggen, and G.W. De Keulenaer. 2007. Role of neuregulin-1/ErbB signaling in cardiovascular physiology and disease: implications for therapy of heart failure. *Circulation*. 116:954-960.

Levine, B., J. Kalman, L. Mayer, H.M. Fillit, and M. Packer. 1990. Elevated circulating levels of tumor necrosis factor in severe chronic heart failure. *N Engl J Med*. 323:236-241.

Li, H., A. Ambade, and F. Re. 2009. Cutting edge: Necrosis activates the NLRP3 inflammasome. *J Immunol*. 183:1528-1532.

Li, Y., T.T. Huang, E.J. Carlson, S. Melov, P.C. Ursell, J.L. Olson, L.J. Noble, M.P. Yoshimura, C. Berger, P.H. Chan, D.C. Wallace, and C.J. Epstein. 1995. Dilated cardiomyopathy and neonatal lethality in mutant mice lacking manganese superoxide dismutase. *Nat Genet*. 11:376-381.

Limat, S., K. Demesmay, L. Voillat, Y. Bernard, E. Deconinck, A. Brion, A. Sabbah, M.C. Woronoff-Lemsi, and J.Y. Cahn. 2003. Early cardiotoxicity of the CHOP regimen in aggressive non-Hodgkin's lymphoma. *Ann Oncol*. 14:277-281.

Lipshultz, S.E., S.R. Lipsitz, S.E. Sallan, V.M. Dalton, S.M. Mone, R.D. Gelber, and S.D. Colan. 2005. Chronic progressive cardiac dysfunction years after doxorubicin therapy for childhood acute lymphoblastic leukemia. *J Clin Oncol*. 23:2629-2636.

Liu, L., T.P. Cash, R.G. Jones, B. Keith, C.B. Thompson, and M.C. Simon. 2006. Hypoxia-induced energy stress regulates mRNA translation and cell growth. *Mol Cell*. 21:521-531.

Liu, T., and B. O'Rourke. 2008. Enhancing mitochondrial Ca2+ uptake in myocytes from failing hearts restores energy supply and demand matching. *Circ Res*. 103:279-288.

Liu, T., E. Takimoto, V.L. Dimaano, D. DeMazumder, S. Kettlewell, G. Smith, A. Sidor, T.P. Abraham, and B. O'Rourke. 2014. Inhibiting mitochondrial Na+/Ca2+ exchange prevents sudden death in a Guinea pig model of heart failure. *Circ Res*. 115:44-54.

Lujan, H.L., H. Janbaih, H.Z. Feng, J.P. Jin, and S.E. DiCarlo. 2012. Ventricular function during exercise in mice and rats. *Am J Physiol Regul Integr Comp Physiol*. 302:R68-74.

Lyon, A.R., P.J. Joudrey, D. Jin, R.D. Nass, M.A. Aon, B. O'Rourke, and F.G. Akar. 2010. Optical imaging of mitochondrial function uncovers actively propagating waves of mitochondrial membrane potential collapse across intact heart. *Journal of molecular and cellular cardiology*. 49:565-575.

Lyu, Y.L., J.E. Kerrigan, C.P. Lin, A.M. Azarova, Y.C. Tsai, Y. Ban, and L.F. Liu. 2007. Topoisomerase IIbeta mediated DNA double-strand breaks: implications in doxorubicin cardiotoxicity and prevention by dexrazoxane. *Cancer Res*. 67:8839-8846.

Ma, Y., X. Zhang, H. Bao, S. Mi, W. Cai, H. Yan, Q. Wang, Z. Wang, J. Yan, G.C. Fan, M.L. Lindsey, and Z. Hu. 2012. Toll-like receptor (TLR) 2 and TLR4 differentially regulate doxorubicin induced cardiomyopathy in mice. *PLoS One*. 7:e40763.

Maack, C., S. Cortassa, M.A. Aon, A.N. Ganesan, T. Liu, and B. O'Rourke. 2006. Elevated cytosolic Na+ decreases mitochondrial Ca2+ uptake during excitation-contraction coupling and impairs energetic adaptation in cardiac myocytes. *Circ Res*. 99:172-182.

Maia, L., A. Vala, and L. Mira. 2005. NADH oxidase activity of rat liver xanthine dehydrogenase and xanthine oxidase-contribution for damage mechanisms. *Free Radic Res*. 39:979-986.

Majno, G., and I. Joris. 1995. Apoptosis, oncosis, and necrosis. An overview of cell death. *Am J Pathol*. 146:3-15.

Mallat, Z., C. Heymes, A. Corbaz, D. Logeart, S. Alouani, A. Cohen-Solal, T. Seidler, G. Hasenfuss, Y. Chvatchko, A.M. Shah, and A. Tedgui. 2004. Evidence for altered interleukin 18 (IL)-18 pathway in human heart failure. *FASEB J*. 18:1752-1754.

Mann, D.L. 2002. Inflammatory mediators and the failing heart: past, present, and the foreseeable future. *Circ Res*. 91:988-998.

Marechal, X., D. Montaigne, C. Marciniak, P. Marchetti, S.M. Hassoun, J.C. Beauvillain, S. Lancel, and R. Neviere. 2011. Doxorubicin-induced cardiac dysfunction is attenuated by ciclosporin treatment in mice through improvements in mitochondrial bioenergetics. *Clin Sci (Lond)*. 121:405-413.

Mariathasan, S., D.S. Weiss, K. Newton, J. McBride, K. O'Rourke, M. Roose-Girma, W.P. Lee, Y. Weinrauch, D.M. Monack, and V.M. Dixit. 2006. Cryopyrin activates the inflammasome in response to toxins and ATP. *Nature*. 440:228-232.

Martin, E., A.V. Thougaard, M. Grauslund, P.B. Jensen, F. Bjorkling, B.B. Hasinoff, J. Tjornelund, M. Sehested, and L.H. Jensen. 2009. Evaluation of the topoisomerase II-

inactive bisdioxopiperazine ICRF-161 as a protectant against doxorubicin-induced cardiomyopathy. *Toxicology*. 255:72-79.

Mathur, A., Y. Hong, B.K. Kemp, A.A. Barrientos, and J.D. Erusalimsky. 2000. Evaluation of fluorescent dyes for the detection of mitochondrial membrane potential changes in cultured cardiomyocytes. *Cardiovasc Res*. 46:126-138.

Matsuda, S., and S. Koyasu. 2000. Mechanisms of action of cyclosporine. *Immunopharmacology*. 47:119-125.

Matsumoto-Ida, M., M. Akao, T. Takeda, M. Kato, and T. Kita. 2006. Real-time 2-photon imaging of mitochondrial function in perfused rat hearts subjected to ischemia/reperfusion. *Circulation*. 114:1497-1503.

McCormack, J.G., A.P. Halestrap, and R.M. Denton. 1990. Role of calcium ions in regulation of mammalian intramitochondrial metabolism. *Physiol Rev*. 70:391-425.

McLennan, H.R., and M. Degli Esposti. 2000. The contribution of mitochondrial respiratory complexes to the production of reactive oxygen species. *J Bioenerg Biomembr*. 32:153-162.

Mendel, D.B., A.D. Laird, X. Xin, S.G. Louie, J.G. Christensen, G. Li, R.E. Schreck, T.J. Abrams, T.J. Ngai, L.B. Lee, L.J. Murray, J. Carver, E. Chan, K.G. Moss, J.O. Haznedar, J. Sukbuntherng, R.A. Blake, L. Sun, C. Tang, T. Miller, S. Shirazian, G. McMahon, and J.M. Cherrington. 2003. In vivo antitumor activity of SU11248, a novel tyrosine kinase inhibitor targeting vascular endothelial growth factor and platelet-derived growth factor receptors: determination of a pharmacokinetic/pharmacodynamic relationship. *Clin Cancer Res*. 9:327-337.

Mendelsohn, M.E., and R.H. Karas. 1999. The protective effects of estrogen on the cardiovascular system. *N Engl J Med*. 340:1801-1811.

Mercadier, J.J., A.M. Lompre, P. Duc, K.R. Boheler, J.B. Fraysse, C. Wisnewsky, P.D. Allen, M. Komajda, and K. Schwartz. 1990. Altered sarcoplasmic reticulum Ca2(+)-ATPase gene expression in the human ventricle during end-stage heart failure. *J Clin Invest*. 85:305-309.

Mertens, A.C., Q. Liu, J.P. Neglia, K. Wasilewski, W. Leisenring, G.T. Armstrong, L.L. Robison, and Y. Yasui. 2008. Cause-specific late mortality among 5-year survivors of childhood cancer: the Childhood Cancer Survivor Study. *J Natl Cancer Inst*. 100:1368-1379.

Mettler, F.P., D.M. Young, and J.M. Ward. 1977. Adriamycin-induced cardiotoxicity (cardiomyopathy and congestive heart failure) in rats. *Cancer Res*. 37:2705-2713.

Mewton, N., P. Croisille, G. Gahide, G. Rioufol, E. Bonnefoy, I. Sanchez, T.T. Cung, C. Sportouch, D. Angoulvant, G. Finet, X. Andre-Fouet, G. Derumeaux, C. Piot, H. Vernhet, D. Revel, and M. Ovize. 2010. Effect of cyclosporine on left ventricular remodeling after reperfused myocardial infarction. *J Am Coll Cardiol*. 55:1200-1205.

Middleman, E., J. Luce, and E. Frei, 3rd. 1971. Clinical trials with adriamycin. *Cancer*. 28:844-850.

Migrino, R.Q., D. Aggarwal, E. Konorev, T. Brahmbhatt, M. Bright, and B. Kalyanaraman. 2008. Early detection of doxorubicin cardiomyopathy using two-dimensional strain echocardiography. *Ultrasound Med Biol*. 34:208-214.

Milani-Nejad, N., and P.M. Janssen. 2014. Small and large animal models in cardiac contraction research: advantages and disadvantages. *Pharmacol Ther*. 141:235-249.

Miller, K.D., R.L. Siegel, C.C. Lin, A.B. Mariotto, J.L. Kramer, J.H. Rowland, K.D. Stein, R. Alteri, and A. Jemal. 2016. Cancer treatment and survivorship statistics, 2016. *CA Cancer J Clin*. 66:271-289.

Min, K., O.S. Kwon, A.J. Smuder, M.P. Wiggs, K.J. Sollanek, D.D. Christou, J.K. Yoo, M.H. Hwang, H.H. Szeto, A.N. Kavazis, and S.K. Powers. 2015. Increased mitochondrial emission of reactive oxygen species and calpain activation are required for

doxorubicin-induced cardiac and skeletal muscle myopathy. *J Physiol*. 593:2017-2036.

Mitchell, P. 1961. Coupling of phosphorylation to electron and hydrogen transfer by a chemi-osmotic type of mechanism. *Nature*. 191:144-148.

Mitchell, P., and J. Moyle. 1969. Estimation of membrane potential and pH difference across the cristae membrane of rat liver mitochondria. *Eur J Biochem*. 7:471-484.

Mizushima, N., B. Levine, A.M. Cuervo, and D.J. Klionsky. 2008. Autophagy fights disease through cellular self-digestion. *Nature*. 451:1069-1075.

Monasky, M.M., K.D. Varian, and P.M. Janssen. 2008. Gender comparison of contractile performance and beta-adrenergic response in isolated rat cardiac trabeculae. *J Comp Physiol B*. 178:307-313.

Montaigne, D., X. Marechal, R. Baccouch, T. Modine, S. Preau, K. Zannis, P. Marchetti, S. Lancel, and R. Neviere. 2010. Stabilization of mitochondrial membrane potential prevents doxorubicin-induced cardiotoxicity in isolated rat heart. *Toxicol Appl Pharmacol*. 244:300-307.

Montaigne, D., X. Marechal, S. Preau, R. Baccouch, T. Modine, G. Fayad, S. Lancel, and R. Neviere. 2011. Doxorubicin induces mitochondrial permeability transition and contractile dysfunction in the human myocardium. *Mitochondrion*. 11:22-26.

Montali, U., M. Del Tacca, C. Bernardini, D. Segnini, and G. Solaini. 1985. Cardiotoxic effects of adriamycin and mitochondrial oxidation in rat cardiac tissue. *Drugs Exp Clin Res*. 11:219-222.

Monti, E., E. Prosperi, R. Supino, and G. Bottiroli. 1995. Free radical-dependent DNA lesions are involved in the delayed cardiotoxicity induced by adriamycin in the rat. *Anticancer Res*. 15:193-197.

Mootha, V.K., A.E. Arai, and R.S. Balaban. 1997. Maximum oxidative phosphorylation capacity of the mammalian heart. *Am J Physiol*. 272:H769-775.

Motlagh, N.S., P. Parvin, F. Ghasemi, and F. Atyabi. 2016. Fluorescence properties of several chemotherapy drugs: doxorubicin, paclitaxel and bleomycin. *Biomed Opt Express*. 7:2400-2406.

Motzer, R.J., M.D. Michaelson, B.G. Redman, G.R. Hudes, G. Wilding, R.A. Figlin, M.S. Ginsberg, S.T. Kim, C.M. Baum, S.E. DePrimo, J.Z. Li, C.L. Bello, C.P. Theuer, D.J. George, and B.I. Rini. 2006. Activity of SU11248, a multitargeted inhibitor of vascular endothelial growth factor receptor and platelet-derived growth factor receptor, in patients with metastatic renal cell carcinoma. *J Clin Oncol*. 24:16-24.

Moulin, M., J. Piquereau, P. Mateo, D. Fortin, C. Rucker-Martin, M. Gressette, F. Lefebvre, M. Gresikova, A. Solgadi, V. Veksler, A. Garnier, and R. Ventura-Clapier. 2015. Sexual dimorphism of doxorubicin-mediated cardiotoxicity: potential role of energy metabolism remodeling. *Circ Heart Fail*. 8:98-108.

Mukhopadhyay, P., M. Rajesh, S. Batkai, Y. Kashiwaya, G. Hasko, L. Liaudet, C. Szabo, and P. Pacher. 2009. Role of superoxide, nitric oxide, and peroxynitrite in doxorubicin-induced cell death in vivo and in vitro. *Am J Physiol Heart Circ Physiol*. 296:H1466-1483.

Muller, C., E. Chatelut, V. Gualano, M. De Forni, F. Huguet, M. Attal, P. Canal, and G. Laurent. 1993. Cellular pharmacokinetics of doxorubicin in patients with chronic lymphocytic leukemia: comparison of bolus administration and continuous infusion. *Cancer Chemother Pharmacol*. 32:379-384.

Mulrooney, D.A., M.W. Yeazel, T. Kawashima, A.C. Mertens, P. Mitby, M. Stovall, S.S. Donaldson, D.M. Green, C.A. Sklar, L.L. Robison, and W.M. Leisenring. 2009. Cardiac outcomes in a cohort of adult survivors of childhood and adolescent cancer: retrospective analysis of the Childhood Cancer Survivor Study cohort. *BMJ*. 339:b4606.

Murphy, M.P. 1997. Selective targeting of bioactive compounds to mitochondria. *Trends Biotechnol*. 15:326-330.

Myers, C., R. Bonow, S. Palmeri, J. Jenkins, B. Corden, G. Locker, J. Doroshow, and S. Epstein. 1983. A randomized controlled trial assessing the prevention of doxorubicin cardiomyopathy by N-acetylcysteine. *Semin Oncol*. 10:53-55.

Myers, C.E., L. Gianni, C.B. Simone, R. Klecker, and R. Greene. 1982. Oxidative destruction of erythrocyte ghost membranes catalyzed by the doxorubicin-iron complex. *Biochemistry*. 21:1707-1712.

Nag, A.C. 1980. Study of non-muscle cells of the adult mammalian heart: a fine structural analysis and distribution. *Cytobios*. 28:41-61.

Nakao, K., W. Minobe, R. Roden, M.R. Bristow, and L.A. Leinwand. 1997. Myosin heavy chain gene expression in human heart failure. *J Clin Invest*. 100:2362-2370.

Nicholls, D.G. 1974. The influence of respiration and ATP hydrolysis on the proton-electrochemical gradient across the inner membrane of rat-liver mitochondria as determined by ion distribution. *Eur J Biochem*. 50:305-315.

Nicholls, D.G. 1982. Bioenergetics : an introduction to the chemiosmotic theory. Academic Press, London.

Nicholls, D.G., S.J. Ferguson, and D.G.B. Nicholls. 2002. Bioenergetics 3. Amsterdam ; London ; Academic Press.

Nicholls, D.G., and M.W. Ward. 2000. Mitochondrial membrane potential and neuronal glutamate excitotoxicity: mortality and millivolts. *Trends Neurosci*. 23:166-174.

Nicolay, K., and B. de Kruijff. 1987. Effects of adriamycin on respiratory chain activities in mitochondria from rat liver, rat heart and bovine heart. Evidence for a preferential inhibition of complex III and IV. *Biochim Biophys Acta*. 892:320-330.

O'Farrell, A.M., T.J. Abrams, H.A. Yuen, T.J. Ngai, S.G. Louie, K.W. Yee, L.M. Wong, W. Hong, L.B. Lee, A. Town, B.D. Smolich, W.C. Manning, L.J. Murray, M.C. Heinrich, and J.M. Cherrington. 2003. SU11248 is a novel FLT3 tyrosine kinase inhibitor with potent activity in vitro and in vivo. *Blood*. 101:3597-3605.

Oeffinger, K.C., A.C. Mertens, C.A. Sklar, T. Kawashima, M.M. Hudson, A.T. Meadows, D.L. Friedman, N. Marina, W. Hobbie, N.S. Kadan-Lottick, C.L. Schwartz, W. Leisenring, L.L. Robison, and S. Childhood Cancer Survivor. 2006. Chronic health conditions in adult survivors of childhood cancer. *N Engl J Med*. 355:1572-1582.

Oka, T., S. Hikoso, O. Yamaguchi, M. Taneike, T. Takeda, T. Tamai, J. Oyabu, T. Murakawa, H. Nakayama, K. Nishida, S. Akira, A. Yamamoto, I. Komuro, and K. Otsu. 2012. Mitochondrial DNA that escapes from autophagy causes inflammation and heart failure. *Nature*. 485:251-255.

Oka, T., J. Xu, R.A. Kaiser, J. Melendez, M. Hambleton, M.A. Sargent, A. Lorts, E.W. Brunskill, G.W. Dorn, 2nd, S.J. Conway, B.J. Aronow, J. Robbins, and J.D. Molkentin. 2007. Genetic manipulation of periostin expression reveals a role in cardiac hypertrophy and ventricular remodeling. *Circ Res*. 101:313-321.

Oldenburg, O., M.V. Cohen, D.M. Yellon, and J.M. Downey. 2002. Mitochondrial K(ATP) channels: role in cardioprotection. *Cardiovasc Res*. 55:429-437.

Oliveira, P.J., P.M. Coxito, A.P. Rolo, D.L. Santos, C.M. Palmeira, and A.J. Moreno. 2001. Inhibitory effect of carvedilol in the high-conductance state of the mitochondrial permeability transition pore. *Eur J Pharmacol*. 412:231-237.

Olson, R.E., and W.B. Schwartz. 1951. Myocardial metabolism in congestive heart failure. *Medicine (Baltimore)*. 30:21-41.

Ong, S.B., S. Subrayan, S.Y. Lim, D.M. Yellon, S.M. Davidson, and D.J. Hausenloy. 2010. Inhibiting mitochondrial fission protects the heart against ischemia/reperfusion injury. *Circulation*. 121:2012-2022.

Ottani, F., R. Latini, L. Staszewsky, L. La Vecchia, N. Locuratolo, M. Sicuro, S. Masson, S. Barlera, V. Milani, M. Lombardi, A. Costalunga, N. Mollichelli, A. Santarelli, N. De Cesare, P. Sganzerla, A. Boi, A.P. Maggioni, U. Limbruno, and C. Investigators. 2016. Cyclosporine A in Reperfused Myocardial Infarction: The Multicenter, Controlled, Open-Label CYCLE Trial. *J Am Coll Cardiol*. 67:365-374.

Otterbein, L.E., and A.M. Choi. 2000. Heme oxygenase: colors of defense against cellular stress. *Am J Physiol Lung Cell Mol Physiol*. 279:L1029-1037.

Pagani, F.D., L.S. Baker, C. Hsi, M. Knox, M.P. Fink, and M.S. Visner. 1992. Left ventricular systolic and diastolic dysfunction after infusion of tumor necrosis factor-alpha in conscious dogs. *J Clin Invest*. 90:389-398.

Park, J.S., H.S. Kim, M.Y. Park, C.H. Kim, Y.J. Chung, Y.K. Hong, and T.G. Kim. 2010. Topoisomerase II alpha as a universal tumor antigen: antitumor immunity in murine tumor models and H-2K(b)-restricted T cell epitope. *Cancer Immunol Immunother*. 59:747-757.

Patnaik, J.L., T. Byers, C. DiGuiseppi, D. Dabelea, and T.D. Denberg. 2011. Cardiovascular disease competes with breast cancer as the leading cause of death for older females diagnosed with breast cancer: a retrospective cohort study. *Breast Cancer Res*. 13:R64.

Patyna, S., A.D. Laird, D.B. Mendel, M. O'Farrell A, C. Liang, H. Guan, T. Vojkovsky, S. Vasile, X. Wang, J. Chen, M. Grazzini, C.Y. Yang, J.O. Haznedar, J. Sukbuntherng, W.Z. Zhong, J.M. Cherrington, and D. Hu-Lowe. 2006. SU14813: a novel multiple receptor tyrosine kinase inhibitor with potent antiangiogenic and antitumor activity. *Mol Cancer Ther*. 5:1774-1782.

Pavo, N., M. Raderer, M. Hulsmann, S. Neuhold, C. Adlbrecht, G. Strunk, G. Goliasch, H. Gisslinger, G.G. Steger, M. Hejna, W. Kostler, S. Zochbauer-Muller, C. Marosi, G. Kornek, L. Auerbach, S. Schneider, B. Parschalk, W. Scheithauer, R. Pirker, J. Drach, C. Zielinski, and R. Pacher. 2015. Cardiovascular biomarkers in patients with cancer and their association with all-cause mortality. *Heart*. 101:1874-1880.

Perry, S.W., J.P. Norman, J. Barbieri, E.B. Brown, and H.A. Gelbard. 2011. Mitochondrial membrane potential probes and the proton gradient: a practical usage guide. *Biotechniques*. 50:98-115.

Pieske, B., M. Sutterlin, S. Schmidt-Schweda, K. Minami, M. Meyer, M. Olschewski, C. Holubarsch, H. Just, and G. Hasenfuss. 1996. Diminished post-rest potentiation of contractile force in human dilated cardiomyopathy. Functional evidence for alterations in intracellular Ca2+ handling. *J Clin Invest*. 98:764-776.

Piot, C., P. Croisille, P. Staat, H. Thibault, G. Rioufol, N. Mewton, R. Elbelghiti, T.T. Cung, E. Bonnefoy, D. Angoulvant, C. Macia, F. Raczka, C. Sportouch, G. Gahide, G. Finet, X. Andre-Fouet, D. Revel, G. Kirkorian, J.P. Monassier, G. Derumeaux, and M. Ovize. 2008. Effect of cyclosporine on reperfusion injury in acute myocardial infarction. *N Engl J Med*. 359:473-481.

Pointon, A.V., T.M. Walker, K.M. Phillips, J. Luo, J. Riley, S.D. Zhang, J.D. Parry, J.J. Lyon, E.L. Marczylo, and T.W. Gant. 2010. Doxorubicin in vivo rapidly alters expression and translation of myocardial electron transport chain genes, leads to ATP loss and caspase 3 activation. *PLoS One*. 5:e12733.

Ponikowski, P., A.A. Voors, S.D. Anker, H. Bueno, J.G. Cleland, A.J. Coats, V. Falk, J.R. Gonzalez-Juanatey, V.P. Harjola, E.A. Jankowska, M. Jessup, C. Linde, P. Nihoyannopoulos, J.T. Parissis, B. Pieske, J.P. Riley, G.M. Rosano, L.M. Ruilope, F. Ruschitzka, F.H. Rutten, P. van der Meer, and M. Authors/Task Force. 2016. 2016 ESC Guidelines for the diagnosis and treatment of acute and chronic heart failure: The Task Force for the diagnosis and treatment of acute and chronic heart failure of

the European Society of Cardiology (ESC)Developed with the special contribution of the Heart Failure Association (HFA) of the ESC. *Eur Heart J*. 37:2129-2200.

Qian, J.Y., and L. Guo. 2010. Altered cytosolic Ca2+ dynamics in cultured Guinea pig cardiomyocytes as an in vitro model to identify potential cardiotoxicants. *Toxicol In Vitro*. 24:960-972.

Quiles, J.L., J.R. Huertas, M. Battino, J. Mataix, and M.C. Ramirez-Tortosa. 2002. Antioxidant nutrients and adriamycin toxicity. *Toxicology*. 180:79-95.

Reers, M., S.T. Smiley, C. Mottola-Hartshorn, A. Chen, M. Lin, and L.B. Chen. 1995. Mitochondrial membrane potential monitored by JC-1 dye. *Methods Enzymol*. 260:406-417.

Riad, A., S. Bien, M. Gratz, F. Escher, D. Westermann, M.M. Heimesaat, S. Bereswill, T. Krieg, S.B. Felix, H.P. Schultheiss, H.K. Kroemer, and C. Tschope. 2008. Toll-like receptor-4 deficiency attenuates doxorubicin-induced cardiomyopathy in mice. *Eur J Heart Fail*. 10:233-243.

Rizzuto, R., S. Marchi, M. Bonora, P. Aguiari, A. Bononi, D. De Stefani, C. Giorgi, S. Leo, A. Rimessi, R. Siviero, E. Zecchini, and P. Pinton. 2009. Ca(2+) transfer from the ER to mitochondria: when, how and why. *Biochim Biophys Acta*. 1787:1342-1351.

Robinson, E.S., E.V. Khankin, S.A. Karumanchi, and B.D. Humphreys. 2010. Hypertension induced by vascular endothelial growth factor signaling pathway inhibition: mechanisms and potential use as a biomarker. *Semin Nephrol*. 30:591-601.

Rock, K.L., and H. Kono. 2008. The inflammatory response to cell death. *Annu Rev Pathol*. 3:99-126.

Rolfe, D.F., and G.C. Brown. 1997. Cellular energy utilization and molecular origin of standard metabolic rate in mammals. *Physiol Rev*. 77:731-758.

Rooney, J.P., I.T. Ryde, L.H. Sanders, E.H. Howlett, M.D. Colton, K.E. Germ, G.D. Mayer, J.T. Greenamyre, and J.N. Meyer. 2015. PCR based determination of mitochondrial DNA copy number in multiple species. *Methods Mol Biol*. 1241:23-38.

Rossman, E.I., R.E. Petre, K.W. Chaudhary, V. Piacentino, 3rd, P.M. Janssen, J.P. Gaughan, S.R. Houser, and K.B. Margulies. 2004. Abnormal frequency-dependent responses represent the pathophysiologic signature of contractile failure in human myocardium. *Journal of molecular and cellular cardiology*. 36:33-42.

Rudzinski, T., M. Ciesielczyk, W. Religa, Z. Bednarkiewicz, and M. Krzeminska-Pakula. 2007. Doxorubicin-induced ventricular arrhythmia treated by implantation of an automatic cardioverter-defibrillator. *Europace*. 9:278-280.

Sabbah, H.N., R.C. Gupta, S. Kohli, M. Wang, S. Hachem, and K. Zhang. 2016. Chronic Therapy With Elamipretide (MTP-131), a Novel Mitochondria-Targeting Peptide, Improves Left Ventricular and Mitochondrial Function in Dogs With Advanced Heart Failure. *Circ Heart Fail*. 9:e002206.

Saelens, X., N. Festjens, E. Parthoens, I. Vanoverberghe, M. Kalai, F. van Kuppeveld, and P. Vandenabeele. 2005. Protein synthesis persists during necrotic cell death. *J Cell Biol*. 168:545-551.

Saelens, X., N. Festjens, L. Vande Walle, M. van Gurp, G. van Loo, and P. Vandenabeele. 2004. Toxic proteins released from mitochondria in cell death. *Oncogene*. 23:2861-2874.

Safar, M.E., B.I. Levy, and H. Struijker-Boudier. 2003. Current perspectives on arterial stiffness and pulse pressure in hypertension and cardiovascular diseases. *Circulation*. 107:2864-2869.

Salzer, W.L., M. Devidas, W.L. Carroll, N. Winick, J. Pullen, S.P. Hunger, and B.A. Camitta. 2010. Long-term results of the pediatric oncology group studies for childhood acute lymphoblastic leukemia 1984-2001: a report from the children's oncology group. *Leukemia*. 24:355-370.

Sauter, K.A., L.J. Wood, J. Wong, M. Iordanov, and B.E. Magun. 2011. Doxorubicin and daunorubicin induce processing and release of interleukin-1beta through activation of the NLRP3 inflammasome. *Cancer Biol Ther*. 11:1008-1016.

Sawyer, D.T., and J.S. Valentine. 1981. How super is superoxide? *Accounts of Chemical Research*. 14:393-400.

Scaduto, R.C., Jr., and L.W. Grotyohann. 1999. Measurement of mitochondrial membrane potential using fluorescent rhodamine derivatives. *Biophys J*. 76:469-477.

Scaglia, F., J.A. Towbin, W.J. Craigen, J.W. Belmont, E.O. Smith, S.R. Neish, S.M. Ware, J.V. Hunter, S.D. Fernbach, G.D. Vladutiu, L.J. Wong, and H. Vogel. 2004. Clinical spectrum, morbidity, and mortality in 113 pediatric patients with mitochondrial disease. *Pediatrics*. 114:925-931.

Schaper, J., E. Meiser, and G. Stammler. 1985. Ultrastructural morphometric analysis of myocardium from dogs, rats, hamsters, mice, and from human hearts. *Circ Res*. 56:377-391.

Schmalhausen, E.V., A.P. Pleten, and V.I. Muronetz. 2003. Ascorbate-induced oxidation of glyceraldehyde-3-phosphate dehydrogenase. *Biochem Biophys Res Commun*. 308:492-496.

Schmidinger, M., C.C. Zielinski, U.M. Vogl, A. Bojic, M. Bojic, C. Schukro, M. Ruhsam, M. Hejna, and H. Schmidinger. 2008. Cardiac toxicity of sunitinib and sorafenib in patients with metastatic renal cell carcinoma. *J Clin Oncol*. 26:5204-5212.

Schroder, K., and J. Tschopp. 2010. The inflammasomes. *Cell*. 140:821-832.

Schwarz, E.R., C. Pollick, J. Dow, M. Patterson, Y. Birnbaum, and R.A. Kloner. 1998. A small animal model of non-ischemic cardiomyopathy and its evaluation by transthoracic echocardiography. *Cardiovasc Res*. 39:216-223.

Seidman, A., C. Hudis, M.K. Pierri, S. Shak, V. Paton, M. Ashby, M. Murphy, S.J. Stewart, and D. Keefe. 2002. Cardiac dysfunction in the trastuzumab clinical trials experience. *J Clin Oncol*. 20:1215-1221.

Serrano, J., C.M. Palmeira, D.W. Kuehl, and K.B. Wallace. 1999. Cardioselective and cumulative oxidation of mitochondrial DNA following subchronic doxorubicin administration. *Biochim Biophys Acta*. 1411:201-205.

Shankaran, V., H. Ikeda, A.T. Bruce, J.M. White, P.E. Swanson, L.J. Old, and R.D. Schreiber. 2001. IFNgamma and lymphocytes prevent primary tumour development and shape tumour immunogenicity. *Nature*. 410:1107-1111.

Sharma, U.C., S. Pokharel, C.T. Evelo, and J.G. Maessen. 2005. A systematic review of large scale and heterogeneous gene array data in heart failure. *Journal of molecular and cellular cardiology*. 38:425-432.

Shimauchi, T., T. Numaga-Tomita, T. Ito, A. Nishimura, R. Matsukane, S. Oda, S. Hoka, T. Ide, N. Koitabashi, K. Uchida, H. Sumimoto, Y. Mori, and M. Nishida. 2017. TRPC3-Nox2 complex mediates doxorubicin-induced myocardial atrophy. *JCI Insight*. 2.

Shimizu, H., J. Schredelseker, J. Huang, K. Lu, S. Naghdi, F. Lu, S. Franklin, H.D. Fiji, K. Wang, H. Zhu, C. Tian, B. Lin, H. Nakano, A. Ehrlich, J. Nakai, A.Z. Stieg, J.K. Gimzewski, A. Nakano, J.I. Goldhaber, T.M. Vondriska, G. Hajnoczky, O. Kwon, and J.N. Chen. 2015. Mitochondrial Ca(2+) uptake by the voltage-dependent anion channel 2 regulates cardiac rhythmicity. *Elife*. 4.

Sica, D.A. 2006. Angiogenesis inhibitors and hypertension: an emerging issue. *J Clin Oncol*. 24:1329-1331.

Silvestri, G., F.M. Santorelli, S. Shanske, C.B. Whitley, L.A. Schimmenti, S.A. Smith, and S. DiMauro. 1994. A new mtDNA mutation in the tRNA(Leu(UUR)) gene associated with maternally inherited cardiomyopathy. *Hum Mutat*. 3:37-43.

Skalli, O., W. Schurch, T. Seemayer, R. Lagace, D. Montandon, B. Pittet, and G. Gabbiani. 1989. Myofibroblasts from diverse pathologic settings are heterogeneous in their content of actin isoforms and intermediate filament proteins. *Lab Invest*. 60:275-285.

Skrzypiec-Spring, M., B. Grotthus, A. Szelag, and R. Schulz. 2007. Isolated heart perfusion according to Langendorff---still viable in the new millennium. *J Pharmacol Toxicol Methods*. 55:113-126.

Slamon, D.J., B. Leyland-Jones, S. Shak, H. Fuchs, V. Paton, A. Bajamonde, T. Fleming, W. Eiermann, J. Wolter, M. Pegram, J. Baselga, and L. Norton. 2001. Use of chemotherapy plus a monoclonal antibody against HER2 for metastatic breast cancer that overexpresses HER2. *N Engl J Med*. 344:783-792.

Smith, R.A., G.F. Kelso, A.M. James, and M.P. Murphy. 2004. Targeting coenzyme Q derivatives to mitochondria. *Methods Enzymol*. 382:45-67.

Soldani, C., and A.I. Scovassi. 2002. Poly(ADP-ribose) polymerase-1 cleavage during apoptosis: an update. *Apoptosis*. 7:321-328.

Spallarossa, P., S. Garibaldi, P. Altieri, P. Fabbi, V. Manca, S. Nasti, P. Rossettin, G. Ghigliotti, A. Ballestrero, F. Patrone, A. Barsotti, and C. Brunelli. 2004. Carvedilol prevents doxorubicin-induced free radical release and apoptosis in cardiomyocytes in vitro. *Journal of molecular and cellular cardiology*. 37:837-846.

Speyer, J.L., M.D. Green, E. Kramer, M. Rey, J. Sanger, C. Ward, N. Dubin, V. Ferrans, P. Stecy, A. Zeleniuch-Jacquotte, and et al. 1988. Protective effect of the bispiperazinedione ICRF-187 against doxorubicin-induced cardiac toxicity in women with advanced breast cancer. *N Engl J Med*. 319:745-752.

Springer, J., A. Tschirner, A. Haghikia, S. von Haehling, H. Lal, A. Grzesiak, E. Kaschina, S. Palus, M. Potsch, K. von Websky, B. Hocher, C. Latouche, F. Jaisser, L. Morawietz, A.J. Coats, J. Beadle, J.M. Argiles, T. Thum, G. Foldes, W. Doehner, D. Hilfiker-Kleiner, T. Force, and S.D. Anker. 2014. Prevention of liver cancer cachexia-induced cardiac wasting and heart failure. *Eur Heart J*. 35:932-941.

Spyrou, G., E. Enmark, A. Miranda-Vizuete, and J. Gustafsson. 1997. Cloning and expression of a novel mammalian thioredoxin. *J Biol Chem*. 272:2936-2941.

Stanley, B.A., V. Sivakumaran, S. Shi, I. McDonald, D. Lloyd, W.H. Watson, M.A. Aon, and N. Paolocci. 2011. Thioredoxin reductase-2 is essential for keeping low levels of H(2)O(2) emission from isolated heart mitochondria. *J Biol Chem*. 286:33669-33677.

Stanton, L.W., L.J. Garrard, D. Damm, B.L. Garrick, A. Lam, A.M. Kapoun, Q. Zheng, A.A. Protter, G.F. Schreiner, and R.T. White. 2000. Altered patterns of gene expression in response to myocardial infarction. *Circ Res*. 86:939-945.

Steeghs, N., H. Gelderblom, J.O. Roodt, O. Christensen, P. Rajagopalan, M. Hovens, H. Putter, T.J. Rabelink, and E. de Koning. 2008. Hypertension and rarefaction during treatment with telatinib, a small molecule angiogenesis inhibitor. *Clin Cancer Res*. 14:3470-3476.

Steeghs, N., T.J. Rabelink, J. op 't Roodt, E. Batman, F.H. Cluitmans, N.I. Weijl, E. de Koning, and H. Gelderblom. 2010. Reversibility of capillary density after discontinuation of bevacizumab treatment. *Ann Oncol*. 21:1100-1105.

Steinherz, L.J., P.G. Steinherz, C.T. Tan, G. Heller, and M.L. Murphy. 1991. Cardiac toxicity 4 to 20 years after completing anthracycline therapy. *JAMA*. 266:1672-1677.

Stratton, J.R., W.C. Levy, M.D. Cerqueira, R.S. Schwartz, and I.B. Abrass. 1994. Cardiovascular responses to exercise. Effects of aging and exercise training in healthy men. *Circulation*. 89:1648-1655.

Stutz, A., D.T. Golenbock, and E. Latz. 2009. Inflammasomes: too big to miss. *J Clin Invest*. 119:3502-3511.

Sun, X.M., M. Butterworth, M. MacFarlane, W. Dubiel, A. Ciechanover, and G.M. Cohen. 2004. Caspase activation inhibits proteasome function during apoptosis. *Mol Cell*. 14:81-93.

Suter, T.M., and M.S. Ewer. 2013. Cancer drugs and the heart: importance and management. *Eur Heart J*. 34:1102-1111.

Suzuki, T., D. Hayashi, T. Yamazaki, T. Mizuno, Y. Kanda, I. Komuro, M. Kurabayashi, K. Yamaoki, K. Mitani, H. Hirai, R. Nagai, and Y. Yazaki. 1998. Elevated B-type natriuretic peptide levels after anthracycline administration. *Am Heart J*. 136:362-363.

Swain, S.M., F.S. Whaley, and M.S. Ewer. 2003. Congestive heart failure in patients treated with doxorubicin: a retrospective analysis of three trials. *Cancer*. 97:2869-2879.

Swain, S.M., F.S. Whaley, M.C. Gerber, S. Weisberg, M. York, D. Spicer, S.E. Jones, S. Wadler, A. Desai, C. Vogel, J. Speyer, A. Mittelman, S. Reddy, K. Pendergrass, E. Velez-Garcia, M.S. Ewer, J.R. Bianchine, and R.A. Gams. 1997. Cardioprotection with dexrazoxane for doxorubicin-containing therapy in advanced breast cancer. *J Clin Oncol*. 15:1318-1332.

Syrigos, K.N., E. Karapanagiotou, P. Boura, C. Manegold, and K. Harrington. 2011. Bevacizumab-induced hypertension: pathogenesis and management. *BioDrugs*. 25:159-169.

Tan, C., E. Etcubanas, N. Wollner, G. Rosen, A. Gilladoga, J. Showel, M.L. Murphy, and I.H. Krakoff. 1973. Adriamycin--an antitumor antibiotic in the treatment of neoplastic diseases. *Cancer*. 32:9-17.

Tan, C., H. Tasaka, K.P. Yu, M.L. Murphy, and D.A. Karnofsky. 1967. Daunomycin, an antitumor antibiotic, in the treatment of neoplastic disease. Clinical evaluation with special reference to childhood leukemia. *Cancer*. 20:333-353.

Tangpong, J., S. Miriyala, T. Noel, C. Sinthupibulyakit, P. Jungsuwadee, and D.K. St Clair. 2011. Doxorubicin-induced central nervous system toxicity and protection by xanthone derivative of Garcinia mangostana. *Neuroscience*. 175:292-299.

Taniike, M., H. Fukushima, I. Yanagihara, H. Tsukamoto, J. Tanaka, H. Fujimura, T. Nagai, T. Sano, K. Yamaoka, K. Inui, and et al. 1992. Mitochondrial tRNA(Ile) mutation in fatal cardiomyopathy. *Biochem Biophys Res Commun*. 186:47-53.

Tashakori Beheshti, A., H. Mostafavi Toroghi, G. Hosseini, A. Zarifian, F. Homaei Shandiz, and A. Fazlinezhad. 2016. Carvedilol Administration Can Prevent Doxorubicin-Induced Cardiotoxicity: A Double-Blind Randomized Trial. *Cardiology*. 134:47-53.

Taunk, N.K., B.G. Haffty, J.B. Kostis, and S. Goyal. 2015. Radiation-induced heart disease: pathologic abnormalities and putative mechanisms. *Front Oncol*. 5:39.

Tebbi, C.K., W.B. London, D. Friedman, D. Villaluna, P.A. De Alarcon, L.S. Constine, N.P. Mendenhall, R. Sposto, A. Chauvenet, and C.L. Schwartz. 2007. Dexrazoxane-associated risk for acute myeloid leukemia/myelodysplastic syndrome and other secondary malignancies in pediatric Hodgkin's disease. *J Clin Oncol*. 25:493-500.

Testa, M., M. Yeh, P. Lee, R. Fanelli, F. Loperfido, J.W. Berman, and T.H. LeJemtel. 1996. Circulating levels of cytokines and their endogenous modulators in patients with mild to severe congestive heart failure due to coronary artery disease or hypertension. *J Am Coll Cardiol*. 28:964-971.

Tewey, K.M., T.C. Rowe, L. Yang, B.D. Halligan, and L.F. Liu. 1984. Adriamycin-induced DNA damage mediated by mammalian DNA topoisomerase II. *Science*. 226:466-468.

Thirunavukkarasu, M., S. Addya, B. Juhasz, R. Pant, L. Zhan, S. Surrey, G. Maulik, V.P. Menon, and N. Maulik. 2008. Heterozygous disruption of Flk-1 receptor leads to myocardial ischaemia reperfusion injury in mice: application of affymetrix gene chip analysis. *J Cell Mol Med*. 12:1284-1302.

Thirunavukkarasu, M., B. Juhasz, L. Zhan, V.P. Menon, A. Tosaki, H. Otani, and N. Maulik. 2007. VEGFR1 (Flt-1+/-) gene knockout leads to the disruption of VEGF-mediated

signaling through the nitric oxide/heme oxygenase pathway in ischemic preconditioned myocardium. *Free Radic Biol Med*. 42:1487-1495.

Torre-Amione, G., S. Kapadia, C. Benedict, H. Oral, J.B. Young, and D.L. Mann. 1996a. Proinflammatory cytokine levels in patients with depressed left ventricular ejection fraction: a report from the Studies of Left Ventricular Dysfunction (SOLVD). *J Am Coll Cardiol*. 27:1201-1206.

Torre-Amione, G., S. Kapadia, J. Lee, J.B. Durand, R.D. Bies, J.B. Young, and D.L. Mann. 1996b. Tumor necrosis factor-alpha and tumor necrosis factor receptors in the failing human heart. *Circulation*. 93:704-711.

Tracey, K.J., B. Beutler, S.F. Lowry, J. Merryweather, S. Wolpe, I.W. Milsark, R.J. Hariri, T.J. Fahey, 3rd, A. Zentella, J.D. Albert, and et al. 1986. Shock and tissue injury induced by recombinant human cachectin. *Science*. 234:470-474.

Trapnell, C., A. Roberts, L. Goff, G. Pertea, D. Kim, D.R. Kelley, H. Pimentel, S.L. Salzberg, J.L. Rinn, and L. Pachter. 2012. Differential gene and transcript expression analysis of RNA-seq experiments with TopHat and Cufflinks. *Nat Protoc*. 7:562-578.

Trapnell, C., B.A. Williams, G. Pertea, A. Mortazavi, G. Kwan, M.J. van Baren, S.L. Salzberg, B.J. Wold, and L. Pachter. 2010. Transcript assembly and quantification by RNA-Seq reveals unannotated transcripts and isoform switching during cell differentiation. *Nat Biotechnol*. 28:511-515.

Tretter, L., and V. Adam-Vizi. 2000. Inhibition of Krebs cycle enzymes by hydrogen peroxide: A key role of [alpha]-ketoglutarate dehydrogenase in limiting NADH production under oxidative stress. *J Neurosci*. 20:8972-8979.

Turkseven, S., A. Kruger, C.J. Mingone, P. Kaminski, M. Inaba, L.F. Rodella, S. Ikehara, M.S. Wolin, and N.G. Abraham. 2005. Antioxidant mechanism of heme oxygenase-1 involves an increase in superoxide dismutase and catalase in experimental diabetes. *Am J Physiol Heart Circ Physiol*. 289:H701-707.

Unverferth, D.V., J.M. Jagadeesh, B.J. Unverferth, R.D. Magorien, C.V. Leier, and S.P. Balcerzak. 1983. Attempt to prevent doxorubicin-induced acute human myocardial morphologic damage with acetylcysteine. *J Natl Cancer Inst*. 71:917-920.

van der Veldt, A.A., M.P. de Boer, E. Boven, E.C. Eringa, A.J. van den Eertwegh, V.W. van Hinsbergh, Y.M. Smulders, and E.H. Serne. 2010. Reduction in skin microvascular density and changes in vessel morphology in patients treated with sunitinib. *Anticancer Drugs*. 21:439-446.

Vasquez-Vivar, J., P. Martasek, N. Hogg, B.S. Masters, K.A. Pritchard, Jr., and B. Kalyanaraman. 1997. Endothelial nitric oxide synthase-dependent superoxide generation from adriamycin. *Biochemistry*. 36:11293-11297.

Ventura-Clapier, R., A. Garnier, and V. Veksler. 2004. Energy metabolism in heart failure. *J Physiol*. 555:1-13.

Verheul, H.M., and H.M. Pinedo. 2007. Possible molecular mechanisms involved in the toxicity of angiogenesis inhibition. *Nat Rev Cancer*. 7:475-485.

Verkhivker, G.M. 2007. Exploring sequence-structure relationships in the tyrosine kinome space: functional classification of the binding specificity mechanisms for cancer therapeutics. *Bioinformatics*. 23:1919-1926.

Veronese, M.L., A. Mosenkis, K.T. Flaherty, M. Gallagher, J.P. Stevenson, R.R. Townsend, and P.J. O'Dwyer. 2006. Mechanisms of hypertension associated with BAY 43-9006. *J Clin Oncol*. 24:1363-1369.

Viswanatha Swamy, A.H., U. Wangikar, B.C. Koti, A.H. Thippeswamy, P.M. Ronad, and D.V. Manjula. 2011. Cardioprotective effect of ascorbic acid on doxorubicin-induced myocardial toxicity in rats. *Indian J Pharmacol*. 43:507-511.

Von Hoff, D.D., M.W. Layard, P. Basa, H.L. Davis, Jr., A.L. Von Hoff, M. Rozencweig, and F.M. Muggia. 1979. Risk factors for doxorubicin-induced congestive heart failure. *Ann Intern Med*. 91:710-717.

Wang, Z., M. Gerstein, and M. Snyder. 2009. RNA-Seq: a revolutionary tool for transcriptomics. *Nat Rev Genet*. 10:57-63.

Wardman, P., and L.P. Candeias. 1996. Fenton chemistry: an introduction. *Radiat Res*. 145:523-531.

Weisiger, R.A., and I. Fridovich. 1973. Superoxide dismutase. Organelle specificity. *J Biol Chem*. 248:3582-3592.

Weiss, R.B. 1992. The anthracyclines: will we ever find a better doxorubicin? *Semin Oncol*. 19:670-686.

Will, Y., J.A. Dykens, S. Nadanaciva, B. Hirakawa, J. Jamieson, L.D. Marroquin, J. Hynes, S. Patyna, and B.A. Jessen. 2008. Effect of the multitargeted tyrosine kinase inhibitors imatinib, dasatinib, sunitinib, and sorafenib on mitochondrial function in isolated rat heart mitochondria and H9c2 cells. *Toxicol Sci*. 106:153-161.

Wynn, T.A. 2008. Cellular and molecular mechanisms of fibrosis. *J Pathol*. 214:199-210.

Xie, L., J. Terrand, B. Xu, G. Tsaprailis, J. Boyer, and Q.M. Chen. 2010. Cystatin C increases in cardiac injury: a role in extracellular matrix protein modulation. *Cardiovasc Res*. 87:628-635.

Yancey, D.M., J.L. Guichard, M.I. Ahmed, L. Zhou, M.P. Murphy, M.S. Johnson, G.A. Benavides, J. Collawn, V. Darley-Usmar, and L.J. Dell'Italia. 2015. Cardiomyocyte mitochondrial oxidative stress and cytoskeletal breakdown in the heart with a primary volume overload. *Am J Physiol Heart Circ Physiol*. 308:H651-663.

Yokoyama, T., M. Nakano, J.L. Bednarczyk, B.W. McIntyre, M. Entman, and D.L. Mann. 1997. Tumor necrosis factor-alpha provokes a hypertrophic growth response in adult cardiac myocytes. *Circulation*. 95:1247-1252.

Youle, R.J., and A. Strasser. 2008. The BCL-2 protein family: opposing activities that mediate cell death. *Nat Rev Mol Cell Biol*. 9:47-59.

Young, D.M., J.L. Fioravanti, H.M. Olson, and D.J. Prieur. 1975. Chemical and morphologic alterations of rabbit bone induced by adriamycin. *Calcif Tissue Res*. 18:47-63.

Zak, R. 1974. Development and proliferative capacity of cardiac muscle cells. *Circ Res*. 35:suppl II:17-26.

Zhang, S., X. Liu, T. Bawa-Khalfe, L.S. Lu, Y.L. Lyu, L.F. Liu, and E.T. Yeh. 2012. Identification of the molecular basis of doxorubicin-induced cardiotoxicity. *Nat Med*. 18:1639-1642.

Zhao, K., G.M. Zhao, D. Wu, Y. Soong, A.V. Birk, P.W. Schiller, and H.H. Szeto. 2004. Cell-permeable peptide antioxidants targeted to inner mitochondrial membrane inhibit mitochondrial swelling, oxidative cell death, and reperfusion injury. *J Biol Chem*. 279:34682-34690.

Zhao, S., H. Wu, W. Xia, X. Chen, S. Zhu, S. Zhang, Y. Shao, W. Ma, D. Yang, and J. Zhang. 2014. Periostin expression is upregulated and associated with myocardial fibrosis in human failing hearts. *Journal of cardiology*. 63:373-378.

Zhou, R., A.S. Yazdi, P. Menu, and J. Tschopp. 2011. A role for mitochondria in NLRP3 inflammasome activation. *Nature*. 469:221-225.

Zhou, S., A. Starkov, M.K. Froberg, R.L. Leino, and K.B. Wallace. 2001. Cumulative and irreversible cardiac mitochondrial dysfunction induced by doxorubicin. *Cancer Res*. 61:771-777.

Zhu, J., J. Zhang, D. Xiang, Z. Zhang, L. Zhang, M. Wu, S. Zhu, R. Zhang, and W. Han. 2010. Recombinant human interleukin-1 receptor antagonist protects mice against acute doxorubicin-induced cardiotoxicity. *Eur J Pharmacol*. 643:247-253.

Zsila, F., I. Fitos, G. Bencze, G. Keri, and L. Orfi. 2009. Determination of human serum alpha1-acid glycoprotein and albumin binding of various marketed and preclinical kinase inhibitors. *Curr Med Chem*. 16:1964-1977.